PHOTOPRODUCTION OF $D^{\star\pm}$ and D° MESONS

BY

GLEN RICHARD JAROSS

B.S., University of Illinois, 1982
M.S., University of Illinois, 1983

THESIS

Submitted in partial fulfillment of the requirements
for the degree of Doctor of Philosophy in Physics
in the Graduate College of the
University of Illinois at Urbana-Champaign, 1991

Urbana, Illinois

Mim2001

PHOTOPRODUCTION OF $\mathrm{D}^{\star\pm}$ AND D° MESONS

Glen Richard Jaross, Ph.D.
Department of Physics
University of Illinois at Urbana-Champaign, 1991
J. Wiss, Advisor

The charmed mesons D° and $\mathrm{D}^{\star\pm}$ have been observed in photon-nucleus collisions at the FNAL Wide Band Laboratory. A sample of 5500 inclusive D° events and 1400 $\mathrm{D}^{\star\pm} \rightarrow \mathrm{D}^{\circ}\pi^{\pm}$ events were used to study charm production mechanisms and D° meson decay dynamics.

The cross section for producing D° and $\mathrm{D}^{\star\pm}$ mesons has been measured in the $\mathrm{K}^{\pm}\pi^{\mp}$ and $\mathrm{K}^{\pm}\pi^{-}\pi^{+}\pi^{\mp}$ decay modes of the D° meson as a function of incident photon energy and Feynman x. The results agree reasonably well with previous measurements.

The mean lifetime of the D° meson has been measured as :

$$\tau_D = 0.431 \pm .010 \pm .023 \quad \text{picoseconds}$$

using a sample of 2913 ± 101 events. The decay $\mathrm{D}^{\star\pm} \rightarrow (\mathrm{K}^{+}\mathrm{K}^{-})\pi^{\pm}$ has been observed at a level of 56 ± 14 events, and its branching ratio was calculated to be

$$\frac{\Gamma(\, D^{\star\pm} \rightarrow (K^{+}K^{-})\pi^{\pm}\,)}{\Gamma(\, D^{\star\pm} \rightarrow (K^{+}\pi^{-})\pi\,)} = .118 \pm .032$$

The decay $\mathrm{D}^{\circ} \rightarrow \pi^{+}\pi^{-}\pi^{+}\pi^{-}$ was also observed. Its branching ratio

$$\frac{\Gamma(\, D^{\circ} \rightarrow \pi^{+}\pi^{-}\pi^{+}\pi^{-}\,)}{\Gamma(\, D^{\circ} \rightarrow K^{+}\pi^{-}\pi^{+}\pi^{-}\,)} = .114 \pm .026$$

was calculated on the basis of 235 ± 43 events.

Acknowledgements

Much of my ability to complete this thesis is due to the success of the experiment, E687. As with any modern high energy physics experiment, a large number of people are responsible for the outcome. Many of these people I know only by name, while others I do not know at all. The experimenters who developed E87 and E400 laid the framework for the successful design of E687, and the hard work of many technicians, especially after the fire, was instrumental in its realization. In particular Joel Butler deserves credit for pulling these diverse elements together and making the experiment function.

Many individuals in the E687 collaboration were indispensible; I would have no results without their efforts. In some cases I may not even be aware of the importance of their contributions, but I appreciate them all the same. Of the people with whom I worked, I value most highly my association with Jim Wiss, my advisor. Our frequent interaction on every aspect of my work made it rather difficult for me to "sail off course," and allowed me to accomplish much more than I could have with another advisor. My other colleagues in the University of Illinois group deserve recognition as well. Jeff Wilson and Ray Culbertson are responsible for much of the computer software which I used in my analysis, including the ever important vertex finding algorithm. I also appreciate Jeff's help in solving those annoying computer problems that inevitably occur in a large analysis effort. Karen Lingel's work developing the Monte Carlo into a useable tool saved me an immeasurable amount of time.

Eric Mannel deserves special thanks as well. His knack for ending up with some of the most time consuming and unprestigious jobs in the experiment should not go unnoticed.

Both Jerry Wray and Dave Lesny are responsible for creating and maintaining a computing environment which few other institutions can equal. There is much I could not have accomplished were this not true.

Finally, the many years as graduate student would have been considerably harder without the care and support from family and friends. I am especially grateful to my wife Mary, whose invaluable help and understanding over the last year was often taken for granted. I guess it's my turn to do the dishes now. Most of all I owe my accomplishment to the love and encouragement of my parents which laid the foundation of my education.

This research is funded in part by the U.S. Department of Energy under contract DEAC02-76ER01195.

Contents

Abbreviations

ADC	Analog to Digital Converter
BGM	Beam Gamma Monitor – an electromagnetic shower detector designed to collect uninteracted beam photons
BR	Branching Ratio – in this text, used as ratio between two decay rates
BT	Beam Electron Trigger Counter
CL	Confidence Level – used here primarily as a measure of vertex quality
DAQ	Data Acquisition System
DST	Data Summary Tape
HC	Hadron Calorimeter – a gas calorimeter which measures the energy of charged hadrons
H×V	a scintillator hodoscope for triggering in the low angle portion of the spectrometer
IE	Inner Electromagnetic Calorimeter – covers the low angle region of the spectrometer
MCS	Multiple Coulomb Scattering
MWPC	Multi-wire Proportional Chamber
OE	Outer Electromagnetic Calorimeter – covers angles beyond those of the IE
OH	a scintillator hodoscope for triggering in the large angle region of the spectrometer
PGF	Photon-Gluon Fusion Model
PMT	Photomultiplier Tube
RESH	Recoil Electron Shower Counter – measures the momentum of recoil electrons after bremsstrahlung
SSD	Silicon Microstrip Detector
TR1	Trigger Counter 1 – immediately upstream of SSD system
TR2	Trigger Counter 2 – immediately downstream of SSD system
VDM	Vector Meson Dominance Model

Chapter 1

Introduction

This thesis discusses results obtained from the high energy photoproduction experiment E687 conducted at Fermi National Accelerator Laboratory between June of 1987 and February of 1988. E687 is a fixed target experiment located in the Wide Band Photon Laboratory and features a beryllium target and a large acceptance magnetic spectrometer. Photons with a mean energy of 225 GeV were used to study γ-Be interactions with an emphasis on the production of heavy flavor states such as charm and beauty. A charm sample of roughly 10,000 charmed particles was obtained and has been used to study numerous topics related to charm photoproduction mechanisms and decay dynamics. Results presented in this thesis deal with both of these topics using a high statistics sample of D° and $D^{\star +}$ mesons.

The study of heavy quark production using γ-nucleon interactions began in earnest after the first observations of ψ states 16 years ago. The establishment of a new class of particles involving the charmed quark opened up a new field of study in photoproduction experiments as well as in e^+e^- and hadroproduction experiments. The advantage of charm photoproduction has been its large number of reconstructed charm events relative to the other two types of experiments. Charm states produced in e^+e^- annihilation experiments are produced with far less background than in fixed target experiments, but total yields are higher in photoproduction experiments. Other advantages include the ability to observe simultaneously a large charm quark invariant mass spectrum. High statistics samples of photoproduced charmed mesons and baryons (D and Λ_c) have been used in many important measurements of charm decay dynamics such as branching ratios and lifetimes. Much of the effort in photoproduction experiments has also been in the measurement of charm photoproduction dynamics. Several production models have been proposed that are successful at describing the observed dynamics. Some of these mechanisms are discussed next in the context of recent measurements.

1.1 Production Mechanisms

Studies of the interaction $\gamma N \rightarrow c\bar{c}$ were initially made with ψ production where the diffractive nature of the interaction lead to an understanding of charm production in terms of a vector meson dominance model (VDM). VDM attributes both open and closed charm production to direct coupling between the photon and vector mesons containing $c\bar{c}$ pairs (ψ, ψ', ψ'' mesons) followed by subsequent interaction of vector mesons with the nucleon (see Figure 1-1(a)). VDM does a reasonably good job of accounting for both the level of the charm cross section and the general features of photoproduced charm at low energy.

1.1.1 Diffractive Models

More recently data have been interpreted in the context of a perturbative QCD model called the Photon-Gluon Fusion[1] model (PGF).The two lowest order diagrams are shown in Figure 1-1(b). In this process the incident photon fuses with a gluon in the nucleon to form a $c\bar{c}$ pair. Like VDM, this model predicts diffractive production of final states since the momentum transfer involved in the gluon exchange is necessarily very small. Unlike VDM, PGF makes specific predictions related to QCD parameters, the charm quark mass, and the gluon momentum distribution $G(x)$. Precise measurements of the energy dependence of the charm photoproduction cross section provides information on these interesting production model parameters.

The general cross section behavior predicted by the PGF model is that of a gradually rising cross section at high energies. This is in some contrast with VDM which predicts a cross section at high E_γ which is relatively independent of energy. Numerous experiments have measured the cross sections for ψ and D production as a function of incident photon energy, observing a sharp rise above $c\bar{c}$ production threshold and a more gradual rise beyond. The best comparisons between VDM and PGF are made at $E_\gamma > 100$ GeV, and some recent

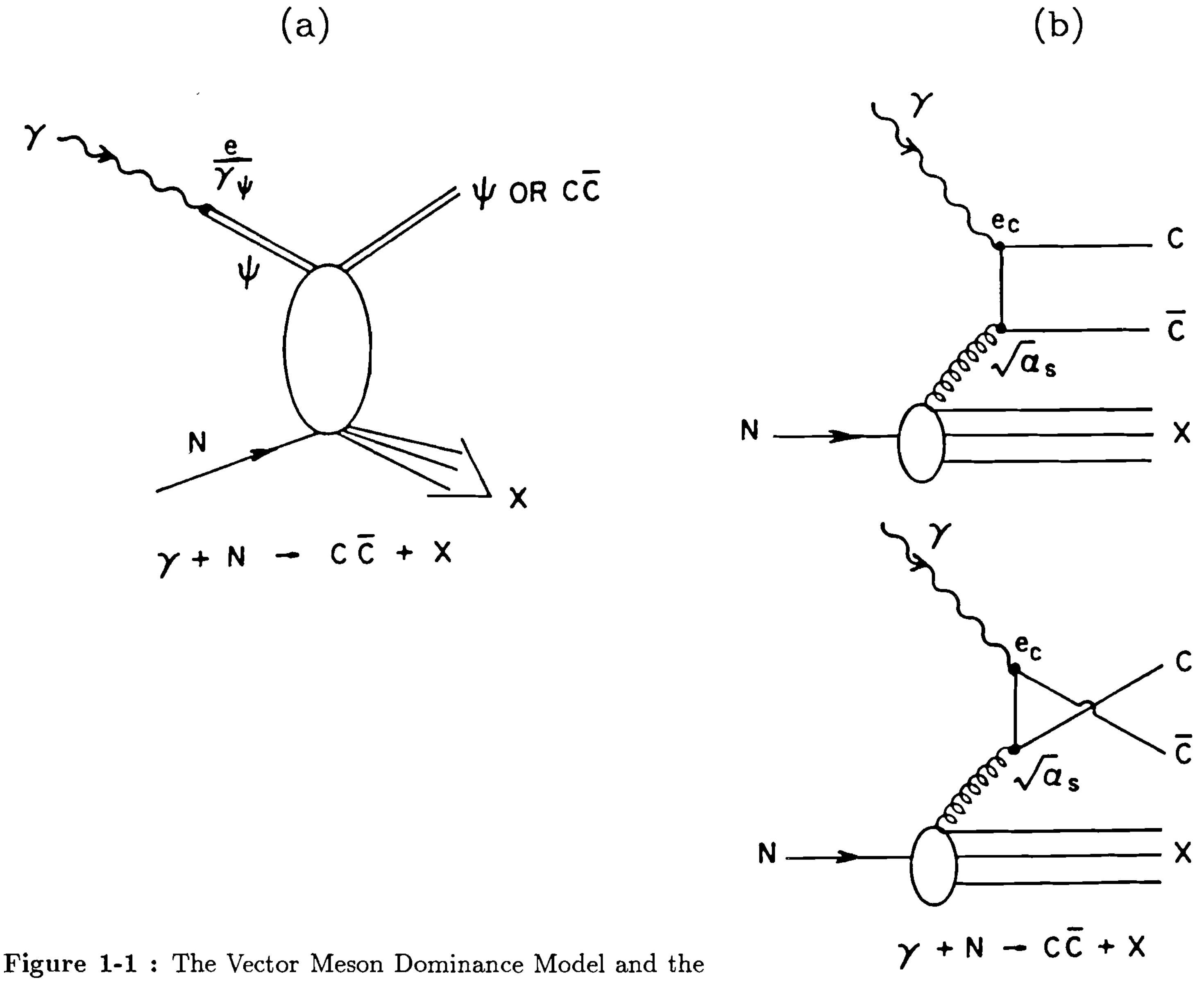

Figure 1-1 : The Vector Meson Dominance Model and the Photon-Gluon Fusion Model

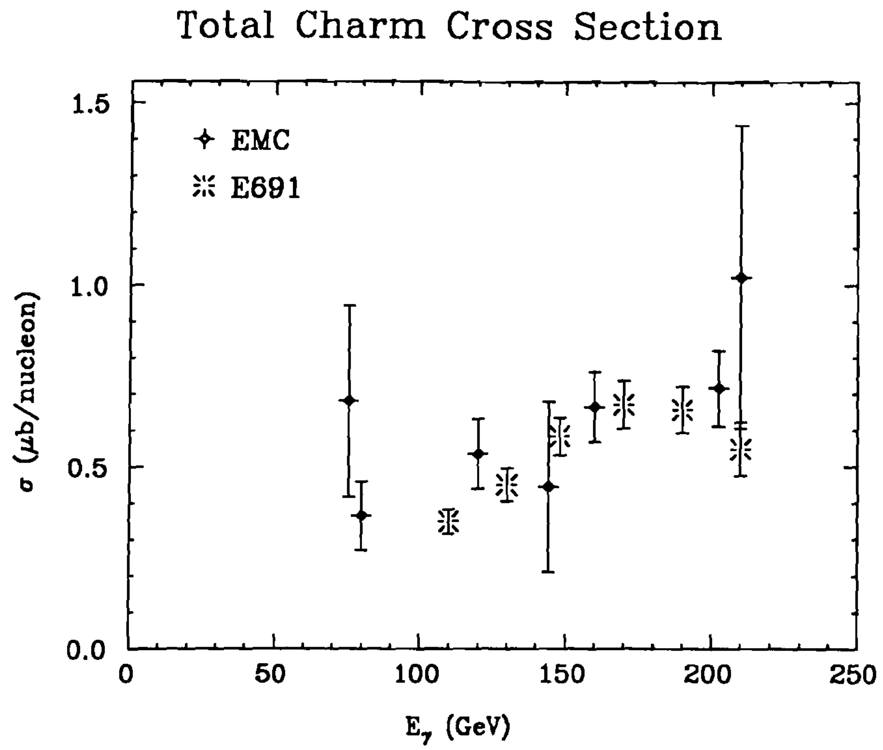

Figure 1-2 : Recent total charm cross section measurements by E691 and EMC, two high energy photoproduction experiments.

experiments[2,3] have measured the energy dependence of the open charm cross section at these energies. The total charm cross sections measured by E691 and EMC (virtual photoproduction) are shown in Figure 1-2 as a function of photon energy. The general trend appears to be that of a rising cross section, but fluctuations in the measurements leave a fairly inconclusive picture. Measurement of cross sections at higher energies and over a larger range are needed. Cross section measurements at several points in E_γ will be presented in Chapter 6, where the measurements of the D° and $D^\star$ meson cross sections extend well beyond those shown in Figure 1-2. Comparisons will be made between measurements presented here and comparable measurements of E691 in an attempt to gauge systematic effects.

Cross sections are also presented as a function of the Feynman x variable. In

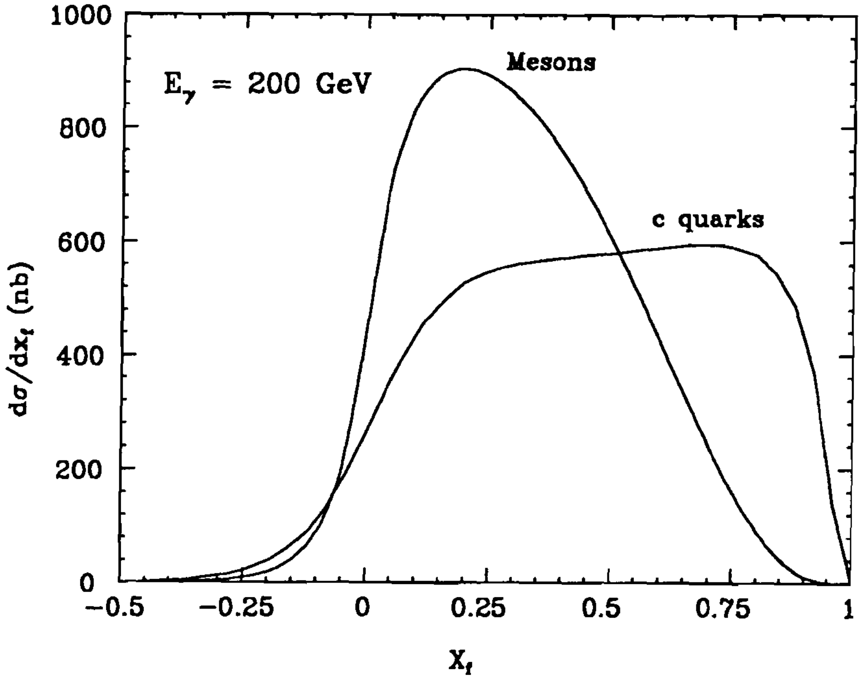

Figure 1-3 : Feynman X (x_f) distribution of quarks predicted by PGF, and the distribution of mesons for a particular dressing mechanism[4].

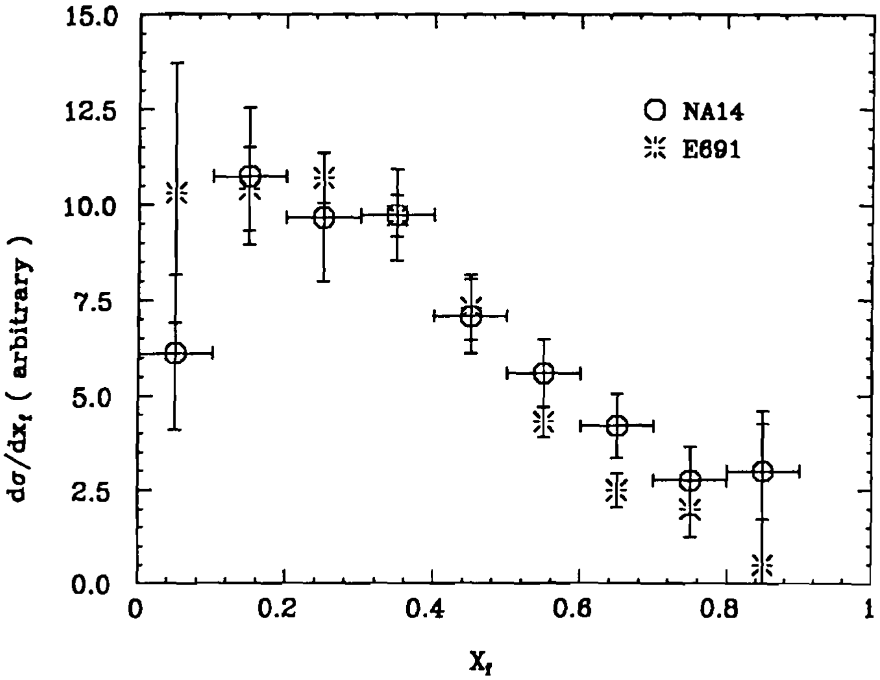

Figure 1-4 : Charm photoproduction cross section versus Feynman X (x_f) as measured by E691 and NA14′.

the case of open charm photoproduction this variable is defined as :

$$x_f = \frac{E_c}{E_\gamma} - \frac{m_c^2 + P_{\perp c}^2}{2m_p\, E_c}$$

where m_p is the mass of the target nucleon. Diffractive models predict that x_f should be distributed about $x_f \sim 0.5$ for each of the charm quarks at large E_γ. In fact PGF makes specific predictions about the distribution in x_f of charm quarks. An example in Figure 1-3 shows the charm quark distribution for the case where $E_\gamma = 200$ GeV. Unfortunately, much of the predictive nature of the PGF model concerning x_f is lost because of the charm quark hadronization process. Also plotted in Figure 1-3 is a possible x_f distribution of D mesons. The softer distribution occurs because the charm quark loses a fraction of its momentum in the dressing process. Such a dramatic dressing may not be so far from reality. Results of E691 and NA14$'$, shown in Figure 1-4, indicate a surprisingly soft distribution of the cross section in x_f. If these results are indeed true, then little can be derived from measurement of D meson x_f distributions unless done very precisely. Measurements presented in Chapter 6 attempt to verify the soft D° meson x_f distribution.

1.1.2 Non-diffractive Models

The diffractive nature of VDM and PGF models that leads to a central x_f distribution also predicts symmetric production of c and $\bar{c}$ quarks. In such models the valence quarks in the target nucleon play no important role in the interaction. It is possible to consider models in which the valence quarks are involved with the photon interaction. In such processes the quark-antiquark asymmetry within the target nucleon introduces asymmetries between the charmed and anticharmed particles that are produced. One such model is Associated Production, where a charmed baryon is produced against an anticharmed meson. A description of this production is shown in Figure 1-5. In these interactions the baryonic line of the target proton stays with the c quark. Thus the forward produced charm state will always involve the $\bar{c}$ quark, favoring the production of $\bar{\mathrm{D}}$ mesons. Experimental

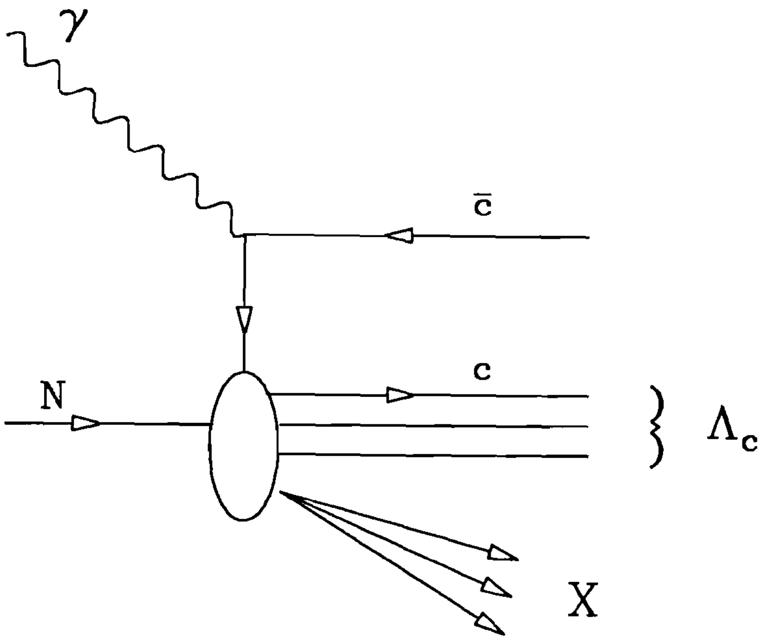

Figure 1-5 : Associated Production

results are consistent with some levels of associated production. The SLAC Hybrid Facility Photon Experiment, which operates very close to charm threshold, sets a level of 35 ± 20% associated production in total charm production. More recent, higher energy experiments are consistent with much lower levels of associated production. A comparison of $D^{\star +}$ and $D^{\star -}$ meson production levels is made in Chapter 5 where a limit is set on the level of associated production in E687.

Another interesting result presented in Chapter 5 is a measurement of the fraction of total D° events which result from $D^{\star\pm}$ decays. A prediction of this fraction can be obtained using a simple spin counting argument. A similar measurement[2] by E691 yielded surprisingly good agreement with this simple model.

1.2 Decay Dynamics

Beyond tests of production mechanisms, the large number of D mesons obtained in E687 is useful in precision measurements involving the dynamics of D meson decays. Studies of properties such as decay rates and relative branching fractions have lead to understandings of the underlying mechanisms involved in these weak decays. The charm mesons have a rich spectroscopy, and numerous decay modes have been observed in E687. The most abundant decays are those of $D^\circ \rightarrow K\pi, K\pi\pi\pi$ and $D^+ \rightarrow K\pi\pi$. Signals in these decay modes amounting to $\sim$ 9700 events are presented in Chapter 3. Observations of several Cabbibo suppressed decay modes of the D° , mostly through $D^{*+} \rightarrow D^\circ\pi^+$, are presented as well.

1.2.1 D° Lifetime

A measurement of the D° mean lifetime will be presented in Chapter 7. These results tend to confirm the somewhat unexpected results of other recent experiments concerning the ratio of D° and D^+ lifetimes.

The lifetime of D mesons was first explained in terms of the spectator picture, shown in Figure 1-6(a). An estimate of the charm quark lifetime is obtained in analogy with muon decay, using m_c = 1.5 GeV and scaling by m^5 (including extra color and flavor factors), giving $\tau_c \approx 7 \times 10^{-13}$ sec. This naive result would be the same for all ground state charm particles. However almost all measurements have revealed a ratio of lifetimes $\tau_{D^+}/\tau_{D^\circ}$ which is about 2.5 : 1. Initial explanations of this phenomenon centered about the W exchange diagram, shown in Figure 1-6(b), which only contributes to D° decays. But more recent arguments concerned with helicity suppression at the light quark vertex suggest that this process may have a rather small amplitude[5]. Other recent studies have indicated that an interference diagram could account for a factor of 2 higher lifetime ratio than had been previously estimated. This diagram, shown in Figure 1-7(b), will interfere with the original spectator diagram, shown in Figure 1-7(a), when the light quark of the D is a $\bar{d}$ and will add incoherently

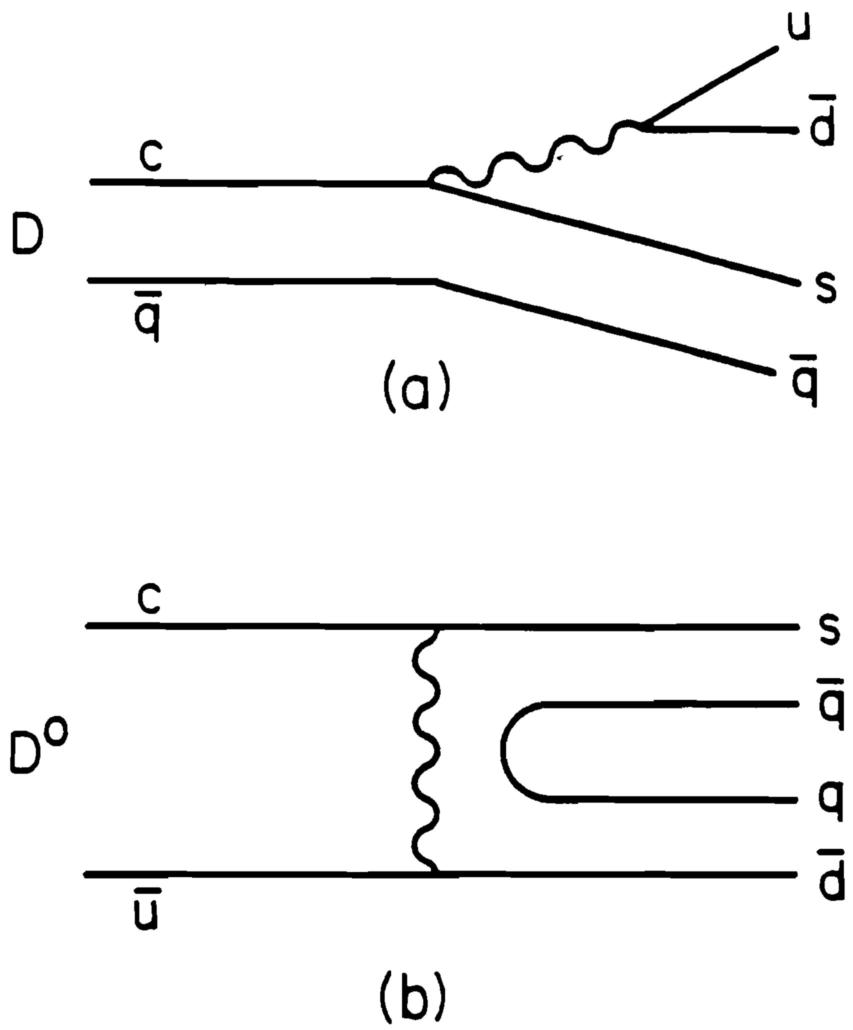

Figure 1-6 : Spectator and W exchange diagrams, contributors to D meson lifetimes.

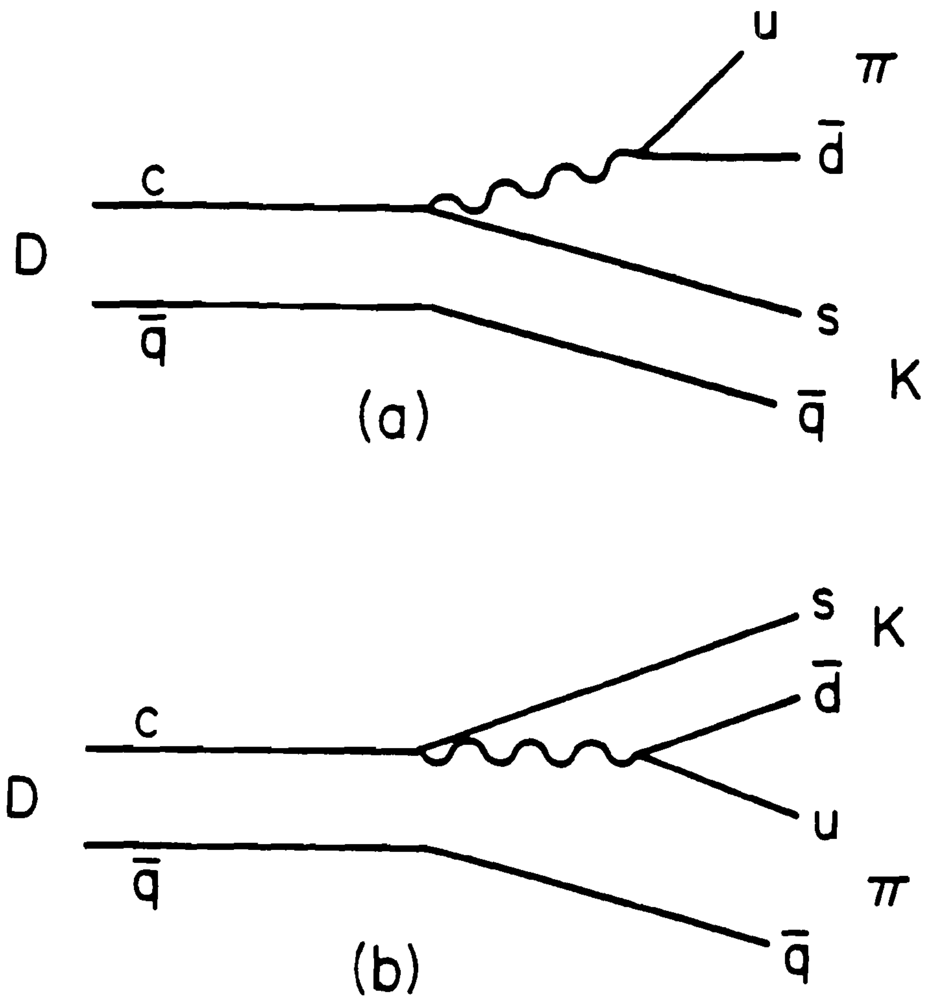

Figure 1-7 : Spectator diagrams – original and interference diagram.

when it is a $\bar{u}$. It is also possible to explain the observed differences with other less elegant mechanisms such as those involving final state strong interactions. Therefore it is still rather unclear what mechanism is really responsible for the observed decay rate difference.

1.2.2 D° Decay Branching Ratios

Another area which has provided some interesting results is that of the branching ratio between Cabbibo favored and suppressed decay modes. Two ratios have been measured and are presented in Chapter 5.

The first ratio measured is that of $\Gamma(D^\circ \rightarrow K^+K^-)/\Gamma(D^\circ \rightarrow K^+\pi^-)$. The spectator diagram for the Cabbibo allowed decay $D^\circ \rightarrow K^+\pi^-$ is shown in Figure 1-8(a) and the diagram for the Cabbibo suppressed decay $D^\circ \rightarrow K^+K^-$ is shown in Figure 1-8(b). The diagram for another suppressed decay $D^\circ \rightarrow \pi^+\pi^-$ is shown in Figure 1-8(c). The factors at the W boson vertices include the $\cos\theta_c$ and $\sin\theta_c$ Cabbibo factors relating c quark decays into s or d quarks. Based on these diagrams, the predicted branching ratio between either KK or $\pi\pi$ decays and the $K\pi$ decay is expected to be $\tan^2\theta_c$, which at the present value of $\theta_c = .23$ rad. is about 5 percent. When measured by Mark II and Mark III [6,7]the branching ratios were found to be

$$\frac{\Gamma(D^\circ \rightarrow K^+K^-)}{\Gamma(D^\circ \rightarrow K^+\pi^-)} = .119 \pm .018$$

$$\frac{\Gamma(D^\circ \rightarrow \pi^+\pi^-)}{\Gamma(D^\circ \rightarrow K^+\pi^-)} = .034 \pm .009$$

The surprisingly high branching ratio into the KK decay mode prompted further phenomenological examination with the conclusion that final state hadronic interactions may play a bigger role than in the $D^\circ \rightarrow \pi^+\pi^-$ decay. Further measurement of the $D^\circ \rightarrow K^+K^-$ decay is interesting therefore from the standpoint of confirming these earlier results.

An equally interesting measurement, presented in Chapter 5 as well, is the branching ratio $\Gamma(D^\circ \rightarrow \pi^+\pi^-\pi^+\pi^-)/\Gamma(D^\circ \rightarrow K^+\pi^-\pi^+\pi^-)$. This ratio, which

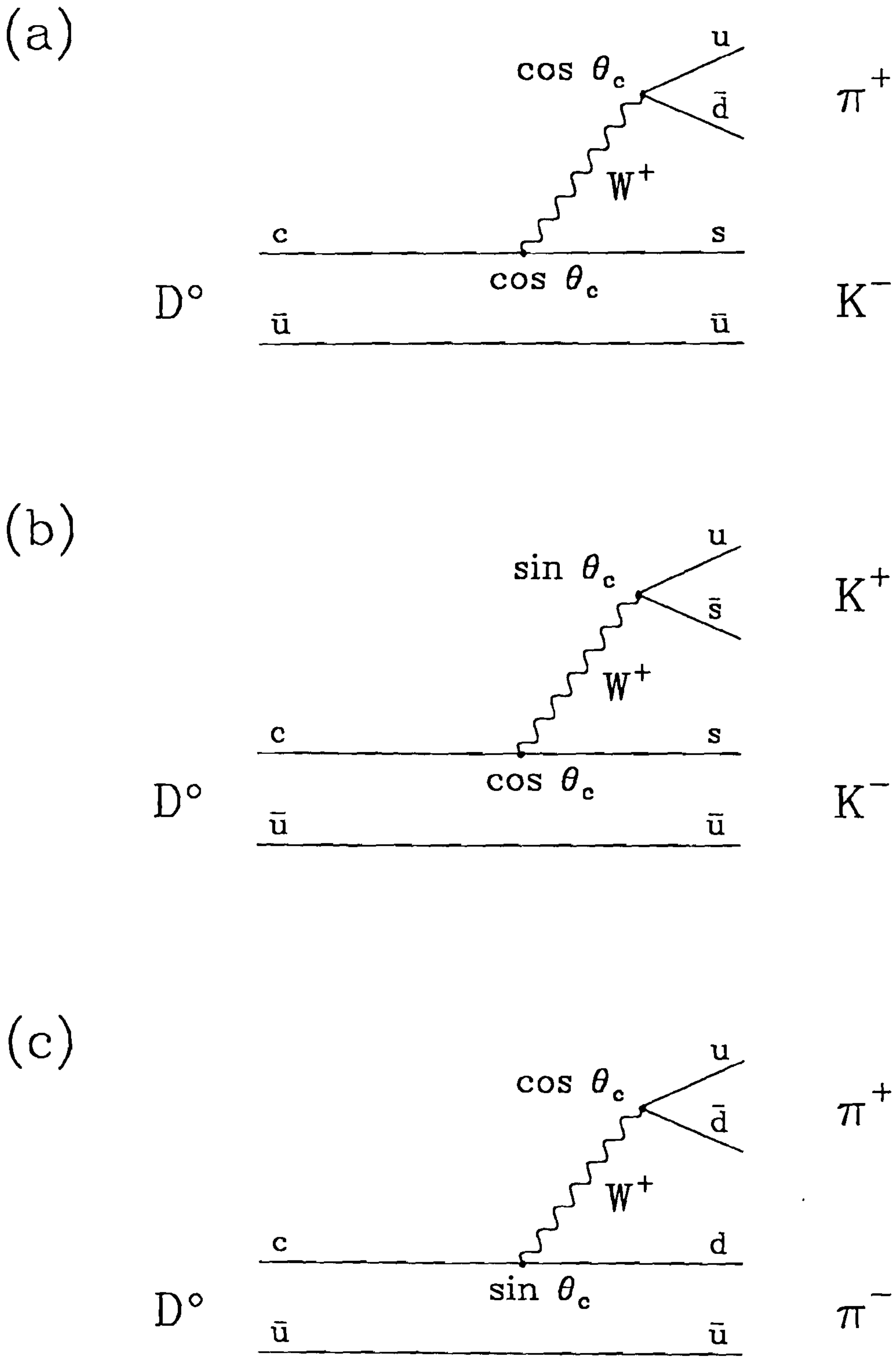

Figure 1-8 : Lowest order quark diagrams for several D° decay modes.

is presently measured[8] as .13 ± .08, may afford insight as well into the Cabbibo suppression problem when measured more precisely.

Chapter 2

The Experiment

Experiment 687 is located in the Wide Band Photon Laboratory at Fermi National Accelerator Laboratory. High energy photons are transported into the laboratory and interact in an experimental target located at the upstream end of the laboratory. Much of the remainder of the experiment is designed to detect the products of photon-nucleon interactions in the target. This is accomplished by a large acceptance, high rate, particle spectrometer located just downstream of the target. A schematic of the general experimental layout is shown in Figure 2-1. The spectrometer is divided into two detector regions, referred to as the inner and outer regions, defined by the aperture of the second analysis magnet. The inner region encompasses particles detected at $\theta_x < 30$ mrad and $\theta_y < 50$ mrad, while the outer region adds active detector area out to $\theta_x \sim 100$ mrad and $\theta_y \sim 150$ mrad. The apparatus downstream of the 2nd magnet detects only in the inner region, whereas most of the detectors upstream cover both inner and outer regions. The location and size of each detector is given in Table 2-1.

Major features of the spectrometer include charged particle tracking and identification, as well as detection of electromagnetic and hadronic showers. The tracking system consists of a high resolution silicon microstrip system located just downstream of the target, and beyond that is a magnetic spectrometer with two magnets and five multi-wire proportional chambers. Charged particles are identified by several types of detectors including three threshold Čerenkov detectors. The analyses presented in this thesis utilizes charged particle tracking and Čerenkov identification, so discussion will concentrate on these aspects. In addition, two electromagnetic calorimeters were used to identify electrons and photons by detecting electromagnetic showers, while an array of scintillator hodoscopes and proportional tubes was used for muon identification.

The experiment also included a hadron calorimeter which was used predominantly for triggering purposes. It was accompanied in this task by an assortment

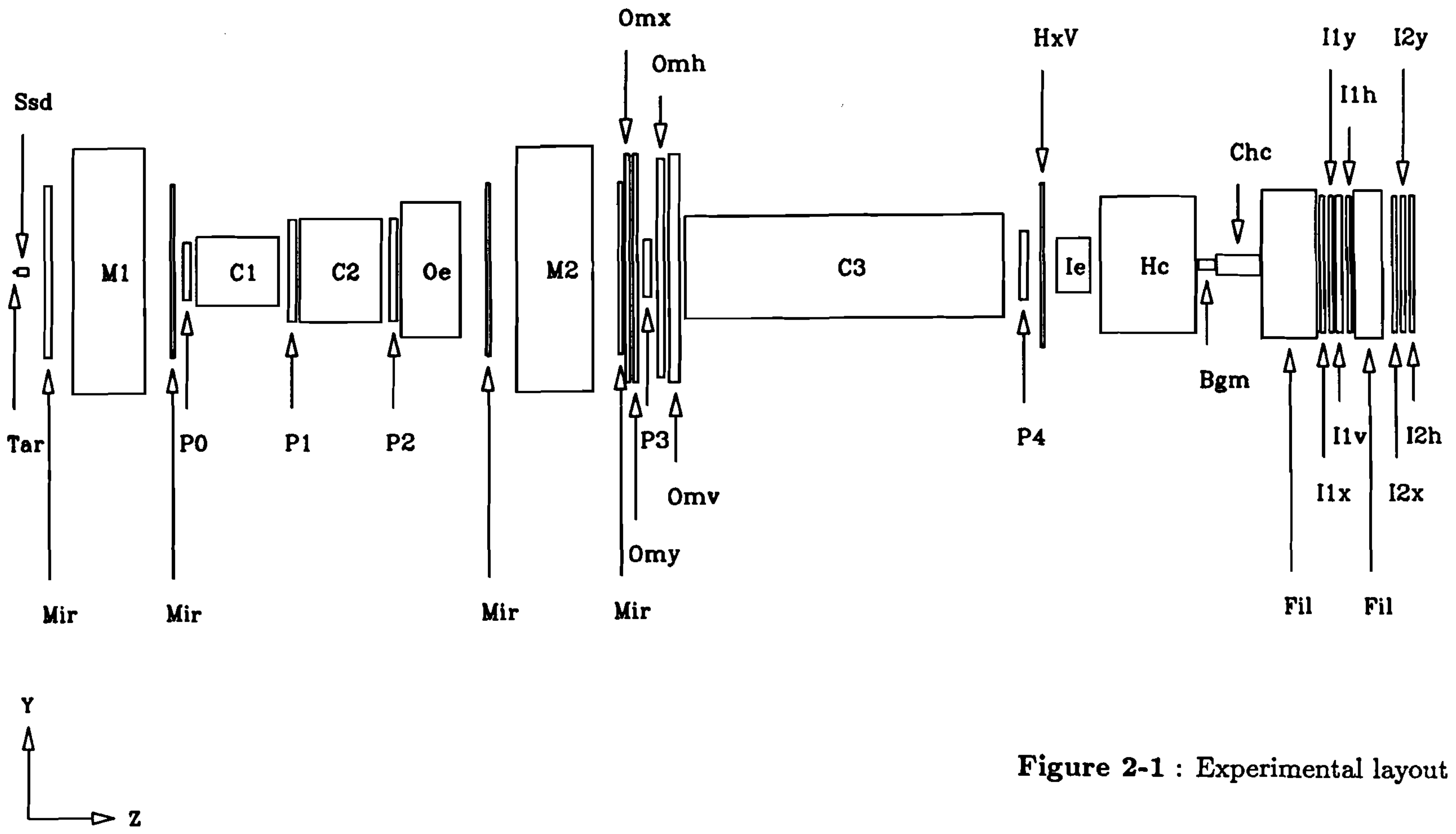

E–687 Spectrometer

Figure 2-1 : Experimental layout

Table 2-1 : E687 Spectrometer

Device	Z location† (cm)	Z length (cm)	Area (cm^2)
Be-5 Target	-3.11	4.11	2.54 × 2.54
SSD-1	4.63	1.07	2.48 × 3.50
SSD-2	10.69	1.07	4.96 × 4.96
SSD-3	16.72	1.07	4.96 × 4.96
SSD-4	28.66	1.07	4.96 × 4.96
M1 Up. Shield hole	77.44	17.78	25.4 × 101.6
M1 aperture	220.95	167.64	76.2 × 127.0
M1 Dwn. Shield hole	370.17	8.90	76.2 × 127.0
P0	405.08	17.78	76.2 × 127.0
C1	519.75	187.96	132.1 × 182.9
P1	644.26	17.78	152.4 × 228.6
C2	757.00	187.96	152.4 × 228.6
P2	878.47	17.78	152.4 × 228.6
OH	896.00	2.00	270.0 × 250.0
OH aperture	896.00	2.00	48.6 × 83.2
OE	962.99	132.40	270.0 × 300.0
OE aperture	962.99	132.40	48.6 × 83.2
M2 Up. Shield hole	1091.43	8.90	76.2 × 127.0
M2 aperture	1238.11	167.64	76.2 × 127.0
M2 Dwn. Shield hole	1383.52	8.90	76.2 × 127.0
Oμ Prop. X	1399.24	10.00	304.8 × 508.0
Oμ Prop. X hole	1399.24	10.00	101.6 × 162.6
Oμ Prop. Y	1416.94	10	304.8 × 508.0
Oμ Prop. Y hole	1416.94	10.00	101.6 × 162.6

† Z locations measured at the center of the device with respect to the Granite Block

Table 2-1 : Continued

Device	Z location (cm)	Z length (cm)	Area (cm^2)
P3	1442.6	17.78	76.2 × 127.0
Oμ Scint. Y	1474.56	15.00	304.8 × 487.7
Oμ Scint. Y hole	1474.56	15.00	121.9 × 152.4
Oμ Scint. X	1505.06	22.80	304.8 × 487.7
Oμ Scint. X hole	1505.06	22.80	121.9 × 152.4
C3	1884.42	703.58	190.5 × 228.6
P4	2288.89	17.78	101.6 × 152.4
H× V	2328.19	9.22	141.6 × 246.0
H× V gap	2328.19	9.22	7.1 × 365.8
IE	2399.67	76.84	123.1 × 123.1
IE hole	2399.67	76.84	10.2 × 10.2
HC	2569.78	219.30	203.2 × 304.8
HC hole	2569.78	219.30	30.0 (dia.)
BGM	2704.03	40.64	25.4 × 22.9
CHC	2778.00	101.60	45.72 × 45.72
μ filter 1	2895.66	128.60	231.1 × 330.2
Iμ 1 Prop. X	2973.48	10.00	203.2 × 304.8
Iμ 1 Prop. Y	2993.21	10.00	203.2 × 304.8
Iμ 1 Scint. X	3012.52	15.30	213.4 × 304.8
Iμ 1 Scint. Y	3036.07	9.00	203.2 × 304.8
μ filter 2	3079.66	63.00	231.1 × 330.2
Iμ 1 Prop. X	3138.95	10.00	203.2 × 304.8
Iμ 1 Prop. Y	3158.09	10.00	203.2 × 304.8
Iμ 1 Scint. Y	3178.25	9.00	203.2 × 304.8

of scintillator counters and a calorimeter measuring the incident photon beam. These detectors enabled the experiment to ignore spurious interactions in the apparatus as well as electromagnetic interactions which comprise 99 percent of the target interactions. The photon beam calorimeters indirectly measured the energy of each photon interacting in the target. These measurements were useful not only in triggering, but provided an estimate of the incident photon energy. Discussion begins with a description of the photon beam.

2.1 The Beam

The incident photon beam is produced through a series of processes initiated by the primary proton beam which is extracted from the main accelerator at 800 GeV/c. Protons from the accelerator are transported to a beryllium target located far upstream of the experiment. Amongst the myriad of particles produced from interactions in the target are neutral pions and etas. These decay immediately into a pair of high energy photons. Most other charged particles are swept out of the beam by magnets leaving a forward traveling beam of neutral particles. The high intensity beam of photons has an unacceptable level of long lived neutral contaminants such as neutrons and K^0_L mesons, so a scheme is used to purify the beam. The beam is allowed to strike a piece of lead known as a converter ($\approx 50\% X_o$) in which many of the photons interact electromagnetically to form e^+e^- pairs. Most other neutral particles do not interact and travel forward into a large beam dump where they are completely absorbed. The electrons produced in the converter are transported around the dump by a series of magnets with optics arranged to transport a nominal energy of 350 GeV with a momenta bite of roughly ±15%. A large momentum bite is required for high luminosity. Positrons were not transported during the 1987-88 run of E687, though provisions have subsequently been made to include them. A small number of other charged particles, predominantly π^- mesons from interactions in the converter, are transported around the dump as well.

The electrons are transported to Wide Band Laboratory where they strike yet another piece of lead known as the radiator. A large fraction of electrons create bremsstrahlung photons which travel forward into the experimental target. Noninteracting electrons and those recoiling from bremsstrahlung interactions are swept away from the photon beam by a magnet. The lead radiator was chosen with a thickness corresponding to 20 percent of a radiation length to maximize luminosity and minimize multiple bremsstrahlung interactions and photon reconversions. Even so 2 - 3 bremsstrahlung photons are typically produced above 10 GeV by each electron interacting in the radiator. The yield of photons follows a $1/\omega$ bremsstrahlung spectrum to first order with an endpoint energy near the nominal electron beam energy. All charged contaminants of the beam are removed by the sweeping magnet leaving a very low level of neutral hadrons. Their interactions in the target create a background at a level of about 10^{-4} that of photon interactions.

2.2 Beam Tagging

Electrons which have not interacted in the radiator are swept out of the beam and are absorbed in a lead dump just outside the beam pipe. Electrons which underwent bremsstrahlung will have lost some of their initial momentum and are swept at a larger angle than nominal electrons. To detect these electrons, a Recoil Electron Shower (RESH) detector is placed 4.1 inches transverse to the beam pipe, downstream of the sweeping magnet. The transverse offset of this detector sets the minimum electron energy loss (E_{loss}) high enough that only electrons with E_{loss} greater than roughly 110 GeV enter the detector. When the RESH detector is used in the trigger, this cutoff excludes many of the less interesting low ω interactions in the target.

The RESH detector itself is segmented into 10 cells oriented transversely to the beam direction. Each segment represents a calorimeter made up of stacks of lead and scintillator, read out by a single photomultiplier tube. In principle the energy of each recoil electron can be determined from the PMT pulse height in a particular segment. But a redundant momentum measurement is made using

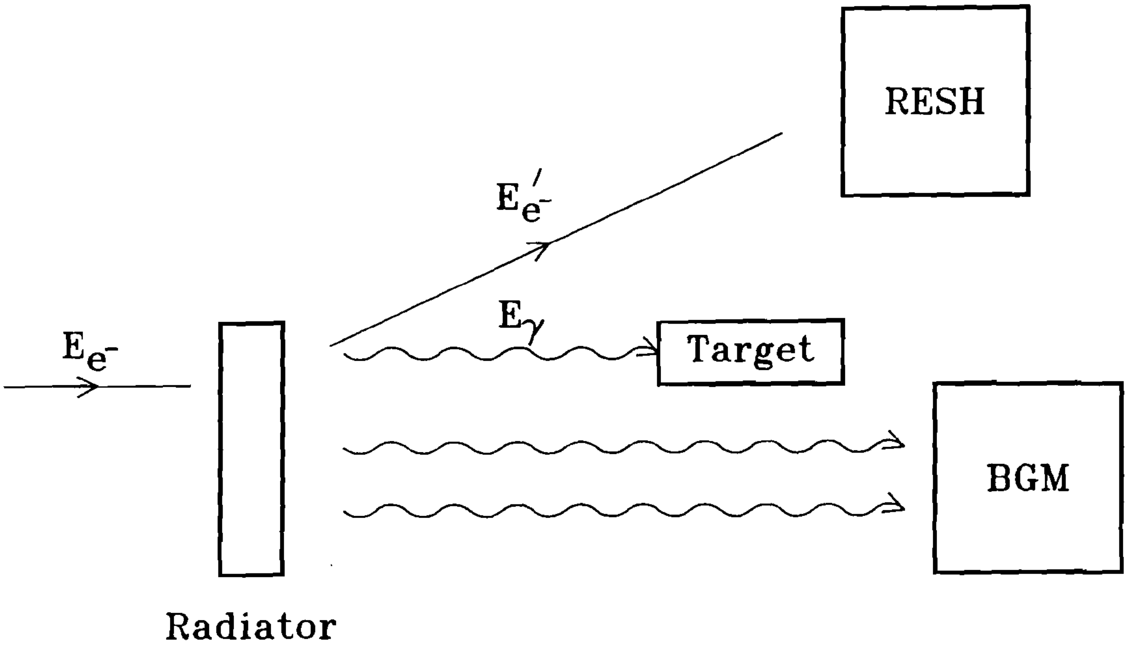

$$E_\gamma = E_{e^-} - E_{RESH} - E_{BGM}$$

$$\sigma (E_\gamma) = 46 \text{ GeV}$$

Figure 2-2 : Representation of photon energy measurement.

the *kick* of the sweeping magnet and the transverse position of RESH segments. A requirement that the calorimetrically determined energy exceeds $\sim$ 20% of the magnetically determined energy is a minimal requirement used in a RESH trigger. Finally, additional granularity is obtained by assuming the interaction occurs at the boundary between segments when two adjacent segments show significant pulse height.

E_{loss} alone does not specify the energy of a given photon which interacts in the target, since it includes the energy of all photons radiated by the incident electron. More than one photon is always produced, but typically only one will interact hadronically in the target. Energy measurement of non-interacting *multi-brem* photons along with E_{loss} then *tags* the energy of the interacting photon. The energy of these non-interacting photons is measured by the Beam Gamma

Calorimeter (BGM), which is located directly in line with the incident photon beam at the far downstream end of the experiment. Thus the energy of a hadronically interacting photon is given by

$$E_\gamma = E_{beam} - E_{RESH} - E_{BGM}$$

A schematic representation of this measurement is shown in Figure 2-2.

2.3 Targets

Three different targets were used during the course of the experiment. Two of them were pure beryllium of differing geometries, and the third was an active silicon and beryllium mixture. The Be-5 target, so called because it consisted of 5 separate beryllium segments, was used for about 60 percent of the running period. This target, shown in Figure 2-3, had two large transverse area segments (for beam profile monitoring) followed by three smaller segments, for a total length of 4 cm (10 percent of an interaction length and about 11.5 percent of a radiation length). The Be-4 target had one fewer of the large beryllium segments and was used during 20 percent of the running period. The silicon hybrid target, used during the remaining time, had 4.7 percent of an interaction length of material and 14 percent of a radiation length. All these targets seemed reasonable at the time of the experiment.

2.4 Spectrometer Magnets

The spectrometer portion of the experiment is located downstream of the target. Momentum measurement of charged particles uses two large aperture magnets referred to as M1 and M2. The first magnet is centered 225 cm downstream of the target while the second is about 1240 cm downstream. Besides providing momentum analysis, the magnets dispersed particles and eased the effects of clustering in coarse granularity detectors such as calorimeters and Čerenkov detectors. The magnets were run with opposite polarity and provided kicks in the transverse direction of 0.4 GeV/p (M1) and -0.85 GeV/p (M2). Opposite polarity produces a plane with zero magnetic dispersion near the BGM calorimeter.

2.5 Charged Particle Tracking

Charged particle tracking is provided by Multi-wire Proportional Chambers (MWPC) and Silicon Strip Detectors (SSD). The MWPC system is located downstream of M1 and provides spatial information for particle tracks which have been bent by the analysis magnets. The SSD system, which is far smaller in size, is located between the target and M1 and provides the much finer spatial information for tracks emerging from the target.

The MWPC system is a set of 5 wire chambers located throughout the main spectrometer (the area downstream of M1). The chamber called P0 is located directly at the downstream end of M1, and is followed by P1 and P2 at spacings of roughly 75 inches. The two remaining chambers are located in the inner spectrometer region, downstream of M2. P3 is immediately downstream of M2 while P4 is located near the focus point of the magnets. The placing of these chambers provides good position information with which to determine particle track trajectories on either side of M2. Each chamber consists of four anode planes labeled Y, V, U, X each with a different wire orientation. Y planes have wires oriented horizontally and measure position in the y (vertical) direction. V and U wires are oriented at ±11.3 degrees with respect to Y wires, and X wires measure the horizontal coordinate. The P4 chamber lacked a Y plane. Anode wire spacings were 2 - 3 mm depending on the particular chamber, and the total number of instrumented wires in each chamber was either 2296 or 2944. The gas in all the chambers was a 65/35 Argon-Ethane mixture with trace amounts of alcohol and the cathode planes had a voltage to ground between 3.3 and 3.5 kV.

Ionization of the gas by a charged particle traversing a chamber produces a pulse on one or more wires in each plane which are referred to as hits. These pulses are amplified and recorded as a *hit* for each individual wire.

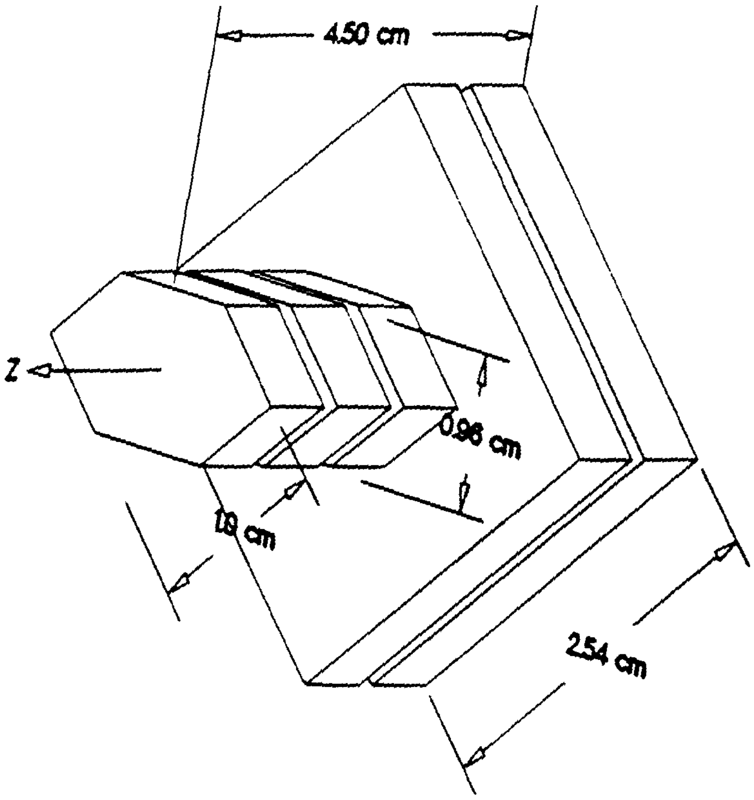

Figure 2-3 : The Be-5 target.

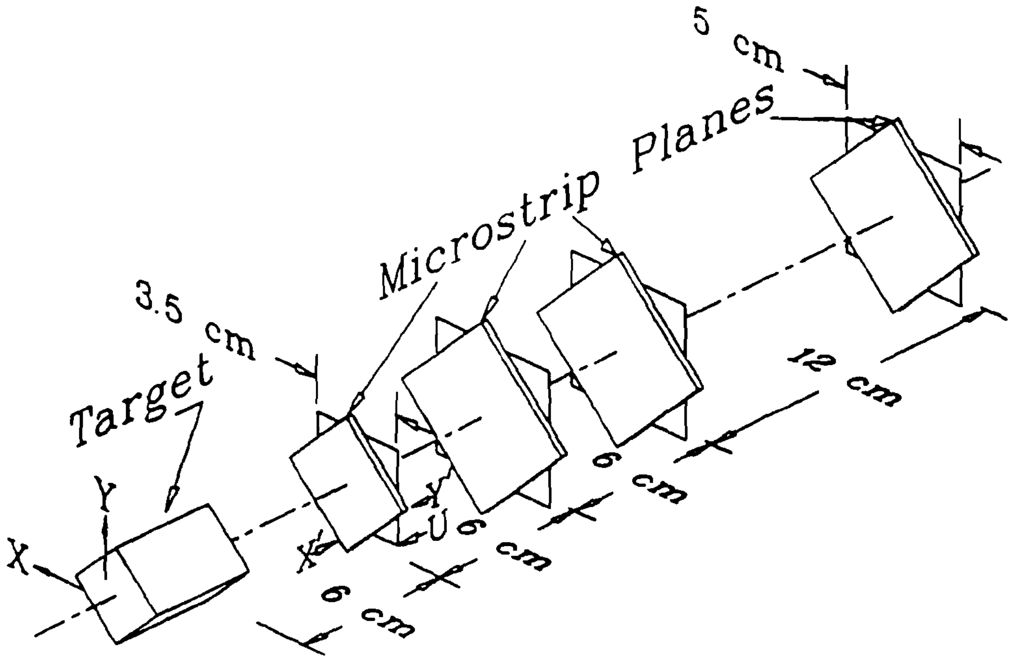

Figure 2-4 : The SSD system.

The SSD system, which is similar in many respects to the MWPC system, is shown in Figure 2-4. The system has 4 stations, each of which resembles a wire chamber, situated at about 6 cm spacings. There is a 7 cm gap between the target and the first SSD station. Each station consists of 3 planes of doped silicon deposited in strips. Strips are oriented horizontally and at ±45 degrees with respect to horizontal. There are 688 strips in each plane with a nominal pitch of 50 μm (25 μm in the first station). The outer portion of each plane is a low resolution region where the pitch is twice the nominal value. Each strip pulse is amplified and sent to an ADC where a count above pedestal is recorded as a hit. Pulse height information is sometimes used in the case of multiple hits. Particle track information from the high resolution regions of the SSD system allows transverse resolutions of about 9 μm for infinite momentum tracks when extrapolated to the center of the target.

2.6 Čerenkov Identification

There are three threshold Čerenkov detectors in the experiment, referred to as C1, C2, and C3. These multi-cell detectors are filled with gas at atmospheric pressure and run in threshold mode. The ADC information from each cell of these detectors is only used to determine whether the cell had detected light or not. Using gases with different indices of refraction (i.e. different light velocities) establishes different momenta at which a particle of given mass will begin to radiate Čerenkov light. These momenta are referred to as *threshold momenta.* A list of threshold momenta for pions, kaons, and protons in each of the three detectors is found in Table 2-2. Electron threshold momenta are below 65 MeV, and muon momenta are near those of pions. The experimental response of the detectors is shown in Figure 2-5 which plots the fraction of particle tracks which create light in each of the Čerenkov detectors as a function of momentum. Increases in the fraction of particles producing light are observed at each of the particle thresholds indicated.

An unknown particle track with a known momentum will create light in one or more of the Čerenkov detectors but not others. Each combination of *on* and *off* detectors is characteristic of one or more of these long lived particles. Beyond certain particle momenta all detectors are *on* and the means to discriminate between particle types is lost. So this particular set of thresholds allows particles to be distinguished in specific momentum ranges only. The particle identification momentum ranges are summarized in Table 2-3.

Table 2-2 : Characteristics of Čerenkov Detectors

Counter	Gas	Threshold (GeV/c)			No. of Cells
		pion	kaon	proton	
C1	He-N_2	6.6	23.3	44.3	90
C2	N_2O	4.5	15.9	30.2	110
C3	He	17.2	60.8	115.5	100

Table 2-3 : Identification Regions

Particle ident.	5-chamber track	3-chamber track
$e^{\pm}$	0 - 17.2 GeV	0 - 6.6 GeV
$\pi^{\pm}$	4.9 - 17.2 GeV	4.9 - 6.6 GeV
$e^{\pm}$ or $\pi^{\pm}$	17.2 - 60.8 GeV	6.6 - 23.3 GeV
$K^{\pm}$	17.2 - 44.3 GeV	17.2 - 23.3 GeV
P	17.2 - 44.3, 65.7 - 115.5 GeV	17.2 - 44.3 GeV
$K^{\pm}$ or P	4.9 - 17.2 GeV	4.9 - 17.2 GeV

2.6.1 C1

The Čerenkov detector C1 is the most upstream of the three detectors, lying just beyond the first analysis magnet, between the first two wire chambers P0 and P1. The counter has a pion threshold of 6.6 GeV, between those of C2 and C3. The gas used was a helium-nitrogen mixture, and the total length of the counter gas volume along the beam direction is 71 inches. A schematic of the detector is shown in Figure 2-6. Side and top views are shown in Figure 2-7.

The active area of the counter spans 80 inches in the magnet bend direction (y) and 50 inches in the x direction. It is divided into 90 cells by a series of mirrors covering the downstream plane of the gas volume. The cell geometry as viewed from upstream of the detector is shown in Figure 2-8(a). This geometry was determined from photographic information and the results of calibration with a muon beam. The mirrors are organized into two readout systems, planar and focusing. The focusing readouts use 2mm thick plastic mirrors designed to focus Čerenkov light onto individual phototubes located upstream of the mirrors, just outside the fiducial volume. The 40 focusing mirrors (each is a cell) are all located in the outer portions of the counter. The corresponding 40 phototubes have diameters of 3 or 5 inches; the smaller ones require additional collection cones to ensure complete light collection. All phototubes were protected from helium diffusion by flushing a fast stream of N_2 between quartz windows and the PMT face. The remaining cells comprise the planar mirror section, located at the center of the back plane. Two thin (.032 in.) glass, planar mirrors, each 14 × 32 inches, are oriented at 90 degrees with respect to each other and 45 degrees with respect to the beam direction. Light reflecting off these is detected by 2 and 3 inch diameter phototubes, 25 on each side of the counter, oriented exactly transverse to the beam direction. Light collection cones are located in front of the phototubes, and are close-packed to ensure that no light reflected from the planar mirrors escapes detection. These collection cones are constructed of specular quality *Coilzak* aluminum. All reflective surfaces were coated with MgF_2 for optimum reflectivity at 350 nm.

The response of the counter can be described in terms of the average number of photoelectrons detected in a particular cell radiated by a $\beta = 1$ particle, given that the Čerenkov cone is completely enclosed in the cell. Under these criteria the typical cell in the C1 planar section sees 3.6 photoelectrons while the focusing cells see about 2.5 photoelectrons. This corresponds to a figure of merit of 45

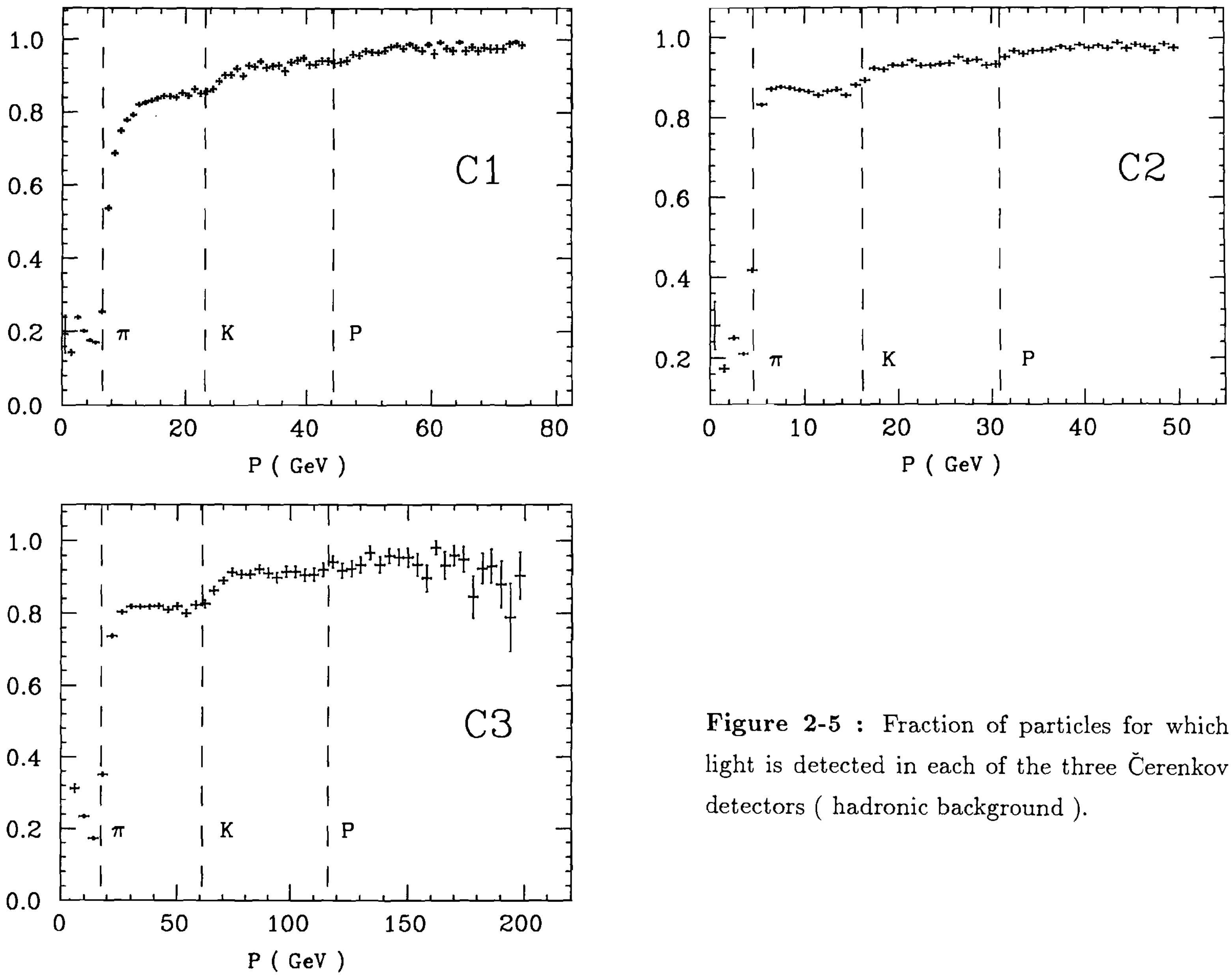

Figure 2-5 : Fraction of particles for which light is detected in each of the three Čerenkov detectors (hadronic background).

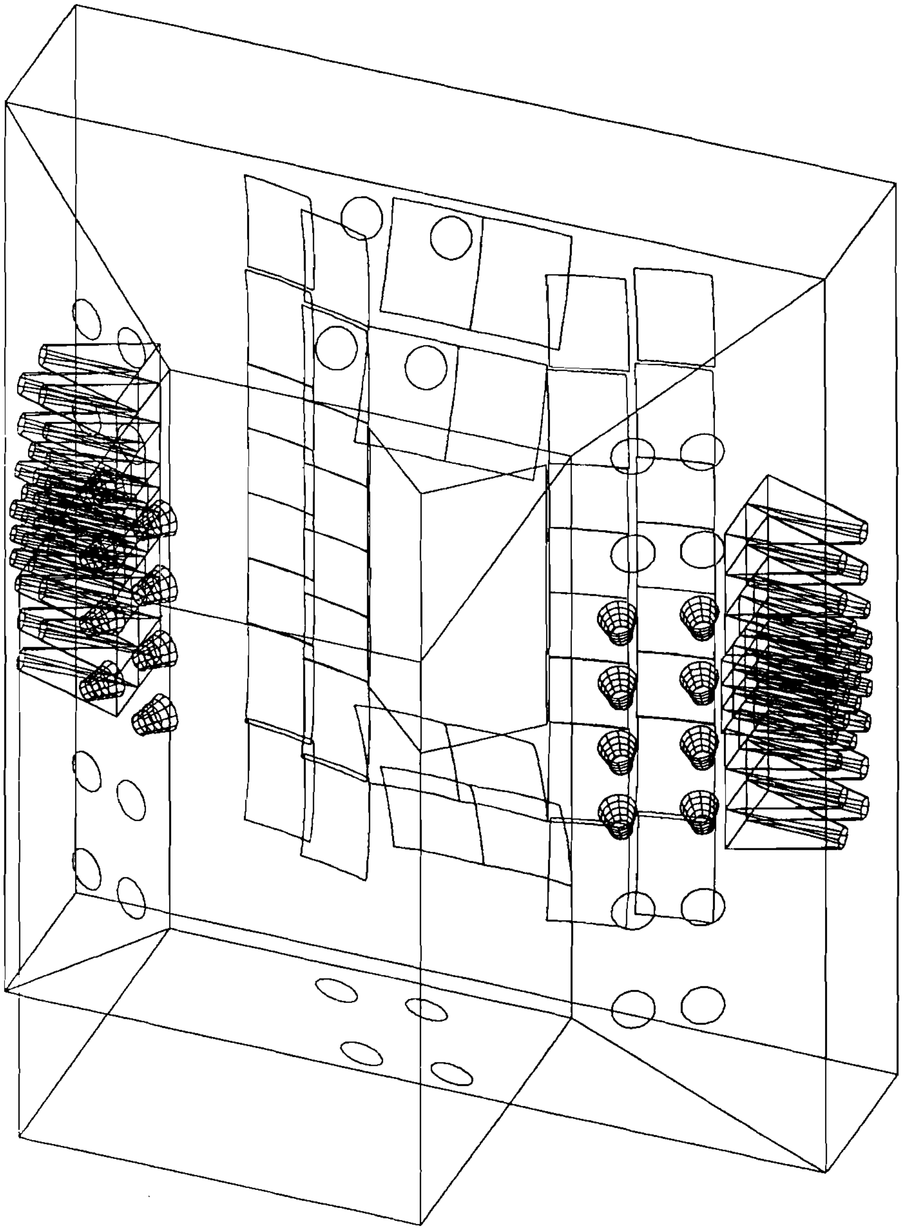

Figure 2-6 : C1 schematic.

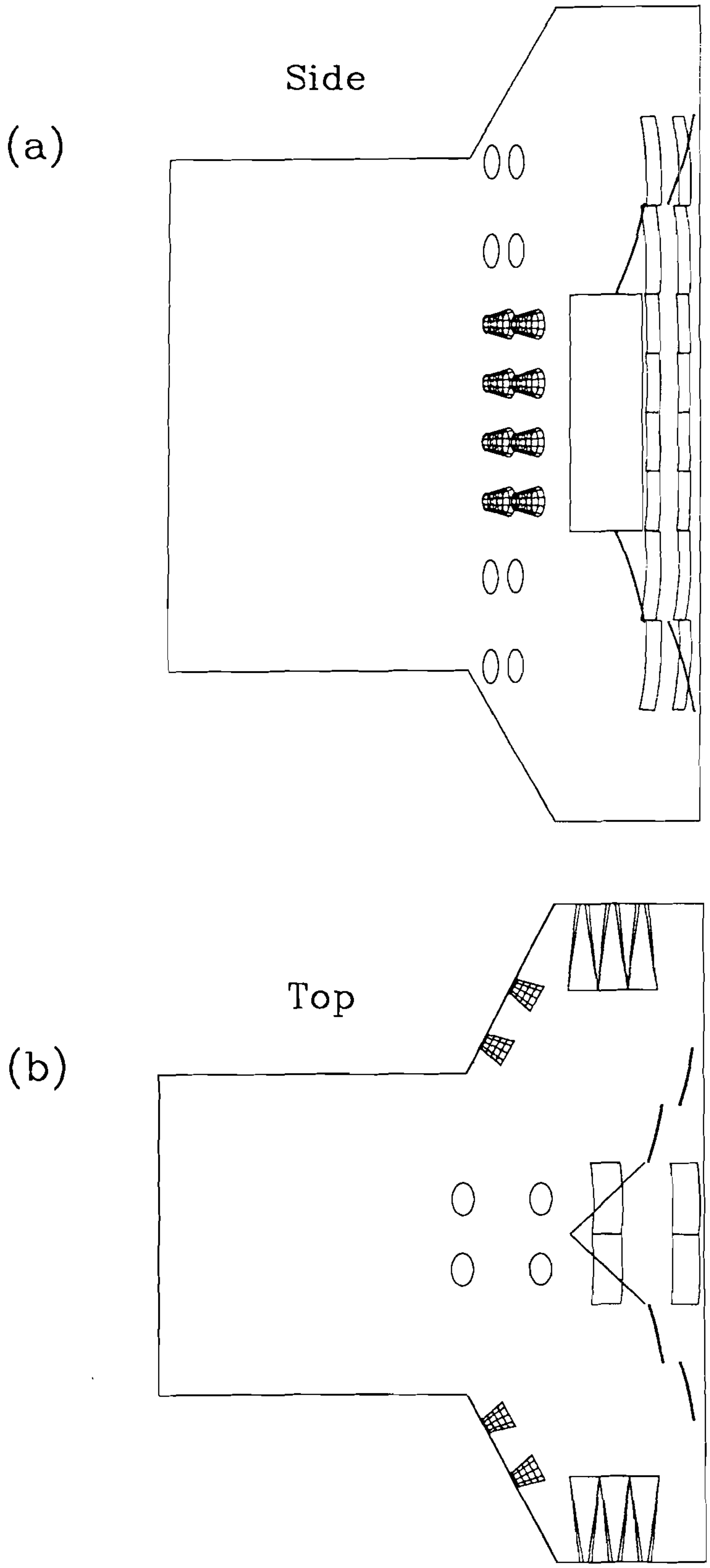

Figure 2-7 : Side and top views of C1.

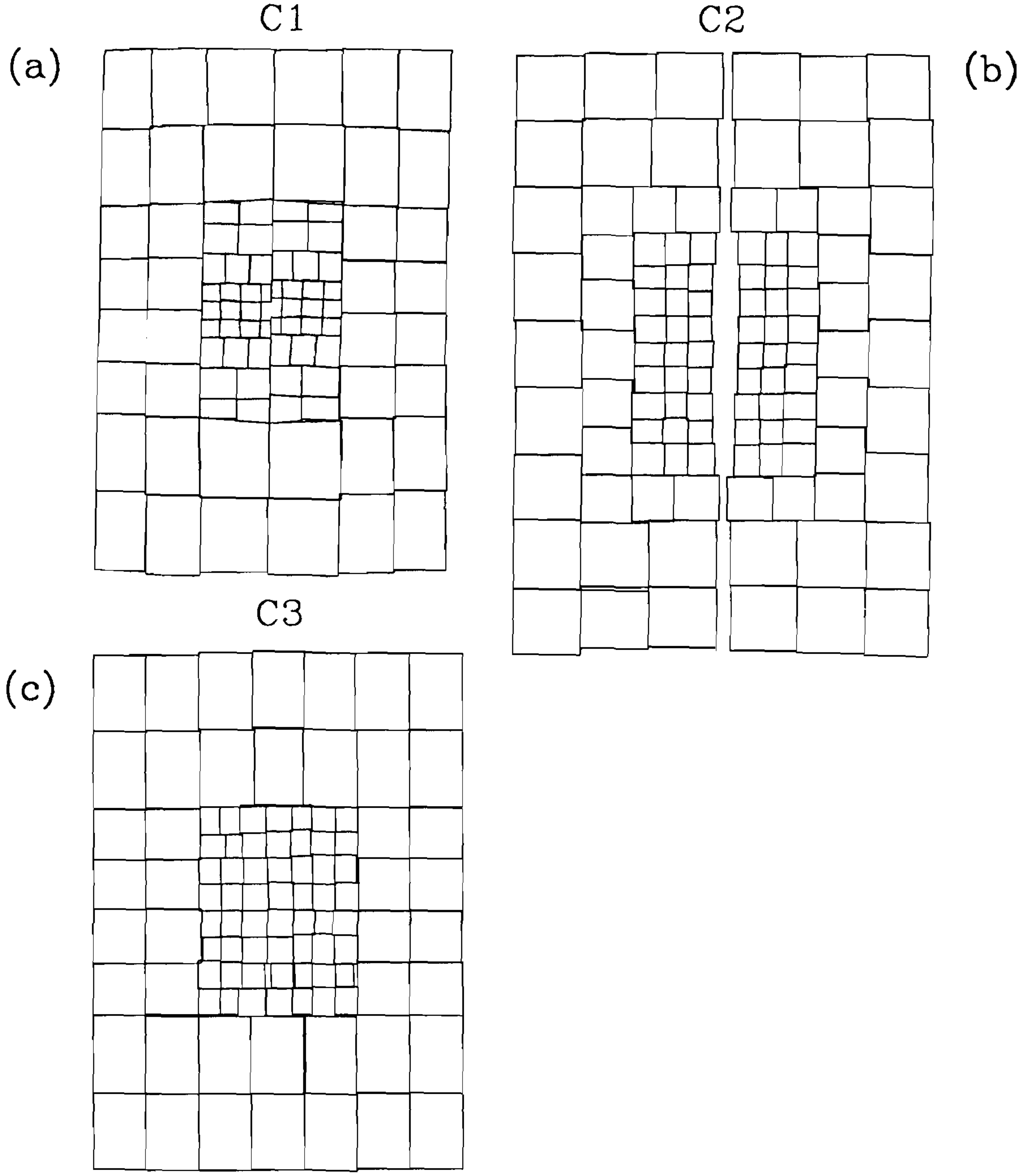

Figure 2-8 : Čerenkov detector cell geometries.

detected photoelectrons per cm per steradian^2.

2.6.2 C2

The Čerenkov detector C2 has the lowest threshold of the three detectors with a pion threshold of 4.5 GeV/c. The gas used was pure N_2O, and the total length of the counter gas volume along the beam direction is 74 inches. The detector is located between P1 and P2.

The active area of the detector spans 100 inches in the magnet bend direction and 64 inches in the transverse direction. This area is divided into 110 cells with the geometry shown in Figure 2-8(b). All cells are organized in a planar mirror readout system similar to the central section of C1. Each of the two mirror sections measures 44 × 92 inches and is made up of 1mm thick glass. The vertical gap shown in Figure 2-8(b) was intended to reduce the amount of material in the region of high photon and e^+e^- pair flux.

The typical cell in C2 detected 10 photoelectrons with yields in individual cells ranging from 5 to 16 photoelectrons. This corresponds to a figure of merit of 80 detected photoelectrons per cm per steradian^2.

2.6.3 C3

The Čerenkov detector C3 has the highest threshold with a pion threshold of 17.2 GeV/c. The gas used was pure helium and the total length of the counter gas volume along the beam direction is 277 inches. The detector is located between P3 and P4.

The active area of the detector spans 200 cm in the magnet bend direction and 140 cm in the transverse direction. This area is divided into 100 cells with the geometry shown in Figure 2-8(c). All cells are defined by the boundaries of focusing mirrors located at the downstream end of the gas volume. The glass mirrors were 1.5 mm thick and were coated to maximize reflectivity at 140 nm. All phototubes were protected from helium diffusion by flushing a fast stream of N_2 between either CaF_2 or quartz windows and the PMT face.

The typical cell in C3 detected 9 photoelectrons with yields in individual cells ranging from 3 to 17 photoelectrons. This corresponds to a figure of merit of 190 detected photoelectrons per cm per steradian^2.

2.7 Electromagnetic Calorimeters

The electromagnetic calorimetry provides identification of electrons and momentum measurement of photons which are products of hadronic interactions in the target. There are two main calorimeters detecting electromagnetic showers in the inner and outer regions of the spectrometer. The Inner Electromagnetic calorimeter (IE) is located downstream of the last wire chamber, and the Outer Electromagnetic calorimeter (OE) sits just upstream of M2. It has a large opening in the middle which is matched to the aperture of M2. Both are lead-scintillator calorimeters providing good hadron discrimination by having a large number of radiation lengths of material and a relatively small number of interaction lengths. The Inner Electromagnetic calorimeter (IE) has 25.4 radiation lengths and 1.36 interaction lengths, and the Outer Electromagnetic calorimeter (OE) has 21.6 radiation lengths and 1.96 interaction lengths. Scintillator light is detected in a total of 1018 separate photomultiplier tubes, which are pulse height analyzed by ADC's.

2.8 Muon Identification

A muon detection system, consisting of scintillator hodoscopes and proportional tubes, is similarly set up in an inner and outer configuration. The fact that muons will not often create electromagnetic showers is used to advantage in their detection. Detectors are placed behind the OE and IE calorimeters along with additional material to ensure that all particles are filtered out except muons. The Outer Muon (OM) counters are located just downstream of the yoke of M2, and the Inner Muon (IM) counters are the very last downstream elements in the experiment. Both have several planes of hodoscopes and proportional tubes detecting the minimum ionizing particles. Hodoscope information is used in triggering the data acquisition and both hodoscope and proportional tube information are recorded for later analysis.

2.9 Hadron Calorimeter

The Hadron Calorimeter (HC) consists of two devices located just downstream of the Inner Electromagnetic Calorimeter intended to detect hadronic energy. Most electromagnetic energy will have been deposited in the IE leaving predominantly hadrons to shower in the calorimeter. The main portion of the HC consists of 28 iron plates (8 interaction lengths) interspersed with a 50/50 mixture of Argon-Ethane gas. Each plane has an array of anode pads to detect ionization from the shower particles. A small calorimeter is situated at the center of the HC and uses uranium and scintillator.

The main purpose of the Hadron Calorimeter was to reject electromagnetic events in the trigger. A requirement of > 35 GeV of deposited hadronic energy reduces the likelihood of a purely electromagnetic interaction in the target by ensuring that a large fraction of the photon energy went into a hadronic final state. The threshold of 35 GeV was the lowest possible hadronic energy with reasonable noise suppression, and corresponds to the point were the HC trigger was 50 percent efficient.

2.10 The Trigger

A major problem in all photoproduction experiments is the high rate of e^+e^- pair production relative to $\gamma N \rightarrow$ hadrons ($\sim 300 : 1$ in E687). This rate, which can be as high as several MHz, has the affect of inducing large dead time for suppressed hadronic events since the data acquisition system (DAQ) operates at less than 1 kHz. The purpose of the trigger is therefore to reduce dead time by ignoring e^+e^- events at the trigger level. The rejection of e^+e^- pair events is done in two stages.

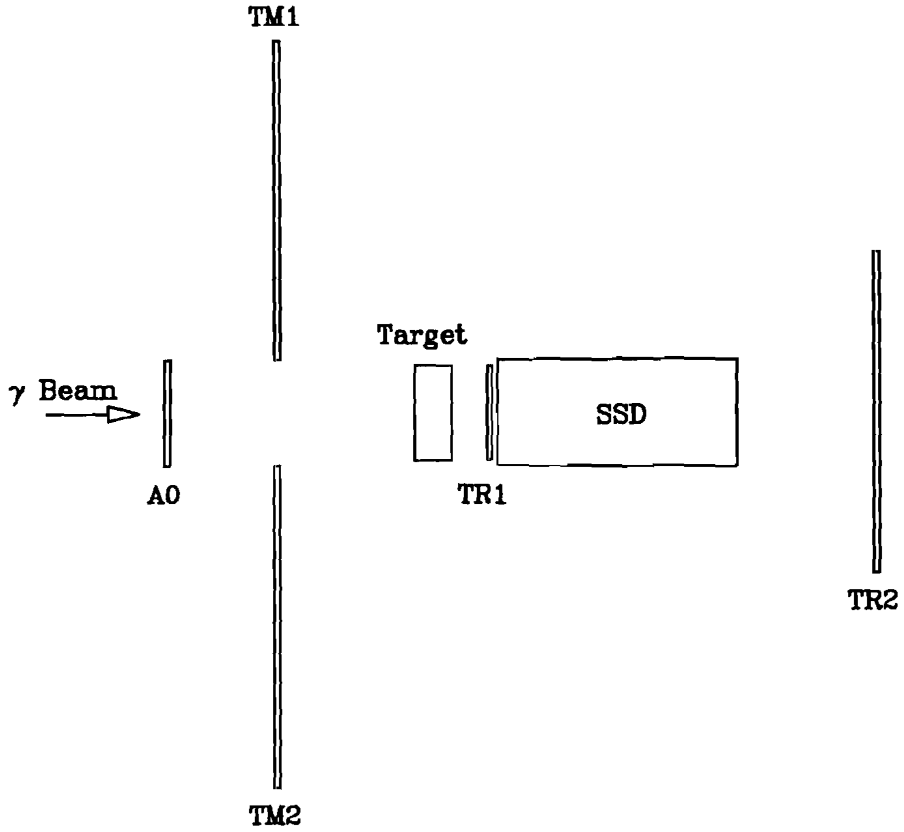

Figure 2-9 : Trigger counters in the target region.

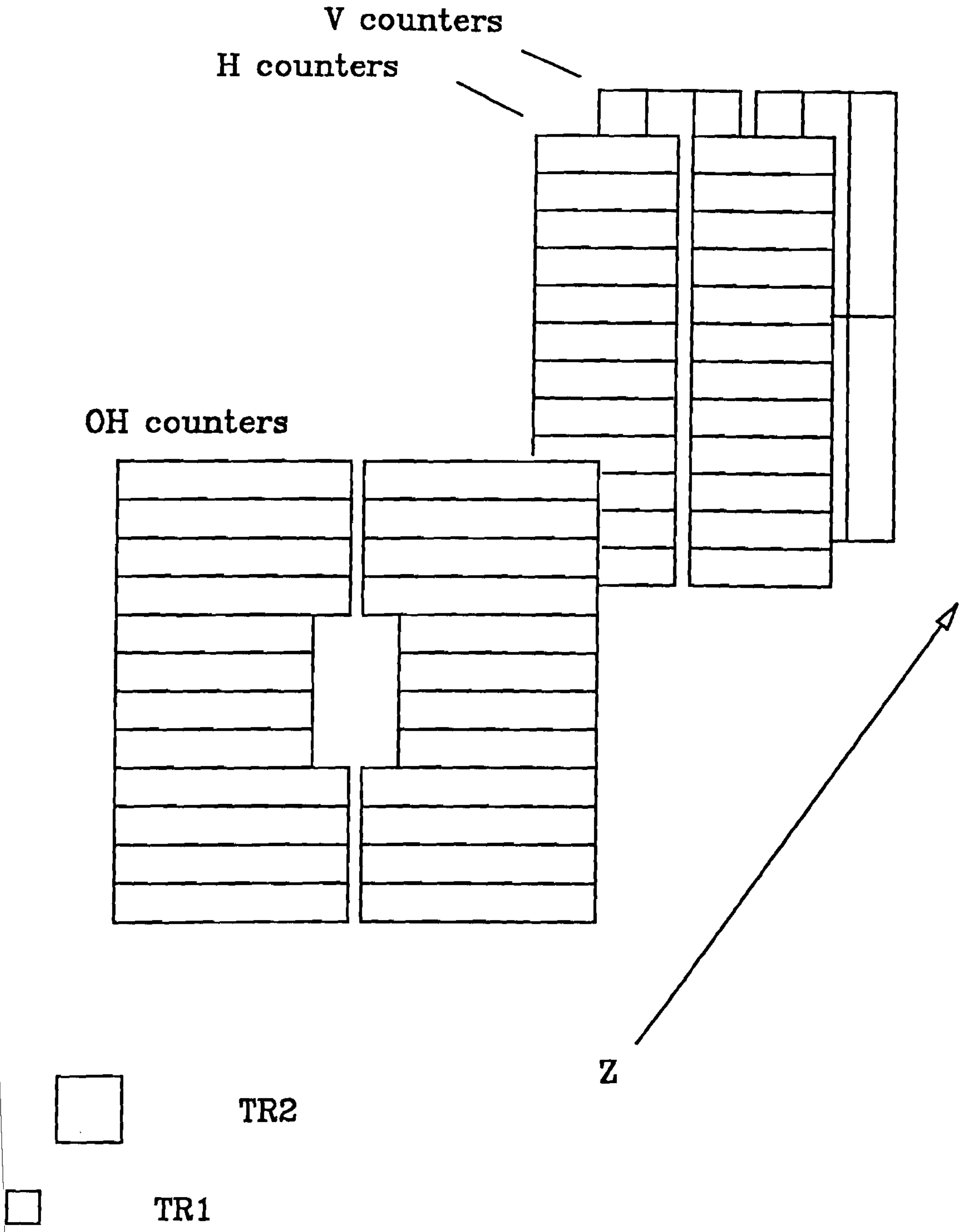

Figure 2-10 : Main upstream and downstream trigger counters.

2.10.1 First Level Trigger

The first stage uses specialized scintillation trigger counters to signify an interaction. Events which do not satisfy a preset pattern of hits in these counters are ignored. All regions of geometrical acceptance are covered by these trigger counters except the narrow vertical band in the center of the experiment which is populated mostly by e^+e^- pairs (~ 2 mrad). Two trigger counters called TR1 and TR2 are located on either side of the SSD system (see Figure 2-9). A coincidence between these two indicates an event occurred upstream of the SSD system. Hodoscope counters called H×V and OH cover the acceptance of the inner and outer portions respectively of the main spectrometer (see Figure 2-10). The H×V is located just downstream of P4 and the OH is just upstream of the OE. A coincidence is required between the two TR counters and at least one of these hodoscope arrays. Since the H×V and OH are arrays of counters, it is possible to make a further requirement that they record at least two simultaneous hits. This improves the likelihood of a hadronic interaction. Finally, a series of counters are located upstream of the target to veto charged particle contamination in the photon beam and stray muons which follow the beam in a diffuse halo. The rate reduction obtained through this first level trigger (about $20 : 1$) is still not sufficient, so a second level is used as well.

2.10.2 Second Level Trigger

When an event satisfies the correct pattern required by the trigger counters a signal called the *master gate* is generated. This strobe is used to gate the response of all ADC's. The rate of master gates, which is typically 20 kHz, is still unacceptably high relative to the DAQ rate. In order to reduce the rate still further, information from several slower detectors was utilized to form a *second level trigger.* To provide the settling time necessary to make this second level decision, the master gate provides a 2.4 μs dead time to hold off additional events. The second level trigger requires :

1. ≥ 1 hit in P0 outside the vertical e^+e^- band

2. $E_{tot} > 35$ GeV as registered in the Hadron Calorimeter by a fast ADC
3. A valid RESH response (corresponding to $E_\gamma \sim 140 GeV$)

When an event satisfies the second level trigger criteria data acquisition and digitization begin. Otherwise the detector readouts are cleared. Several other trigger patterns were used in addition to the ones listed above primarily for monitoring purposes.

2.11 Data Acquisition

Data acquisition begins when a master gate has been created and the second level trigger is satisfied. A 1.4 ms dead time is initiated to inhibit subsequent events from piling up during data acquisition from the original event. All information from an event is digitized and read into memory buffers during this dead time. A fraction (25 %) of all master gates were lost because of either the master gate or second level trigger dead time. Beam from the accelerator was not continuous, but came in cycles called spills. These spills occurred every minute and lasted 20 seconds. Typically 2500 events were recorded for each spill. Information from each event amounting to 6 kbytes was entered sequentially into the 18 Mbytes of buffer memory during the course of the spill. As the memory filled up on one side, the slower tape logging process began reading information from the other side. A fraction of the events were put in an event pool for monitoring tasks. All events were written to 6250 bpi tapes which held about 45,000 events. The total number of events recorded during the $3\frac{1}{2}$ month running period which satisfied the standard trigger was 54.5×10^6.

Chapter 3

Data Analysis

Data were recorded in Experiment 687 from June of 1987 until February of 1988. Detectors were not considered fully operational until September, and data acquisition was halted by a fire at the beginning of October. Data obtained in the period preceding the fire did not undergo the full analysis described here. The "post-fire" data was obtained from December until February and consisted of 55 million events recorded on twelve hundred 6250 bpi data tapes. Each event, defined as the detector information read in during a single master gate, consists of approximately 6 kilobytes of information. The bulk of this information is ADC, TDC and latch responses.

The analysis of the data was divided into three distinct phases: reconstruction, skim, and DST analysis. The reconstruction program, first analysis of the raw data, was run between April of 1989 and August of 1989 using the Fermilab ACP computer system. Each event was processed independently through the entire reconstruction chain, which consisted of :

1. SSD track reconstruction
2. SSD vertex finding
3. MWPC track reconstruction
4. MWPC and SSD track linking
5. MWPC vertex finding
6. Neutral Vee finding
7. Čerenkov analysis

Approximately 80 percent of the events survived reconstruction and were written to a second set of tapes.

The reconstructed data were analyzed for interesting events in two separate and complete edits of the data called "skims". The second skim, which is the basis of analyses in this thesis, ran on the Fermilab Amdahl between January and May of 1990. The total skim amounted to over 30 % of the data but the particular skim stream used in these analyses was a reduction down to 13 % of the data. The skimmed events then underwent compression, throwing out unneeded information, and were written to data summary tapes (DST). These tapes were subsequently analyzed on the University of Illinois High Energy Physics group's VAX Cluster.

3.1 Track Reconstruction

The process of reconstructing tracks involves deducing the existence of a charged track in the E687 spectrometer on the basis of hit wires in the MWPC system or hit strips in the SSD system. In general track reconstruction was performed independently in these two systems then combined through a linking procedure. One notable exception exists and will be discussed in conjunction with MWPC tracks.

3.1.1 MWPC Track Reconstruction.

The majority of tracks were classified as 3 or 5 chamber tracks, their main difference being whether they were reconstructed in P0 - P2 or P0 - P4. There are also special categories of tracks which pass through 1, 2, or 4 chambers. The number of these tracks is a small fraction of the total and their reconstruction is handled through specialized routines apart from the main reconstruction algorithm.

The main reconstruction algorithm proceeds by searching through all wire hits in a particular view (U, V, Y, and X) for 2-dimensional track projections. Views where the track projection would undergo bending in M2 (all but the X view) are modeled as two straight trajectories with a "kink" at the center of M2. Every track projection must have at least one hit associated with it in P0, the most upstream chamber. Actual tracks were chosen by matching at least two of the projections along with confirming hits in other views. No track could be missing more than 5 of the total possible hits, and no more than 2 in a single chamber. Arbitration is performed to eliminate duplicate tracks associated with the same hits. Using the simple kink approximation, 5 chamber tracks are assigned an approximate momentum. All the hits associated with a track are then fit to a 3-dimensional track trajectory including a trace through the full magnetic field in the case of 5 chamber tracks. This procedure is then iterated using successively improved momentum information to better the magnetic corrections. Finally, cutting on the χ^2 of the fit further rejects poor track candidates.

In addition to the main algorithm, several track finding programs existed in an effort to recover specific track topologies. Tracks found in only 3 chambers do not benefit from magnetic corrections since no momentum information exists. The momentum of the 3 chamber track is calculated either by linking it to an upstream SSD track segment or to an upstream vertex (see section 3.2). A recovery routine is then run to trace 3 chamber tracks, when possible, through M2 and search for as yet unassigned hits in P3 and P4. Another class of low momentum tracks exists which exit the spectrometer after passing through only one or two chambers. SSD tracks were used as seeds to find unused hits in P0 and P1 which might form a track segment.

Once all potential tracks are found, they are entered into a list not exceeding 30 tracks. Such a restriction reduces reconstruction time by putting a check on events which are likely to have massive chamber oscillations. The track list includes the fit results: slope and intercept information for each track in each spectrometer region as well as momentum and charge information in the case of 5 chamber tracks. The overall efficiency of the MWPC track reconstruction has been estimated by Monte Carlo simulation to be in excess of 98 percent efficient with less than 0.5 percent false tracks.

3.1.2 SSD Track Reconstruction

Reconstruction of tracks in the SSD system is very much similar to the MWPC track reconstruction just described. A significant simplification is the absence of magnetic corrections. On the other hand the situation is complicated by the different granularity regions in the microstrips and the non-negligible multiple coulomb scattering (MCS) effects (since each SSD plane consists of 300 μm thick silicon).

Track finding proceeds, in analogy with the MWPC system, by searching all hits in a single view (x,y, or u see Figure 2-4) for track projections. Since SSD track finding is done independently, no information about momentum, and consequently MCS effects, is available. Each hit is therefore given a simple granularity weighting. Cuts on the initial track quality are rather loose. Similarly few restrictions are made about the sharing of hits between different track projections. Track projections are combined to form 3-dimensional track candidates and the hits fit again. Loose cuts on the fit quality leave a large number of tracks sharing track projections. After some additional arbitration to reduce duplicate tracks, many of the remaining track candidates are to be found clustered about the true tracks. These clusters are then reduced to single tracks on the basis of the number of shared hits and their spacing.

Once all SSD tracks are found, their slope and intercept information is entered into a special track list with a maximum of 50 tracks. A recovery program is then run using as yet unused hits and greater allowances for missing hits to pick up additional tracks. This recovery scheme is intended predominantly for wide angle tracks not completely accepted by the SSD system.

Monte Carlo studies indicate that the overall asymptotic efficiency for SSD track reconstruction reaches 99 percent by 10 GeV, with an efficiency of about 90 percent at 2.5 GeV. The relative percentage of reconstructed spurious tracks is about 2.7 percent.

3.2 Vertex Finding

Several vertex finding routines were used in E687 at various stages of the data analysis. The routines discussed in this section were used to find vertices in the target region. Main spectrometer vertices are those found using only MWPC track parameters and momentum information, while SSD vertices use only SSD track information. The small strip spacing of the SSD system allows vertex routines to easily resolve the primary production and secondary decay vertices indicative of charm events. However in the analyses presented here the SSD vertex routine is used primarily for determining 3 chamber track momenta and neutral Vee finding. Analyses of D mesons uses a third algorithm, the candidate driven vertex algorithm, which is discussed in section 3.9 . Main spectrometer vertices are used exclusively for momentum determination, and then only when SSD vertex information is unavailable, so discussion will concentrate on the latter. Included is a discussion of vertex resolutions which is relevant to all vertex finding routines using SSD track information.

Both Main Spectrometer and SSD vertices are found in essentially the same way. A single vertex is formed with available tracks in the event. Tracks are then removed to improve the quality of the vertex, and the vertex is accepted if it passes certain χ^2 criteria. Tracks removed from the vertex are used to seed other vertices which then undergo the same process.

In order to form good vertices it is critical that resolution effects are well understood, since better resolved tracks should be weighted more heavily than poor ones in any fit. The main factors determining resolution in the E687 spectrometer are granularity (wire or strip spacing) and MCS effects. In fitting the MWPC or SSD hits the optimal track parameters are related to the hits by a transformation matrix

$$t_\alpha = P_{\alpha i} X_i$$

The track covariance matrix is then related to the coordinate (or hit) covariance matrix by

$$\langle \delta t_\alpha \delta t_\beta \rangle \;=\; P_{\alpha i}\, P_{\beta j}\, \langle \delta X_i \delta X_j \rangle \tag{3.1}$$

where summation over the repeated indices is implied in both equations. The correct covariance matrix $\langle \delta X_i \delta X_j \rangle$ contains a diagonal granularity term plus a momentum dependent off diagonal MCS term

$$\langle \delta X_i \delta X_j \rangle \;=\; \frac{\delta_{ij}}{12} + \frac{a_{ij}}{P^2} \tag{3.2}$$

The off diagonal elements arise because the scattering of a track introduces deviations in its measured downstream coordinates which are correlated. For expediency, the track parameters are found by a simple least squares fitting which neglects the a_{ij} term. However, it is possible to include MCS effects in the complete track covariance matrix which is used in all vertex fits. Correlations are taken into account in the track covariance matrix by combining Equations 3.1 & 3.2

$$\langle \delta t_\alpha \delta t_\beta \rangle \;=\; \left(1 + \frac{P^{*2}_{\alpha\beta}}{P^2}\right) \langle \delta t_\alpha \delta t_\beta \rangle_\infty$$

where $P^{*2}_{\alpha\beta}$ parameterizes the MCS effects. The variance used in vertex fits is simply

$$\sigma_\alpha \;=\; \sigma_{\alpha\infty} \sqrt{1 + \frac{P^{*2}}{P^2}} \tag{3.3}$$

where $\sigma_{\alpha\infty}$ is the anticipated error of the track parameter α if the track were of infinite momentum (i.e. granularity resolution only). The value of P^* is computed directly from spectrometer layout and serves as an effective momentum below which MCS effects begin to dominate. In E687 the x-y resolution of a track extrapolated to the center of the target entirely through high resolution strips of the SSD detector is calculated to be :

$$\begin{aligned} \sigma_x &= 11\mu m\,\sqrt{1+\left(\frac{17.5GeV}{p}\right)^2} \\ \sigma_y &= 7.7\mu m\,\sqrt{1+\left(\frac{25GeV}{p}\right)^2} \end{aligned} \qquad (3.4)$$

Rather than calculate a separate set of anticipated resolutions for every track trajectory through the silicon microstrips, a simplification is employed where the resolution is averaged over low and high granularity portions of the SSD system.

$$\sigma^2 \;=\; f_{hi}\,\sigma_{hi}^2 + (1 - f_{hi})\,\sigma_{low}^2$$

Here f_{hi} refers to the fraction of SSD planes which the track intersected in the high granularity region. Tests with track vertices in data have shown that actual combined track and vertex resolutions are within roughly 10 percent (see section 3.12) of calculated resolutions found with these formulae. In order to correctly anticipate these resolutions it is necessary to know the track momenta. In the case of SSD tracks this means a connection must be made with an MWPC track. The method for linking tracks is discussed next.

3.3 Linking of SSD and MWPC Tracks

Linking of the two tracking systems turns out to be an extremely important aspect of track reconstruction and analysis. Tracks found in the MWPC system have momentum information and particle identification but no precise vertex information. Without the excellent vertex resolution of the SSD system, much of the analyses presented here would not be possible. Likewise the tracks found in the SSD system are of little use without momentum information. A routine is therefore used to match the tracks of particles which pass through both systems.

The linking routine compares the 2-dimensional miss distance and slope (x' only for 3 chamber tracks) of all SSD tracks with each MWPC track at the center of M1. Combinations which pass a set of loose linking criteria are each fit, using the relevant hits in all 32 planes, to the hypothesis of a single track. MCS corrections are not included in the fit, but the minimum χ^2 of each fit is adjusted upward in order to crudely compensate for MCS effects. This 32 plane χ^2 is then used to arbitrate between different SSD tracks which are candidate links with a particular MWPC track. The result is that each MWPC track is linked to a unique SSD track while an SSD track may be used more than once. The best approach to the linking may have been to use the MCS corrected track uncertainties, but studies have shown that their omission is not critical. If the separation of tracks at the comparison plane is much larger than their mean resolution including MCS effects, then few mistakes are made in choosing an SSD track provided the χ^2 cuts are loose. Studies have been made of the linking efficiency and are presented in section 4.2.2 in conjunction with tests of linking in the Monte Carlo. Those results indicate that more than 90 percent of both 3 and 5 chamber tracks have an SSD link. This fraction reflects both the efficiencies for finding an SSD track as well as the linking efficiency.

3.4 Momentum Determination

Once main spectrometer tracks have been linked to SSD tracks and vertices are found it is possible to determine the best momentum of 3 chamber tracks. Particle momenta are determined iteratively by selecting the momentum giving agreement with the upstream SSD track segment. As in the case of 5 chamber tracks, the charge is then determined from the bend direction. For tracks which remain unlinked it is necessary to choose a vertex position with which to fix the momentum. If only one vertex was found in the event, the unlinked track is assigned to it. In lieu of an SSD vertex, a main spectrometer vertex is used. Barring that, the center of the target is chosen. If more than one SSD vertex exists the choice is made by closest x projected approach to each vertex using an approximated momentum for the track.

The anticipated momentum resolution is computed from the spectrometer layout. The resolutions, which include MCS effects are specifically

$$\begin{aligned} \frac{\sigma_p}{p} &= 3.4\% \left(\frac{p}{100GeV}\right) \sqrt{1+\left(\frac{17GeV}{p}\right)^2} \qquad M1 \\ \frac{\sigma_p}{p} &= 1.4\% \left(\frac{p}{100GeV}\right) \sqrt{1+\left(\frac{23GeV}{p}\right)^2} \qquad M2 \end{aligned} \tag{3.5}$$

The asymptotic portion of these expressions, $\sigma \propto p^2$, is due entirely to the granularity of the MWPC system. As expected, the resolution using only 3 of the 5 chambers is somewhat poorer. However the MCS effects are larger for 5 chamber tracks, as evidenced by the larger effective momentum. This is because the effect of a scatter becomes magnified over the length of the spectrometer. These resolutions have been verified by comparing track momenta measured with M1 and M2. Studies of their error normalized difference imply an understanding of the resolution to within 10 percent, and an understanding of systematic differences to within 0.5 percent.

3.5 Neutral Vees

The most copious particle decays which can be reconstructed with the magnetic spectrometer are neutral vees, so called because the undetected parent particle decays into 2 charged tracks which are detected. Decays which are reconstructed in this way are :

$$\Lambda^\circ \to p^+ \pi^-$$

$$K_s \to \pi^+ \pi^-$$

These states are particularly useful because they are produced in charm meson and baryon decays. Their strong signals also make them useful in analyzing the effectiveness of the experiment's particle identification. Their usefulness depends to a large degree on how well the signals can be resolved from background. These factors can both be related to momenta of the constituents, opening angle, azimuth of the decay plane, and the decay region. The region of the decay is important because it affects the type of track information available. The lifetime of these states is long enough that a significant fraction will decay beyond the SSD system. Thus it is useful for the purpose of reconstructing neutral vees to divide them into topologies corresponding to different tracking capabilities. Descriptions of each of these topologies and the reconstruction method is discussed below. Signals for neutral vee states are shown in Figure 3-1 for several of the more copious topologies.

3.5.1 Target Region Vees

The method of searching for neutral Vees in all topologies involves forming the total momenta and invariant masses from all unique pair-wise combinations of tracks. To be considered, a combination must have a $p\pi$ invariant mass near that of the Λ^0 or a $\pi\pi$ mass near that of the K_s (or both), and the tracks must be oppositely charged. Neutral Vees from the target region will have decayed early enough that there is frequently SSD track information. Both tracks are required to be linked so that the resulting Vee will have momentum information. The best vertex position is calculated using the SSD track information and a cut of $< 120\mu$m is made on their miss distance at the vertex plane. Track resolution in the SSD system is sufficiently good that the neutral vee can be expected to backwards extrapolate to a primary vertex. Requiring that the vee vertex *point back* to within 1mm of a vertex found by the SSD vertex routine and that the two vertices be separated in z by greater than $20\sigma_z$ is very effective at reducing combinatoric background. The *point back* distance is the closest approach distance between the primary vertex and a vector passing through the vee vertex directed along the vee momentum vector. If more than one vertex is found by the SSD vertex routine the most downstream vertex is chosen.

A fair fraction of neutral vees will decay downstream of the first set of SSD planes yet still inside the SSD system ($\sim$ 18cm). In these cases, tracks will not be found by the SSD track finding routine. A special routine exists to search for unused hits in the SSD system with unlinked MWPC tracks as seeds. Matching

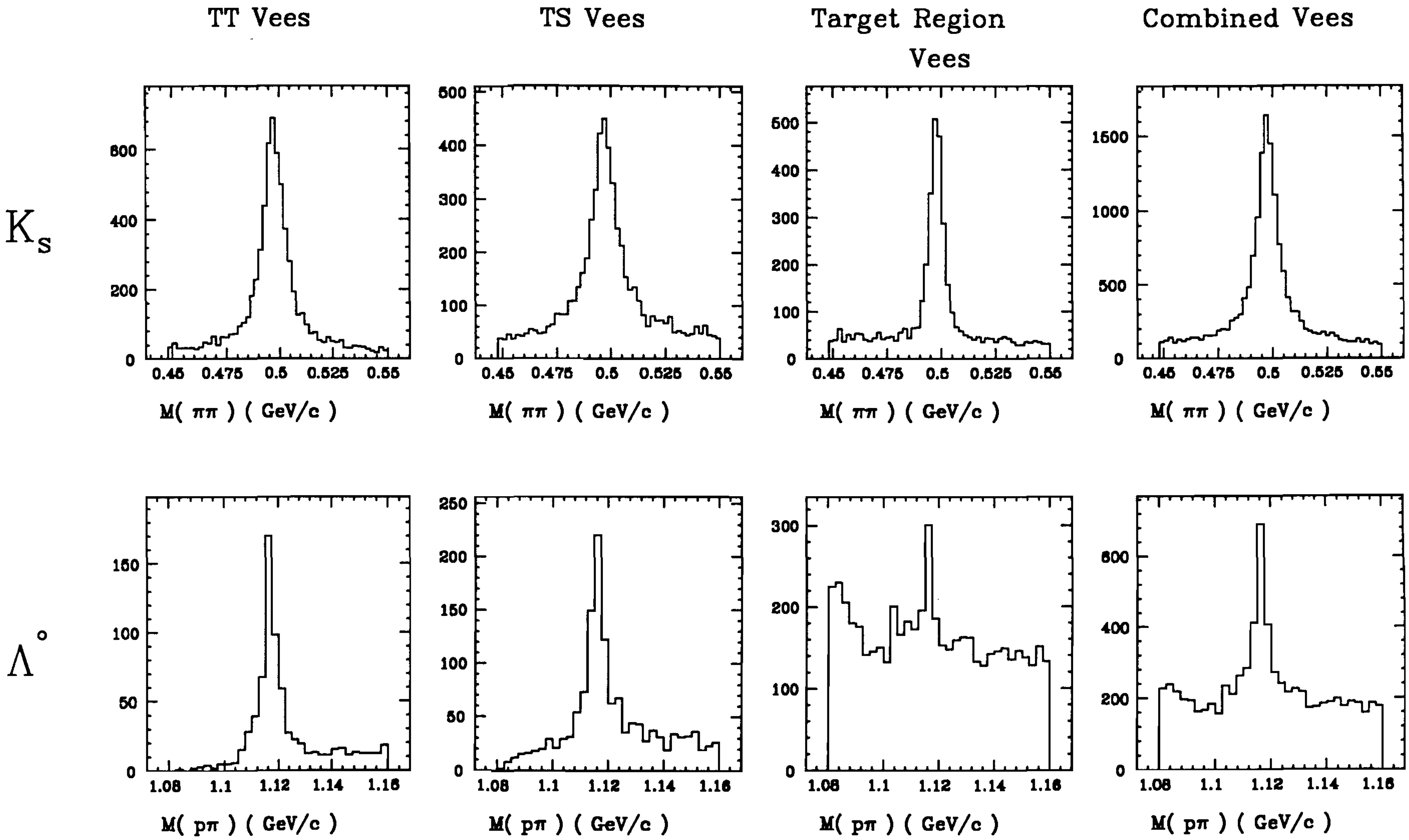

Figure 3-1 : Signals from some of the neutral vee topologies

hits in at least two SSD stations plus additional constraints are necessary to identify the combination as a neutral vee.

3.5.2 Magnet Region Vees

The region between the SSD system and P0 contains a large number of neutral vee decays. Vees in this region are distinct because they lack SSD track information but have complete MWPC track information. They are further categorized according the MWPC track information as

1. TT vees: both 5 chamber tracks
2. TS vees: a 3 and a 5 chamber track
3. SS vees: both 3 chamber tracks

The search proceeds as before forming 2-body combinations and searching for good vertices. Except for TT vees, the presence of the magnetic field allowed comparison of the x (non-bend) track projections only. Once an initial vertex was found an iterative procedure of tracing the tracks through the magnetic field was used to determine the best vertex location and best momentum for 3 chamber tracks. Vee candidates tracks were then refit using the full track covariance matrix, including MCS effects, and the best (minimum χ^2) vertex found again. The fit hypothesis is that the two tracks form a 3-dimensional vertex and the resulting vee vector points back to an SSD found vertex. Track candidates were not allowed to be linked. Candidates failing a χ^2 cut were rejected.

3.5.3 Reconstruction Vees

This category includes vees which decay downstream of P0 yet upstream of P3. Charged tracks in this region would not have been found through normal track reconstruction, but because of additional constraints enough information exists to find track segments. These segments are formed out of chamber hits not assigned to tracks in the MWPC track reconstruction. The vee search is conducted by searching for vertices first in the P0 - P1 region, then in the P1 - P2, and so on. Candidates are subject to a fit with the constraint of a common vertex, which compensates for missing chamber information. At least one chamber downstream of M2 must contain hits to provide momentum measurement. Even so a direct momentum determination is difficult for vee decays with no chamber information upstream of M2 or only one chamber on either side of the magnet. In these cases the neutral vees are constrained by point back to a target vertex.

3.6 Particle Identification

Charged particle identification is made with the three threshold Čerenkov detectors. Identification in the form of electromagnetic calorimetry and muon counters is also available but was not used in these analyses. Charged tracks traversing the Čerenkov detectors can be categorized as either electrons, pions, kaons, or protons (muons are close enough in mass to be categorized as pions). These 4 particles, which comprise the majority of all tracks emitting Čerenkov radiation in the experiment, have varying threshold momenta at which they begin to radiate (see Table 2-2). The detectors through which they pass can be expected to detect light or not detect light depending the actual track identity and momentum. This then, is the basis of categorizing the tracks as one of the 4 types.

The analysis begins by setting up an on/off code for every cell in each detector. This is determined by the presence or absence of a phototube pulse height above an ADC cutoff. This cutoff was chosen to exclude the pedestal and corresponds to a few picocoulombs of charge deposited in the ADC. The algorithm then considers every track in each counter individually. First the principal cell that a particular track passed through is determined. Using the momentum of the track, the detector threshold, and a particle hypothesis, the amount of light expected in the principal and adjacent cells is calculated. The particle hypothesis used to calculate the expected light yield is that of a pion above the detector's pion threshold and of an electron below the threshold. A track is called *on* by the algorithm when one or more cells is on and some light was expected, and *off* when a reasonable amount of light was expected and the cells are off. If neither condition exists, the track is given a *confused* status. The process of assigning tracks to these categories is the heart of the identification process and is discussed in Appendix A.

Once the Čerenkov responses are determined for a track (*on*, *off*, or *confused*), they are compared to the track momentum and the detector thresholds given in Table 2-2. For each of the four particle hypotheses there is an anticipated *on/off* status for the track at its given momentum and in a given detector. This anticipated status is summarized in Figure 3-2 which graphs the momentum at which light should be detected for each particle type. The actual status will either corroborate or contradict this. A four bit word is used to contain this comparison. Each bit location is associated with one of the 4 particle types so that, starting with the least significant bit :

Bit 1 : electron status

Bit 2 : pion status

Bit 3 : kaon status

Bit 4 : proton status

The bit in question is 1 if the particle hypothesis is satisfied and 0 if it is contradicted. A matrix, shown in Table 3-1, displays the bit values in this word for all possible combinations of momentum and track status in a single detector.

Table 3-1 : Individual Čerenkov Status words

Track momentum region	Track *off*	Track *on*	Track *confused*
$0 < p < P_\pi$	1110	0001	1111
$P_\pi < p < P_k$	1100	0011	1111
$P_k < p < P_p$	1000	0111	1111
$p > P_p$	0000	1111	1111

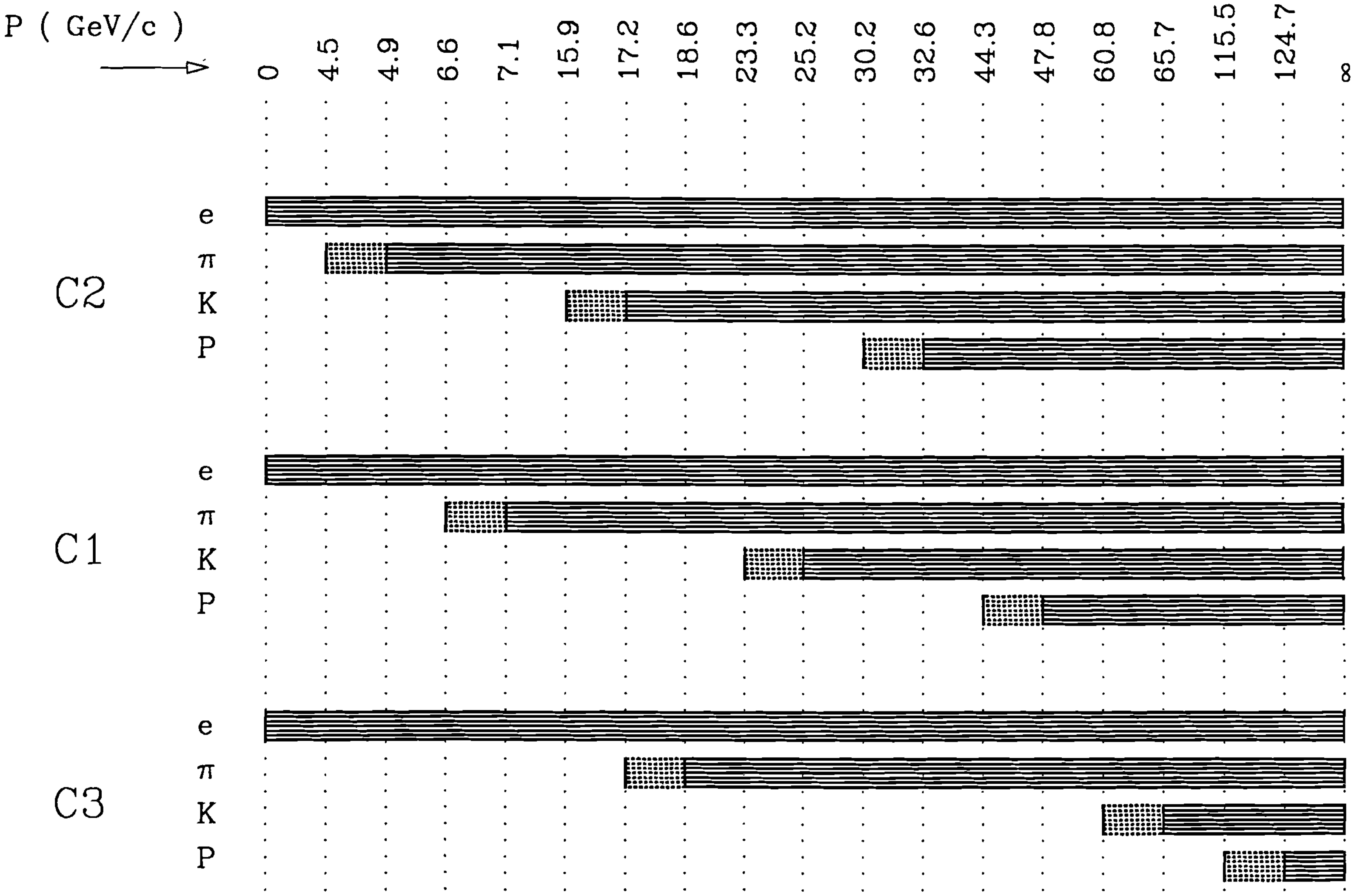

Figure 3-2 : Čerenkov detector identification regions

The values of P_π, P_k, and P_p are given in Table 2-2. The status word from all 3 detectors are logically *ANDED* to give the final status word of the track called ISTAT.

Consider for example a 40 GeV track with a status of on, on, and off in C1, C2, and C3 respectively. Referring to Figure 3-2, this momentum is above both pion and kaon thresholds in C1, but below its proton threshold. The relevant status word, from Table 3-1, describing the track status in C1, is then 0111 with a value of 7. This means that the *on* status of the track is consistent with being any of the 4 particles except a proton. The detector C2 will respond with 1111 meaning that any particle could have created the Čerenkov light it saw. C3 will respond with 1100. The final value of ISTAT is then $0111 \cap 1111 \cap 1100 = 4$, saying that the track could have only been a kaon. Identifications corresponding to each of the ISTAT codes is given in Table 3-2.

Table 3-2 : ISTAT Codes

ISTAT	Identification
0	Inconsistent information
1	$e^\pm$
2	$\pi^\pm$
3	$e^\pm$ or $\pi^\pm$
4	$K^\pm$
7	$e^\pm$, $\pi^\pm$ or $K^\pm$
8	$P^\pm$
12	$K^\pm$ or $P^\pm$
14	$\pi^\pm$, $K^\pm$ or $P^\pm$
15	$e^\pm$, $\pi^\pm$, $K^\pm$ or $P^\pm$

When a detector returns a *confused* status for a track, it is effectively taken out of the decision process with a status word of 15. If C1 had been confused in the above example, an ISTAT of 12 would be returned indicating the track could have been a kaon or a proton. Detectors can return contradictory information such that the *AND* of their words returns 0. Had C1 been "off" and C3 "on" in the above example, this would have indicated something abnormal such as phototube efficiency or noise problems. The only time these problems can be corrected is in the case of a track called *off* when its momentum is above the proton threshold in the detector. In these instances the detector is obviously returning incorrect information and is removed from the *logic* decision by changing its status word from a 0 to a 15.

A slight complication arises because detector threshold is not a step function but rather a gradual increase in light above threshold. The number of photoelectrons expected above threshold is

$$N_{pe} = N_{pe}(p \rightarrow \infty)\left(1 - \frac{P_T^2}{p^2}\right)$$

This slow rise is exhibited in the threshold curves of Figure 2-5. A pion with momentum just above the threshold value will leave far less light than anticipated under the electron hypothesis. In such a case the light might easily remain undetected and the detector would negate the track's identification as a pion. One way dealing with this is to use the correct hypothesis for the light yield. As discussed above, the pion hypothesis is used unless the track is below the pion threshold in which case an electron hypothesis is used. If the final ISTAT contradicts the original hypothesis, though, the entire analysis of the track is redone under the new hypothesis.

This process would become quite time consuming if the same were done with kaons and protons, so a second approach is used as well. Tracks in threshold momentum regions of detectors are treated somewhat differently than in the 4 main momentum regions. Each detector has three threshold regions, one for pions, kaons, and protons, which are taken to be between the threshold momentum and 1.08 times its value. This factor, determined from a Monte Carlo simulation, defines the momentum above which light should generally be detected. The new regions are indicated as shaded portions of lines in Figure 3-2. A new set of status words similar to those in Table 3-1 is given in Table 3-3 for these three regions. The change involves using the original threshold value for light predictions when the cell is on and the higher threshold value when the cell is off.

Table 3-3 : Additional momentum regions

Track momentum region	Track *off*	Track *on*	Track *confused*
$P_\pi < p < 1.08 \cdot P_\pi$	1110	0011	1111
$P_k < p < 1.08 \cdot P_k$	1100	0111	1111
$P_p < p < 1.08 \cdot P_p$	1000	1111	1111

Codes corresponding to *on* and *confused* tracks remain the same as in Table 3-1, but *off* codes reflect the feature that missing light in a threshold region is discounted and cannot be used used to call a track *off*. The main momentum regions now start at 1.08 $\times P_T$ with the same status codes as before. So it is actually the status word from one of the 7 momentum regions in each detector that is combined to produce ISTAT.

3.7 Photon Energy Measurement

The incident photon energy in each event is determined by two detectors, the Recoil Electron Shower counter (RESH) and the Beam Gamma Calorimeter (BGM). Both are described in section 2.2 . The RESH measured the energy of the recoil electron in the bremsstrahlung process. The difference between the RESH energy and the incident electron energy thus gives the total energy lost into photons.

$$E_{loss} = E_{beam} - E_{RESH}$$

Contributions to E_{loss} is typically from 2 to 3 photons above 10 GeV, of which at most one will usually interact hadronically in the target. The BGM detects

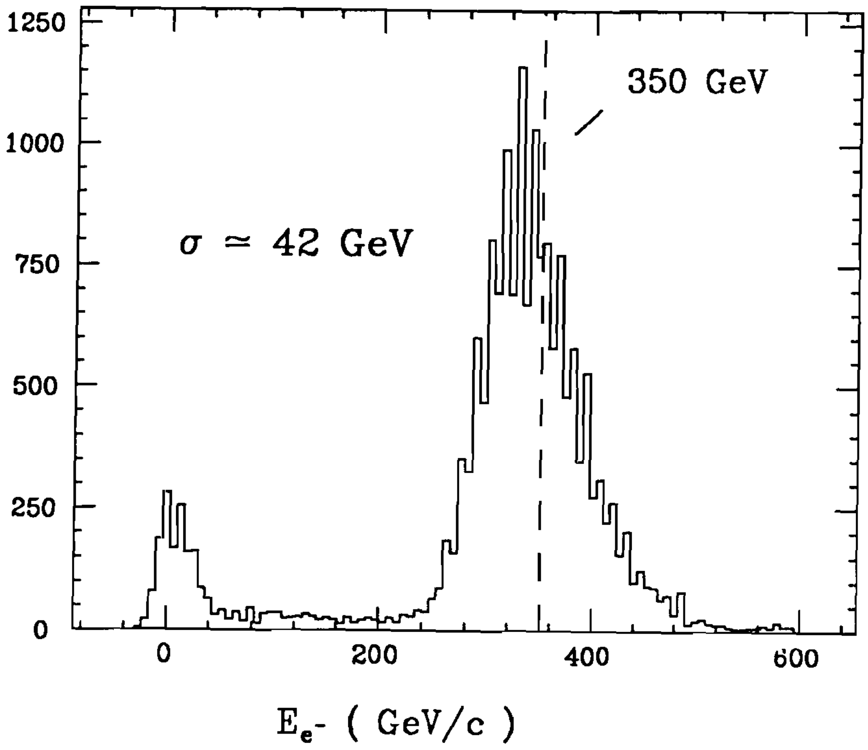

Figure 3-3 : Incident electron beam energy distribution.

all non-hadronically interacting photons downstream of the target so that the estimate of the photon energy incident on the target becomes

$$E_\gamma = E_{beam} - E_{RESH} - E_{BGM} \tag{3.6}$$

A schematic representation of the measurement is shown Figure 2-2. The radiation length of the beryllium target is about 10 % implying a large fraction of incident photons convert into e^+e^- pairs in the target. The opposite magnet currents meant that the e^+e^-pairs created in the target struck the center of the BGM, depositing energy equivalent to the original photon energy.

Each of the three quantities in Equation 3.6 has an intrinsic resolution which contributes to the overall photon energy resolution. By far the largest contribution is from the incident beam energy spread. A wide range of electron momenta was transported to maintain a high photon flux. Figure 3-3 shows a direct measurement of the electron beam spectrum using the BGM. This histogram, which corresponds to a nominal beam energy of 350 GeV, has an RMS spread of about 42 GeV. The resolution of the BGM is typically less than 10 GeV, so most of the spread is due to the incident beam. The RESH energy resolution contributes to the overall resolution as well. Measurement of the recoil electron energy in the RESH is quantized, because only the position of the electron in the RESH counter and the sweeping magnet kick is used to calculate its momentum. The position is fixed at the center of one of ten RESH segments except when two adjacent counters fire, in which case it is positioned at their boundary. Division of the energy spectrum into 19 discrete values results in a resolution of roughly 5 percent or less. Combining this with the beam spread and BGM resolution forms an estimate of the E_γ resolution, $\sigma(E_\gamma) = 46$ GeV. The effects of this rather poor measurement are discussed in Chapter 6 in conjunction with the cross section calculation.

In addition to poor resolution in the measurement of E_γ, evidence for systematic shifts in this measurement exist as well. Comparison of the energy spectrum measured in the BGM with the anticipated spectrum indicates an excess of events at high E_{BGM}. This excess is roughly consistent with a 25 percent *pile up* rate in the BGM calorimeter. *Pile up* occurs when photons from more than one bremsstrahlung event fall in a single gate ($\sim$ 40 ns) of the BGM ADC. The affect on the BGM response curve then is to deplete regions of low E_{BGM} and add to high regions. The result is that photons energies determined from Equation 3.6 will be systematically low. Since the pile-up effect cannot be corrected in each event, an independent estimator has been created[9] to adjust the value of E_γ. The estimator utilizes the fact that $E_\gamma > \sum p_i$, the sum over momenta of charged tracks. In events where the momentum sum is greater than E_γ measured, it is used instead to estimate the photon energy incident on the target. But estimates of E_γ will still be below the true value, especially at low energies. The spectrum of measured photon energies is shown in Figure 3-4 for events containing $D^\star$ candidates. The most obvious feature in the figure are the spikes caused by the quantized RESH measurement when little or no energy was deposited in the

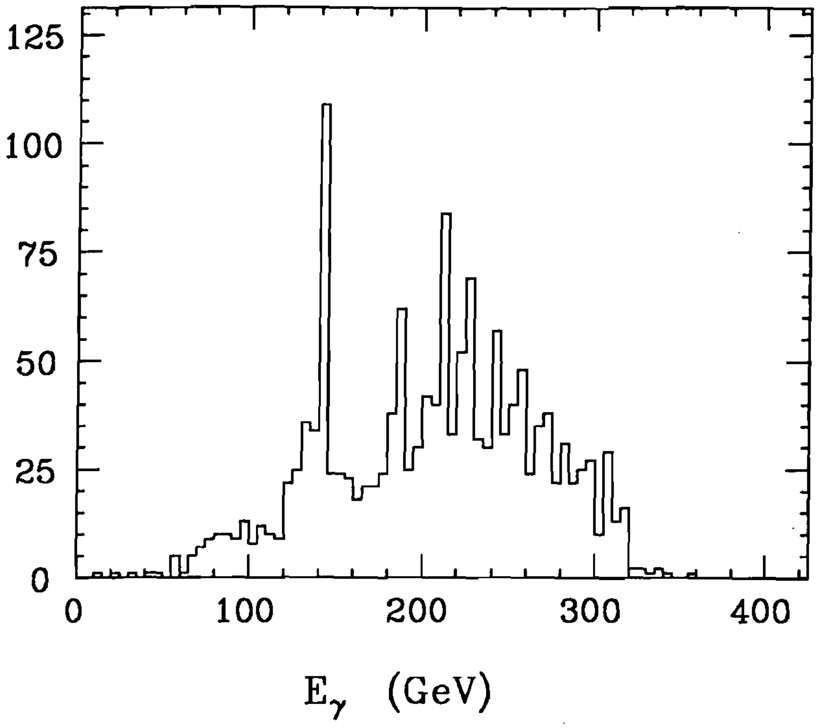

Figure 3-4 : Measured photon energy distriution (D* events).

BGM. The largest contribution to the E_γ bias, the beam spread, is not obvious from the figure but it greatly affects the cross section measurement.

3.8 Photon Luminosity

Measurement of the number of photons incident on the experimental target is necessary in determining cross sections. The two approaches to luminosity measurements can be described as *direct* and *indirect* methods. Indirect methods involve calculation of known cross sections using experimental data taken under the same running conditions as the events of interest. An example of this is a calculation of the photon flux necessary to produce the observed number of hadronic events using the known hadronic cross section. The direct measurement involves actual counts of the incident or noninteracted flux. The detector information necessary in each method tends to be different, and hence one is usually more reliable or easier than the other. For such reasons the *direct* method of measuring luminosities was chosen and is described next.

There are basically two measurements that are directly related to the photon flux, a count of electrons incident on the radiator and a count of photons which did not interact hadronically in the target. Incident electrons are scaled by a counter upstream of the radiator called the BT counter, while photons are measured by the BGM calorimeter. Each measurement has its specific problems, not least of which is that neither is a direct count of the photons striking the target. Because each electron typically produces 2 - 3 *multi-brem* photons, an understanding of the electron beam spectrum, the bremsstrahlung process, and the beam profile at the target are essential to calculating the photon flux from the detector counts. Beyond that each counter had characteristic responses which affect the count rate. Therefore the easiest way to measure photon fluxes was with a Monte Carlo simulation of the bremsstrahlung production process and the detector responses. Using a simulation, a direct relationship can be established between monitor detector counts and the spectrum of photons impinging on the target. The absolute photon flux need never be calculated. Rather the luminosity count in data was compared to that of the Monte Carlo and used to correct the cross section directly. This procedure is discussed in detail in Appendix D, while the Monte Carlo simulations are discussed in section 4.1.2 .

The choice was made to monitor photons with the BGM rather than the electron beam monitor (BT) because the latter is susceptible to charged pion contamination in the beam and because the electron beam counter experienced *pile up* problems similar to those discussed in the previous section. Two electrons can arrive at times separated by less than the time resolution of the scaler so that only one count is recorded. This is illustrated in Figure 3-5(a) which plots beam hodoscope counter (BT) response as a function of the number of primary beam protons. Lines of varying slope reflect different primary beam efficiency and duty factors. A line has been drawn which corresponds to $e^-/p^+ = 3.85 \times 10^{-5}$. An indication of pile-up is that the BT counts fewer electrons than expected at high incident proton rates. While the BGM suffered from *pile up* as well, the count

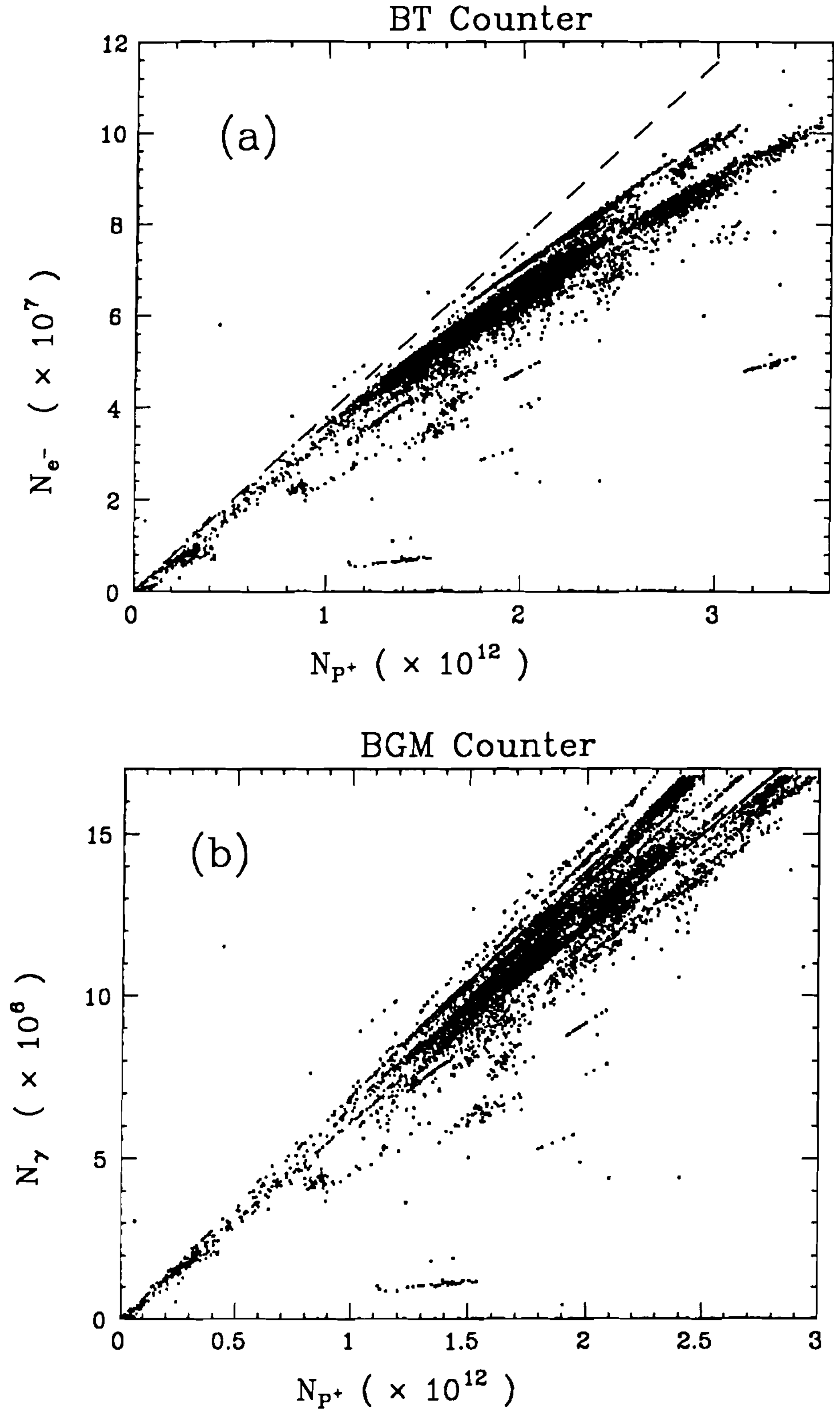

Figure 3-5 : Incident electron count (BT) and incident photon count (BGM) versus primary proton count.

rate does not reflect this. Signals from the BGM were sent to scalers which are efficient at counting above a certain pulse height set to about 133 GeV deposited in the counter. Photons from two events with insufficient energy to pass this threshold can pile up to form a pulse height in the calorimeter large enough to be scaled. These extra false counts nearly compensate for counts lost from *pile-up* of photons above threshold. Figure 3-5(b) serves to demonstrate this point by plotting, in analogy with Figure 3-5(a), the number of BGM photons per primary beam proton. None of the high rate depletion apparent in the BT counter plot is evident here.

Several aspects of the luminosity count were not modeled in the Monte Carlo, and therefore had to be accounted for separately. First of all allowance was made for the dead time of the data acquisition system. A fraction of events is not recorded because the DAQ is busy with the previous event. This fraction is determined to be 25 % from a ratio of the master gates seen by the DAQ and an independent scaling of master gates. The luminosity scaler count must be lowered by 25 percent since DAQ dead time does not affect them. Another process affecting the luminosity count is e^+e^-pair production from photons interacting downstream of M1. The e^+e^-pairs will not be focused correctly onto the BGM and therefore go uncounted. A study has shown[10] that the luminosity count is therefore 6 percent too low.

3.9 Candidate Driven Vertex Algorithm

The purpose of a vertex finding algorithm in the context of analyzing charm events is twofold. First and foremost the ability to see both a primary production vertex and a secondary decay vertex in an event is a powerful background reduction tool. Background events rarely have well separated vertices whereas charm events will exhibit a secondary decay vertex provided there is sufficient vertex resolution. Secondly the presence of production and decay vertices is of course essential in measuring the lifetime of a particular state.

The SSD vertex routine described in section 3.2 is very good at finding multiple vertices in the target region, an essential ingredient in charm background reduction. In fact several analyses have been completed[11] with it as the only vertex finding tool. The algorithm has several drawbacks, however, the worst being poor efficiency. If a free form algorithm is to find multiple vertices, each vertex must be formed cleanly or be well separated from other vertices. The first of these biases the routine against high momentum (small angle) tracks while the second means a poorer efficiency at finding short lived states. The solution to these problems is to help the vertex routine out with some added constraints. If a vertex routine is told exactly which tracks comprise a particular vertex, then it is rather easy for it to find another good vertex with the remaining tracks. This type of routine is called a candidate driven vertex algorithm and is used extensively throughout the analyses presented in this thesis.

3.9.1 Basic Routine

The standard routine[12] is supplied with a list of tracks which are hypothetical decay products of a charm particle. These tracks are usually chosen kinematically so that they form a favorable invariant mass, but the vertex routine has nothing to do with their selection. With the tracks supplied, a candidate charm track is formed with a fit using the full covariance matrix (x, x', y, y', p) of each individual track. A standard requirement is that all secondary vertex tracks are linked so that the candidate charm track will have the same resolution as other SSD tracks. Candidates involving a K_s are exceptions to the linkage requirements, and are discussed below as a special case.

Remaining SSD tracks (linked and unlinked) are selected on the basis of a good (confidence level > 2 %) vertex with the candidate track and placed in a list of potential primary vertex tracks. The routine has *failed* to find a primary vertex if there are no tracks with a sufficient confidence level. The best 3-track vertex, using two tracks from the list and the candidate track, is then the seed primary vertex. If no 3-track combination has a confidence level (CL) above

2 %, the best 2-track combination is chosen as the primary vertex. Using the seed vertex, remaining tracks in the list are added one at a time, and the best one is included in the primary seed provided the CL cut is still satisfied. This last process is repeated until no more tracks can be added without violating the CL requirement of the primary vertex. The position and error of the primary vertex is found by fitting the selected SSD tracks without the candidate track to a single vertex.

The two vertices are then subjected to a common fit to determine their separation ℓ. During this fit the primary vertex position is fixed and the best secondary vertex chosen along the candidate momentum vector. The value of ℓ is actually no more precise than the Δz between the two vertices, but is found for historical reasons (it seemed a good idea at the time). The ℓ fit has been useful in cases where the primary vertex is not already constrained by the secondary vertex, such as in the *free form* vertex algorithms described in section 3.2 . Along with the value of ℓ, the fit returns its uncertainty σ_ℓ . The size of σ_ℓ is tied to the covariance matrices of all the tracks involved on the two vertices, and measures the precision with which the vertex separation is determined. The best measure of the vertex separation is therefore a normalized detachment criterion given by ℓ/σ_ℓ . It is the significance of detachment ℓ/σ_ℓ which is the tool most often used in these analysis to remove non-charm background. Therefore it is important to understand the performance of this cutting tool. The algorithm was designed to find vertices in events containing charm particle decays, so a study of its performance is best done with charm events. Since the D^0 and $D^\star$ decays used in this study are also the objects of analyses in this thesis, this discussion is deferred to section 3.13 .

3.9.2 Inclusion of K_s Mesons

A variation of the algorithm just described allows inclusion of D meson decay modes involving K_s mesons. These present a special problem because many of the K_s mesons have vertices downstream of the SSD system, and hence have no high resolution track information. In such cases the K_s will have good 3-momentum information but poor position resolution. The resulting K_s track is treated the same as other linked tracks in forming the secondary vertex, but its (x,y) errors are not allowed to contribute to the D meson covariance matrix. The secondary vertex must therefore have at least two linked tracks to precisely determine the D candidate track. However it is possible to determine the vertex separation for candidates involving only one K_s and one linked track, such as $D^{\pm} \rightarrow K_s\pi$. In these cases the secondary vertex is constrained only to lie along the vector of the linked track. The additional constraint necessary in finding the exact secondary vertex position is provided by the primary vertex, which is found independently in this case.

3.10 The Data Skim

Numerous analyses searching for charm and other interesting events in the reconstructed data were run simultaneously during the skim processing. Each analysis selected events to be kept which were written to output tape. Each event had an identifier describing which of the individual skim analyses selected the event. The discussion here is primarily concerned with one of these skim analyses, the D meson skim, since the work presented in this thesis is based almost exclusively on events obtained through this skim.

While not the only skim analysis of D mesons, this skim was the most comprehensive and was designed to search for a large number of charged decay modes of D° , $D^{\pm}$, $D_s^{\pm}$ and $D^{\star\pm}$ mesons. The decay modes included in the search were those involving $\pi^{\pm}$, $K^{\pm}$, and K_s in combinations of up to 7 bodies. These combinations are listed in Table 3-4 where they are categorized in terms of the parent particle and the charge/strangeness correlations involved with Cabbibo suppression. "Wrong sign" charge combinations which were also included in the skim are omitted from the table. The total skim consisted of well over 100 unique decay modes ! Few of these is likely to result in an observable signal, but it cannot be known which these are until a search is made.

Table 3-4 : D Meson Skim

D^{*+} Decay Modes

Cabbibo Allowed

$(K\pi)\pi$	$(K_s\pi\pi)\pi$	$(K\pi\pi\pi)\pi$	$(K_s\pi\pi\pi\pi)\pi$	$(K\pi\pi\pi\pi\pi)\pi$	
$(K_sKK)\pi$	$(K_sK_sK_s)\pi$	$(KKK\pi)\pi$	$(K_sK_sK\pi)\pi$	$(K_sKK\pi\pi)\pi$	$(K_sK_sK_s\pi\pi)\pi$

Cabbibo Suppressed

$(\pi\pi)\pi$	$(\pi\pi\pi\pi)\pi$	$(\pi\pi\pi\pi\pi\pi)\pi$			
$(KK)\pi$	$(K_sK_s)\pi$	$(K_sK\pi)\pi$	$(KK\pi\pi)\pi$	$(K_sK_s\pi\pi)\pi$	$(K_sK\pi\pi\pi)\pi$
$(KK\pi\pi\pi\pi)\pi$	$(K_sK_s\pi\pi\pi\pi)\pi$				

D^+ (D_s^+) Decay Modes

Cabbibo Allowed (Suppressed)

$K_s\pi$	$K\pi\pi$	$K_s\pi\pi\pi$	$K\pi\pi\pi\pi$	$K_s\pi\pi\pi\pi\pi$
K_sK_sK	$K_sKK\pi$	$K_sK_sK_s\pi$	$KKK\pi\pi$	$K_sK_sK\pi\pi$

Cabbibo Suppressed (Allowed)

$\pi\pi\pi$	$\pi\pi\pi\pi\pi$		
K_sK	$KK\pi$	$K_sK_s\pi$	$K_sK\pi\pi$
$KK\pi\pi\pi$	$K_sK_s\pi\pi\pi$	$K_sK\pi\pi\pi\pi$	

D° Decay Modes

Cabbibo Allowed

$K\pi$	$K_s\pi\pi$	$K\pi\pi\pi$	$K_s\pi\pi\pi\pi$	$K\pi\pi\pi\pi\pi$	
K_sKK	$K_sK_sK_s$	$KKK\pi$	$K_sK_sK\pi$	$K_sKK\pi\pi$	$K_sK_sK_s\pi\pi$

Cabbibo Suppressed

$\pi\pi$	$\pi\pi\pi\pi$	$\pi\pi\pi\pi\pi\pi$			
KK	K_sK_s	$K_sK\pi$	$KK\pi\pi$	$K_sK_s\pi\pi$	$K_sK\pi\pi\pi$
$KK\pi\pi\pi\pi$	$K_sK_s\pi\pi\pi\pi$				

Table 3-5 : $D^\star$ Skim Criteria

	$> \ell/\sigma$	F_τ	F_{mc}	Skim Frac.
$K\pi$	all	1.0	–	.06
$K_s 2\pi$	all	1.0	–	.03
$K3\pi$	all	1.0	–	.16
$K_s 4\pi$	all	1.0	–	.02
$K5\pi$	all	1.0	–	.02
2π	0.	1.0	$> .80$	.02
4π	1.0	.89	$> .90$	.10
6π	0.	1.0	–	.04
$2Kn\pi$	all	1.0	–	.06
$3Kn\pi$	all	1.0	–	.01

Table 3-6 : D^0 Skim Criteria

	$> \ell/\sigma$	F_τ	F_{mc}	Skim Frac.
$K\pi$	1.0	.89	$.87 \pm .04$	.12
$K_s 2\pi$	1.5	.81	$.88 \pm .03$	.04
$K3\pi$	1.5	.85	$.81 \pm .02$	.18
$K_s 4\pi$	1.0	.88	–	.03
$K5\pi$	0.	1.0	–	.02
2π	2.0	.80	$> .95$	.04
4π	3.0	.71	$.68 \pm .14$	.09
6π	2.0	.80	–	.03
$2K$	1.0	.89	$.88 \pm .13$	.04
$K_s K\pi$	1.0	.87	–	.04
$2K2\pi$	1.5	.85	–	.06
$K_s K3\pi$	0.	1.0	–	.02
$2K4\pi$	0.	1.0	–	.01
$3Kn\pi$	0.	1.0	$.90 \pm .06$	.03

Table 3-7 : $D^\pm$, $D_s^\pm$ Skim Criteria

	$> \ell/\sigma$	F_τ	F_{mc}	Skim Frac.
$K_s\pi$	0.	–	$.85 \pm .08$	.07
$K2\pi$	2.5	.89	$.83 \pm .05$	.14
$K_s 3\pi$	1.75	.91	$.86 \pm .06$	.05
$K4\pi$	2.0	.91	–	.07
$K_s 5\pi$	0.	1.0	–	.01
3π	4.0	.84	–	.05
5π	4.0	.84	–	.05
$K_s K$	0.	–	–	.04
$2K\pi$	2.0	.91	$.88 \pm .06$	.09
$K_s K2\pi$	1.0	.95	–	.04
$2K3\pi$	0.5	.98	–	.05
$K_s K4\pi$	-100.	1.0	–	.01
$3Kn\pi$	0.5	.98	–	.05

The event selection was made with a single search algorithm. An event was kept if it contained at least one D meson candidate which passed a certain set of skim criteria. Candidates were found through a kinematic search where an invariant mass was formed of the constituent tracks and required to fall in a specific range. That the D meson skim was able to perform this search in an efficient manner is due to a somewhat unique algorithmic approach. The standard approach involves combinatoric loops over the number of available tracks nested n deep, where n is the number of tracks in a particular decay state. These loops are complicated by the assignment of particle identification to each of the tracks and the additional requirement that combinations not be duplicated. This approach can be quite efficient when considering a single decay state, especially if it has a low multiplicity. But searches for more states can involve substantial increases in the execution time and coding complications. The result in the past is that each pass through the data has been limited to searches for a small number of decay modes, usually the most common ones. Attempts to search for rarer decay modes then involve additional skims through the data sample.

The alternative approach in this D meson skim algorithm involves the use of just two combinatoric loops, regardless of the number of decay modes. All MWPC tracks and neutral vees in an event are assigned to a specific bit in a 32 bit word. Each event has a 30 MWPC track maximum but a typical event contains less than 10 tracks (and vees). Each value of the word then corresponds to a unique combination of tracks, and the values from 3 to $2^N - 1$ form a complete set of combinations of N tracks. Testing the bit status of the word tells which tracks are to be used in a particular combination. The number of combinations to be checked is still large, but this number is significantly reduced by overall charge restrictions, the maximum final state multiplicity, and the requirement that all tracks be linked. In order to form a total invariant mass, each track must be assigned a mass (π, K, or K_s). If a vee is included in a combination its mass is fixed. But MWPC tracks can be either kaons or pions. Amongst the n tracks in a combination there will be $2^n - 1$ different ways of assigning the two particle identifications. This then lends itself to a second, inner combinatoric loop over particle assignments similar to the one used for track combinations. This pool of combinations is again reduced by requirements of positive Čerenkov identification of kaons and tighter restrictions on the χ^2 of vee candidates (see section 3.6). Finally, only those combinations within a narrow range of invariant mass are selected.

Mass Cuts :

$$1.6 \text{ GeV} < M(D^\circ) < 2.12 \text{ GeV}.$$

$$1.6 \text{ GeV} < M(D^\pm) < 2.22 \text{ GeV}.$$

$$M(D^{\star\pm}) - M(D^\circ) < 0.16 \text{ GeV}.$$

A few complications are introduced in searching for $D^\star$ candidates. The cascade pion involved in the decay to a D° is not required to be linked. Therefore $D^\star$ candidates are formed from existing D° candidates by calculating an invariant mass with a cascade pion candidate selected from a pool of unused tracks. Only candidates with sufficiently small $D^\star - D^\circ$ mass difference are selected.

If the events were selected purely by kinematic and Čerenkov criteria discussed thus far, they would represent about 40 percent of the entire data sample. In order to reduce this to the final 13 percent skim background events were removed by the requirement of detached vertices. Few non-charm events (with the exception of SSD vees) are expected to have more than one vertex in the target region, so evidence for multiple vertices in an event is often enough to eliminate a large fraction of the background events. The candidate driven vertex algorithm discussed in section 3.9 was used to find multiple vertices in events and select on the basis of the vertex separation. It is well suited to a first level skim because of the ability to tune detachment cuts to specific decay modes, and because the lifetime distribution remains unbiased beyond the detachment cut used in the edit. This last point is very important for measuring lifetimes, and is discussed at length in Chapter 7. The ability to tune cuts to specific decay modes is desirable because it reduces potential biases against certain decay modes introduced by a single vertex detachment criterion (as is the case with the *free form* SSD vertex finding algorithm).

The candidate driven vertex algorithm performs a fit to find the best value of the vertex separation. This separation ℓ is divided by the error of the fit to form a normalized detachment criteria, referred to as ℓ/σ_ℓ . The minimum detachment criteria used for the different decay modes is listed in Tables 3-5 through 3-7. In decay modes with charged kaons these cuts are used in conjunction with a standard kaon identification requirement. This requirement, commonly referred to as KP7, corresponds to Čerenkov identification of kaons as (see Table 3-2): definite kaon or kaon/proton ambiguous or kaon/pion/electron ambiguous for momenta above 60 GeV, the kaon threshold of C3. In an effort to reduce momentum biases from Čerenkov identification, candidates with a poorer kaon identification, kaon consistent (kaon bit in ISTAT *on*), are selected as well. These candidates must pass larger detachment criteria than is listed in the table though. In addition to a detachment cut, candidates are required to have a well formed secondary vertex. The vertex algorithm searches for the best vertex amongst the candidate tracks, but makes no requirements as to its quality before proceeding. The skim, however, requires that the log confidence level of the vertex in the majority of candidates be better than 5.

An indication of the skimming efficiency is given in Tables 3-5,6,7 as well. The columns labeled F_τ refer to the fraction of events that might be expected to survive the detachment cut listed in the previous column. Using the relation $\ell/\sigma_\ell \cong t/\sigma_t$, an anticipated resolution σ_t (see section 3.12) based on secondary vertex multiplicity, and the known D meson lifetimes, a simple exponential decay model is used to calculate F_τ. However, because of resolution effects the actual fraction will be somewhat lower. So a full Monte Carlo simulation is used to calculate the actual expected fraction F_{mc} for a few of the many decay modes, demonstrating reasonably good agreement with the simple model. The last column is the fraction of all selected events which contain the particular decay mode, showing that no single decay mode overwhelms the skim.

D° candidate decays which have a $D^\star$ *tag* ($M(D^{\star\pm}) - M(D^\circ) < 0.16$ GeV) have sufficiently low background that all but 3 of the decay modes are selected entirely kinematically, without reference to vertex information. While no such criteria were required in the skim, much of the subsequent analysis uses vertex information in events containing $D^\star$ mesons. Vertex finding proceeds by ignoring the information of the cascade pion and treating the subsequent D° as any other. Much of the analysis in this thesis discusses "$D^\star$" decay modes and lifetimes for the sake of expediency. In fact it is a D° decay mode or lifetime being discussed, where the D° is specifically from the decay $D^{\star\pm} \rightarrow D^\circ\pi^\pm$.

One final point involves a time saving measure incorporated into the D meson skim. Much of the processing involved with combinatoric loops and vertex finding is very time consuming. So in addition to the original reconstruction information in each event, candidate information was written to the output skim tape as well. This meant that D meson candidates were found only once, thus avoiding the usual time delays involved in reprocessing skim tapes.

3.11 D Meson Analysis

After completion of the D meson skim, the remaining events underwent a format compression which reduced the necessary tape space by a factor of 10. Information such as wire and strip hits and ADC counts were discarded in favor of more summarized information involving track and vee lists, Čerenkov codes, and skim candidates.

The analysis of the summary tapes for D meson states was simplified by the candidate list written during the skim. Some minor reprocessing was necessary in order to form invariant masses, but vertex detachment information was complete. Thus searches for specific decay modes was simply a matter of histogramming the invariant mass subject to some additional cuts. These cuts varied depending on the desired signal resolution, but usually amounted to combinations of a few criteria. Background reduction tools most often employed were :

1. Vertex detachment : Cuts are applied on ℓ/σ_ℓ greater than those used in the D meson skim (see Tables 3-5,6,7).
2. Čerenkov identification : Kaons are often required to be KP7 (ISTAT = 4, 12, or 7 (P>60.8 GeV)), K/P (ISTAT = 4 or 12), or KDEF (ISTAT = 4). These are applied in several combinations for multi-kaon decay modes. Pions can be required to be PICON (ISTAT = 2,3,7,14,15), PI23 (ISTAT = 2 or 3), or PIDEF (ISTAT = 2). Usually only some of the pions must be identified, e.g. any 2 of the pions in $D^0 \rightarrow \pi\pi\pi\pi$ must be identified as PI23.
3. Vertex quality : The confidence level (CL) of the D meson vertex must be high. This is typically chosen to be $|\text{Ln CL}| > 5.0$. This applies only to $D^\star$ candidates, since the same cut was already imposed in the skim for other D mesons.
4. $D^{\star\pm}$ - D^0 mass difference : Mass difference is generally required to be in the range 0.143 GeV $< \Delta M <$ 0.148 GeV.
5. Pion in primary : Cascade pion from $D^\star$ decay must be one of the primary vertex tracks.
6. Clean K_s : Vee quality requirements beyond those used in the skim

By far the most powerful of these cuts is that of vertex detachment (ℓ/σ_ℓ) used in combination with a vertex quality cut (CL). Often vertex detachment and vertex quality are the only background reduction tools necessary to develop a signal. For instance, the invariant mass of all events in the D meson skim can be histogrammed together using ℓ/σ_ℓ as the only means of reducing background. These histograms are shown in Figure 3-6 for each of the four D mesons. Every decay mode in Table 3-4 is included one of these four histograms. The detachment cuts used are much larger than necessary to resolve a single decay mode, but this demonstrates the background reduction capabilities of ℓ/σ_ℓ cuts as well as a large D meson sample.

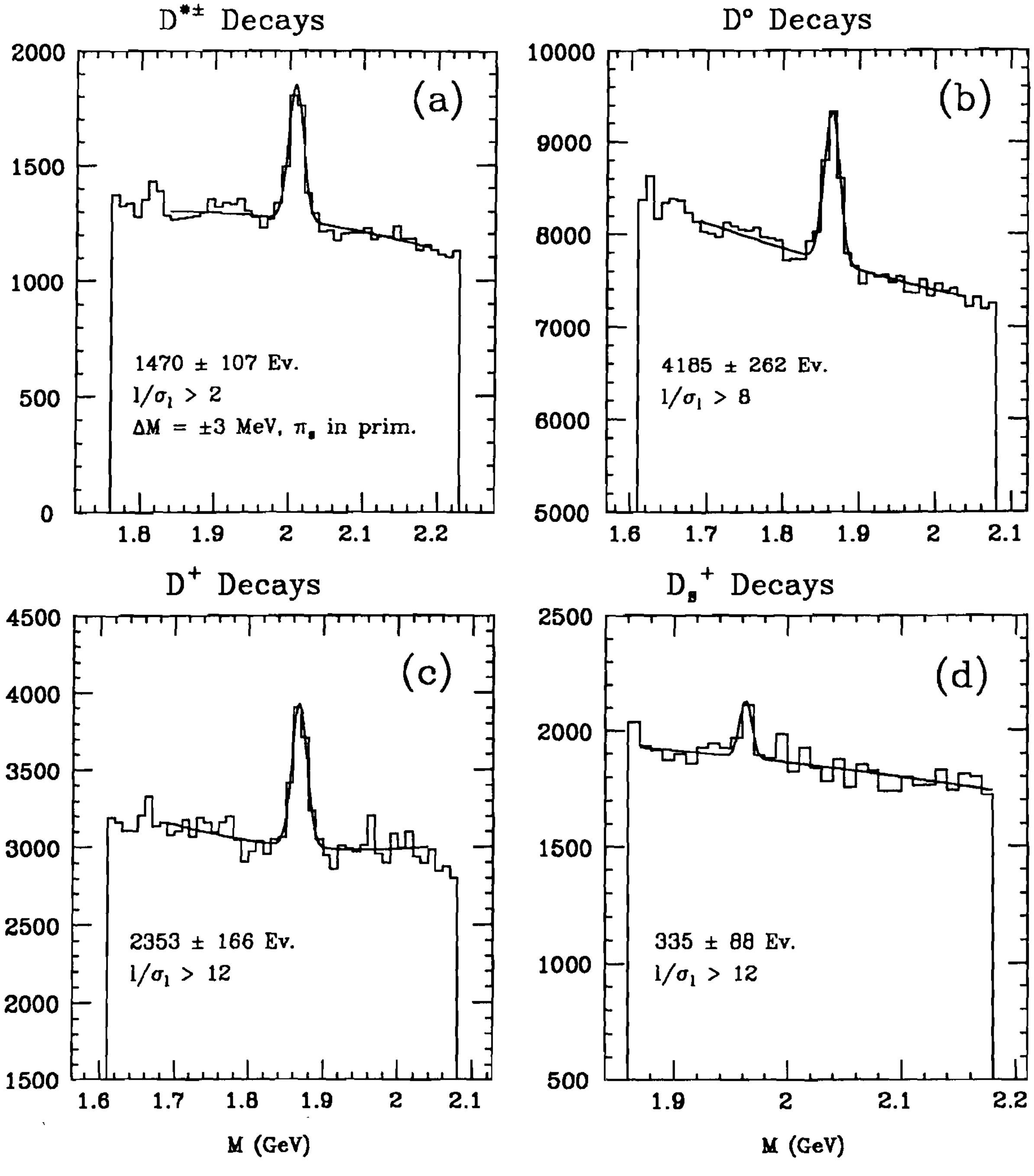

Figure 3-6 : All inclusive D meson signals.

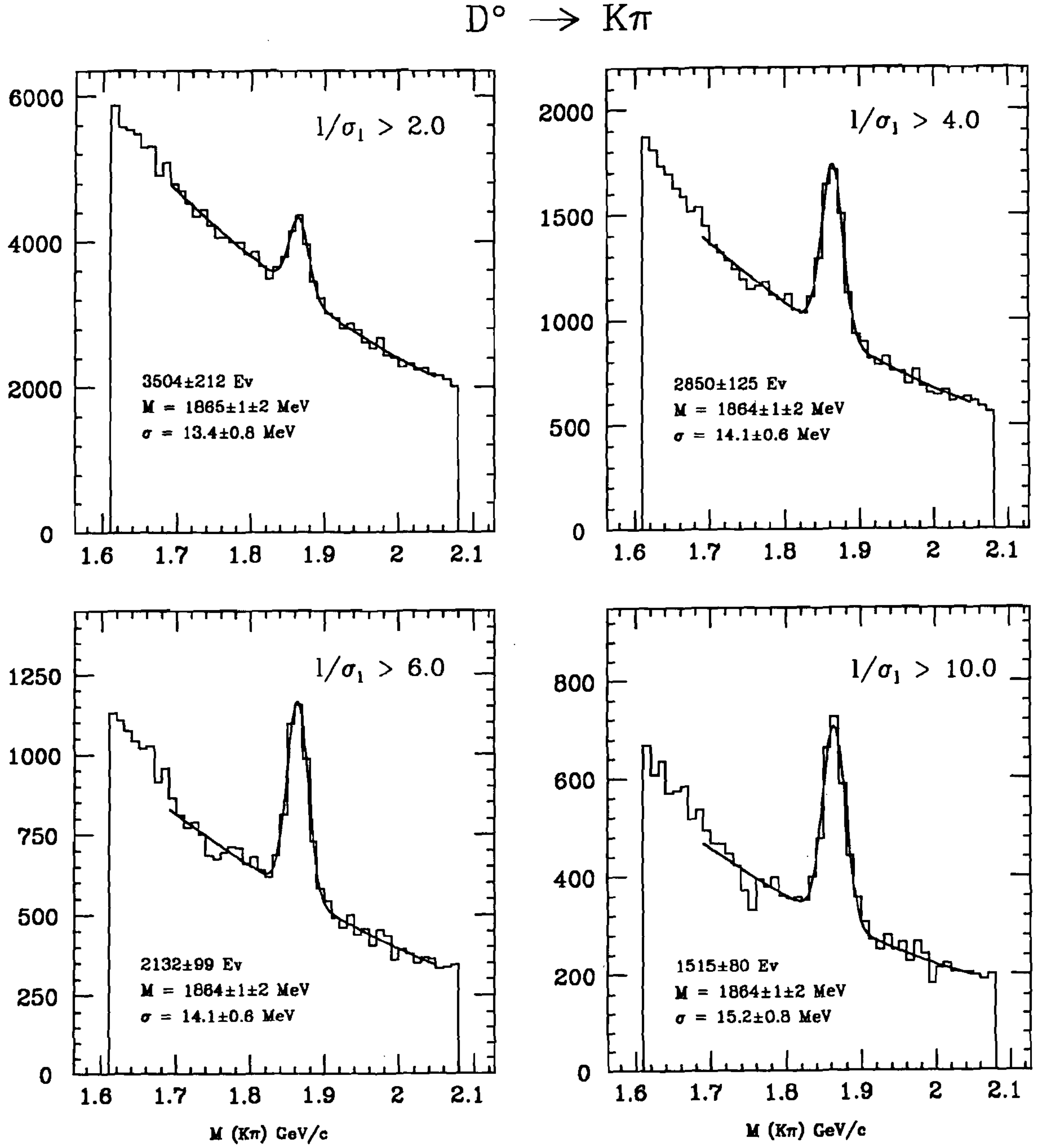

Figure 3-7 : D° → Kπ inclusive signal for several minimum vertex detachment criteria.

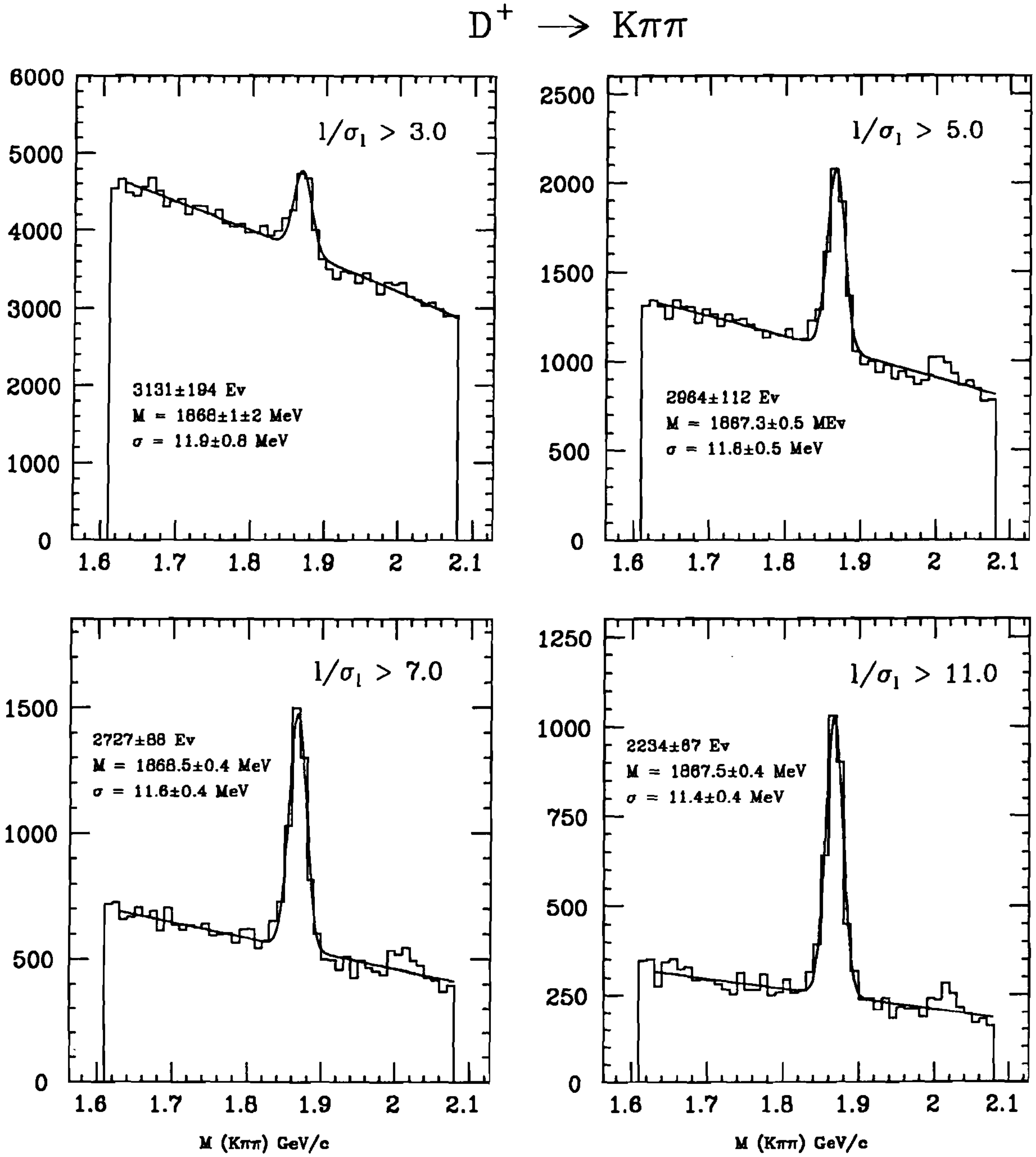

Figure 3-8 : $D^+ \rightarrow K\pi\pi$ signal for several minimum vertex detachment criteria.

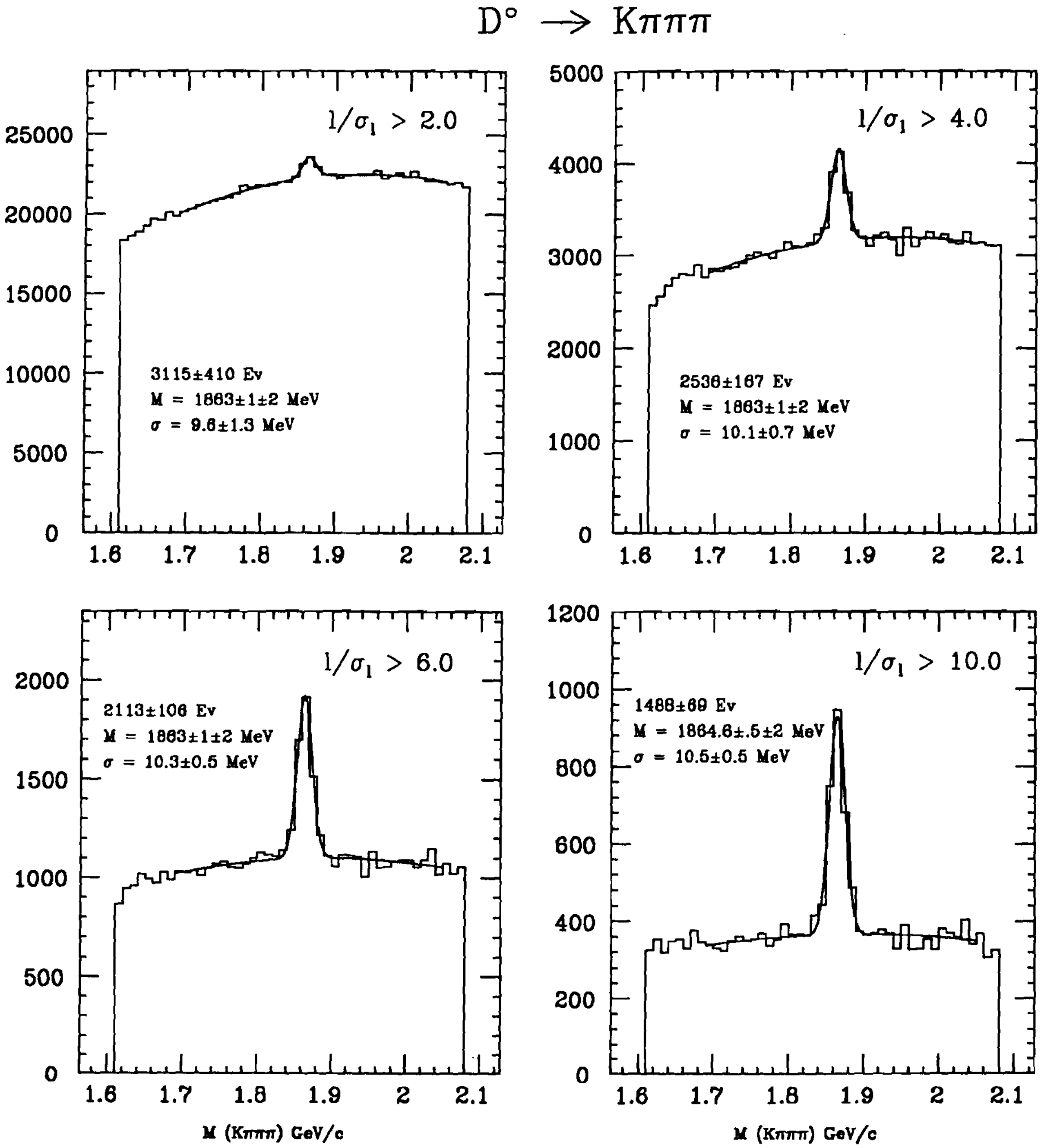

Figure 3-9 : D° → Kπππ inclusive signal for several minimum vertex detachment criteria.

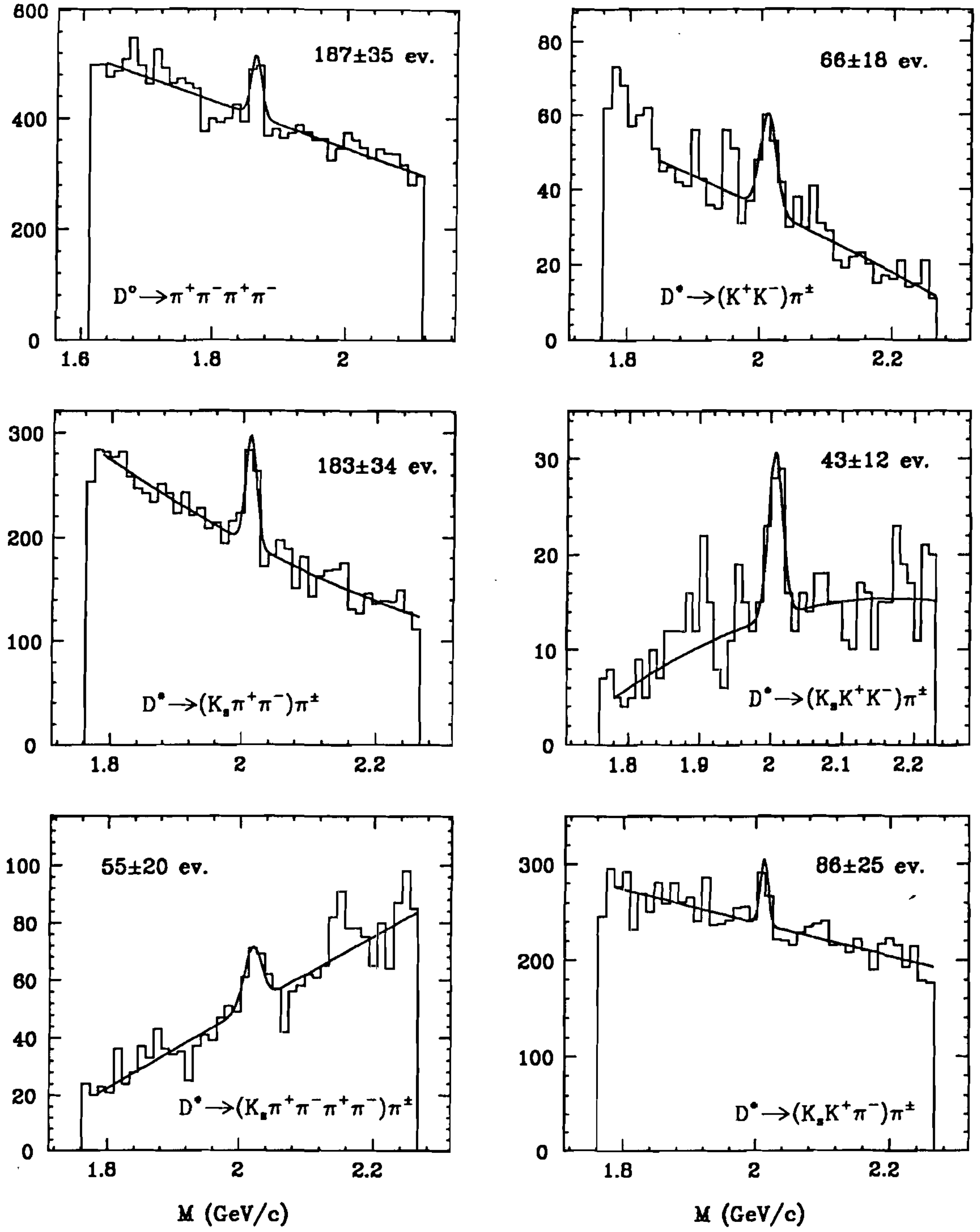

Figure 3-10 : Low level and Cabbibo suppressed decay signals.

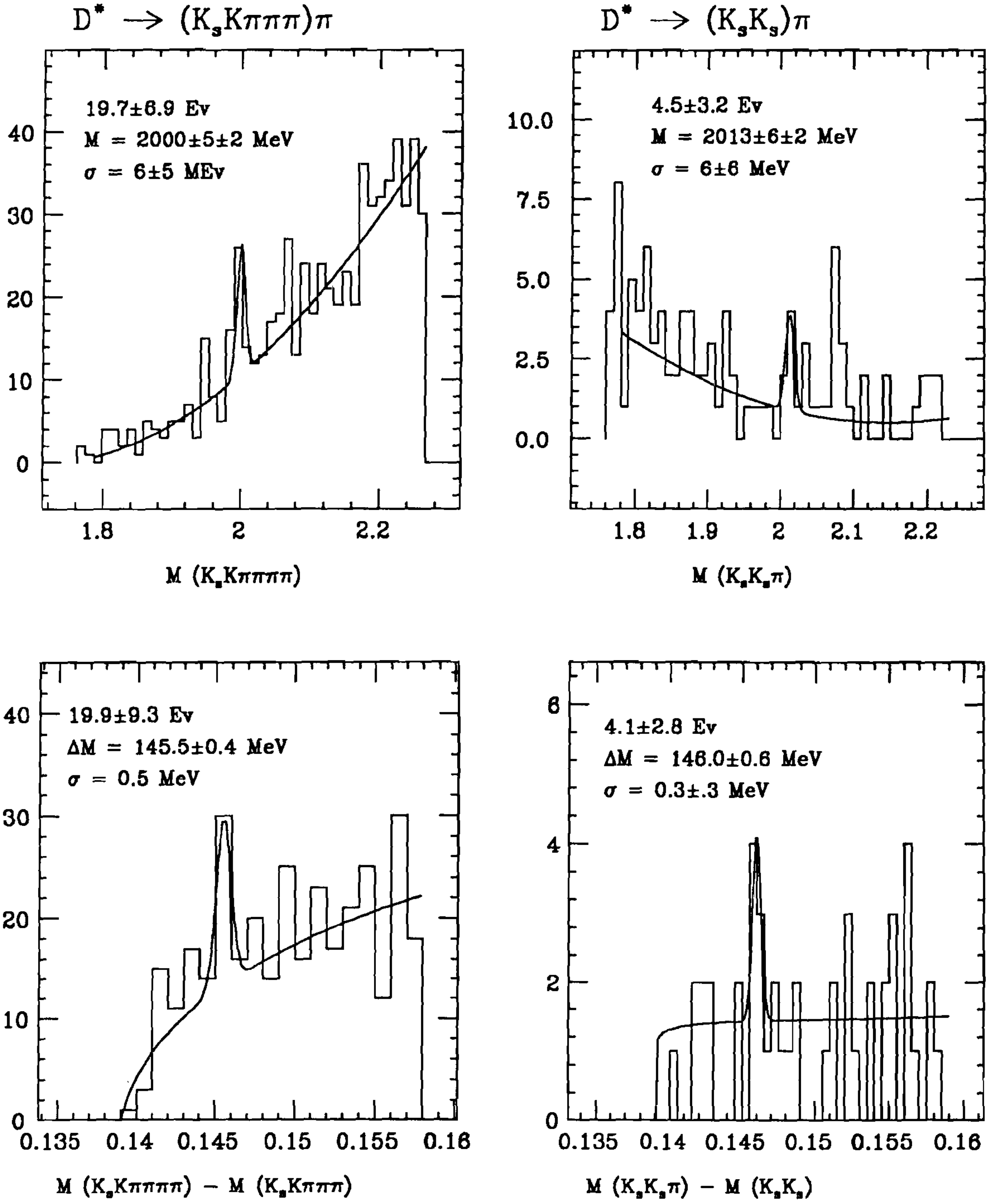

Figure 3-11 : Very low level signals.

By far the largest signals are in the three decay modes

$$D^\circ \rightarrow K\pi$$
$$D^\pm \rightarrow K\pi\pi$$
$$D^\circ \rightarrow K\pi\pi\pi$$

They are shown in Figures 3-7 through 3-9 for several values of ℓ/σ_ℓ . The ℓ/σ_ℓ cut is the only additional requirement beyond those of the skim. The ability of this cut to reject background events is evident in all three decay modes. The only other cut capable of comparable background reduction is the mass difference criterion of the D* *tag*. Figure 3-14(a) shows the D* signal in the Kπ and K$\pi\pi\pi$ decay modes with no vertex requirements other than a vertex quality cut. Signal/background levels are roughly equivalent to a vertex detachment cut of $\ell/\sigma_\ell > 2$ on an inclusive D° signal.

In addition to these "standard" decay modes, several low level decay modes have been observed. They are

$$\begin{aligned} D^\circ &\rightarrow \pi^+\pi^-\pi^+\pi^- \\ D^{\star\pm} &\rightarrow D^\circ\pi^\pm \\ &\rightarrow K^+K^- \\ &\rightarrow K_s\pi^+\pi^- \\ &\rightarrow K_sK^+K^- \\ &\rightarrow K_s\pi^+\pi^-\pi^+\pi^- \\ &\rightarrow K_sK^\pm\pi^\mp \end{aligned}$$

and are shown in Figure 3-10. Indications of signals have been observed in several rather rare decay modes. The signals, seen in Figure 3-11 are of sufficiently poor statistical significance that no claim is made here as to their validity.

The three main decay modes, Kπ, K$\pi\pi$ and K$\pi\pi\pi$, account for roughly 90 percent of all observable D mesons, about 10,000 events. The D meson analyses presented in this thesis concentrate the two D° decay modes. Roughly 25 percent of the inclusive D° sample comes from $D^{\star\pm}$ decays. Where appropriate, these events are considered separately from the inclusive sample.

3.11.1 D* Counting

Figures 3-12(a) shows the ΔM histograms for the decay mode $D^{\star} \to (K\pi)\pi$. This is obtained by histogramming the ΔM of all D° mesons with an invariant mass between 1.82 and 1.9 GeV. The number of events in the signal region is the true number of $D^{\star}$ mesons in that particular decay mode. The $D^{\star}$ invariant mass shown in Figures 3-12(b) is obtained by histogramming the D° mass plus ΔM for events where ΔM falls within the cuts shown. When fitting histograms for the yield of $D^{\star}$ mesons, it is far easier to fit these histograms than the ΔM histograms. However a fit to $D^{\star}$ invariant mass histograms will tend to over the actual number of events. This happens because of the large number of D° mesons which are not products of $D^{\star\pm}$ decays. Tracks mimicking the cascade pion are combined with these D° mesons to create a ΔM background. A narrow cut in ΔM will, when added to the D° mass, create a background $D^{\star}$ of about the same width as the real signal.

An estimate of 5 percent over-counting is provided by simulating a sample of $D^{\circ} \to K\pi$ events, then counting the false $D^{\star}$ events. However reliance solely on Monte Carlo tests should be avoided if possible. Several other methods exist to test over-counting with data. They are :

1. Histogram and fit the invariant mass of the wrong sign decay $D^{\star\pm} \to (K^{\pm}\pi^{\mp})\pi^{\pm}$ with a ΔM cut. Such signals should not be observable except at the levels of $D^{\circ} - \bar{D}^{\circ}$ mixing or because of an unexpectedly large doubly Cabbibo suppressed decay. Therefore evidence of a signal can be attributed to the over-counting mechanism described above. See Figure 3-12(c).
2. Shift the ΔM cut above the mass difference peak and histogram the $D^{\star\pm}$ mass. The yield should represent the over number provided the background

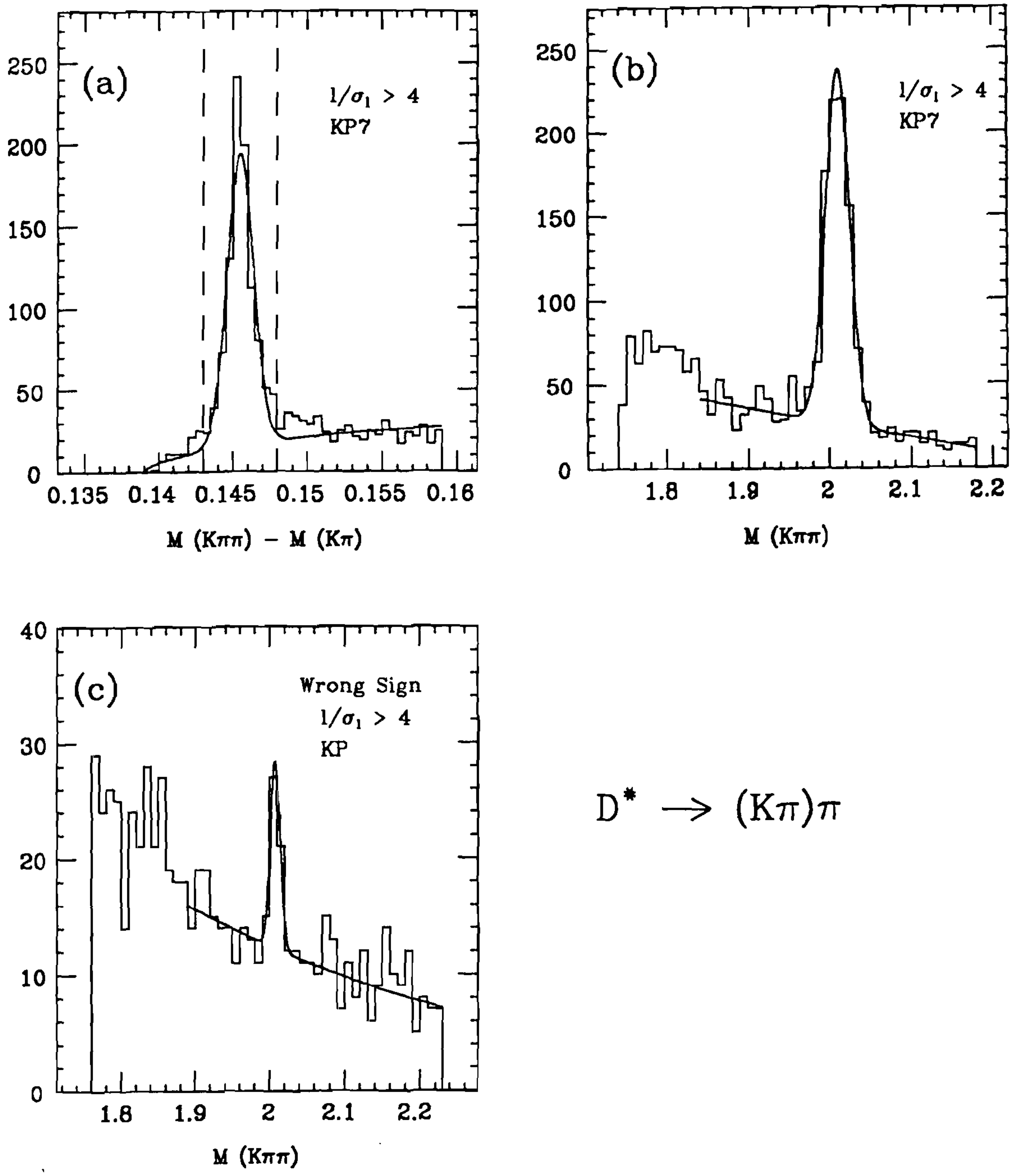

$D^* \longrightarrow (K\pi)\pi$

Figure 3-12 : $D^* \rightarrow (K\pi)\pi$ signals in the $K\pi\pi$ invariant mass and the D^*- D° mass difference.

levels are the same.

3. Fit the $D^{\star\pm}$ signal in a weighted histogram, where positive weights are assigned if in the correct ΔM region, and negative if in a sideband ΔM region. This method is similar to point 2.

Results of each of these tests is given in Table 3-8 in terms of the fraction of total $D^{\star\pm}$ events which are false events.

Table 3-8 : $D^\star$(false)/$D^\star$

	$K\pi$	$K\pi\pi\pi$
Monte Carlo	.048 ± .002	-
wrong sign	.050 ± .017	-
ΔM shift	.050 ± .021	.058 ± .029
weighted hist.	.037 ± .025	.043 ± .023

Many of the calculations presented in the thesis are the result of fitting the $D^\star$ invariant mass histogram under various circumstances. Based on the study presented above, all values of $D^\star$ meson yields used in calculations where an absolute count is necessary have been adjusted downward by 5 percent.

3.11.2 Normalized Invariant Mass

Many of the results reported here involve the counting of charm events. The statistical uncertainty of all these measurements can be improved by increasing the the number of events used in a measurement. Since fundamental processes measured with D mesons should not depend on their decay mode, it is useful to combine the $K\pi$ and $K\pi\pi\pi$ decay modes when conducting measurements with D° inclusive and $D^\star$ mesons. The simplest way to combine them is by entering their invariant masses into the same histogram. Differing topologies and momentum distributions of their constituent particles will cause the mass resolution of these two states to be somewhat different, and thus the resultant mass plot cannot be fit to a single Gaussian. It is therefore useful to normalize the invariant mass by the anticipated mass resolution in each event before histogramming. The anticipated invariant mass resolution is found directly from the track covariance matrix.

A histogram of the normalized invariant mass is obtained by entering the value $(M_D - M_D^{nom})/\sigma_m$ for every event. If the effects contributing to mass resolution in the experiment are understood, these histogram peaks should be unit Gaussians centered at zero. These histograms are shown in Figure 3-13 for the separate and summed D° decay modes Kπ and K$\pi\pi\pi$. The signals shown in the figure are actually of D* events as a ΔM cut has been applied to the D° signal. This is preferred to a histogram of the normalized D* mass because the possibility of an unlinked cascade pion creates difficulties in calculating mass resolutions. These histograms indicate an understanding of the mass resolution to within about 15 percent.

3.12 Vertex Algorithm Performance

A performance study of the candidate driven vertex algorithm was made with the sample of inclusive D° and D* decays into Kπ and K$\pi\pi\pi$, the two largest charged decay modes of the D° . The vertex algorithm is described in section 3.9 where the significance of detachment ℓ/σ_ℓ was introduced as a background reduction tool. The performance of the algorithm can be broken into two components, the efficiency for finding a primary vertex and, having done that, the performance versus ℓ/σ_ℓ .

The D* $\rightarrow$ (Kπ)π sample is particularly suited to efficiency studies because it is obtained without information from the vertex algorithm. Figure 3-14(a) shows the invariant mass of D* $\rightarrow$ (Kπ)π events with mass difference, kaon identification, and good secondary vertex requirements. The D* $\rightarrow$ (K$\pi\pi\pi$)π signal is included as well to contrast the two decay modes. Figure 3-14(b) shows the same histograms as in Figure 3-14(a) with the additional requirement that the vertex algorithm has found a primary vertex in each event. The ratio of the yields in these two Kπ histograms then gives an estimate of the efficiency for finding the

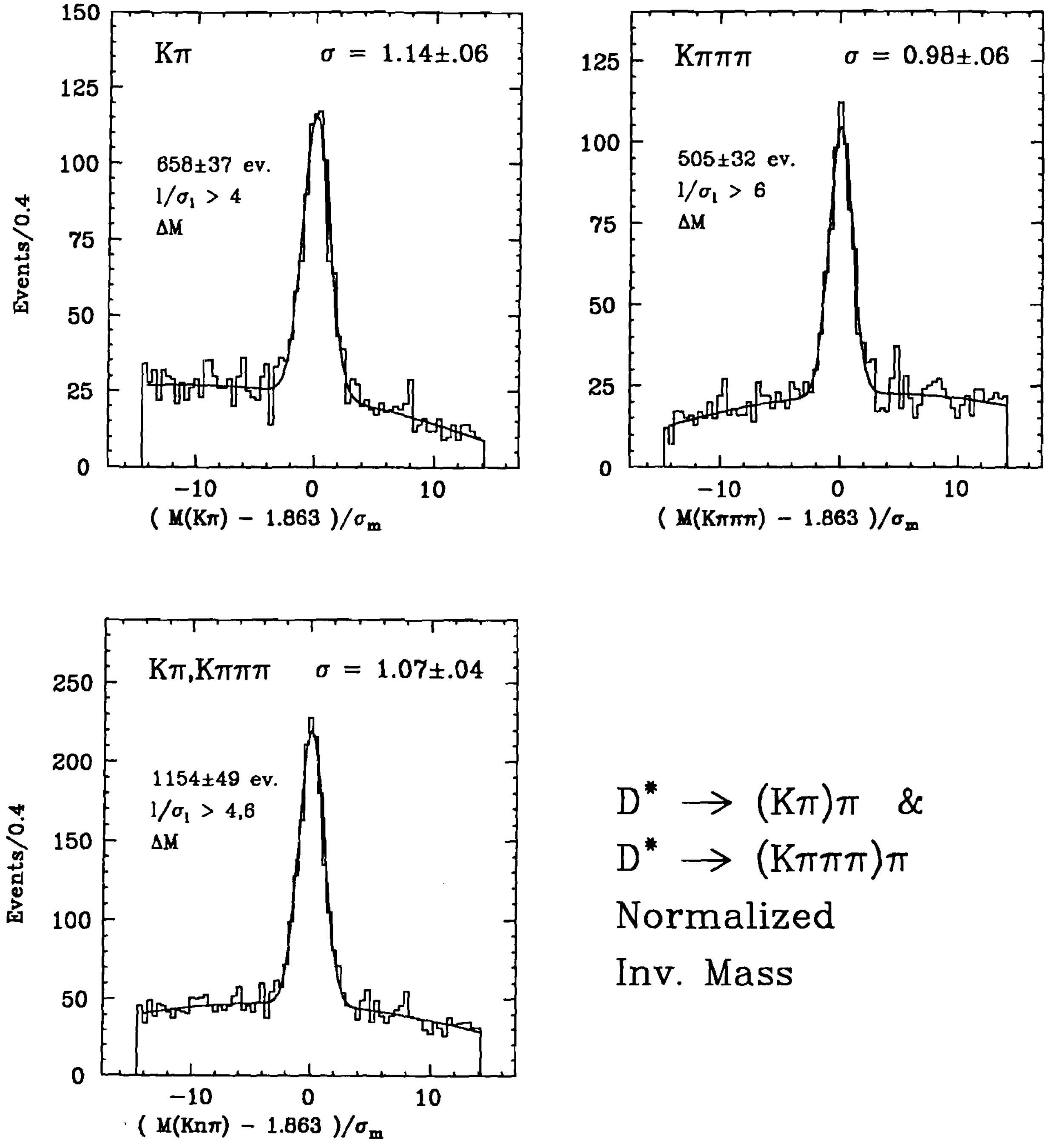

$D^* \rightarrow (K\pi)\pi$ &

$D^* \rightarrow (K\pi\pi\pi)\pi$

Normalized

Inv. Mass

Figure 3-13 : Normalized invariant mass distributions, D^* decays.

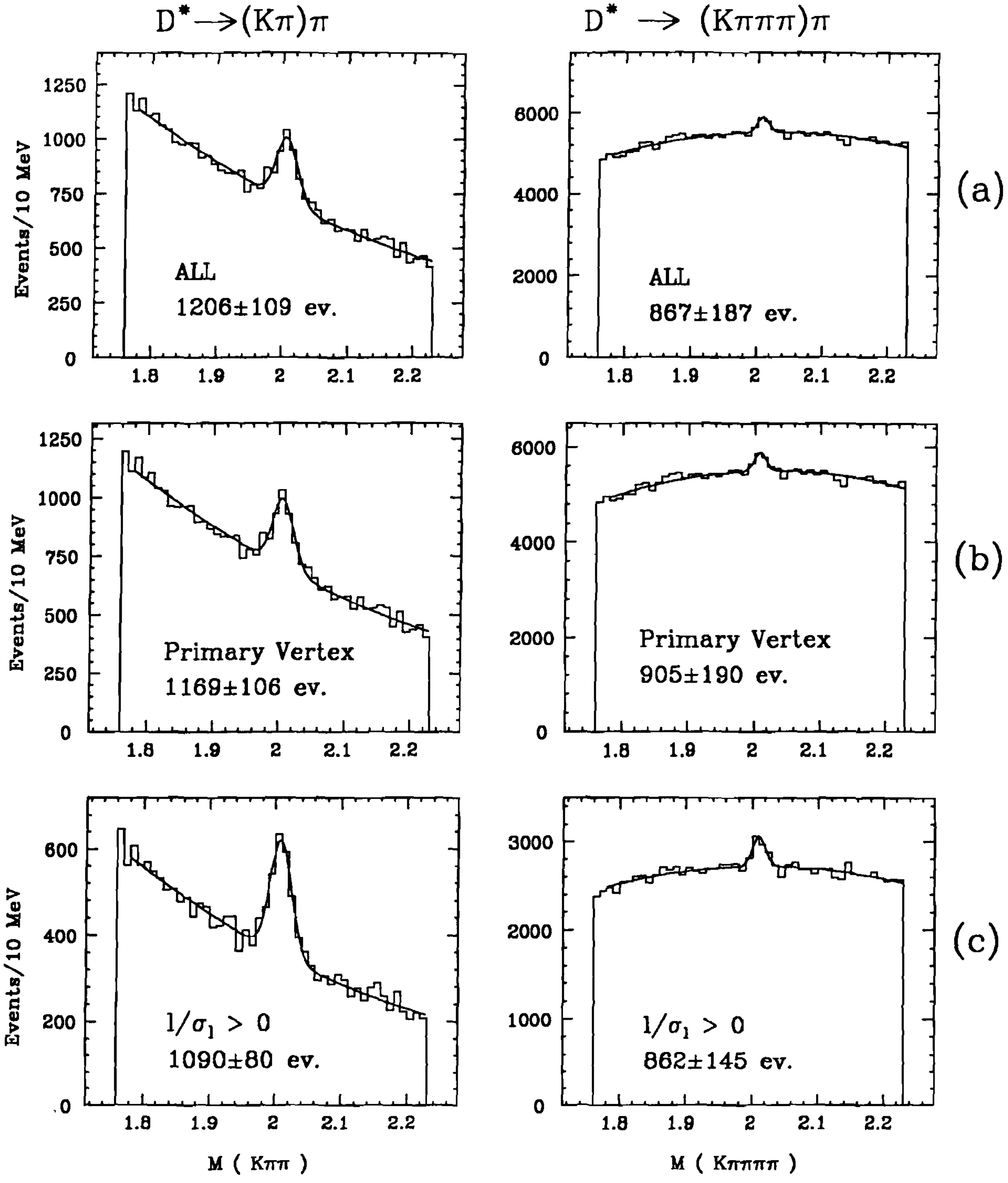

Figure 3-14 : Efficiency study of vertex algorithm using D^* signals.

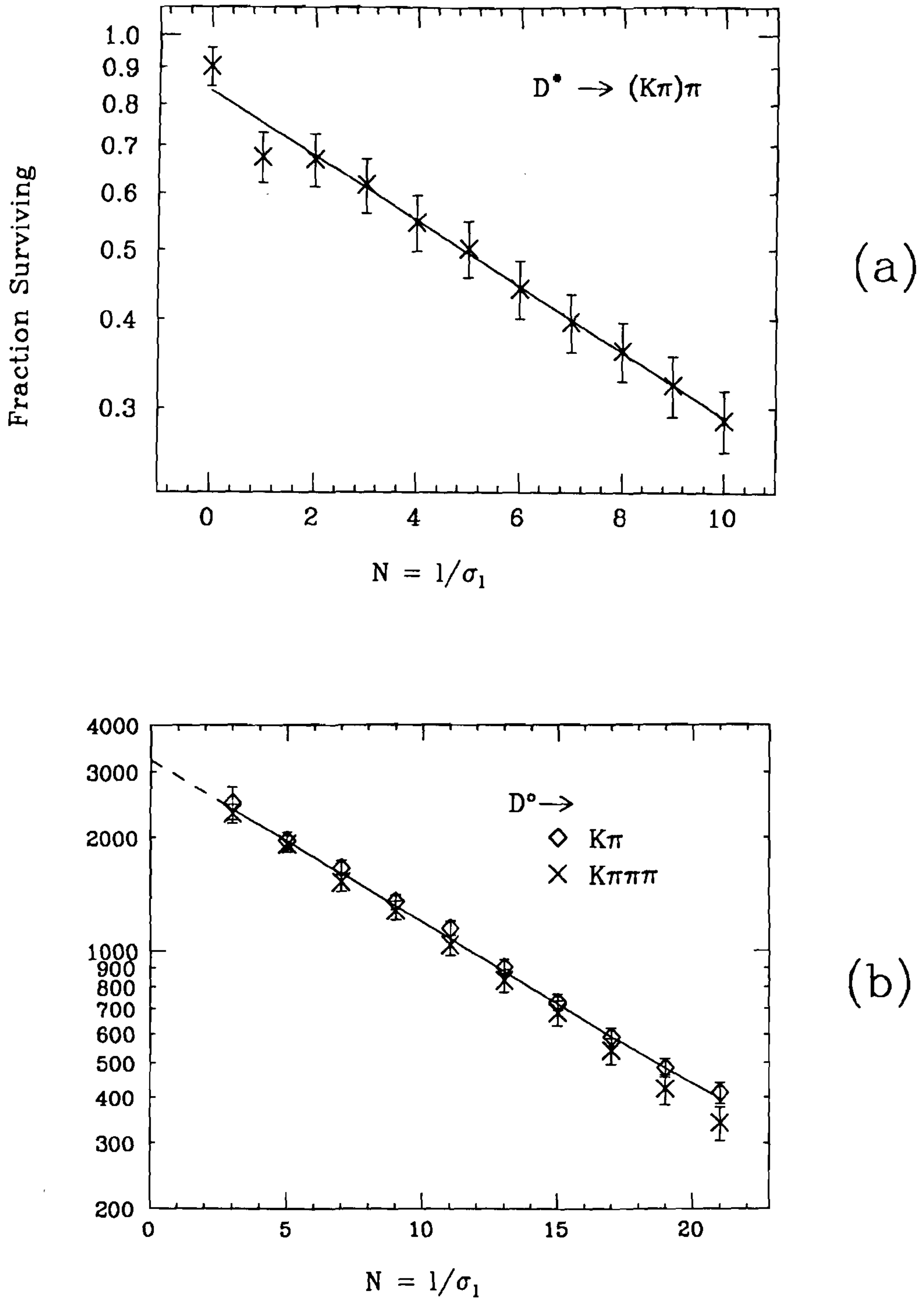

Figure 3-15 : $D^\star \to K\pi$ and D° signal yield surviving ℓ/σ_ℓ cut.

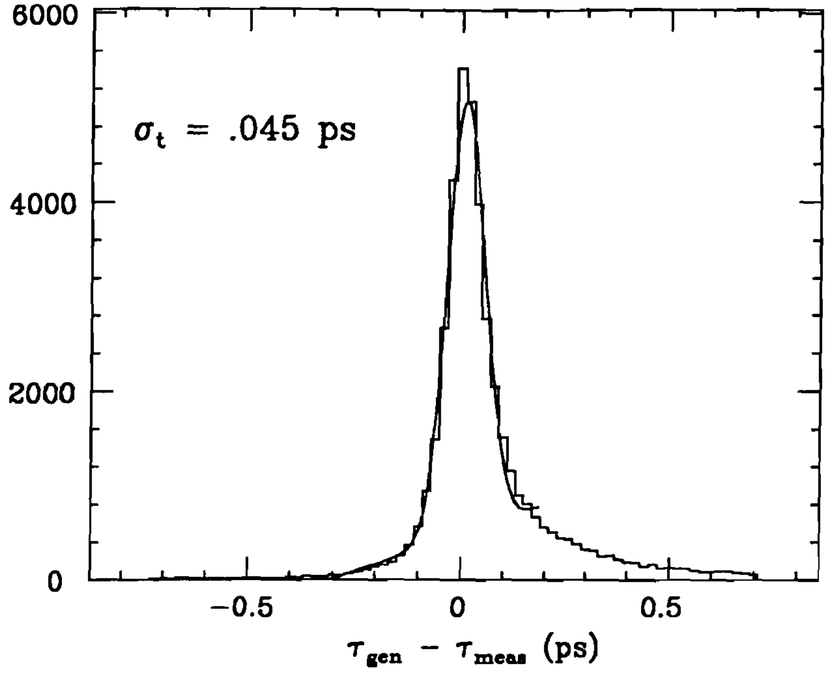

Figure 3-16 : Monte Carlo vertex resolution.

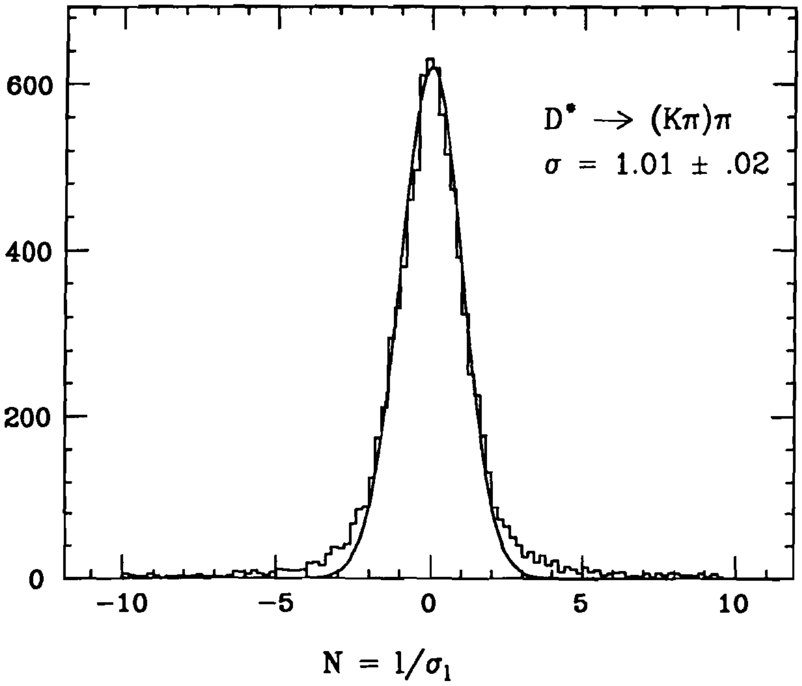

Figure 3-17 : Gaussian distribution of $D^\star \rightarrow (K\pi)\pi$ background events.

primary vertex which is roughly 97 percent. If it is further required that the secondary vertex is found downstream of the primary vertex, as seen in Figure 3-14(c), the ratio drops to about 90 percent. The difference between the two numbers is mainly an effect of the finite vertex resolution and does not represent an inefficiency of the algorithm. D° events which decay immediately after being produced ($t \simeq 0$) have an equal probability of being measured with $\ell < 0$ as $\ell > 0$. If ever larger vertex detachment cuts are then imposed on the D° signal, it is possible to show that the fall in signal strength should follow an exponential decay law. The relationship between the vertex separation ℓ and the proper time separation of vertices for a relativistic particle is

$$t = m_D \ell / p_D c \tag{3.7}$$

A similar relation exist for σ_t so that $\ell/\sigma_\ell \cong t/\sigma_t = n_t$. The spatial resolution σ_ℓ should be roughly proportional to momentum because of its relation to vertex opening angle. Therefore, in analogy with Equation 3.7, σ_t should be roughly constant. If this is true, the decay probability of a D° meson as a function of proper time t can be written in terms of the number of standard deviations σ_t that separate production and decay

$$\mathrm{e}^{-t/\tau_D} = \mathrm{e}^{-n_t \sigma_t/\tau_D} \tag{3.8}$$

where τ_D is the mean lifetime of the D° meson. Figure 3-15(a) is a plot on a logarithmic scale of the fraction of $\mathrm{D}^\star \rightarrow (\mathrm{K}\pi)\pi$ events surviving a vertex detachment cut. The exponential behavior (linear on the plot) indicates that σ_t is in fact roughly constant. The linearity of the plot to near zero separation demonstrates the lack of lifetime bias of the candidate driven vertex algorithm. A similar plot is shown in Figure 3-15(b) for $\mathrm{K}\pi$ and $\mathrm{K}\pi\pi\pi$ decays of inclusive D° mesons.

The proper time resolution does have a distribution because of the finite resolution of the SSD system. Figure 3-16 demonstrates this in the case of Monte

Carlo events. The mean value of σ_t in proper time is found from a combined sample of 4800 inclusive $D^\circ \to K\pi +\ K\pi\pi\pi$ events using a plot similar to Figure 3-15(b). As indicated in Equation 3.8, $\bar{\sigma}_t$ is found in terms of the mean D° lifetime from the slope of the line.

$$\bar{\sigma}_t = (.100 \pm .006)\tau_D$$

This indicates a resolution of .043 picoseconds based on the known lifetime of the D° meson.

A confirmation of the computed resolutions is obtained by observing the distribution of vertex separations in background events. Such a distribution should be a Gaussian centered on the primary vertex position. Therefore if the resolutions σ_ℓ (and hence σ_t) are understood, a distribution in ℓ/σ_ℓ should be a unit Gaussian centered at zero. Figure 3-17 demonstrates the excellent agreement of the background distribution with a unit Gaussian. Fits to this and similar histograms indicate an understanding of vertex resolutions within about 10 percent.

3.13 Background Composition

Another aspect of the vertex algorithm performance is its affect on the background. The preceding discussion demonstrated that the signal strength behaves in the anticipated exponential fashion as the minimum vertex separation is increased. In principle there should be no vertices other than charm decays with moderately small vertex separations. However because of the finite vertex resolution, pure combinatoric background contributes to the D° and $D^\star$ signals at vertex separations on the order of the resolution. Normalized invariant mass histograms of $D^\circ \to K\pi\pi\pi$, shown in Figure 3-18 for successively larger vertex detachments, display the progressive expected improvement in signal/background. A similar set of histograms for $D^\circ \to K\pi$, shown in Figure 3-19, displays quite a different behavior. Initially, background levels decrease relative to the signal as expected,

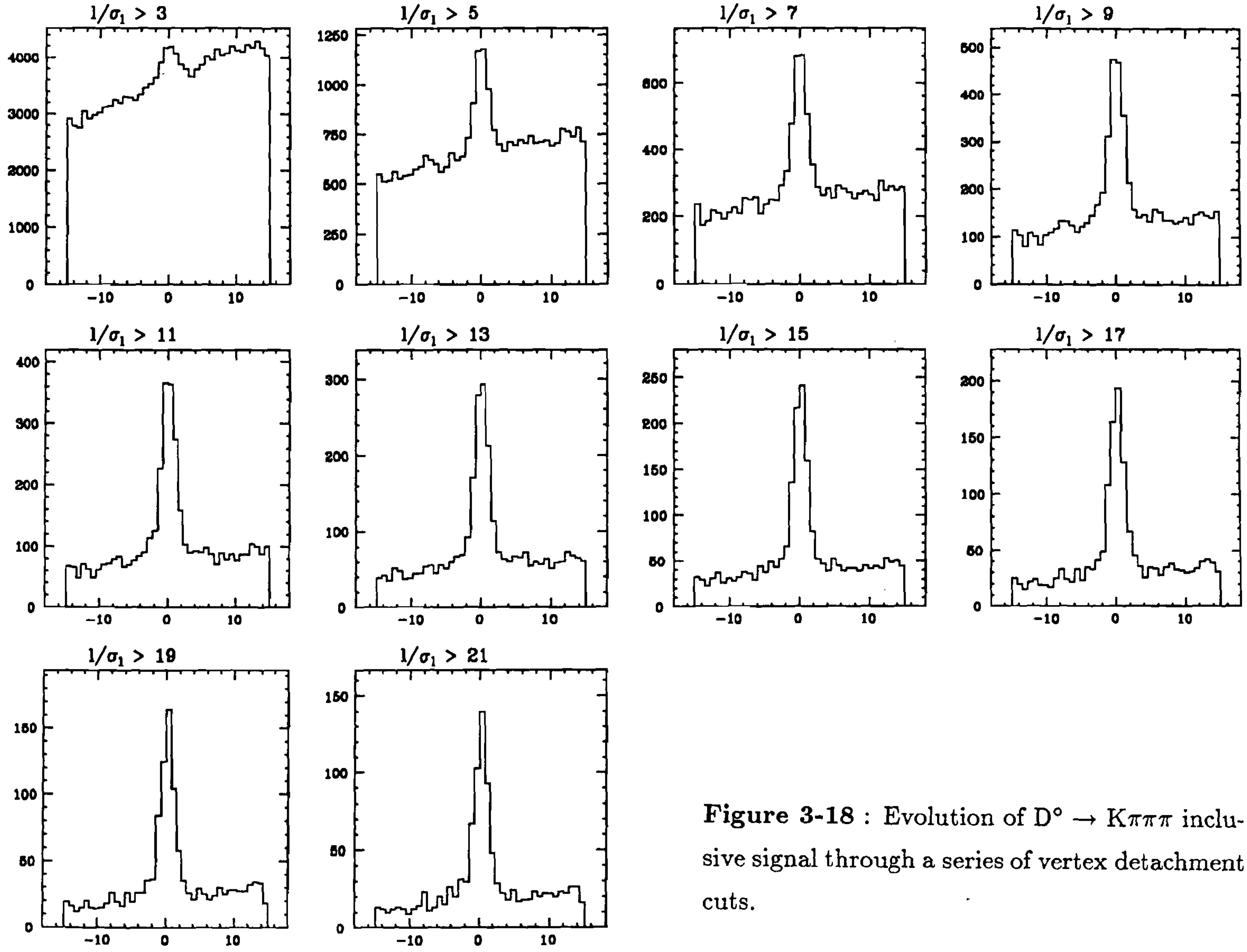

Figure 3-18 : Evolution of $D^\circ \to K\pi\pi\pi$ inclusive signal through a series of vertex detachment cuts.

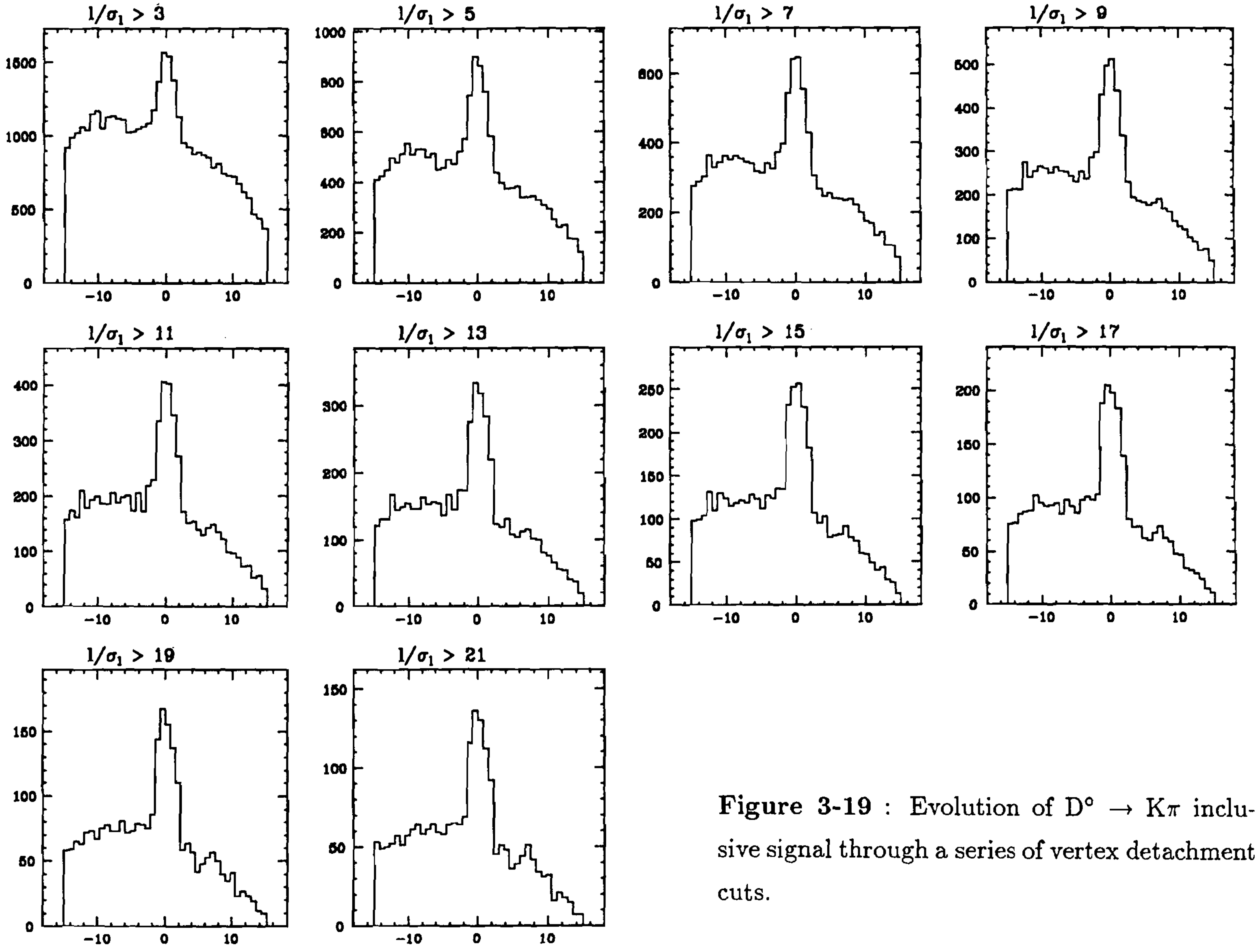

Figure 3-19 : Evolution of $D^\circ \to K\pi$ inclusive signal through a series of vertex detachment cuts.

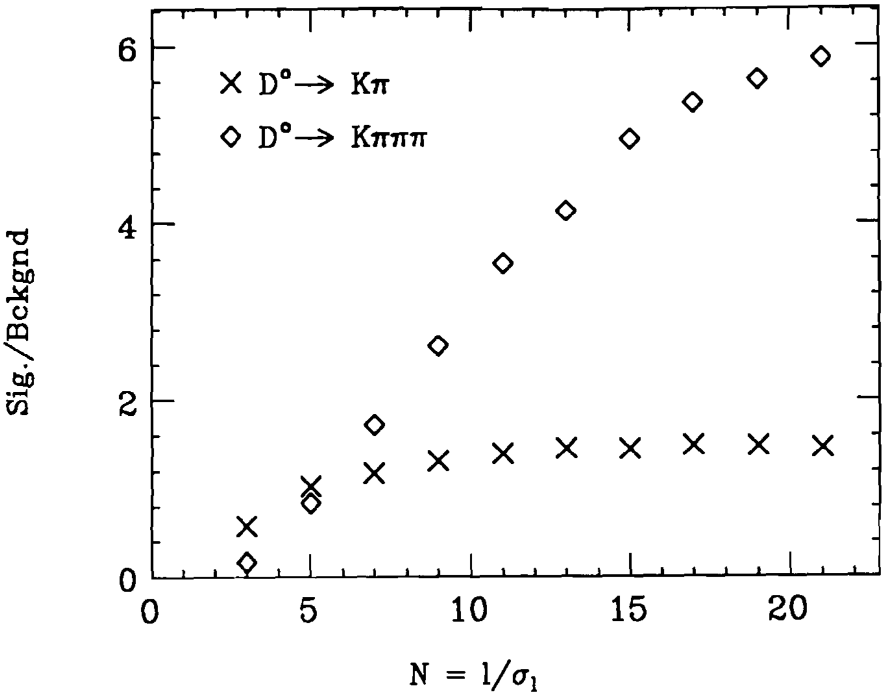

Figure 3-20 : Signal/background of Kπππ and Kπ signals versus ℓ/σ_ℓ cut.

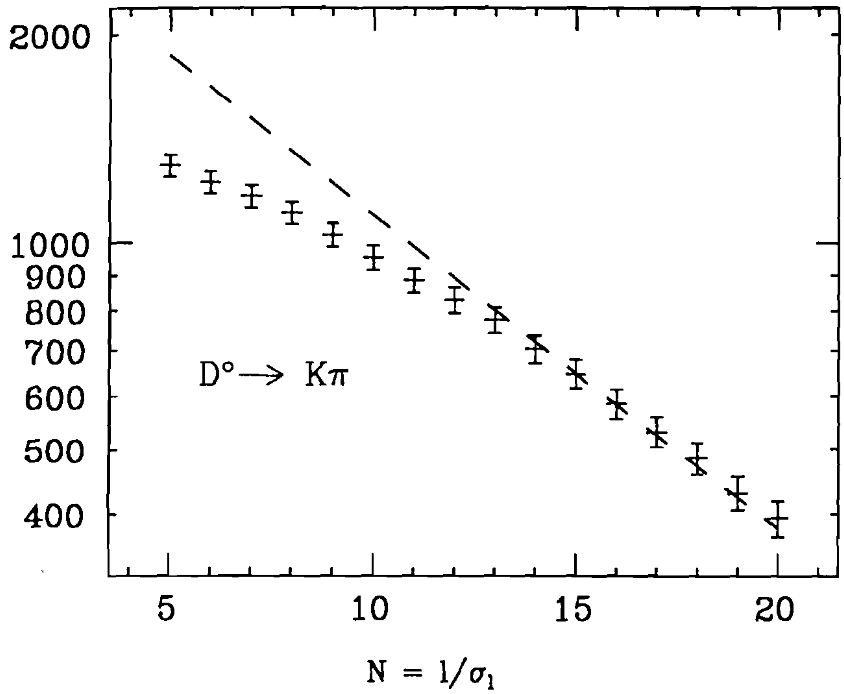

Figure 3-21 : D° → Kπ inclusive signal yield surviving ℓ/σ_ℓ cut when employing vertex isolation cuts.

but at large separations ($\ell/\sigma_\ell > 10$) there is still a significant number of background events. This contrasts with the K$\pi\pi\pi$ decay, where the background is almost completely eliminated at separations greater than 15 σ_ℓ .

A comparison of the signal/background ratios versus ℓ/σ_ℓ , shown in Figure 3-20, displays the difference between the two decay modes quite well. The signal/background ratio for K$\pi\pi\pi$ events continues to increase through successive detachment cuts while the ratio for Kπ events ceases to increase quite soon, indicating that the background events are long lived. Since the relative signal and background levels of $D^\circ \to K\pi$ remain constant through successively larger vertex separations, it is possible to conclude that the lifetime of these background events is roughly the same as the D° .

This important clue suggests that one or more of the tracks in a true charm vertex is being included in a false vertex, thereby causing a large apparent separation. If this is true, then charm events evidently represent the dominant source of background at large vertex separations. The reason that the level is so much higher in the Kπ decays is the ease with which a good 2-track vertex can be formed relative to 3 or 4-track vertices. Studies have shown[13] that secondary vertex improvements, such as requiring tracks to be isolated from the primary vertex, reduce $D^\circ \to K\pi$ backgrounds to levels comparable with the other two decays. However in applying these cuts, the vertex algorithm becomes biased against events at small vertex separations, and thus loses the pure exponential behavior there (see Figure 3-21 compared to Figure 3-15(b)). Freedom from these biases is important in the D° lifetime studies to be discussed in Chapter 7, so no such "improvements" were made to the vertex algorithm.

3.14 Čerenkov Performance

It is possible to gauge the performance of the Čerenkov system (detectors and the analysis combined) by studying the identification of known particles. Each of the four basic particles, electrons, pions, kaons, and protons, can be identified independently through a known decay topology, then checked against the response of the Čerenkov system. The decay topologies used in studying various particle identifications are :

Electrons : $\gamma \rightarrow e^+e^-$

Pions : $K_s \rightarrow \pi^+\pi^-$

Kaons : $\phi \rightarrow K^+K^-$, D° ,$D^\pm \rightarrow K\pi, K\pi\pi, K\pi\pi\pi$

Protons : $\Lambda \rightarrow p^+\pi^-$

Each of these was studied to varying degrees. The kaon identification, for instance, is particularly important in the context of the analyses presented in this thesis and was studied in some detail. The study of electron identification, shown in Figure 3-22, was purely qualitative. Figure 3-22(a) is the x' (dx/dz) distribution of events taken with a hadronic trigger. This histogram shows a broad distribution of hadronic events plus a central ***spike*** which is presumably the result of embedded e^+e^-pairs. These are the result of Bethe-Heitler production occurring in the same master gate as the hadronic event (of over 6 Rf buckets duration). Figure 3-22(b) shows the same histogram with the added requirement that each track is identified as a definite electron (ISTAT = 1). The reduction of hadronic "background" is quite remarkable. Conversely, Figure 3-22(c) shows the event distribution where no track is consistent with being an electron. The e^+e^-***spike*** is all but gone, indicating an excellent ability to reject these tracks.

The remaining particles were each studied using a sideband subtraction technique. In this method the signal is developed without the use of Čerenkov identification, then tracks of events in the signal region are categorized by their Čerenkov identification. These categories are listed in Table 3-2. The contribution to the categories from background events is estimated from sideband regions and subtracted from the signal contribution. The decay signals, listed above, are shown in Figure 3-23 with the signal and sideband regions indicated.

Neutral vee signals were developed using vertex quality and detachment cuts. The small amount of background in the K_s signal (Figure 3-23(a)) is mostly

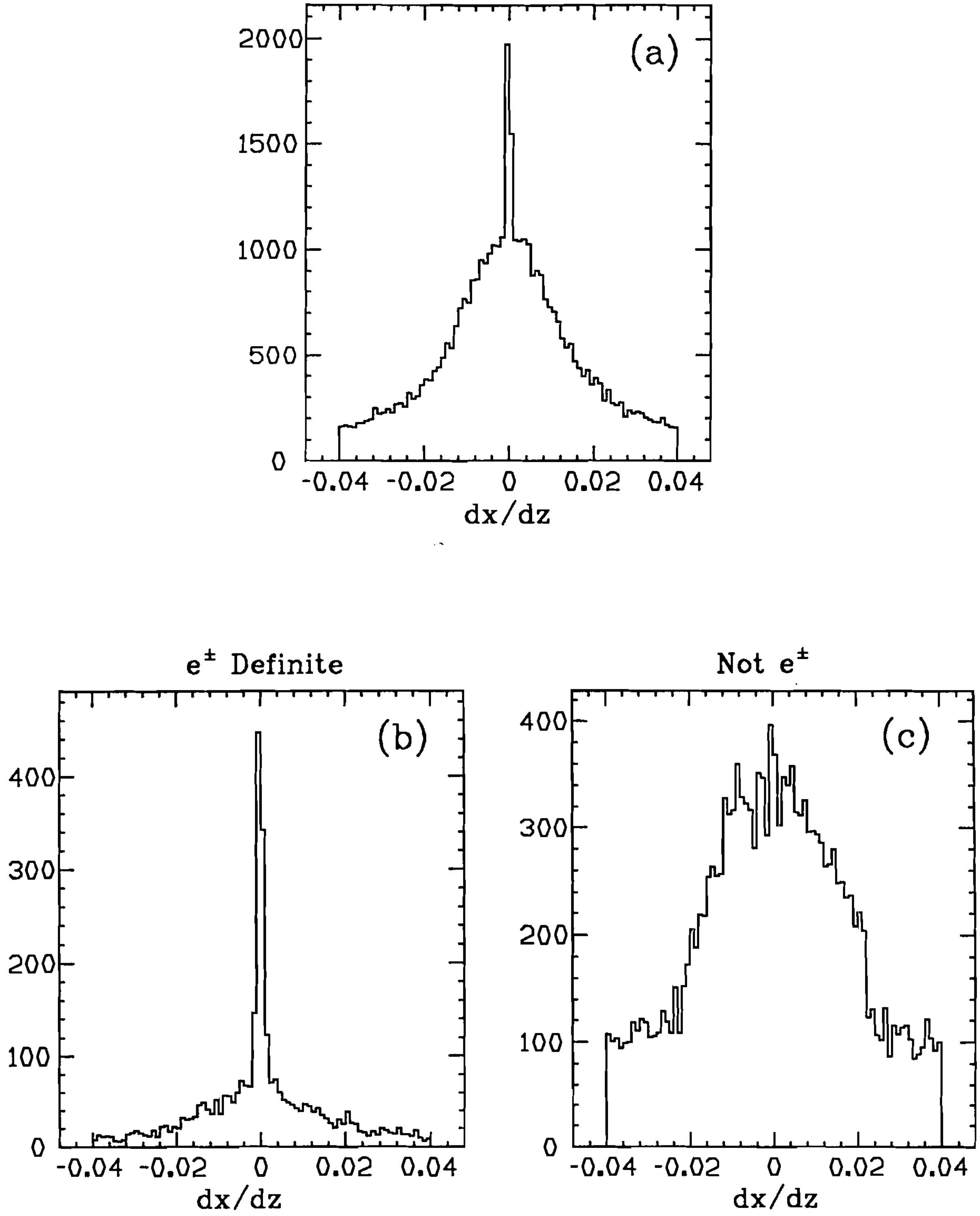

Figure 3-22 : Topological electron identification by the Čerenkov system.

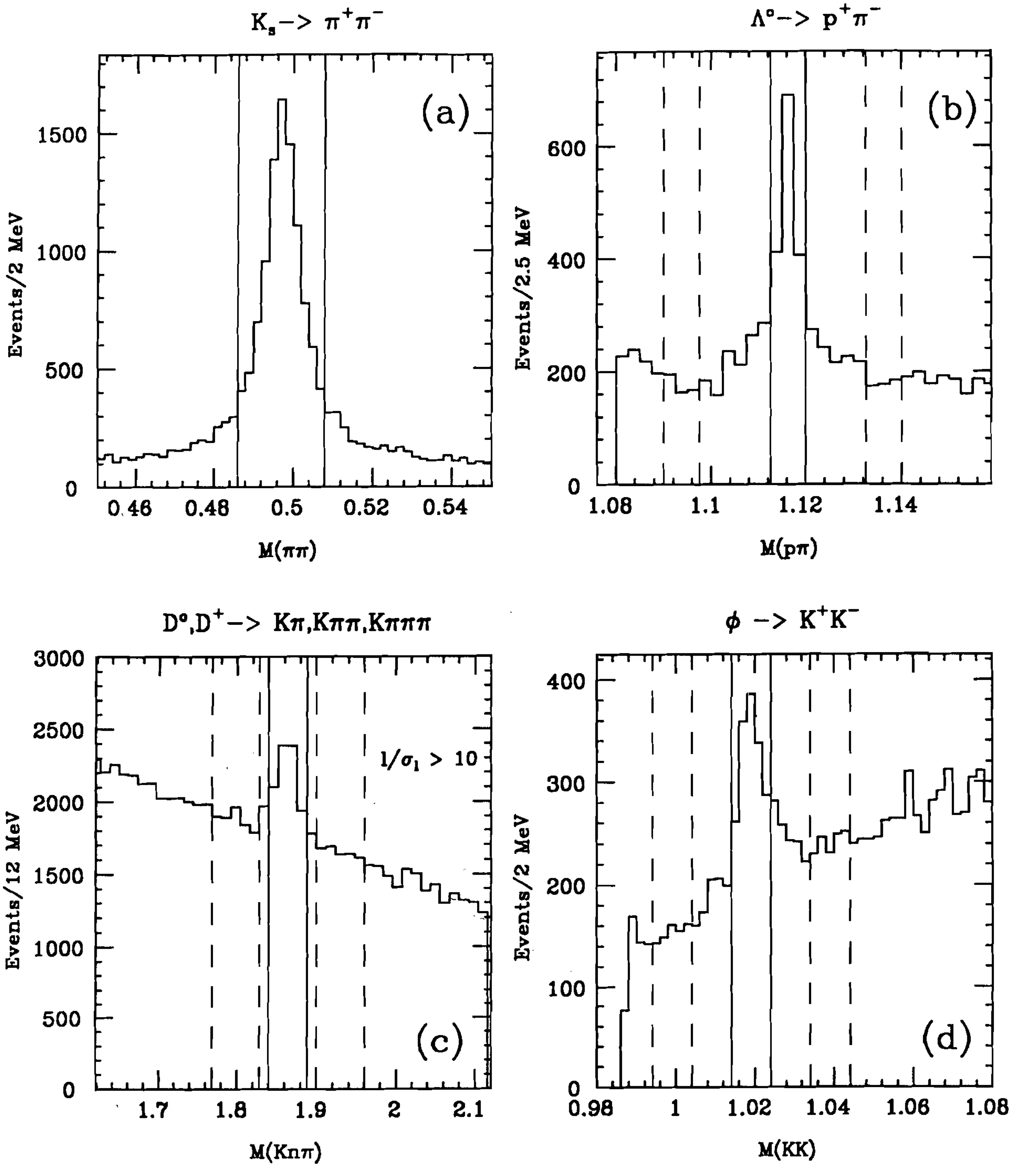

Figure 3-23 : Signals used in testing performance of Čerenkov identification.

pions, so the signal was studied without sideband subtraction. Both pions in a decay were considered in the study. The ϕ signal (Figure 3-23(c)) was developed with purely kinematic constraints and a requirement that one kaon be identified by the Čerenkov system as a definite kaon (ISTAT $= 4$). The other kaon, which has no identification requirement, is then the subject of study. The D meson signals are each developed kinematically and a vertex detachment requirement imposed. The signals are combined with a common mean mass to produce the histogram shown in Figure 3-23(d).

Results of particle identifications for each of the 4 meson decays discussed are given in Table 3-9. A given decay mode is broken down by the fraction of topologically identified particles in each Čerenkov identification category. Thus each Λ and D decay contributes one particle to an identification category, while each K_s contributes two and a ϕ somewhat less than two. The errors represent uncertainties in the fraction based in counting statistics of all entries, signal and sideband, into a particular identification category. Negative fractions arise because of the sideband subtraction. At the bottom of the table are listed several common identification categories often used in data analysis. For instance a positively identified kaon is often considered to be one which is a definite kaon or kaon/proton ambiguous (K or K/P), as determined by the Čerenkov system. Identification fractions in the relevant summary categories is given for each of the particles. The fraction of particles given an inconsistent identification is listed as well. These are cases where the Čerenkov system identified the track in question in a category which was not even consistent with the particle's actual identity (i.e. the relevant ISTAT bit was not *on*).

Identification of some particles, such as protons, is very good. In fact the ability of the Čerenkov system to identify particles is better than the fractions in Table 3-9 indicate. As shown in Table 2-3, particle identifications are only possible in certain momentum ranges. The fractions listed in Table 3-9 are the Čerenkov efficiencies averaged over the entire momentum spectrum of a decay particle.

Table 3-9 : Čerenkov Identification by Category

ID-cat.	kaons (D)	kaons (ϕ)	protons (Λ)	pions (K_s)
none	.009±.015	.040±.010	.068±.013	.026±.002
e	-.009±.020	.003±.007	.003±.008	.030±.002
π	.035±.038	.014±.014	-.037±.015	.306±.006
e/π	-.008±.055	.106±.030	.037±.028	.347±.006
K	.265±.019	.402±.020	.069±.013	.014±.001
K/π	.010±.004	.005±.003	.002±.001	.004±.001
K/π/e	.140±.023	-.011±.009	.011±.010	.016±.001
P	.040±.012	.050±.009	.378±.026	.005±.001
P/K	.400±.030	.380±.020	.426±.028	.012±.001
P/K/π	.060±.050	.010±.007	.029±.010	.210±.005
P/K/π/e	.060±.020	.001±.013	.018±.009	.030±.002
π or e/π	–	–	–	.653±.008
K or K/P	.670±.036	.780±.028	–	–
P or K/P	–	–	.804±.038	–
inconsist.	.071±.070	.210±.030	.153±.039	.087±.003

These fractions are therefore a measure of the absolute identification efficiency for a specific decay and not a measure of the true Čerenkov efficiency. Thus it is no surprise that relatively slower kaons from ϕ decays are identified somewhat differently than the faster kaons from D decays. A proper study might involve dividing the particle identification into the momentum regions defined by Figure 3-2.

Chapter 4

The Monte Carlo

This chapter describes the computer simulation of the experiment, otherwise known as the Monte Carlo. The multitude of detectors in the experiment each contributes to detection inefficiencies, often in ways which are not easily predicted. The monte carlo simulation is a means of de-coupling the complicated interplay of detector responses from the underlying processes taking place in the target. These processes are usually parameterized in a few variables such as incident photon energy, final state momenta, and production angles. With adequate parameterization and detector simulation, the detector response to an event with a fixed set of parameters will, on average, be the same in data and monte carlo. Measurement of fundamental properties of an interaction are therefore only as good as the monte carlo detector simulations, so some effort has been made to verify their accuracy. Some critical comparisons between monte carlo and data are presented at the end of this chapter.

4.1 The Monte Carlo Event Sample

The production of a monte carlo event sample is divided into two separate processes. The event generation is a description of photon-nucleon interactions producing charm and the subsequent particle decays, while the event simulation is the simulation of detector responses to those events. Events are generated according to a specific model for charm photoproduction. In principle an accurate simulation of charm production mechanisms is not necessary. In practise production model dependences exist, but can be minimized by a choosing a production model which is well matched to empirical properties of photoproduced charm. In this particular case a completely empirical model was used. Some apparatus simulations are performed in the event generation as they pertain to photon interactions in the target, but most are performed in the event simulation process which begins after an entire event sample has been created. Full detector simulations are performed for each event separately and proceed only if the simulated master gate and trigger are satisfied by the event in question. Event information from each of the detectors is the same as in data, and is written to tape in the same format. This event sample is then processed through the complete reconstruction procedure described in Chapter 3.

4.1.1 Event Generator

The experiment was actually designed to detect two different interactions, that of photoproduction in the target and the bremsstrahlung interaction in the radiator. Since measurements of photon luminosity and energy depend on knowledge of each bremsstrahlung interaction, event generation must begin upstream of the radiator.[14]

An event is generated for each beam electron striking the radiator. The process begins with a full simulation of an electromagnetic shower of the incident electron in the lead radiator. The simulated electron beam spectrum approximates the measured spectrum, discussed in section 3.7, with a gaussian distribution centered at 350 GeV and a spread $\sigma = 11\%$. Products of this shower typically include 2 to 3 bremsstrahlung photons and an occasional e^+e^- pair. Each of the *multi-brem* photons has a probability of interacting in the target which is related to an interaction length. The interaction length for a given photon depends on its energy through the particular cross section model. The model used was based on a parameterization of the energy dependence recently measured by FNAL E691.[2]

$$\sigma(\omega) = 1.905\,(\omega - 5.0\ \text{GeV})$$

Only one of the *multi-brem* photons is allowed to interact per event. This introduces complications related to normalization which are discussed in Appendix D.1 . Photons which do not interact to produce charm are allowed to produce e^+e^- pairs in the target.

When a photon has interacted, a $c\bar{c}$ is produced and hadronized in a specified manner. For the work described in this thesis, one of the two charm quarks was always chosen to hadronize as a $D^{\star\pm}$ meson. Hadronization of the other was chosen randomly amongst charmed mesons and baryons according to a model of

$$\begin{array}{llll} 30\%\ D^{\star\pm} & 30\%\ D^{\star o} & 20\%\ \Lambda_c^{\pm} & \\ 15\%\ D_s^{\star\pm} & 10\%\ D^{o} & 10\%\ D^{\pm} & 5\%\ D_s^{\pm} \end{array}$$

The dynamics of both charm species was chosen to match parameterizations from E691 in terms of x_f and $p_\perp$.

$$\frac{d\sigma}{dp_\perp} \propto e^{-1.07p_\perp^2}$$

$$\frac{d\sigma}{dx_f} \propto (1+19x_f)(1-x_f)^{2.96}$$

The primary $D^{\star\pm}$ meson was forced to decay into a D^o meson. This D^o was then required to decay into a specific decay mode in any given set of monte carlo events. The lifetime distribution of these events was that of a pure exponential with a decay constant equaling the present world average. The recoil charm were allowed to decay randomly according to known branching fractions of the specific charm particles. Secondary particles of intermediate lifetimes, such as K_s mesons were given standard decay lengths, typically creating vees somewhere in the spectrometer. All particle decays are chosen to be isotropic except for those with known angular distribution constrained by symmetry consistency such as $D_s^+ \to \phi\pi^+$.

Each monte carlo event then consists of a tree list of particles containing each one's 3-momentum and lifetime.

4.1.2 The Detector Simulation

After a complete event is created, simulation of individual detector responses to that event is begun. Some of the events may not be detected at all, others only partially. The result is that only a fraction of the events generated will be detected completely. The fraction of detected events is influenced by the detector response, hopefully the in the same way as in data.

Simulation begins by tracing the monte carlo particles through the magnetic fields of the two analysis magnets. Low momentum tracks can leave the experimental aperture at various points in the spectrometer just as in data. The effects of coulomb scattering are incorporated as well.

Charged tracks which pass through trigger hodoscope counters will generally set them on. Most trigger hodoscopes are assumed 100 % efficient, but measured efficiencies are used for H × V and OH counters. The response of other trigger devices, such as the RESH and HC detectors, is based on calculated energy deposition. Recoil electrons are traced to a specific segment of the RESH detector. The deposited energy of the electron is determined according to a Gaussian distribution about the nominal energy, and the particular segment is set *on* if the energy deposited is above a minimum value. Detector efficiencies are assumed perfect above the minimum energy. The HC detector response is simulated in the this way as well. Trigger efficiencies of the HC have been determined from calibration[15] as a function of particle momentum, and their parameterization was used in the Monte Carlo simulation.

The response of MWPC and SSD systems is simulated by registering hits on wires or strips based on the proximity of a particular track. More than one wire or strip in a single plane may register from one track because of charge sharing. Both detector simulations have a mechanism for creating inefficiencies, but random noise hits are only simulated in the SSD.

Other detectors, such as calorimeters and muon proportional tubes, each have individual simulations with varying degrees of sophistication. They are not discussed here as they have no bearing on the results presented in this thesis. Several other simulations are critical to these results, though. They are discussed in the following subsections.

1. Photon beam profile

The profile of the incident photon beam has a significant impact on calculations related to cross sections since the targets were undersized. The relevant photon luminosity for use in a cross section calculation should include only those photons which enter the target. The beryllium target used during most of the running period had a maximum size of 1 inch square. Thus it is highly unlikely that all of the beam photons impinged on the target. Furthermore, there is evidence that the centroid of the beam was not at the center of the target, and that its position varied throughout running period.

A examination of the photon beam profile was performed[16] by studying the x,y distribution of vertices in the TR1 counter during different time periods. These vertex distributions were parameterized in terms of elliptical contours where the x distribution was roughly twice as broad as the y distribution.

2. BGM simulation

Simulation of the BGM response to deposited energy is similar to that of the RESH detector. However particular attention is paid to the spectrum of particles hitting the BGM. All photons not producing charm pairs deposit energy in the BGM, either as photons or e^+e^- pairs. In addition, the effects of *pile up* are simulated by including bremsstrahlung photon energies from a second unbiased event at a rate of 25 %. The BGM scaler count is incremented whenever the total energy deposited is greater than 133 GeV.

3. Time dependent simulations

The experimental run had natural divisions corresponding to distinct running conditions. These 8 periods are distinguished by the target choice and other changes in the apparatus. The Monte Carlo accommodates these changes by simulating events in each of these periods in relative proportion to the data. Not all aspects of the experiment were monitored in specific run periods, so the Monte Carlo simulates only a few time dependent conditions. These include :

- target type,
- photon beam parameterization and target profile,

- MWPC efficiencies,
- and HC trigger efficiency.

4. Čerenkov simulations

Each Čerenkov detector response is simulated separately and is divided into 3 parts: photon simulation, photon detection, and electronic response.

a. *Photon simulation*

Photons are produced along the path of a track provided its velocity surpasses the nominal radiation condition $\beta/\beta_T > 1$. The value of β_T represents the threshold velocity in the detector, which depends on the rest mass of the particle track and the gas index of refraction. The distribution of generated photons is :

$$\mathcal{P}(\ell) = e^{-\ell/\lambda} \qquad \lambda \propto \left(1 - \left(\frac{p_T}{p}\right)^2\right)^{-1}.$$

where ℓ is the distance traveled in the gas volume and λ is the mean free path between photon emissions (which result in a photoelectron) which depends on the momentum above threshold p_T (see Table 2-2). The asymptotic value of λ is chosen to reflect the maximum possible photon detection efficiency in a given detector. An emitted photon is produced at an angle

$$\theta_c = \frac{m}{p_T}\sqrt{1 - \left(\frac{p_T}{p}\right)^2}$$

and random azimuth with respect to the track vector. Each photon is then traced to a mirror.

b. *Photon detection*

There are two basic types of mirror systems employed in the three Čerenkov counters, planar and focusing. The optics of these systems is described in more detail in section 2.6 . Photons reflected from the planar mirrors are collected in a series of close-packed collection cones, while those from focusing mirrors are focused directly onto photomultiplier tubes.

Tracing the photon's path begins by finding its intersection with the planar mirror. The simulation ceases if the photon enters the central beam hole or was produced downstream of the mirrors. If the photon intersects outside the physical dimensions of the two mirrors, simulation is passed to a section dealing with focusing mirrors. The present simulation uses the nominal 45 degree orientation of the planar mirrors to determine the reflection angle of Čerenkov photons. The intersection of the photon and the collection cone plane is then found and the correct cell determined. Photons falling outside the planar mirror section are intersected with the nominal focusing mirror plane and the correct cell/mirror is determined.

Once the correct cell is found for a particular photon, an additional efficiency factor is introduced to represent the variable probability that the photon is detected. This factor incorporates variations in optical transmittance, photomultiplier efficiencies, and optical alignments between cells. Thus photons entering a cell are rejected on the basis of this relative factor to reflect the true photon collection efficiency of the given cell.

c. *Electronic response*

Once a photon is detected, it is given a PMT pulse height which is Gaussian distributed about a nominal pulse height. Pulse heights are uniquely associated with ADC channel numbers. Additional photons in a single cell have their ADC response added to any pre-existing ADC count.

4.2 Monte Carlo *Post Hoc* Corrections

Most all of the results presented in this thesis depend in some part on Monte Carlo predictions to correct for detector inefficiencies and acceptance. Since it is critical that the apparatus is adequately simulated, independent checks of Monte

Carlo predictions are employed whenever possible. These checks usually involved comparisons of detector responses in data and Monte Carlo with the result that simulations were often altered to account for characteristics observed in data. However some processes are either difficult to model in Monte Carlo or are not well understood. In such cases it may be easier to employ a *post hoc* correction which merely matches the Monte Carlo response to a measured response in data. For instance Monte Carlo simulations are often too efficient because of the lack of noise or other random effects. A *post hoc* correction simply reduces the efficiency to match that of data by randomly discarding Monte Carlo events. The major drawback of this procedure is that it relies on a proper parameterization of the measured quantity, so these corrections have been applied only in cases of gross discrepancy between Monte Carlo and data. Such discrepancies have been observed in MWPC/SSD track linking and Čerenkov identification of kaons. In addition, the Monte Carlo does not simulate hadronic absorption. Absorption of hadrons in the target is also included by means of a *post hoc* correction for historical reasons.

4.2.1 Hadronic Absorption

Long lived products of target interactions have finite probabilities of being absorbed in the material of the experiment before being detected by the spectrometer. If any one of the D meson decay secondaries is absorbed the state will escape detection. Without simulated absorption, the Monte Carlo detection efficiencies are too high, more so for high multiplicity states rather than low ones. A list of material contributing to hadronic absorption of mesons in the apparatus is listed in Table 4-1. By far the largest amount of absorption occurs in the target. The largest absorber, the Be-5 target, was used during most of the running period. The material listed downstream of the target includes matter from the first SSD plane up to the first plane of P2, beyond which the particle should have been reconstructed.

Table 4-1 : Absorption Lengths

	Frac. of Abs. length
SSD - C2	0.019
Be-5 targ.	0.067
Be-4 targ.	0.053
Si targ	0.031

These numbers are then used in determining the probability that a given particle is absorbed. No distinction is made between pions and kaons, and it is assumed that the effect of absorption is independent of momentum. Absorption of D mesons prior to their decay is ignored.

Since the amount of material downstream of the decay vertex determines the absorption probability, each event in the monte carlo was rejected according to a probability related to the position of its secondary vertex and the multiplicity of the final state. The considerable care which went into modeling interactions in the target, discussed in Appendix D.1, proved valuable in this regard since it provided an accurate description of vertex distributions. Events were rejected randomly according to the probability $1 - \exp^{-nf}$, where f is the computed absorption length fraction per track and n is the final state multiplicity.

The event reduction in Monte Carlo resulting from the *post hoc* absorption correction was found to be 10 percent in the $D^\star \rightarrow (K\pi)\pi$ decay mode and 16 percent in the $D^\star \rightarrow (K\pi\pi\pi)\pi$ decay mode.

4.2.2 MWPC/SSD Linking Corrections

The linking of SSD tracks to MWPC tracks is performed through the procedure discussed in section 3.3 . It is possible to determine a combined efficiency for the linking procedure and SSD track finding efficiency from the fraction of MWPC tracks for which an SSD track link was found. Due to the particular linking procedure it is not necessary to divorce the linking efficiency from the

SSD track finding efficiency. Some differences can be expected to exist between linking efficiencies measured in Monte Carlo and data. Event topologies in Monte Carlo tend to be different than that of the hadronic background events which are used to measure the efficiency in data, so direct comparisons may not be conclusive. A significant difference appears to exist between Monte Carlo and data and a correction was deemed necessary since D meson reconstruction requires linked tracks.

The linking efficiency is calculated as the fraction of MWPC tracks associated with an SSD vertex which are linked. Association with a vertex found by the SSD vertex finding algorithm (section 3.2) ensures that the MWPC track was not spurious or a long lived vee secondary. The miss distance of MWPC tracks from parent vertices is expected to be Gaussian distributed, so tracks not associated with the Gaussian peak fall into the background and are not counted by the fit. Histograms of miss distances in the x projection of all MWPC tracks therefore counts the total number of tracks considered in the calculation. Dividing the histograms into linked and unlinked tracks then gives a measure of the overall linking efficiency. These histograms are shown in Figures 4-1(a) & (b) for linked and unlinked 3-chamber tracks respectively in data. These histograms were further divided into momentum bins and the appropriate efficiency calculation performed on each set. The results are shown in Figure 4-2.

Figure 4-2(a) plots the linking efficiency of 3-chamber tracks as a function of momentum, while Figure 4-2(b) is the same for 5-chamber tracks. The gradual drop in efficiency at low momenta reflects the effects of multiple coulomb scattering on the SSD tracking efficiency. Similar plots for the linking efficiency in Monte Carlo events, shown in Figures 4-2(c) & (d), exhibit an overall higher efficiency as well as far less momentum dependence than in data. This is a possible indication that simulations of SSD tracking are not adequate with regards to MCS effects and spurious strip hits.

To apply a correction to the Monte Carlo data sample, each of the plots in

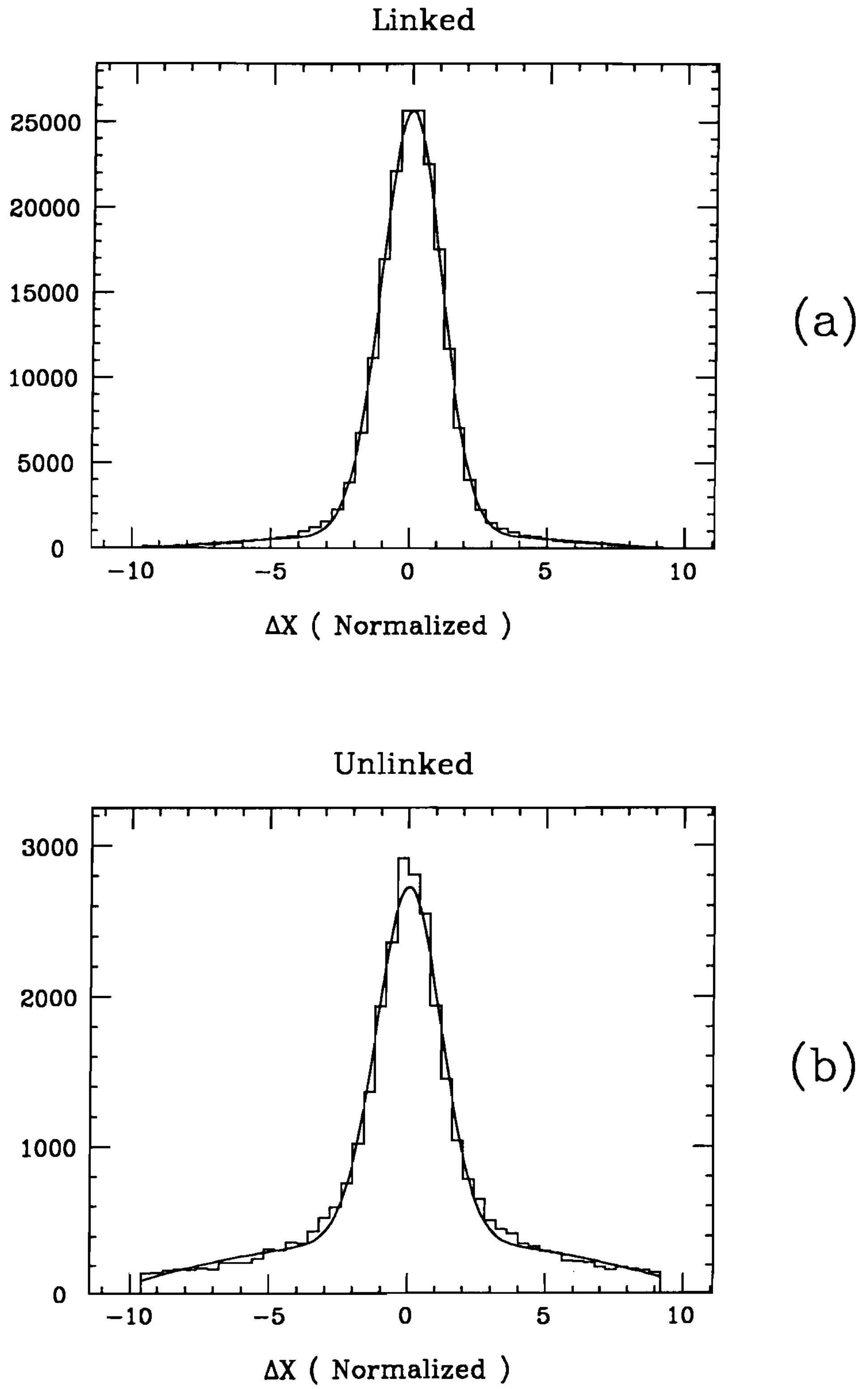

Figure 4-1 : Error normalized x miss distance of linked and unlinked 3 chamber tracks.

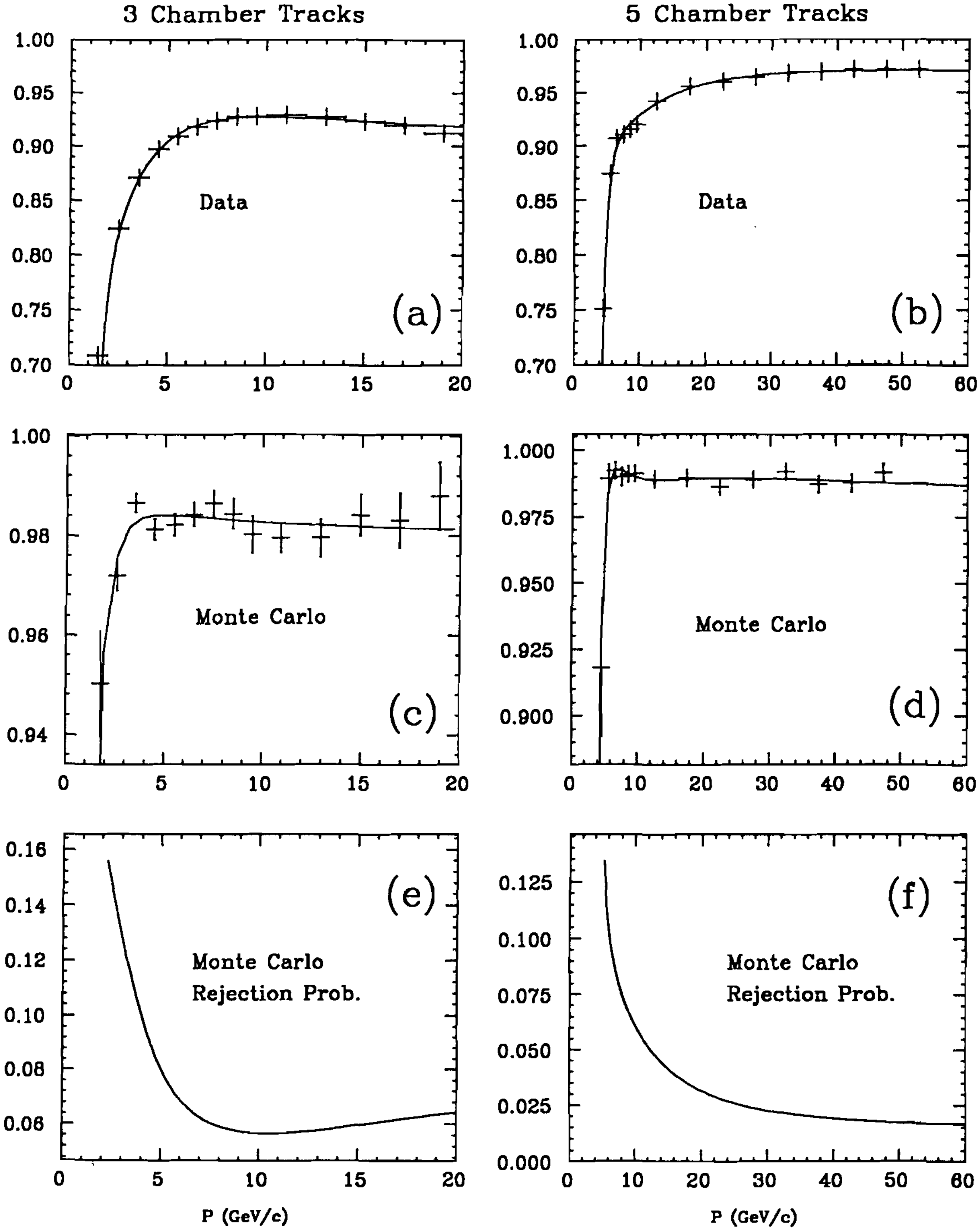

Figure 4-2 : Linking efficiencies and correction functions for 3 and 5 chamber tracks.

Figure 4-2 was first fit to a fourth order polynomial in momentum. These fits are shown in each of the plots. The ratio of these polynomials is then used to determine the probability that a Monte Carlo track should be unlinked. This probability, $1 - \mathcal{E}(p)_{data}/\mathcal{E}(p)_{mc}$, is plotted in Figures 4-2(e) & (f) for 3 and 5 chamber tracks respectively. These plots indicate a difference in efficiency of roughly 6 - 7 percent for 3 chamber tracks and about 2 percent for 5 chamber tracks. Since the analysis involving D° mesons requires decay secondary tracks to be linked, events were discarded if any one of the tracks was chosen to be unlinked. An exception to this is the cascade pion of $D^\star$ decays, which are not required to be linked during D reconstruction.

4.2.3 Kaon Identification

All of the analyses of D mesons through the D meson skim involves a requirement that kaons be positively identified by the Čerenkov system. In particular the analyses presented in this thesis require all kaons to have a minimal identification of KP7 (definite kaon or kaon/proton ambiguous or electron/pion/kaon ambiguous). This section discusses a study comparing the Čerenkov identification of kaons in data and Monte Carlo, and then presents the specific correction to the Monte Carlo event sample.

A study was presented in section 3.14 regarding the Čerenkov identification of kaons. Specifically a signal, shown in Figure 3-23, of $D \rightarrow K\pi, K\pi\pi, K\pi\pi\pi$ was obtained from a vertex based skim without Čerenkov requirements, and used to analyze the ISTAT category of the single kaon in each event. A more detailed analysis was performed by histogramming the same events with an additional requirement that the kaon be identified as KP7. The ratio of yields in histograms with and without the requirement is a measure of the absolute (all momenta) kaon identification efficiency in D events. The resulting histograms and their fits are shown in Figure 4-3, where they have been separated according to the reconstruction topology of the kaon. Figures 4-3(a) & (b) are the uncut and cut histograms respectively in the case where all kaons in the D meson sample are

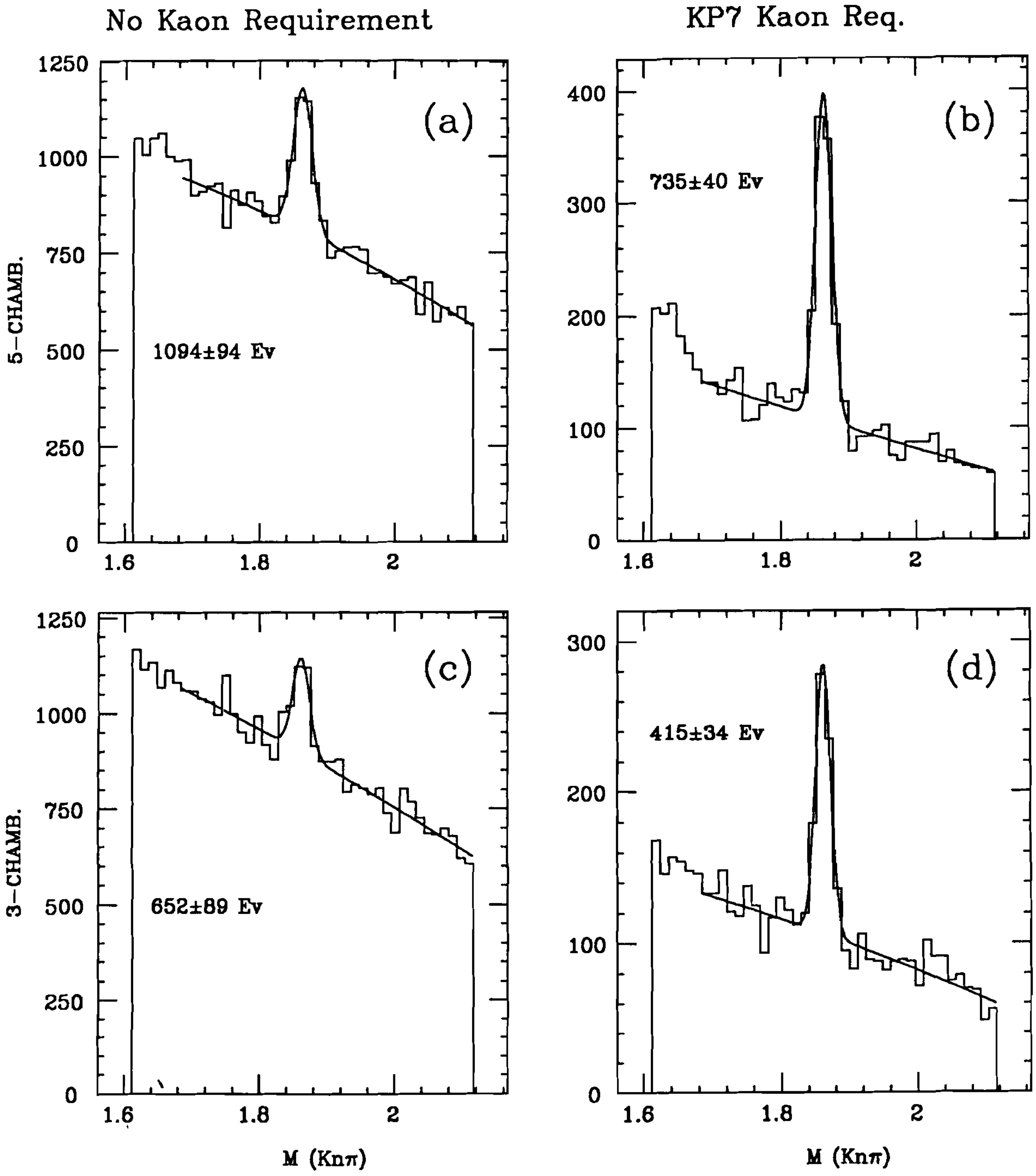

Figure 4-3 : D°,D+ → Kπ,Kππ,Kπππ histograms demonstrating the kaon identification efficiency.

5-chamber tracks, and similarly in Figures 4-3(c) & (d) for 3-chamber tracks. A similar set of histograms was made using Monte Carlo events. In that particular case only $D^\circ \rightarrow K\pi$ and $K\pi\pi\pi$ events were simulated. The results of yield ratios from all the histograms is listed in Table 4-2 below.

Table 4-2 : KP7 identification efficiencies

	5-chamber kaons	3-chamber kaons
Data	$.670 \pm .052$	$.641 \pm .082$
Monte Carlo	$.843 \pm .024$	$.698 \pm .034$

There is an obvious discrepancy between data and Monte Carlo, especially in the case of 5-chamber tracks. A difference might be expected if the momentum spectrum of kaons were different in Monte Carlo and data, however there is no evidence to suggest a momentum dependence to this correction. Simulation of the Čerenkov detectors does not include the affects of stray light created by downstream pair conversions or similar processes. Since most kaon identification is made with the absence of light, this stray light would tend to corrupt information from some of the detectors. In fact C3 is known to have a relatively high level of false *on* tracks, which may well explain the large difference between Monte Carlo and data efficiencies for 5-chamber tracks.

Regardless of the reason for this difference, the result is that on average the Monte Carlo positively identifies 20 percent more kaons than in data. Such a difference is wholly unacceptable in yield dependent analyses such as the cross section measurement, so a *post hoc* correction was applied to Monte Carlo events similar to that used for linking. No apparent momentum dependence exists in the relative kaon identification, so the rejection probability was constant for either 3 or 5-chamber tracks and was again related to the ratio of Monte Carlo and data efficiencies.

Chapter 5

Miscellaneous Results

This chapter presents the results of several measurements involving signals of $D^\star$ and D° mesons.

5.1 $D^{\star\pm}$ Charge Asymmetry

The mechanism called Associated Production was described in Chapter 1 as a means of explaining higher levels of produced $\bar{D}$ mesons than D mesons. While it is certainly not the dominant production mechanism in E687, associated production could be occurring at low levels relative to symmetric $D\bar{D}$ production. A specific measurement of the fraction f of events which occur through associated production can be made by counting the excess of $D^{\star-}$ over $D^{\star+}$ mesons. No $D^{\star+}$ mesons should be created through associated production, so their yield should be

$$N(D^{\star+}) \propto (1-f)\epsilon_s$$

where ϵ_s refers to an acceptance factor for symmetric production. An equal number of $D^{\star-}$ mesons is created in symmetric production so that the total number including those from associated production is

$$N(D^{\star+}) \propto (1-f)\epsilon_s + f\epsilon_a$$

where ϵ_a is the acceptance factor in associated production. The ratio of charged $D^\star$ mesons is then

$$R = \frac{N(D^{\star-})}{N(D^{\star+})} = \frac{(1-f) + f \cdot \epsilon_a/\epsilon_s}{1-f} \simeq \frac{1}{1-f} \qquad \text{if } \epsilon_s \sim \epsilon_a$$

Actual measurement of $D^{\star-}/D^{\star+}$ asymmetries is relatively straightforward, as there is no anticipated bias between charges. Therefore Monte Carlo corrections are unnecessary and a direct measurement of signal strengths in each charge state should represent a valid comparison.

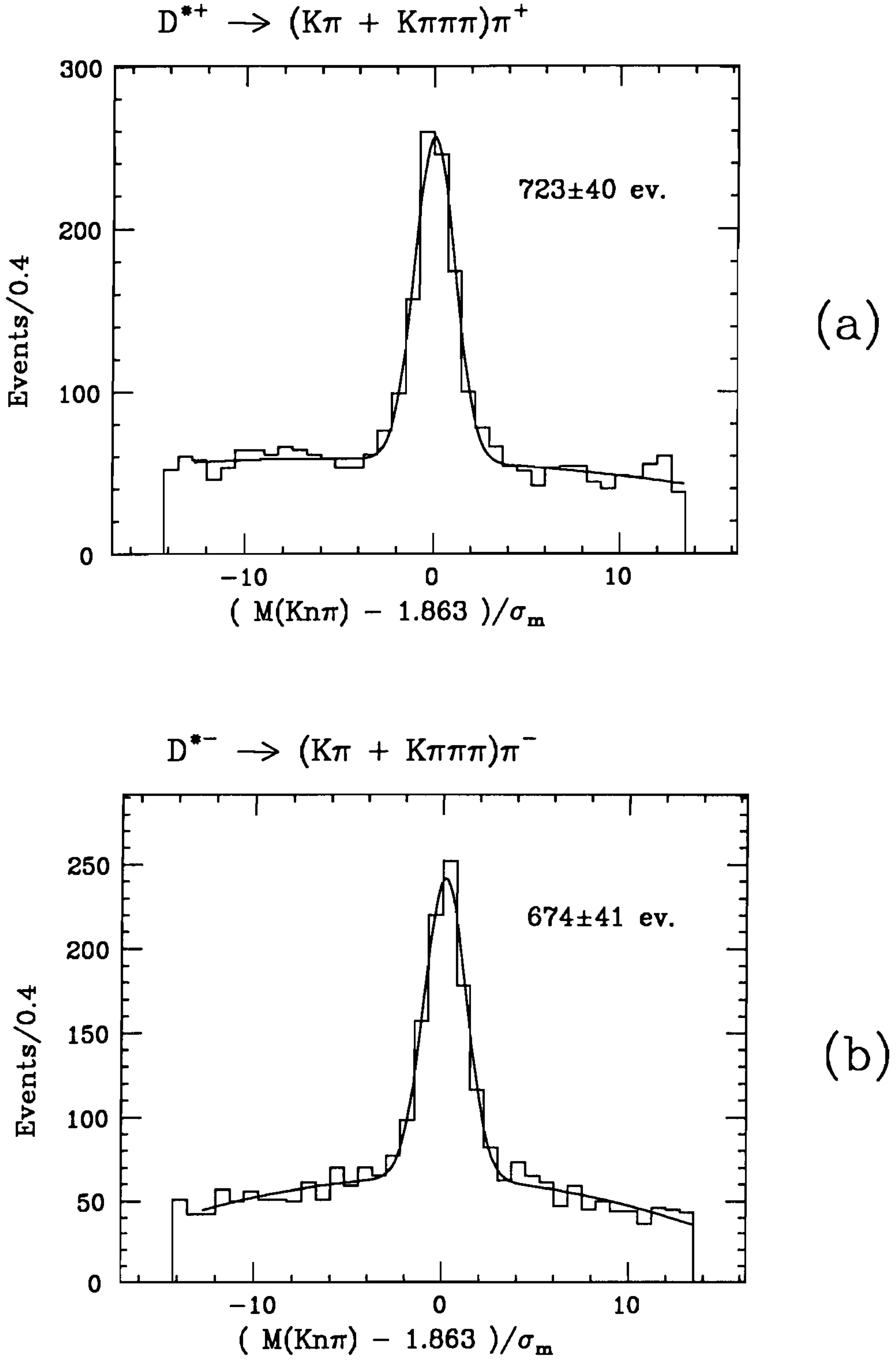

Figure 5-1 : $D^{\star +}$ and $D^{\star -}$ signals used in measuring charge asymmetry.

Charge segregated histograms of combined Kπ and K$\pi\pi\pi$ D* decay modes are shown in Figure 5-1. The yield of D$^{\star -}$ decays is 674 ± 41 events and the yield of D$^{\star +}$ decays is 723 ± 40 events resulting in a value $R = .93 \pm .08$. Solving the above expression for f gives :

$$f \;=\; -.074 \pm .088 \pm .035$$

which is the fraction of events where the D$^{\star -}$ is produced in association with a Λ_c^+. The last uncertainty in f reflects a systematic error which is estimated from independent measurements of f using the Kπ and K$\pi\pi\pi$ decay modes. The negative value of f indicates that no evidence is seen for associated production using D* mesons. The statistical uncertainty of f however implies consistency with $< 10\%$ associated production at the 95% confidence level.

The value of f reported above is somewhat lower than the 7.5 ± 2.1 % level of associated production found by E691[2],but levels may well depend on production energies making comparisons difficult.[4]

5.2 Ratio of D* to Inclusive D$^\circ$ Production

Another simple measurement is the fraction $f_\star$ of inclusive D$^\circ$ events coming from D$^{\star\pm}$ decays. A simple spin counting argument can be used to predict the value of $f_\star$.

Under the assumption that charm meson spin and isospin states are evenly populated, D* mesons (spin 1) are 3 times more copious than D mesons (spin 0) neglecting phase space differences at high energy. If a total of N D mesons are produced, this assumption implies that population of the species will be :

$$\mathrm{D}^{\circ} : \frac{N}{8} \qquad \mathrm{D}^{+} : \frac{N}{8}$$

$$\mathrm{D}^{\star\circ} : \frac{3N}{8} \qquad \mathrm{D}^{\star\pm} : \frac{3N}{8}$$

The $\mathrm{D}^{\star}$ mesons always decay into D mesons with branching fractions that can be parameterized as :

$$\begin{array}{rl} D^{\star\pm} \rightarrow D^{\circ}\pi^{\pm} & \text{prob.} = B \\ D^{\star\pm} \rightarrow D^{\pm}X & \text{prob.} = 1 - B \\ \mathrm{D}^{\star\circ} \rightarrow \mathrm{D}^{\circ}X & \text{prob.} = 1 \end{array}$$

The number of $\mathrm{D}^{\star\pm}$ mesons which decay into D° is then $3B \cdot N/8$. The total number of D° mesons expected is found by adding the various contributions :

$\frac{N}{8}$	from direct production
$\frac{3N}{8}$	from $\mathrm{D}^{\star\circ}$ mesons
$\frac{3N}{8}B$	from $\mathrm{D}^{\star\pm}$ mesons
$(3B+4)\frac{N}{8}$	Total

The observed $\mathrm{D}^{\star\pm}/\mathrm{D}^{\circ}_{incl}$ ratio is then written :

$$f_{\star} \equiv \frac{D^{\star\pm} \rightarrow D^{\circ}\pi^{\pm}}{D^{\circ}_{incl}} = \frac{B}{B + \frac{4}{3}}$$

A similar expression can be written for the observed ratio of $\mathrm{D}^{\pm}$ and inclusive D° mesons :

$$f_{+} \equiv \frac{D^{+}}{D^{\circ}_{incl}} = \frac{1 - \frac{3}{4}B}{1 + \frac{3}{4}B}$$

Using the present measured value of B = 0.49 ± .08, the fraction of $\mathrm{D}^{\star\pm}$ mesons decaying into D° mesons, a prediction for these ratios is obtained.

$$f_\star = 0.27 \pm .03$$
$$f_+ = 0.46 \pm .07$$

Until now the best available measurement[2] of $f_\star$ was 0.32 ± 0.01 ± 0.03 .

The combined decay modes of D° → Kπ & Kπππ shown in Figures 5-2(a) & (b) can be used as a high statistics sample for determining $f_\star$. These signals represent 5379 ± 248 events of inclusive D° decays and 1154 ± 49 events of D° decays with a D* tag. The two decay modes are subjected to slightly different ℓ/σ_ℓ cuts which should not bear on the results since only the D* and inclusive D° in a particular D° decay channel need have the same analysis cuts.

The value of $f_\star$ is very nearly the ratio of yields in Figures 5-2(a) & (b). However it is necessary to correct by the extra acceptance factor for reconstructing the cascade pion as well as the absorption of this pion. Neither of these have much momentum dependence. The combined correction factor is :

$$\epsilon = 0.864 \pm .005$$

irrespective of the D° decay mode. The yield of D* tagged D° mesons shown in Figure 5-2(b) has been over-counted by 5 percent, based on the argument presented in section 3.11.1, so the D* yield must be reduced accordingly. The factor $f_\star$ can then be calculated

$$f_\star = \frac{1154}{5379} \cdot \frac{1}{0.864} \cdot \frac{1}{1.05} = 0.237 \pm 0.013$$

An estimate of systematic errors can be obtained by calculating $f_\star$ separately for the Kπ and Kπππ decay modes. Following the same procedure as described

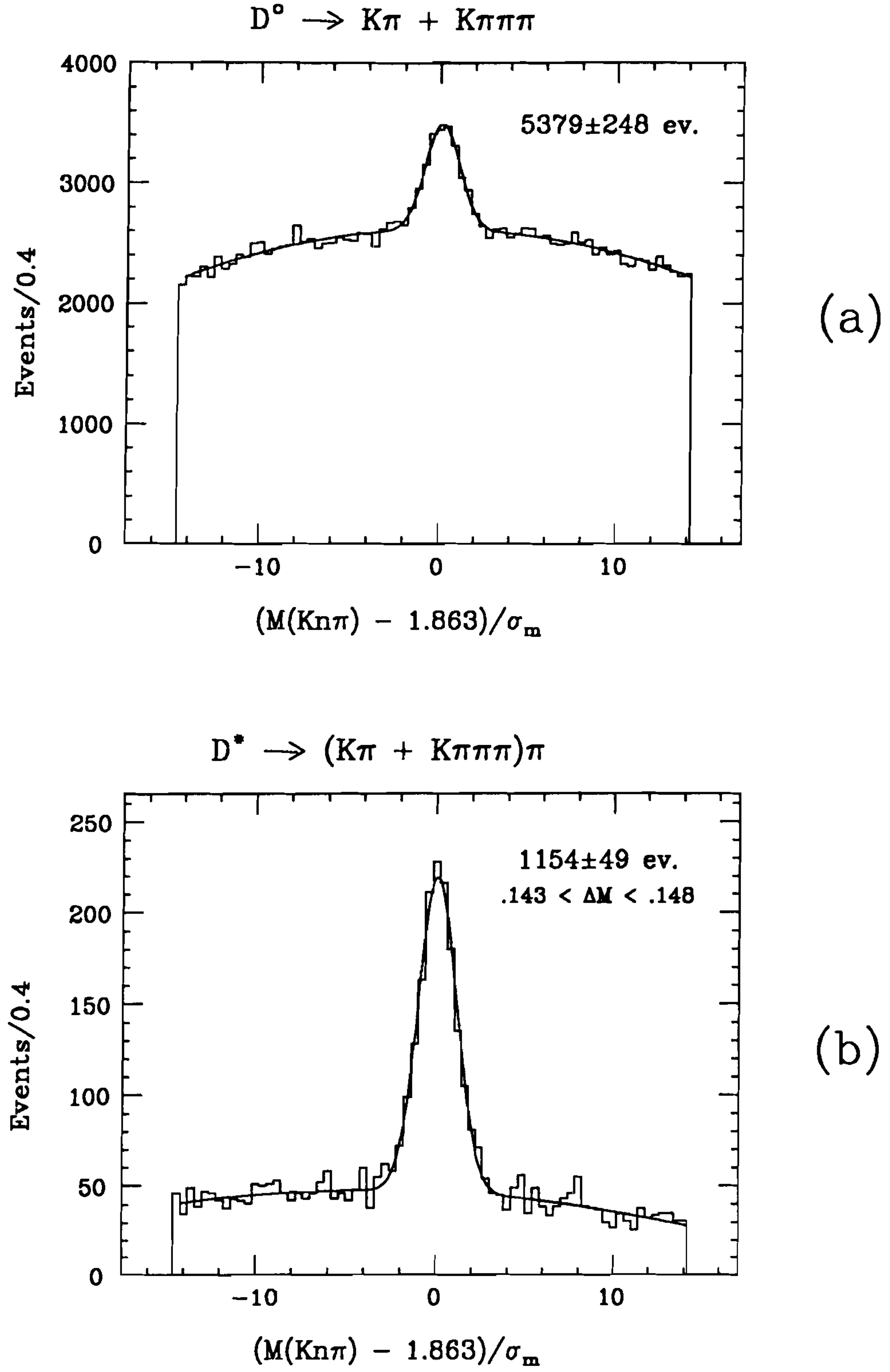

Figure 5-2 : D* and D° inclusive signals used in measuring the $D^{*\pm}/D^{\circ}$ ratio.

above,

$$f_\star(K\pi) = 0.241 \pm 0.018$$
$$f_\star(K\pi\pi\pi) = 0.233 \pm 0.019$$

These numbers represent the minimum systematic error, so that the true error is more likely in the range of ± 0.01 .

The value of $f_\star = .237 \pm .013 \pm .01$ is in good agreement with the simple prediction of .27 ± .03 but in poorer agreement with previous measurements. However there is no reason that this ratio should not be energy dependent. The measurement presented here is unique at these photon energies.

5.3 $K\pi\pi\pi/K\pi$ Branching Ratio

A study has been undertaken to determine the branching ratio between $D^\circ \to K\pi$ and $D^\circ \to K\pi\pi\pi$ decays. This ratio has been studied in previous experiments, and has a world average [8] of

$$Br = \frac{\Gamma(D^\circ \to K\pi\pi\pi)}{\Gamma(D^\circ \to K\pi)} = 2.10 \pm .20$$

The event sample in these two decay modes does not allow E687 to improve upon the accuracy of this number. However the calculation provides a test of systematic effects in the experiment. Systematic effects which are shared in common between the two decay modes, such as the luminosity determination, are not addressed in this test. But the relative acceptance of 2-body versus 4-body decays will strongly affect the branching ratio.

The signals in the two decay modes have a raw yield ratio of about 1:1 while the world average branching ratio implies a 2:1 ratio. The presumption is that the $K\pi\pi\pi$ decay mode has a low acceptance related to its multiplicity. A Monte Carlo simulation of each decay mode is therefore used to compute the acceptance in each decay mode. The overall acceptance includes detector efficiencies as well as geometrical acceptance, so the Monte Carlo simulation serves as a correction for these as well. If the simulation of the apparatus were perfect the prediction for the acceptance fraction in a particular decay mode would still depend on the D meson production model and decay dynamics. If it is further assumed that the D meson decay dynamics are well understood (see Appendix B), only inaccuracies in the D meson photoproduction models can affect the results. Any production model dependencies that may exist can be parameterized in terms of D meson momentum and $p_\perp$. Dependence of the acceptance on a $p_\perp$ is very slight[4], so any difference between reality and the production model can be written in terms of the D momentum. The acceptance in each decay mode is therefore parameterized in terms of the momentum alone.

5.3.1 Determining the Acceptance

An acceptance function $\mathcal{E}(p)$ is determined by subjecting Monte Carlo events to the analysis cuts used in data. Accumulating the analyzed events in bins of D momentum and dividing by the number of events generated in each momentum bin gives $\bar{\mathcal{E}}_i$ in each bin i. If the momentum bins are small enough $\mathcal{E}$ will be roughly constant in each bin and all production model dependencies in the Monte Carlo are effectively removed.

The K$\pi\pi\pi$/Kπ branching ratio was calculated with the D* signals only and then again with the inclusive D$^\circ$ sample. This was done in case a systematic difference existed between D$^\circ$ mesons with and without a D* *tag*. The Monte Carlo generation of Kπ and K$\pi\pi\pi$ event samples follows the description in section 4.1.1, where one charm quark in every event was required to hadronize as a D$^{\star\pm}$ and subsequently decay via D$^\circ$. Thus the same events are used for determining the acceptance function $\mathcal{E}(p)$ for D* as well as D$^\circ$ events. Acceptance of the cascade pion from D* decays, discussed in section 5.2, is roughly independent of momentum so $\mathcal{E}(p)$ for the two D mesons differ only in scale. Major contributions to the overall acceptance come from :

- triggering
- Geometrical acceptance

- reconstruction efficiency
- analysis cuts

The effect of triggering on the acceptance for the two decay modes is shown as the top set of points in Figures 5-3(a) & (b) as a function of D* momentum. The finite energy range of the RESH trigger is clearly evident in the fall at high momenta (i.e. $E_{RESH} < 20$ GeV). The addition of geometrical acceptance and reconstruction efficiency is shown in the second set of points, and inclusion of analysis cuts is represented by the lowest set. The analysis cuts used in data and Monte Carlo include KP7 kaon identification, a vertex quality cut, and a vertex detachment cut. These are each described in section 3.11 . The D* sample has a mass difference requirement as well. The specific detachment cuts were $\ell/\sigma_\ell > 2.0$ in the D* sample and $\ell/\sigma_\ell > 8.0$ in the inclusive D$^\circ$ sample. The lowest points in Figures 5-3(a) & (b) are the probabilities in each momentum bin for observing D* events in the two decay modes with the particular analysis cuts. These points are fit to a polynomial in momentum to obtain a functional dependence $\bar{\mathcal{E}}(p)$. This fit is shown as the top curves in Figures 5-3(c) & (d) for the Kπ and K$\pi\pi\pi$ decay modes respectively. The bottom curve is the acceptance fraction obtained when *post hoc* corrections are included in the D* Monte Carlo. These corrections, which are described in section 4.2, account for hadronic absorption of the D$^\circ$ decay particles, linking efficiency and Čerenkov identification of kaons. The analysis of the data sample using the acceptance function proceeds first with no *post hoc* corrections.

5.3.2 Event Analysis

A prediction of the total event yield is made using a technique of weighted histograms. Each event of momentum p is given a weight $1/\bar{\mathcal{E}}(p)$ which is entered into a bin of normalized invariant mass much the same as in Figure 5-2. The weighted histogram yield is therefore a prediction of the total number of events produced in a particular decay mode. If each histogram is broken into several parts, each corresponding to a range of momenta, the distribution of yields in

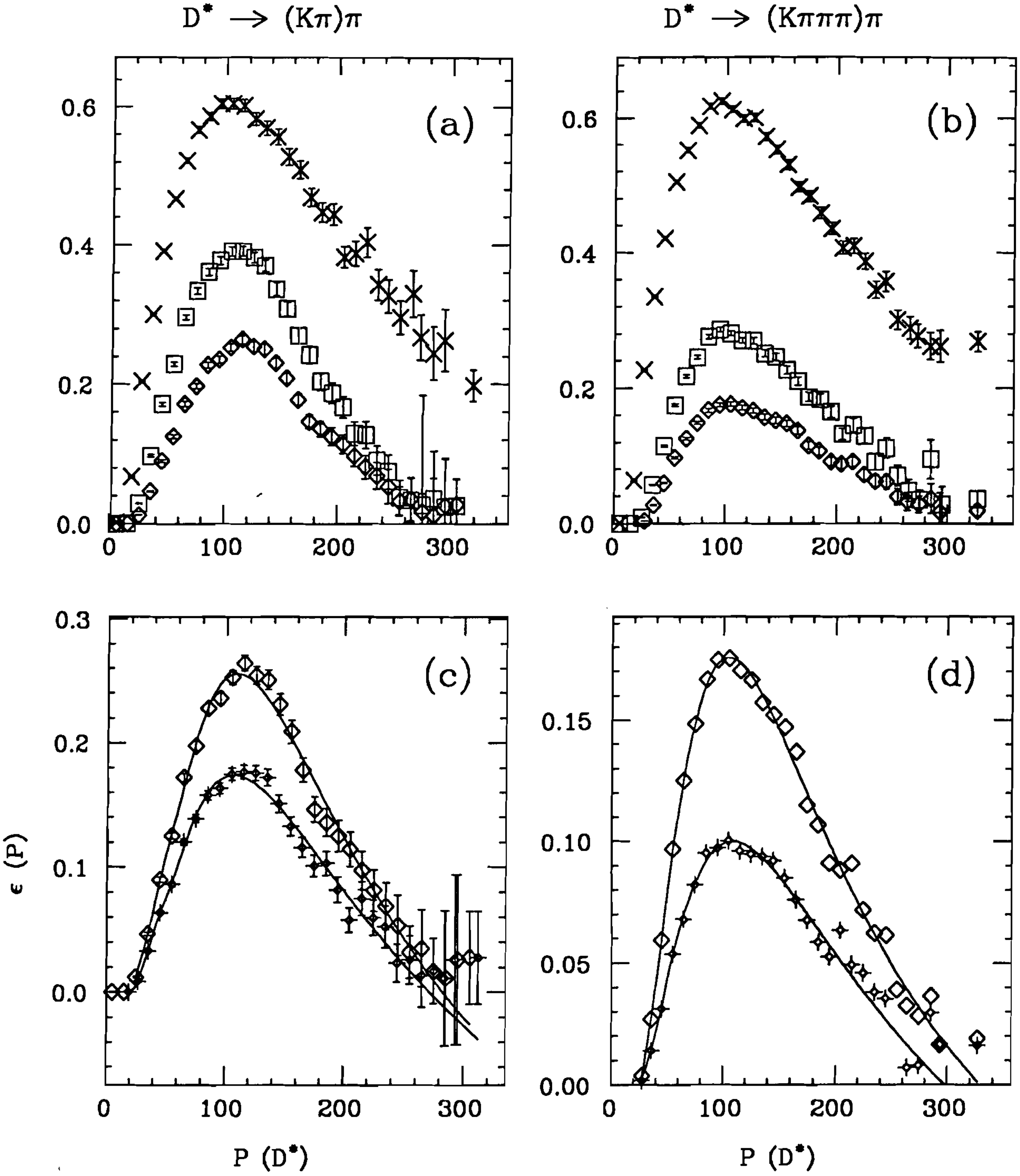

Figure 5-3 : Various acceptances in E687 for Kπππ and Kπ signals. The lowest sets are used in calculating branching ratios.

these bins of momenta is then a coarse description of the parent momentum distribution of D mesons. Statistics limit the number of momentum bins, since it is necessary to fit a mass distribution for each, so that the distribution in each decay mode is represented by only 5 points. The raw signals in the 5 momentum bins are shown in Figure 5-4(a) to (d) for the two decay modes of the $D^\star$ and D° samples. The corresponding weighted histograms are shown in Figure 5-5(a) to (d). The histograms are fit with a width constrained to a unit gaussian and the resulting yields plotted in Figure 5-6. The yields obtained from the $K\pi$ histograms have been scaled by the world average branching ratio 2.1, so that in principle the the $K\pi$ and $K\pi\pi\pi$ total yields should match in every momentum bin.

5.3.3 Systematic Effects

Except for high momenta, the $D^\star$ yields shown in Figure 5-6 appear to match fairly well. However the higher statistics inclusive D° sample exhibits some disagreement between the decay modes at all momenta. This indicates a problem with the Monte Carlo simulation. The same set of weighted histograms has been reproduced using an acceptance function $\mathcal{E}'(p)$ which includes *post hoc* corrections and is shown as the lower curves in Figures 5-3(c) & (d). The results of fits to these histograms is shown in Figures 5-7(a) & (b) for the $D^\star$ and D° cases respectively. Significant improvements in both ratios are observed. Thus much of the apparent discrepancy is explained by relatively higher losses of events in the $K\pi\pi\pi$ decay modes due to absorption and linking. The large (20 %) kaon correction depends only slightly on multiplicity, and so should affect the two decay modes equally.

The plots in Figure 5-7 indicate that some systematic problems remain, particularly at high momenta. No conclusive evidence exists as to the causes, but there are some suspects. The vertex quality (CL) cut is not well understood in the $K\pi\pi\pi$ decay sample. This cut ($CL > 0.6\%$) is over 95 percent efficient in all Monte Carlo events and is equally efficient in the $D^\circ \to K\pi$ decay in data.

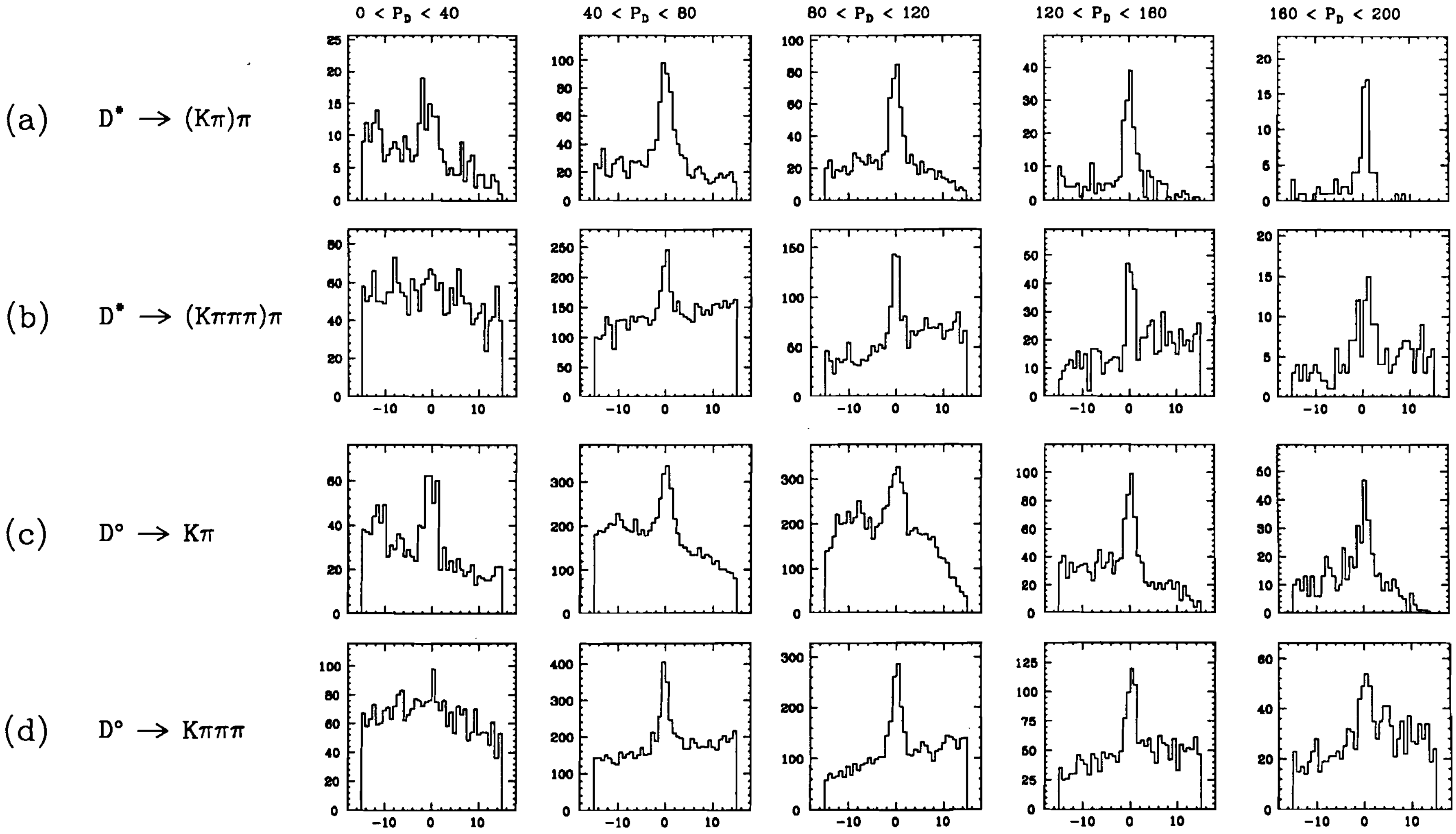

Figure 5-4 : $D^\star$ and D° inclusive signals used for measuring $K\pi\pi\pi/K\pi$ ratio versus D momentum

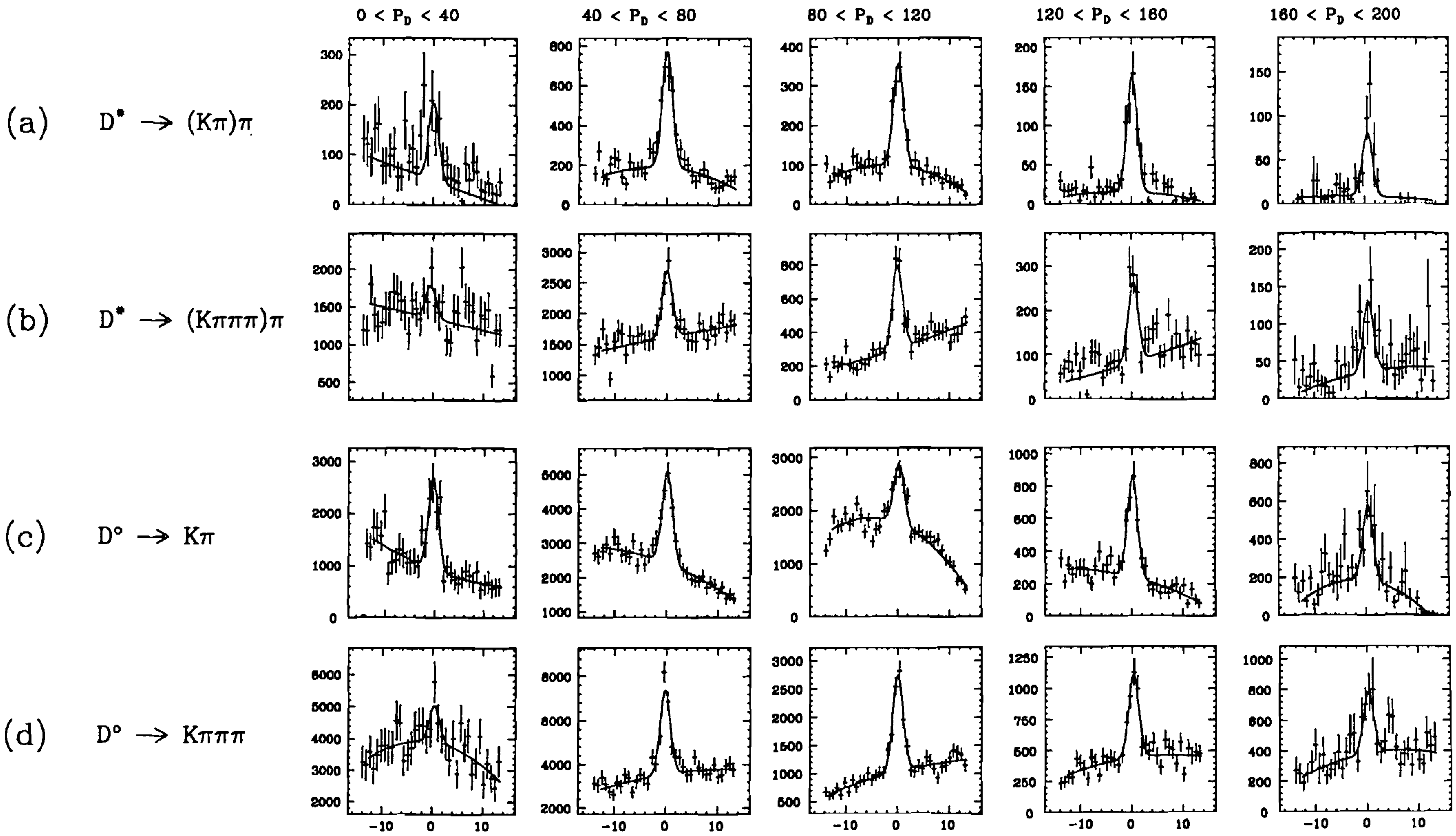

Figure 5-5 : Weighted D* and D° inclusive signals used for measuring $K\pi\pi\pi/K\pi$ ratio versus D momentum

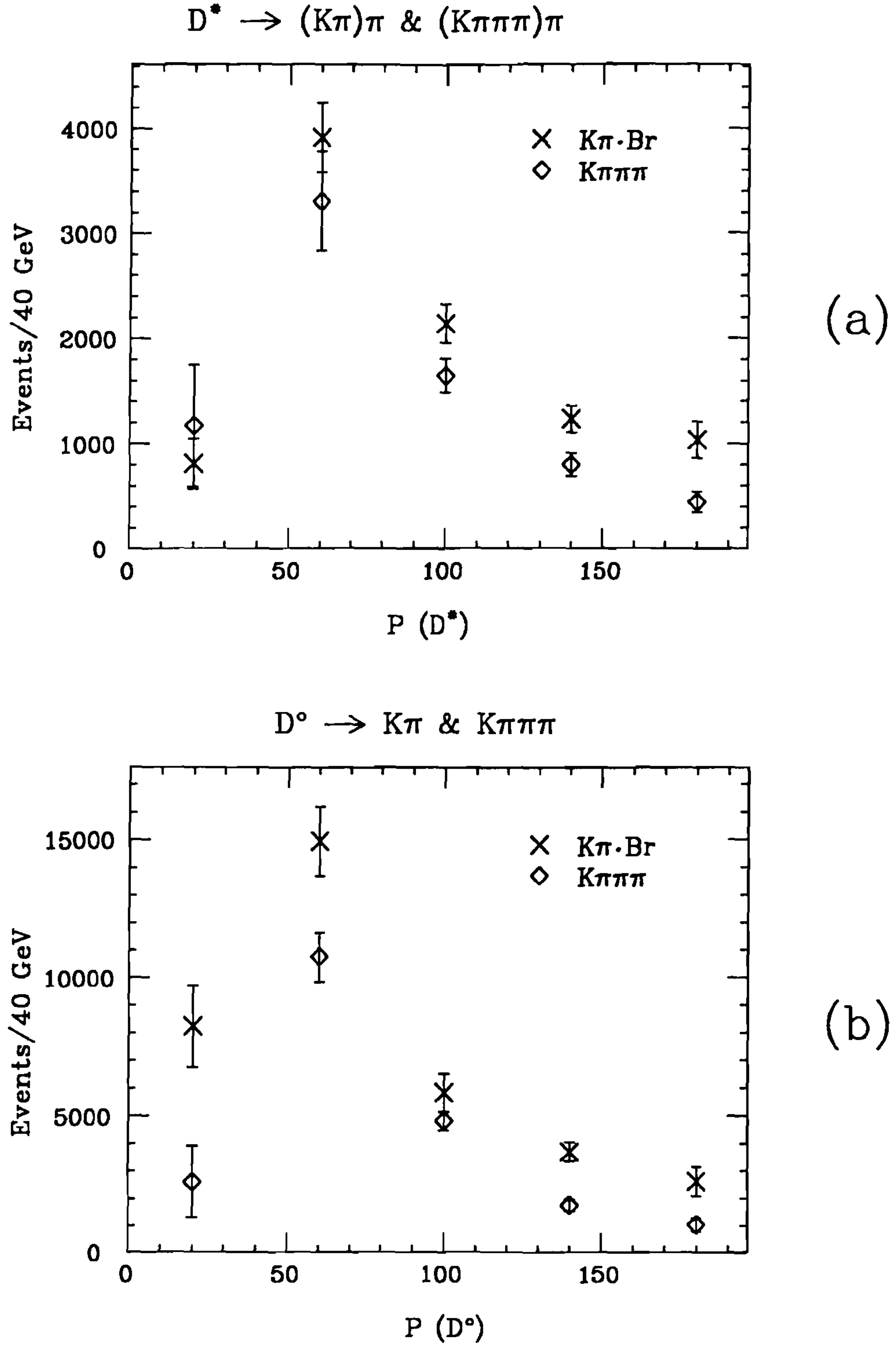

Figure 5-6 : The Kπππ/Kπ calculated yields versus D momentum for D* and D° inclusive signals.

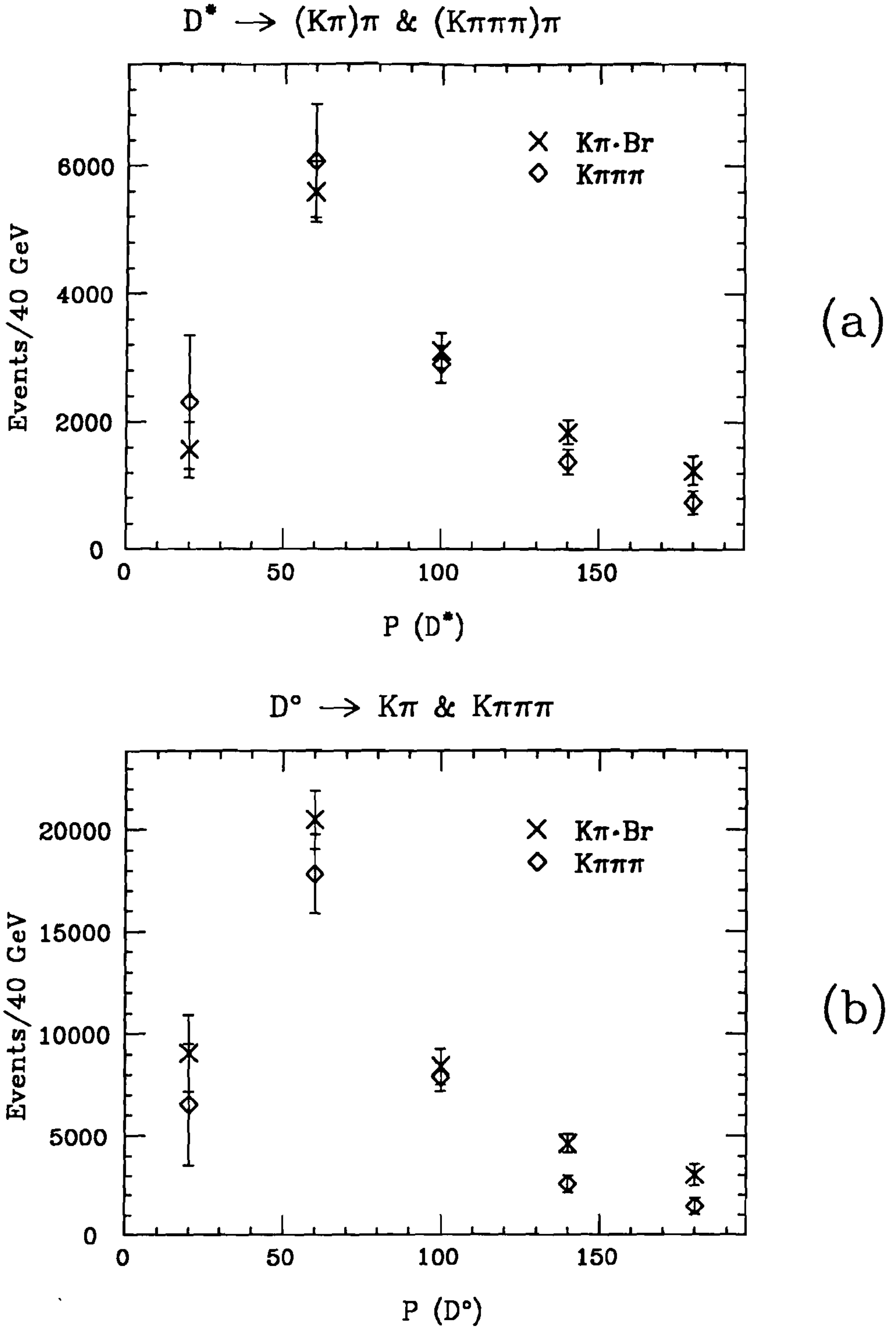

Figure 5-7 : The $K\pi\pi\pi/K\pi$ calculated yields versus D momentum including *post hoc* Monte Carlo corrections.

The cut efficiency in D° → Kπππ, where the cut is most effective in reducing background, appears to be only 85 percent. Also, Monte Carlo studies of the trigger have indicated significant inefficiencies for charm states as evidenced by the top curves in Figure 5-3. The trigger is based on the entire event and is thus a source of considerable model dependency.

5.4 Cabbibo Suppressed Decays

Using the weighting technique just described, the branching ratios $\Gamma(D^\circ \rightarrow (K^+K^-)\pi)/\Gamma(D^\star \rightarrow (K^+\pi^-)\pi)$ and $\Gamma(D^\circ \rightarrow \pi^+\pi^-\pi^+\pi^-)/\Gamma(D^\circ \rightarrow K^+\pi^-\pi^+\pi^-)$ have been calculated. The two Cabbibo suppressed decays $D^\star \rightarrow (K^+K^-)\pi$ and $D^\circ \rightarrow \pi^+\pi^-\pi^+\pi^-$ are naively expected to occur at a level of 5 percent of a similar Cabbibo allowed decay. The allowed decays, $(K^+\pi^-)\pi$ and $K^+\pi^-\pi^+\pi^-$, are therefore chosen minimize differences in decay dynamics. The choice of identical multiplicity in each ratio also reduces Monte Carlo dependencies.

The ratios are calculated in a manner identical to the Kπππ/Kπ branching ratio, except only one weighted mass histogram is accumulated and fit in each decay mode. The branching fraction is then the ratio of yields of the two relevant histograms.

5.4.1 $K^+K^-/K^+\pi^-$ Branching Ratio

A signal for $D^\star \rightarrow (KK)\pi$ is shown in Figures 5-8(a) & (b). The signal shown in Figure 5-8(a) has the requirements of a mass difference cut, a vertex quality cut, and $\ell/\sigma_\ell > 2.0$. Both kaons are required to be Čerenkov identified as KP (see section 3.11). The second, higher mass peak in Figure 5-8(a) is the result of a mass reflection of $D^\star \rightarrow (K\pi)\pi$ where the pion from the D° decay has been mis-identified as a kaon. A similar reflection peak appears in Monte Carlo simulations as well. The false peak in M(KKπ) is fit as well as the true peak to prevent the reflection from influencing the background level. The same histogram made with more restrictive kaon identification (at least one of the two particles is also a definite kaon) is shown in Figure 5-8(b). This figure demonstrates

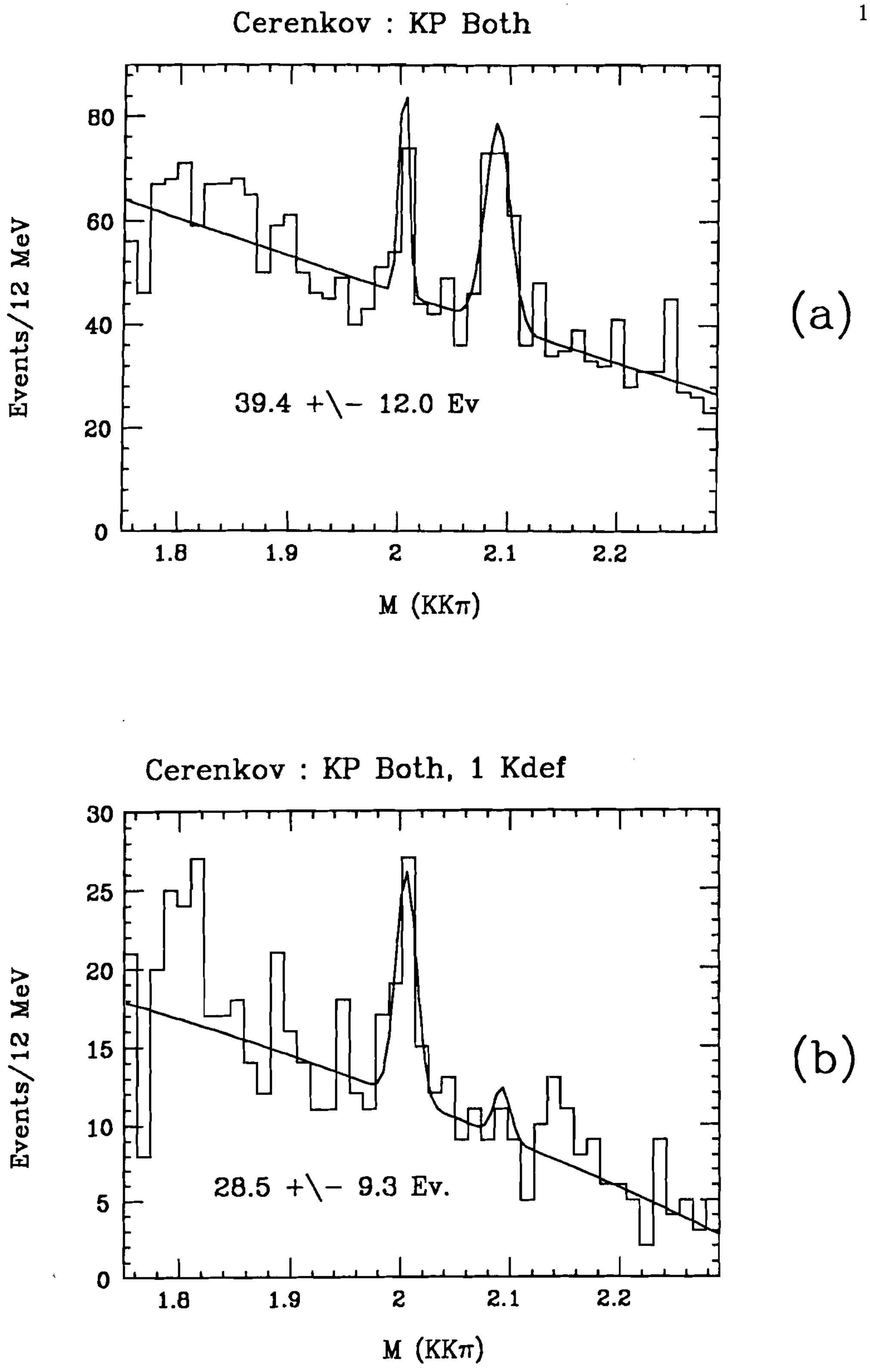

Figure 5-8 : The $D^{\star} \rightarrow (KK)\pi$ signal under different kaon identification cuts.

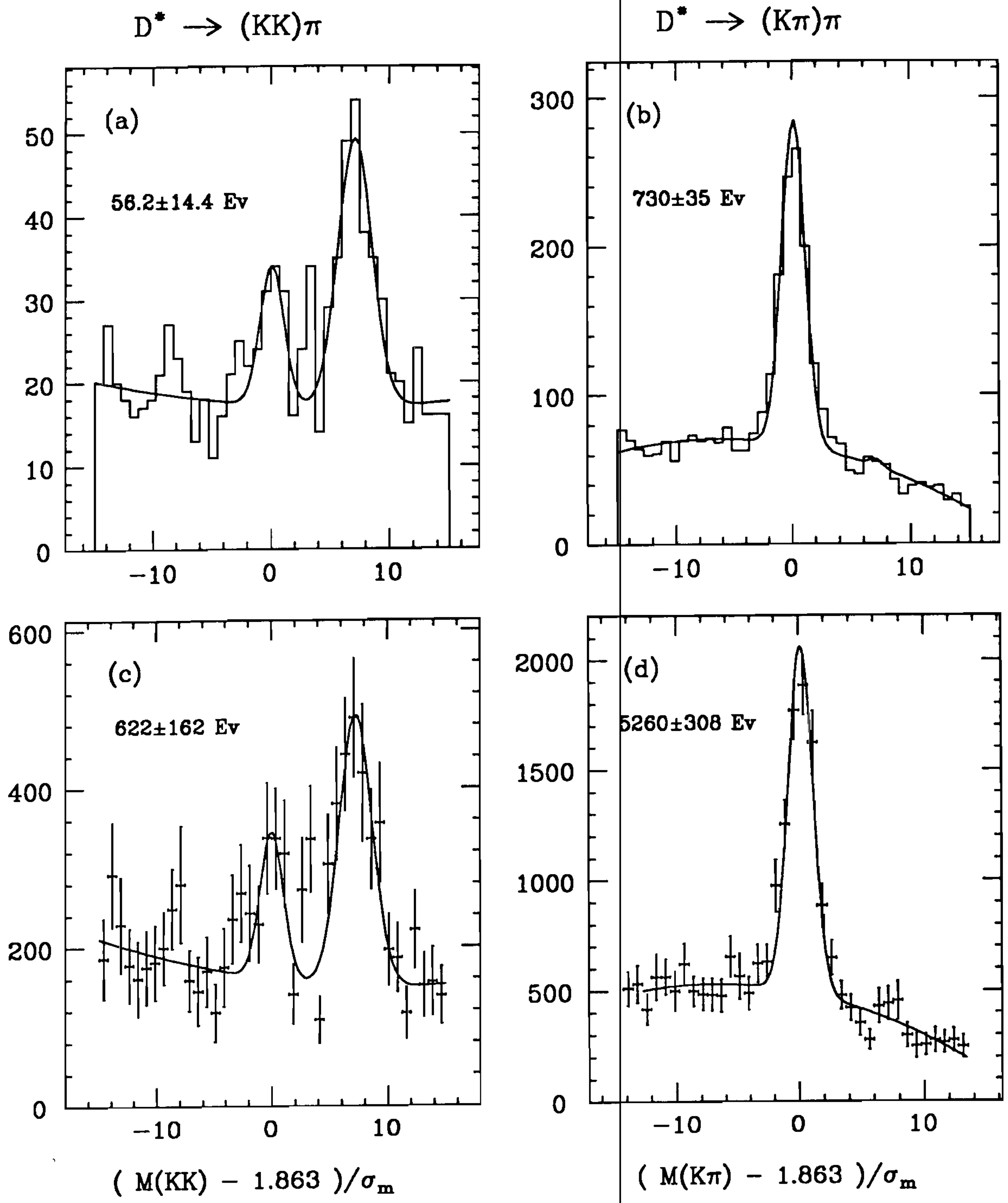

Figure 5-9 : The $D^* \to (KK)\pi$, $(K\pi)\pi$ signals used to calculate the $KK/K\pi$ branching ratio.

the nature of the reflection as well as the ability to remove it through tighter Čerenkov requirements. This removal is done at the cost of true signal events, so kaon requirements are left loose in this analysis.

In analogy with the K$\pi\pi\pi$/Kπ branching ratio calculation, the signal is histogrammed in normalized invariant mass and the fit constrained to a unit Gaussian. These fits are shown in Figures 5-9(a) & (b) for the raw $D^\star \rightarrow (KK)\pi$ and $D^\star \rightarrow (K\pi)\pi$ signals, and yield 56 ± 14 events and 730 ± 35 events respectively. The kinematic and lifetime cuts are identical to those discussed above, except kaons are only required to be identified as KP7. Since the two final states involve different numbers of kaons, the histogram weight ($1/\mathcal{E}'(p)$) includes the *post hoc* kaon identification correction for each kaon. This correction results in a ratio which is about 20% higher than one which ignores the correction. The resulting weighted histograms are shown in Figures 5-9(c) & (d) for the Kπ and KK decay modes respectively. The yields obtained from these two histograms translates into a branching ratio which is :

$$\frac{\Gamma(D^\star \rightarrow (K^+K^-)\pi)}{\Gamma(D^\star \rightarrow (K^+\pi^-)\pi)} = .118 \pm .032$$

This compares very well with the earlier results of MARK II and MARK III where their average ratio was found to be $.119 \pm .018$.[8] These results indicate that the simple spectator picture of $D^\circ \rightarrow KK$ is probably not sufficient to describe the decay.

5.4.2 $\pi^+\pi^-\pi^+\pi^-/K^+\pi^-\pi^+\pi^-$ Branching Ratio

The inclusive signals $D^\circ \rightarrow \pi^+\pi^-\pi^+\pi^-$ and $D^\circ \rightarrow K^+\pi^-\pi^+\pi^-$ are shown in Figures 5-10(a) & (b) respectively. Each signal has a vertex quality cut and requires a minimum vertex detachment of $\ell/\sigma_\ell > 8.0$. The $\pi\pi\pi\pi$ signal has an additional requirement that two of the pions are Čerenkov identified as PI23. The kaon in the K$\pi\pi\pi$ signal must be identified as KP7. The fits, shown in the figures, are constrained to be unit width Gaussian and yield 235 ± 43 events in $\pi\pi\pi\pi$ and 1813 ± 67 events in K$\pi\pi\pi$. The corresponding weighted histograms

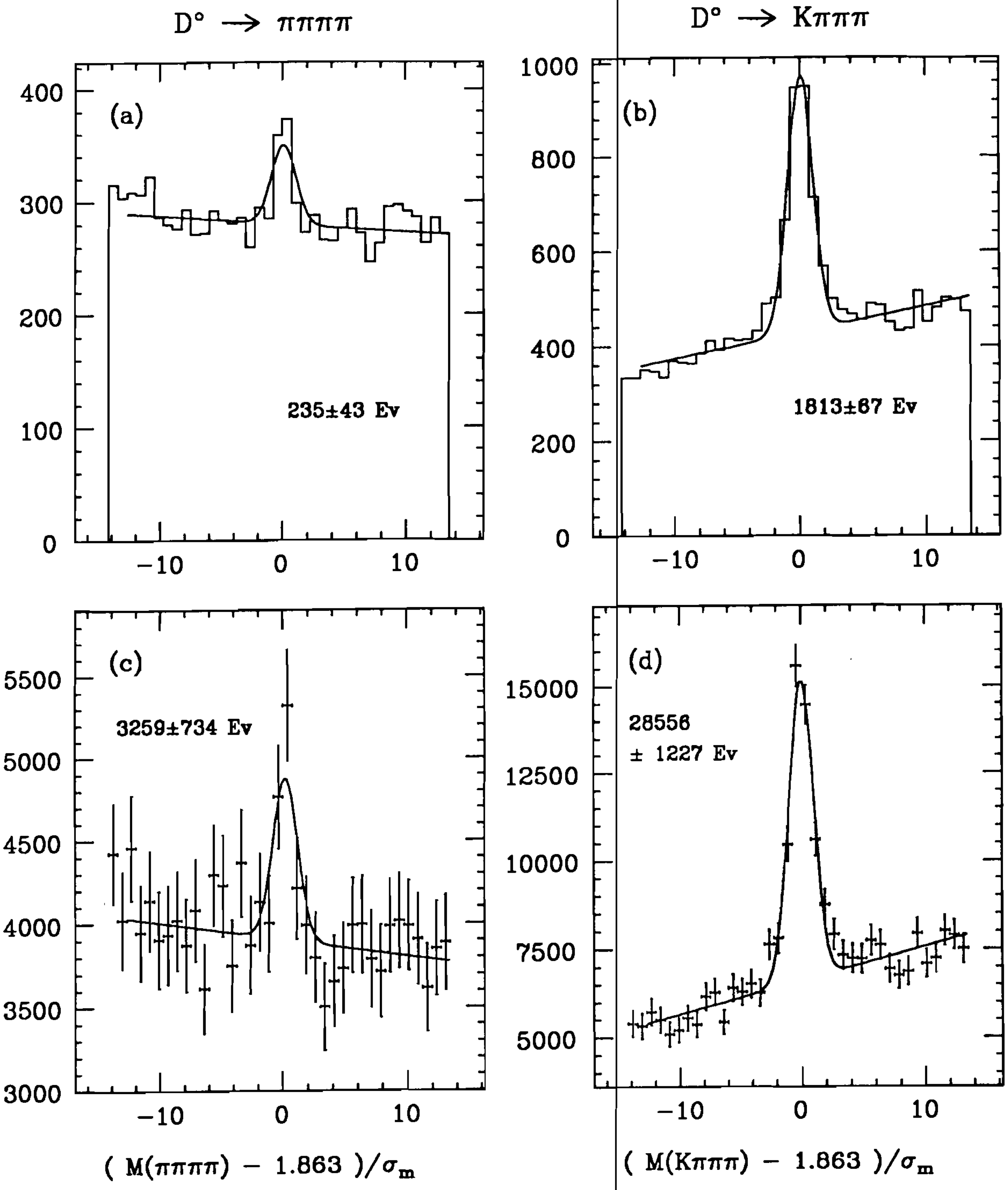

Figure 5-10 : The D° → ππππ, Kπππ signals used to calculate the ππππ/Kπππ branching ratio.

are shown in Figures 5-10(c) & (d). While the K$\pi\pi\pi$ signal includes a *post hoc* correction for kaon identification, no correction for pion identification was applied to the $\pi\pi\pi\pi$ signal. The yields obtained from these two histograms translates into a branching ratio which is :

$$\frac{\Gamma(D^{\circ} \rightarrow \pi^{+}\pi^{-}\pi^{+}\pi^{-})}{\Gamma(D^{\circ} \rightarrow K^{+}\pi^{-}\pi^{+}\pi^{-})} = .114 \pm .026$$

This improves considerably on the accuracy of earlier measurements[6,7,17], and tends to agree more with the measured KK/Kπ ratio than the .034 ± .009 value of the $\pi\pi$/Kπ ratio obtained by MARK II and MARK III. D° $\rightarrow \pi^{+}\pi^{-}\pi^{+}\pi^{-}$ and D° $\rightarrow$ K$^{+}\pi^{-}\pi^{+}\pi^{-}$ decays must include final state interactions beyond those shown in the lowest order spectator diagram, which suggests that these interactions make considerable contributions in the KK and $\pi\pi\pi\pi$ decays of the D° .

5.5 Double D Events

A search was performed for events containing two fully reconstructed D mesons (either charged or neutral). Detailed studies of the correlations between the D and $\bar{\text{D}}$ mesons in double D events provide important tests of models for the photoproduction of charmed quarks which are relatively free from quark dressing uncertainty. For example, the PGF model predicts an increased forward-backward peaking of the charm quarks with respect to the incident photon direction with increasing photon-gluon center of mass energy. The angle between the quark and the incident photon is measured by boosting to a frame where the observed D and $\bar{\text{D}}$ are anticollinear. To the extent that the quark and meson have the same direction in the charm- anticharm center of mass frame, dressing effects create minimal distortion of the angular distribution[18]. Although this was the original motivation for undertaking the double D study, the observed signal was only about 50 events which was thought to be too small to investigate the energy evolution of the quark angular distribution.

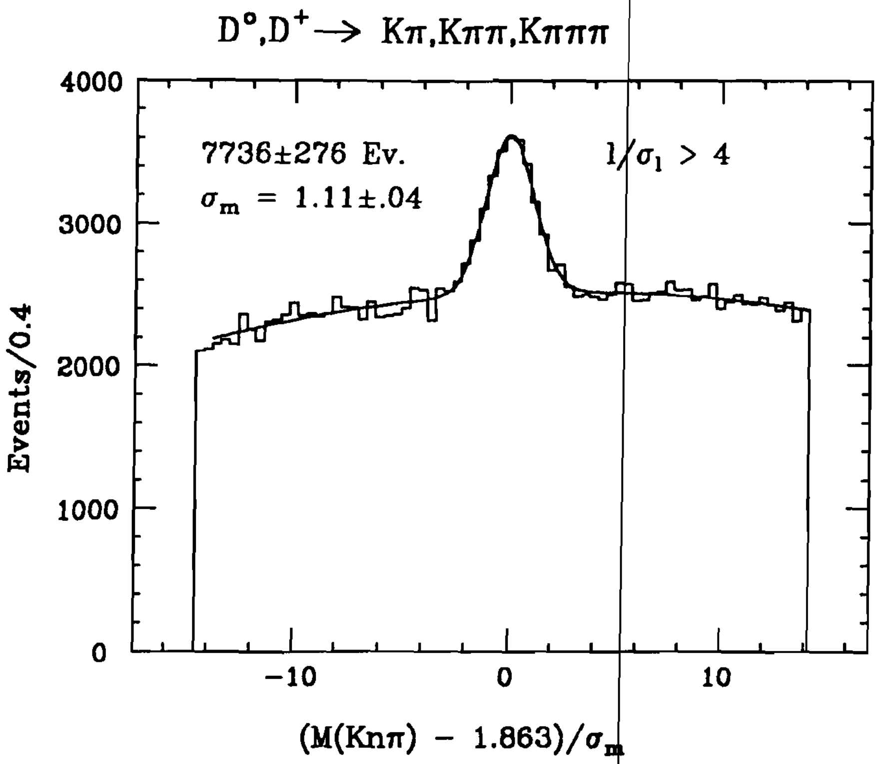

Figure 5-11 : Combined signal of $D^\circ \rightarrow K\pi$, $D^+ \rightarrow K\pi\pi$, and $D^\circ \rightarrow K\pi\pi\pi$ decays with $\ell/\sigma_\ell > 4$.

However, the mere measurement of the yield of double D events provides a powerful check of the Monte Carlo model used throughout this thesis. The Monte Carlo model assumes that charmed mesons are produced against a generic anticharm particle which materials 20% of the time as a baryon, 16 % of the time as a D_s^+ meson, and 64 % of the time as a $\bar{D}$ meson with a 3:1 $D^\star$ to D ratio (in accordance with the results of section 5.2). The ultimate predicted yield of double D events depends on the recoil $\bar{D}$ fraction, and on the D and $\bar{D}$ correlated momentum spectra since the acceptance is a strong function of charm particle momentum.

The event sample used in the search was composed of the decay modes $D^\circ \rightarrow K\pi$, $D^\circ \rightarrow K\pi\pi\pi$, and $D^+ \rightarrow K\pi\pi$. Events were combined using their normalized invariant mass, and are shown in Figure 5-11 for the specific case of $\ell/\sigma_\ell > 4$.

A small fraction of the D mesons shown will have occurred in double D events. For the purposes of this discussion a double D event is one where each charm quark hadronizes as a D meson and subsequently decays through one of the three decays listed.

The method of searching for double D events begins by developing a list of all D candidates in an event. Candidates are then selected from the list which have an invariant mass within $\pm 2.5\sigma$ of the nominal D mass. These are the *primary* D candidates. Each one of these is removed in turn from the general list and the invariant mass of the remaining *recoil* candidates histogrammed. These *recoil* candidates are prohibited from sharing any tracks in common with the *primary* candidate, and the $D\bar{D}$ pair must have oppositely charged kaons. *Primary* and *recoil* D vertices must be separated by at least 4 standard deviations from a primary vertex which is found independently for each. The resulting *recoil* D histogram is shown in Figure 5-12(a). The signal includes all D mesons from double D events as well as some background single D events. This single D background arises because the *primary* D candidates are selected with a simple cut about the nominal mass, and therefore include a non-D background.

In order to estimate the amount of background events, a second histogram is made where *primary* candidates are selected from sideband mass regions. These regions were between 5 and 10 σ on either side of the central peak. The histogram of the *recoil* candidates, shown in Figure 5-12(b), represents the background of false double D events. Each sideband is equal in width to the signal region, so the histogram yield is twice the background D meson count. An important point to note is that the signal/background ratio of these background D events is roughly equal to the original signal (Figure 5-11) while the double D signal has a much higher ratio. This is an expected consequence of true double D events since the double D requirement is a background reduction tool. The subtraction of the two histogram yields is most easily made with a weighted histogram, where events from signal and sideband regions are given appropriate weights. This histogram, shown in Figure 5-12(c), results in 106 ± 19 D mesons.

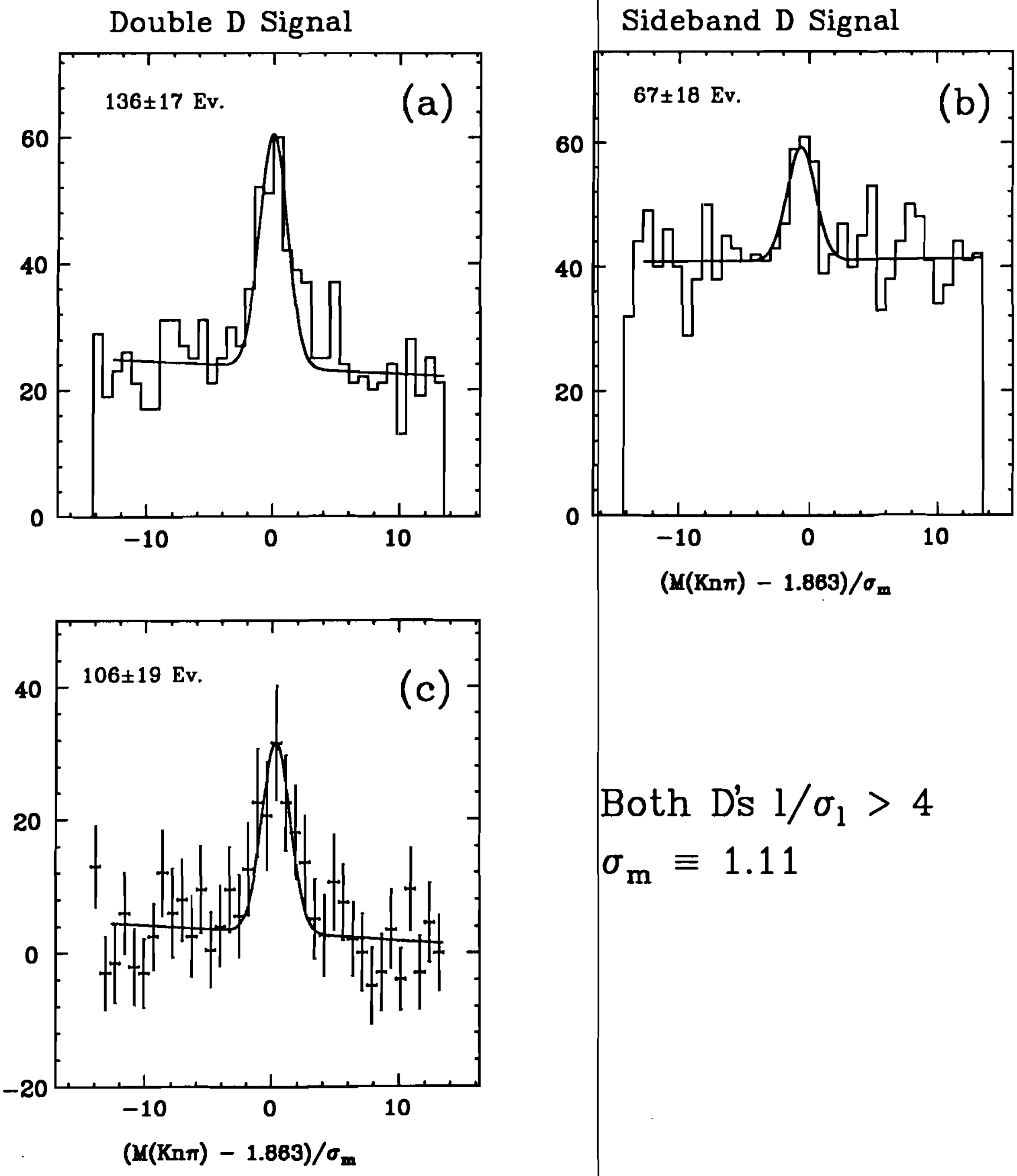

Both D's $1/\sigma_l > 4$

$\sigma_m \equiv 1.11$

Figure 5-12 : Double D signal plus background signal. The background subtracted signal is shown at the bottom.

This number can be compared to a prediction using the Monte Carlo based on the hadronization model presented in section 4.1.1 . Using the same analysis technique as in data, the Monte Carlo predicts that $1.6 \pm 0.2\%$ of the $\ell/\sigma_\ell > 4$ D mesons (< 1 % of the events) will be observed in pairs. The uncertainty in this number arises primarily from the *post hoc* kaon identification correction. This correction along with linking and absorption corrections are applied as multiplicative factors to obtain this percentage.

The implication is that 124 ± 15 double D mesons should be observed with these specific analysis cuts. The consistency between the measured and predicted level of double D events suggests that both the D and $\bar{\mathrm{D}}$ momentum spectrum and the assumed ratio of recoil anti-charmed species mirrors the data. Also, if *post hoc* corrections are neglected the expected yield would rise to about 280 events. This measurement therefore provides an important test of these corrections as well.

In conclusion, roughly 50 out of 7700 D events are found with a reconstructed charm anti-charm pair. While these are probably inadequate for stringent QCD tests, they do provide an important validation of the Monte Carlo model used for many of the measurements presented in this thesis.

Chapter 6

D° and D* Cross Sections

This chapter discusses the inclusive cross section for photoproduced D$^{\star\pm}$ and D° mesons. A description of a technique used to calculate these cross sections in E687 is presented first. Following is a presentation of results with a comparison to other recent data and theoretical predictions. The data sample used in these calculations is essentially the same as used in the discussion of the branching fraction in section 5.3, namely the Kπ and K$\pi\pi\pi$ decays of D° and D$^{\star\pm}$ mesons.

Measurements and theoretical predictions of cross sections are typically parameterized in terms of ω, the incident photon energy, and x_f, the Feynman x variable. The Feynman x of a D meson is related to its momentum and the incident photon energy by

$$x_f = \frac{E_D}{\omega} - \frac{m_D^2 + P_{\perp,D}^2}{2m_p\,E_D} \tag{6.1}$$

It is convenient to assume a cross section dependence which is factorized in terms of these two variables :

$$\begin{gathered}\frac{d\sigma}{dx_f}(x_f,\omega) = \sigma(\omega) f_x(x_f) \\ \text{where} \quad \int_{-1}^{1} f_x(x_f)dx = 1\end{gathered} \tag{6.2}$$

Thus it is possible to talk of a total cross section, averaged over x_f, which is a function of ω, and differential cross section, averaged over ω, which is a function of x_f.

The basic approach to calculating either cross section involves measurement of the D meson yield in bins of ω and x_f. These yield measurements can be converted to cross sections using a Monte Carlo simulation of charm production and detection in the experiment. Division of the measurement into fine bins is essential to remove production model dependencies. The cross section in bins of one variable (called the *dependent* variable) is found by averaging over bins of the other (*transverse*) variable. The resulting average cross section accurately predicts the true cross section to the extent that the efficiencies and resolutions are adequately simulated by the monte carlo.

Calculation of cross sections from data taken in E687 follows an approach similar to that just described. However added complications arise because incident photon energies are not well measured. Uncertainties in ω will affect the measurements of $\sigma(\omega)$, so the anticipated ω resolution is discussed first. In E687 the energy of the interacting photon (see Figure 2-2) is determined by the energy difference between the incident (E_{e^-}) and recoil (E_{resh}) electron minus any accompanying photons produced in the bremsstrahlung process which strike the forward calorimeter (E_{bgm}).

$$\omega = E_{e^-} - E_{resh} - E_{bgm}$$

The average E_{e^-} is about 350 GeV and has an RMS spread of ± 42 GeV. A broad distribution of electron momenta is transported in order to provide a large incident photon flux. The spread in E_{e^-} is the dominant contribution to the ω uncertainty in each event. Combining the beam spread with simulated RESH and BGM responses gives an overall average resolution $\sigma_\omega = 46$ GeV in Monte Carlo.

It is important to consider the effects of a large ω uncertainty on the cross section calculation. In such a discussion it is useful to refer to a measured value of the photon energy ω^* and its true energy ω. Events measured in a bin corresponding to ω^* reflect a convolution of cross sections over a wide ω range. The same is true of x_f^*, which is related to ω^* through Equation 6.1 . It will be shown that as a result the cross sections will have larger uncertainties than in a apparatus with little or no ω resolution problems.

6.1 The Cross Section Technique

Consider first the case were resolution in the dependent variables is not an issue, i.e. σ_ω and σ_{x_f} are small. Measurement of a cross section is made under the assumption of a linear relationship between the cross section and the number of events observed :

$$n(x_{f\alpha},\omega_\alpha) \;=\; \mathcal{L}(\omega_\alpha)\,\epsilon(x_{f\alpha},\omega_\alpha)\,C(x_{f\alpha},\omega_\alpha) \tag{6.3}$$

where each bin α represents a bin in ω or x_f. $C(x_{f\alpha},\omega_\alpha)$ is the average of the total or differential cross section in a bin, $\epsilon(x_{f\alpha},\omega_\alpha)$ is the detection efficiency, and $\mathcal{L}(\omega_\alpha)$ is the luminosity. The luminosity and acceptance factors are calculated through a monte carlo simulation but do not depend on a specific production model given sufficiently small binning. Equation 6.3 suggests a ratio method where in each bin the measured cross section is just the assumed monte carlo cross section times the ratio of measured to monte carlo event yields. Fine binning is necessary to reduce any production model dependencies introduced by the monte carlo. Bin widths are small enough when the cross section does not vary appreciably over the width of a $x_{f\alpha},\omega_\alpha$ bin.

Now consider the case of poor resolution. Events photoproduced at a value x_f from a photon of energy ω will be measured at x_f^* and ω^*. The severity of the mis-measurement in E687 is shown in Figure 6-1.

Here a monte carlo has been used to generate a set of events distributed in x_f. Each histogram in the figure is the x_f distribution of the subset of events which have x_f^* in a narrow bin. The effect of poor resolution is quite obvious. Even more striking is that in the highest x_f^* bins the majority of events originate from a much lower true x_f ! A cross section measurement based on the ratio of generated and measured event yields in each bin becomes ambiguous – which cross section should the ratio correct ? Events measured in one x_f^* bin are actually an accumulation of events from many true x_f bins, and are therefore a convolution of different cross sections C_α.

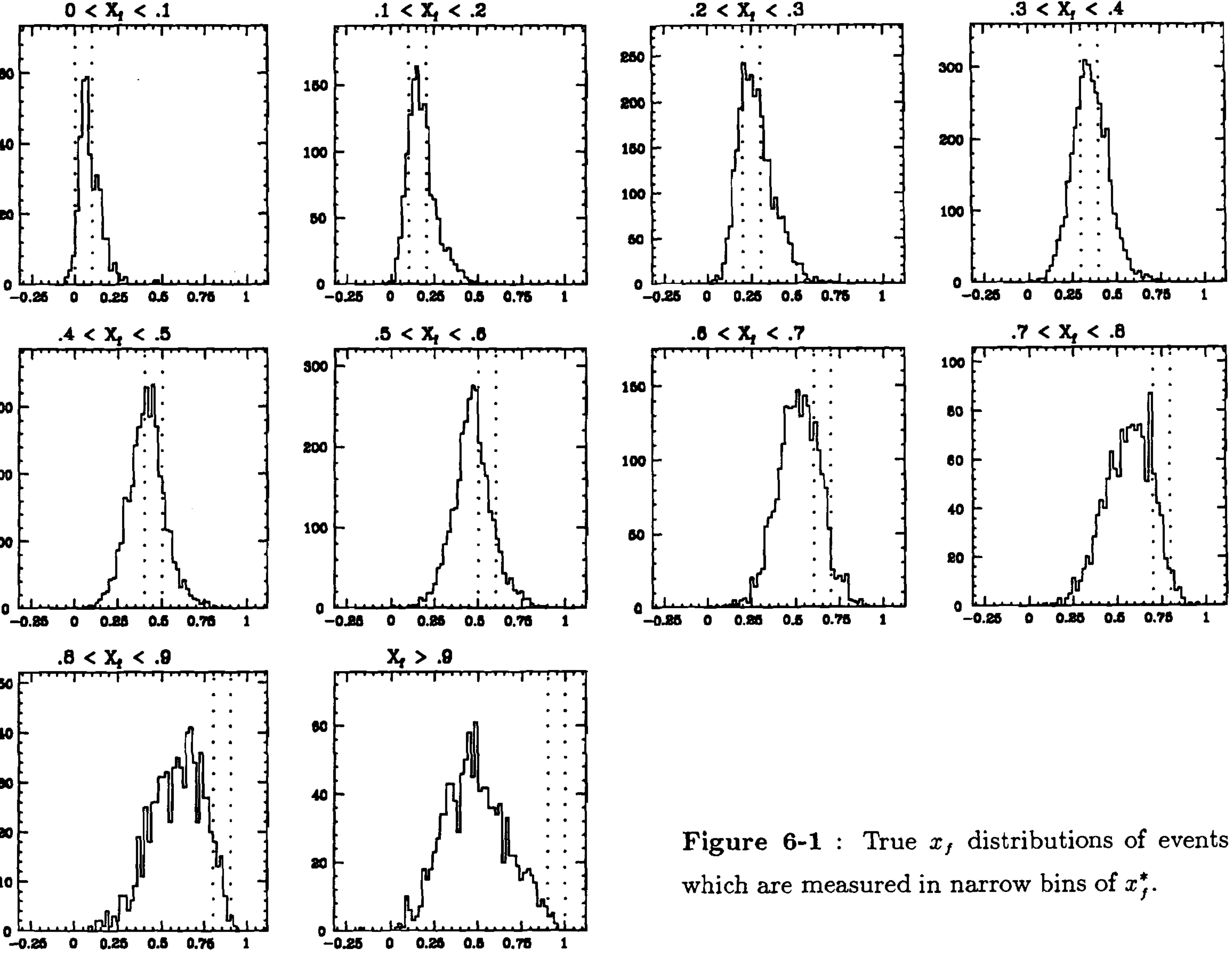

Figure 6-1 : True x_f distributions of events which are measured in narrow bins of x_f^*.

A more accurate description of the situation can be written in analogy with Equation 6.3 . The yield of events in a measurement bin i is written as a sum of the contributing cross sections C_α.

$$n_i = \sum_\alpha R_{i\alpha} C_\alpha \tag{6.4}$$

Here i represents bins of ω^* or x_f^* and α bins of ω or x_f. $R_{i\alpha}$ is proportional to the fraction of events in a bin α which are measured in a bin i, and includes the acceptance and luminosity factors of the previous equation as well as the resolution effects. The matrix $R_{i\alpha}$ is accumulated by a monte carlo which simulates the measurement process as illustrated in Figure 6-1. Equation 6.4 can then be solved for C_α. The solution involves a fit, provided the number of i data points exceeds the number of α parameters. The fit, described in Appendix C, has the general solution

$$C_\alpha = \sum_i \rho_{\alpha i}\, n_i \tag{6.5}$$

In the case of a just-constrained fit where the number of i bins equals the number of α bins, $\rho = \mathbf{R}^{-1}$.

Using Equation 6.5 then, an estimation of the cross section in data can be determined from the number of D* or D° events falling in a measurement bin i. Clearly the measurements C_α are not independent from each other as each datum measured in a given bin i contributes to the entire set of C_α. The de-convolution procedure reflects these correlations as well as increased uncertainties in each C_α measurement. In order to compute these uncertainties, the $\langle \delta C_\alpha \delta C_\beta \rangle$ correlation matrix is constructed. The error associated with a particular value C_α (see Appendix E) is :

$$\begin{aligned} \langle \delta C_\alpha \delta C_\beta \rangle &= \sum_i \rho_{\alpha i}\, \rho_{\beta i}\, n_i \\ \sigma^2(C_\alpha) \;=\; \langle \delta C_\alpha \delta C_\alpha \rangle &= \sum_i \rho_{\alpha i}^2\, n_i \qquad (6.6) \end{aligned}$$

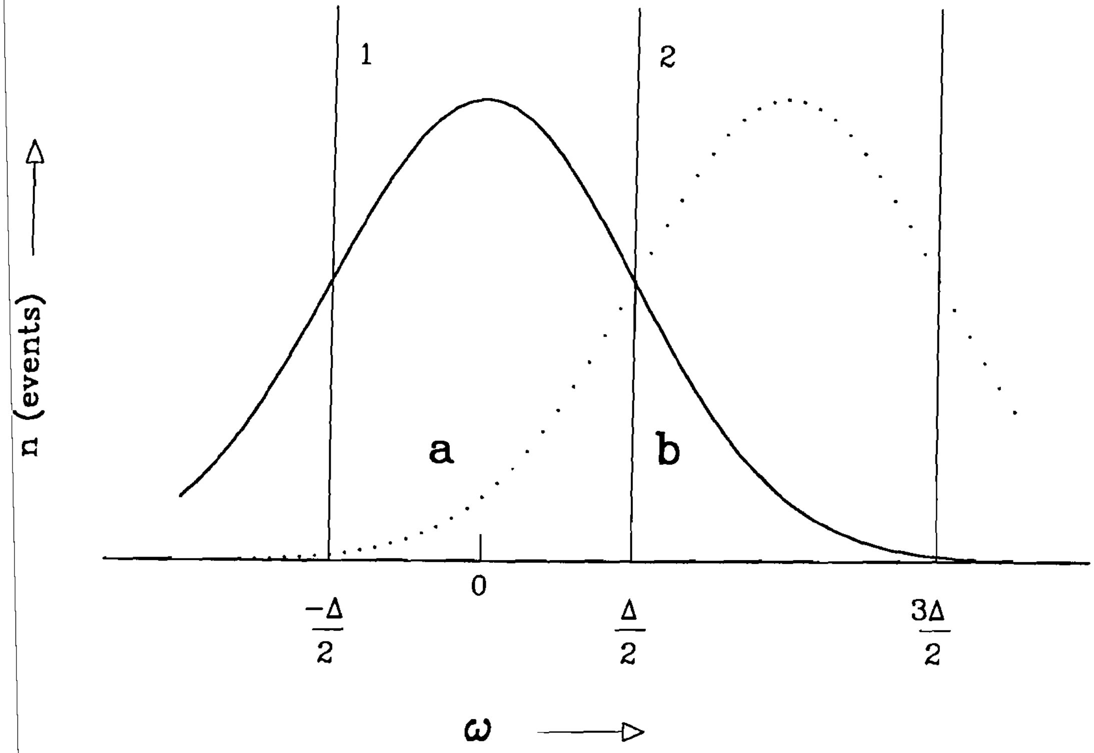

Figure 6-2 : Measured energy distribution for a simple cross section model.

assuming individual measurements n_i are uncorrelated. A simple demonstration can be used to illustrate some consequences of Equation 6.6 .

6.1.1 A Simple Example

Consider the case where the cross section is desired at two values of ω. The events associated with the first of those values will be measured in a distribution illustrated by Figure 6-2.

Each bin will have a width Δ_ω so that a portion a of the events will be measured in the correct bin (bin 1) and b will be measured in the adjacent bin (bin 2). If the events are gaussian distributed, then

$$a \propto \frac{1}{\sqrt{2\pi}} \int_{\frac{-\Delta}{2\sigma}}^{\frac{\Delta}{2\sigma}} d\mu \exp^{-\mu^2/2} \qquad b \propto \frac{1}{\sqrt{2\pi}} \int_{\frac{\Delta}{2\sigma}}^{\frac{3\Delta}{2\sigma}} d\mu \exp^{-\mu^2/2}$$

Furthermore, if a duplicate distribution is centered on bin 2 then the matrix **R** from Equation 6.4 can be expressed in terms of the relevant fractions. For simplification purposes, assume $n = n_1 = n_2$.

$$R_{ij} = \begin{pmatrix} a & b \\ b & a \end{pmatrix}$$

The cross section in each bin j is found by solving Equation 6.4

$$C_j = R^{-1}_{ij} n_i$$
$$R^{-1} = \frac{1}{a^2 - b^2} \begin{pmatrix} a & -b \\ -b & a \end{pmatrix}$$

The uncertainty in the cross section measurement ($C = C_1 = C_2$) becomes :

$$\frac{\sigma_C}{C} = \frac{\sqrt{a^2 + b^2}}{|a^2 - b^2|} \frac{1}{\sqrt{n}}$$

Thus the relative error on C exceeds the $1/\sqrt{n}$ counting statistics error by an augmentation factor of

$$F = \frac{\sqrt{a^2 + b^2}}{|a^2 - b^2|}$$

This function is plotted in Figure 6-3(a) as a function of the bin width Δ_ω.

A distinct rise in the errors above pure $1/\sqrt{n}$ statistical errors occurs when $\Delta_\omega \rightarrow \sigma_\omega$. The relative correlation between two cross sections is defined as

$$\mathrm{Corr}_{\alpha\beta} \equiv \frac{\langle \delta C_\alpha \delta C_\beta \rangle}{\sqrt{\langle \delta C_\alpha \delta C_\alpha \rangle \langle \delta C_\beta \delta C_\beta \rangle}} \tag{6.7}$$

which in this two bin model is

$$\mathrm{Corr}_{12} = \frac{-2ab}{a^2 + b^2}$$

The correlation, shown in Figure 6-3(b) as a function of Δ_ω, demonstrates a nearly 100 percent negative correlation between C_1 and C_2 at bin widths near the ω^* resolution. The negative correlation between adjacent bins reflects the fact that $C_1 + C_2$ is well measured while $C_1 - C_2$ is not.

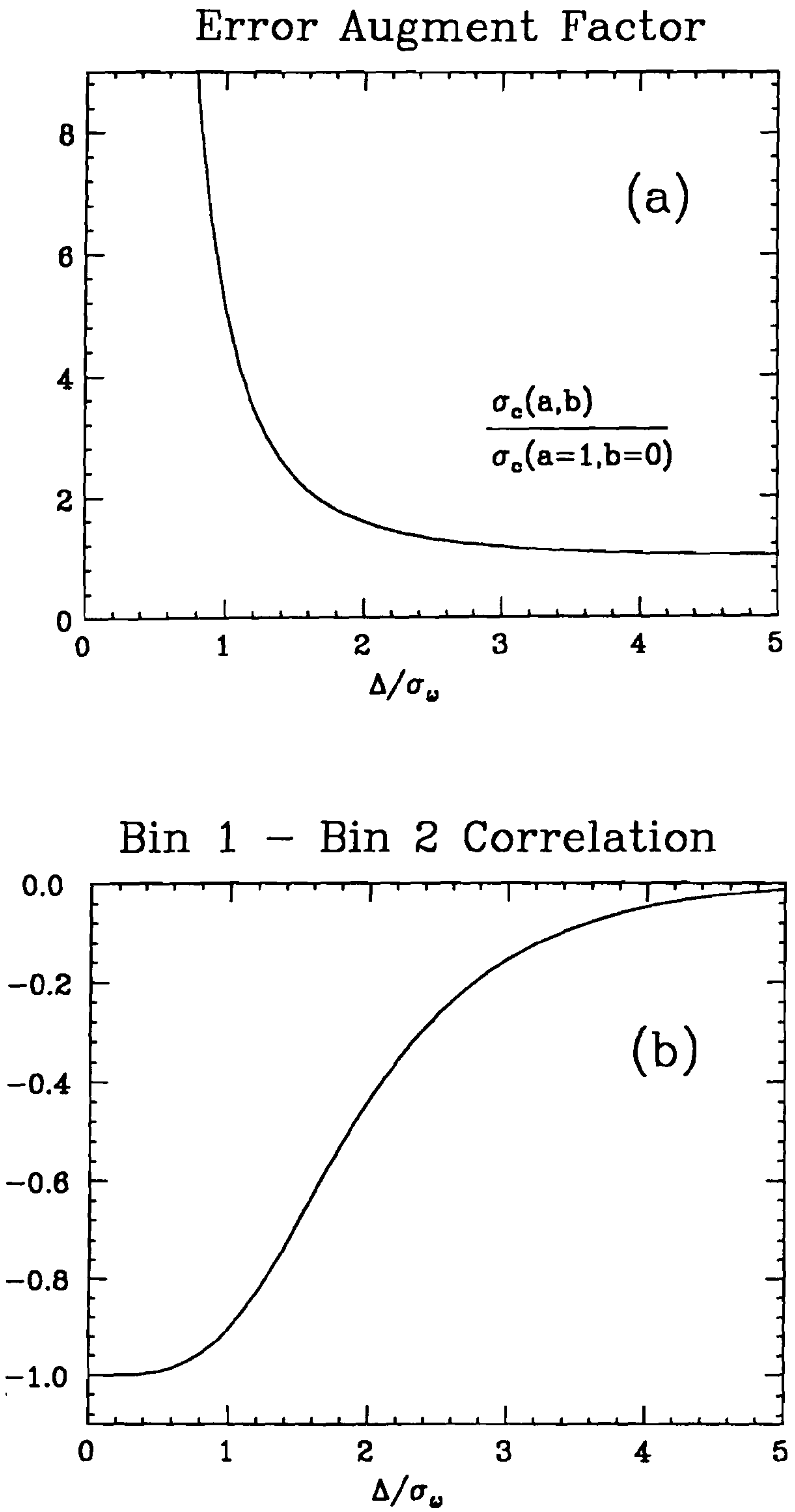

Figure 6-3 : Error augmentation and correlation factors versus bin width.

6.1.2 A Monte Carlo Study

The situation in the data is somewhat more complicated than in this simple case. A full Monte Carlo simulation of the experiment was used to study the anticipated errors and correlations as well as establish the degree of model independence. A large monte carlo event sample was used to generate the ρ matrix with and without resolution effects. A sample of 1000 of these monte carlo events was treated as data and the cross section calculated using Equation 6.5 . Figure 6-4(a) shows the simulated measurement of $d\sigma/dx_f$ for the case where $\omega^* = \omega$ and $x_f^* = x_f$.

The generated distribution is shown as a dashed line and the error bars on the measurements reflect $1/\sqrt{n_i}$ statistical errors. Figure 6-4(b) shows the same distribution where all energy resolution effects are included. The measurements, which in the previous figure reflected the underlying parent distribution quite well, no longer show a clear distribution. Not only do the error bars increase dramatically, but measurements exhibit the adjacent bin anti-correlation effect discussed above. The simple model, summarized in Figure 6-3, predicts that increasing the bin width leads to decreases in both errors and correlations. Figure 6-4(c) demonstrates that use of only 4 bins to span the x_f range significantly reduces the errors. The parent distribution is once again apparent from the measured points. It should be noted, though, that the statistical errors are still much larger than pure $1/\sqrt{n_i}$ errors.

The formalism of Equation 6.5 addresses issues of model dependence as well as poor resolution. Model dependencies are effectively removed if events are binned simultaneously in x_f^* and ω^*. Each x_f^*, ω^* bin can be labeled by the index i which then ranges from 1 to $N_{x_f^*}^{bin} \cdot N_{\omega^*}^{bin}$. If the same is done for the α bins, the entire measurement de-convolution procedure can still be characterized by a 2-dimensional ρ matrix. The model independence of the matrix de-convolution method is demonstrated by a monte carlo simulation. Events are generated with an x_f distribution shown as the dotted line in Figure 6-5. These events are used

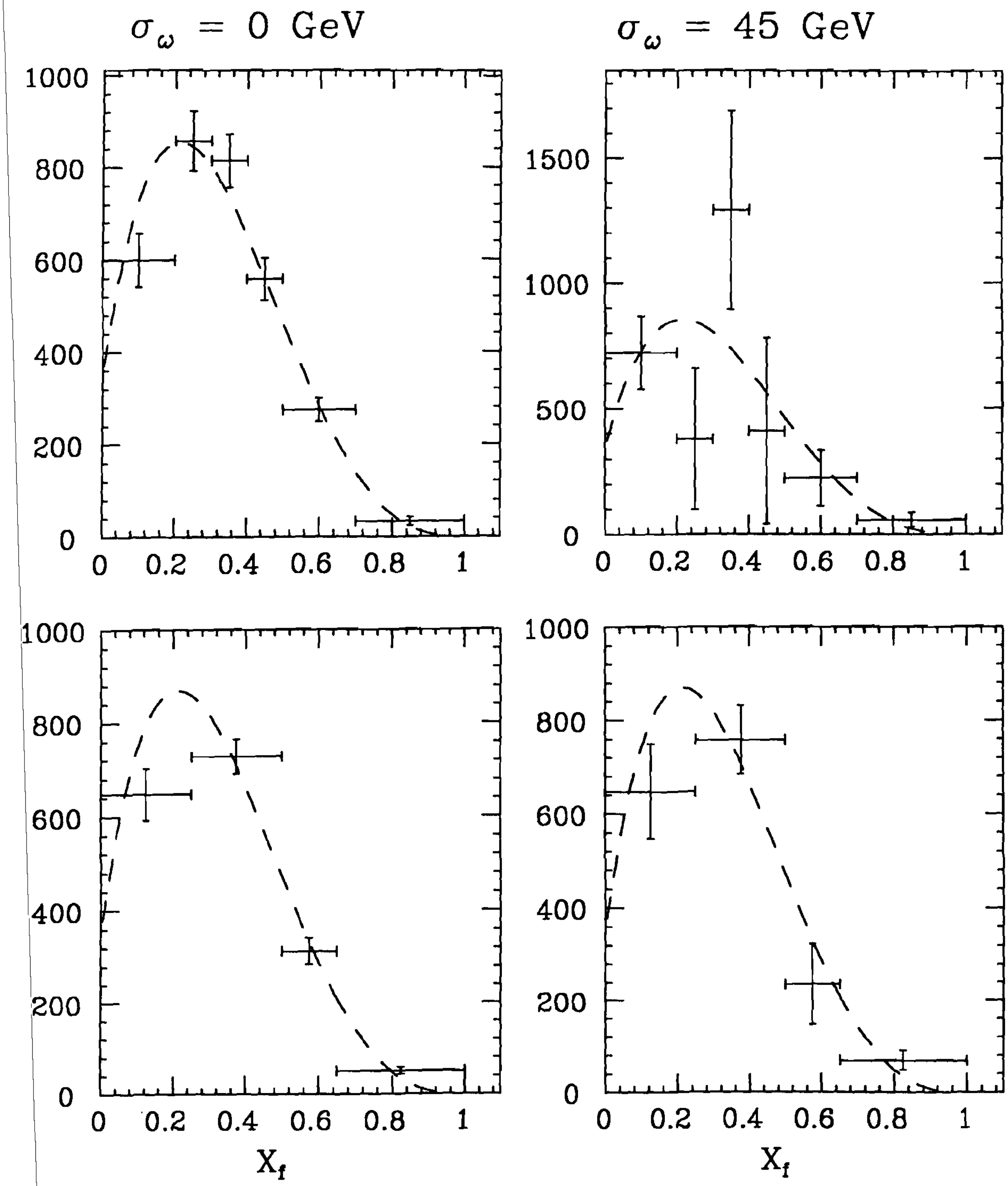

Figure 6-4 : Anticipated x_f^* measurement errors (Monte Carlo).

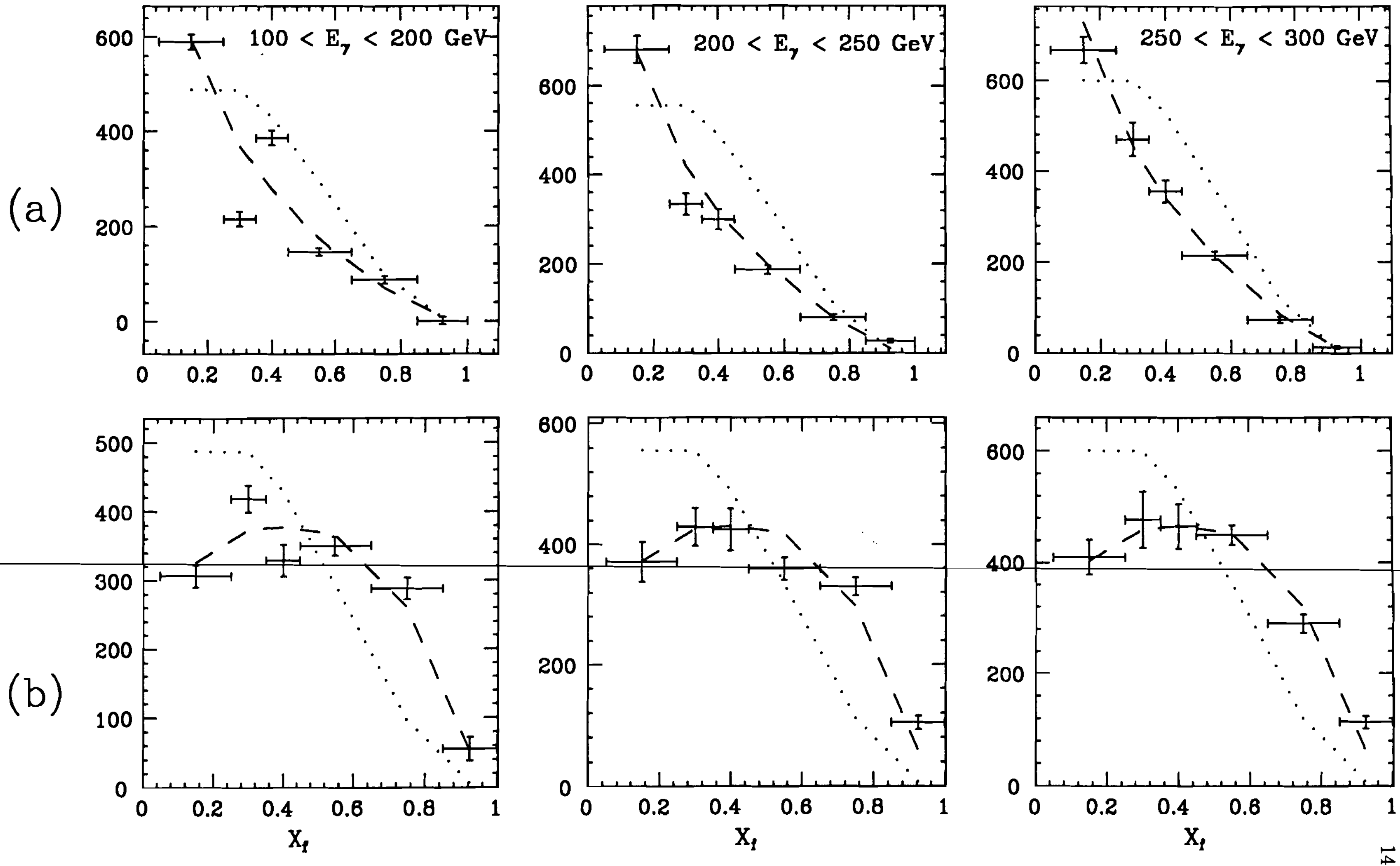

Figure 6-5 : Demostration of model independent measurement of cross section versus x_f

to compute a ρ matrix with 6 bins in x_f and 3 bins in ω. A second high statistics monte carlo is generated with a much softer x_f distribution, shown as the dashed line in Figure 6-5(a), which serves as the "data". The results obtained by the cross section de-convolution, shown in Figure 6-5(a) with error bars, follow the dashed "data" distribution quite well. Similar results are obtained using a hard x_f distribution for "data" and are shown in Figure 6-5(b).

6.2 The Monte Carlo Simulation

The monte carlo simulation used for calculating the ρ matrix does not differ significantly from that discussed in section 4.1 . Since Kπ and K$\pi\pi\pi$ signals are combined in data, a separate monte carlo sample was generated in each decay mode. Maintaining the ratio of generated events at the known branching ratio of the two decay modes, it was possible to combine the two data sets. The relevant monte carlo numbers are given in Table 6-1 below. All simulations were of $D^{\star\pm}$ decays. Calculations of the D° inclusive cross section use the same monte carlo events. This should be fairly realistic as most D° mesons come from $D^\star$ decays (see section 5.2). The cross section parameterization used in the monte carlo is discussed in section 4.1.1 .

Table 6-1 : Monte Carlo Events

	BGM counts	generated	reconstructed	after cuts	*post hoc* corrections
Kπ	1.21×10^6	214,600	36,450	11,488	7959
K$\pi\pi\pi$	2.15×10^6	450,000	59,900	19,844	11,040

The analysis cuts employed were the same as those used with the data. In addition to the analysis cuts, *post hoc* corrections were applied to the Monte Carlo event sample. These corrections, described in section 4.2, reject additional Monte Carlo events to account for absorption and to better match Čerenkov identification and linking efficiencies observed in data. The number of events remaining in each decay mode are shown in the last column of Table 6-1. These

19,000 events are then used as inputs to generate ρ matrices. Different matrices are generated for each of the two D* and D° decay modes, even though the data are to be combined later. The simulation of the beam spread and detector resolutions used in the monte carlo are discussed in section 4.1.2 . Measurement of ω then mimics the procedure used in data. The ω^* distributions in monte carlo and data for D* events are compared in Figures 6-6(a) & (b).

6.2.1 Constructing the ρ Matrix

The ρ matrix relates the two generated quantities, ω and x_f, to the two measured quantities ω^* and x_f^*. The ρ matrix construction involves incrementing the appropriate element of $R_{i\alpha}$ for each monte carlo event and dividing by the assumed production cross section C_α. Each monte carlo event carries information about ω^* and x_f^* as well as the generated quantities ω and x_f, thus specifying the i and α bin in a given event. By counting only monte carlo D mesons which pass the final analysis cuts, the geometrical acceptance and various efficiencies as a function of ω and x_f are automatically folded into the cross section determination. The luminosity is implicitly included as well apart from a scaling factor (see Appendix D.2).

Before constructing the matrices, the appropriate binning must be chosen. The α bins must be chosen small enough so that both monte carlo and data cross sections can be assumed constant in the interval. However if the cross sections were reported in each of these small bins their relative correlations and error augmentation factors would be enormous. Instead it is useful to compute a partial cross section in each bin α yet report on the average over several bins, thereby reducing the correlations. The average partial cross section in a bin α is defined as

$$\frac{\overline{d\sigma}}{dx_f}(\omega_\alpha, x_{f\alpha}) = \frac{1}{\Delta\omega_\alpha}\int_{\omega_1^\alpha}^{\omega_2^\alpha} \sigma(\omega)d\omega \quad \frac{1}{\Delta x_{f\alpha}}\int_{x_1^\alpha}^{x_2^\alpha} f_x(x_f)dx_f \tag{6.8}$$

which follows from Equation 6.2 . If the quantity C_α is defined as the partial

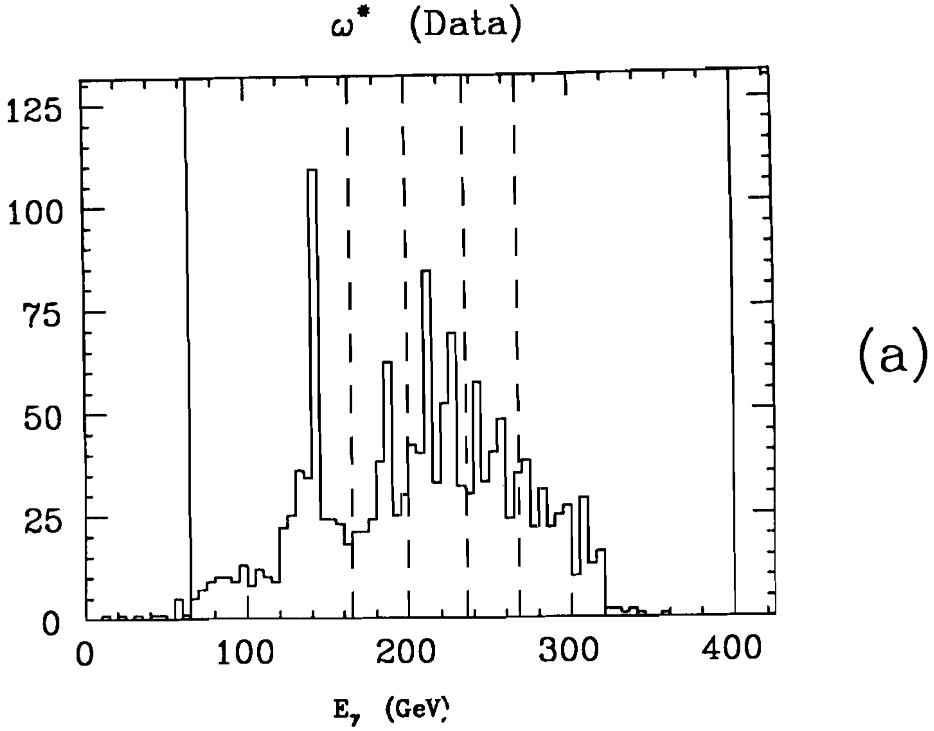

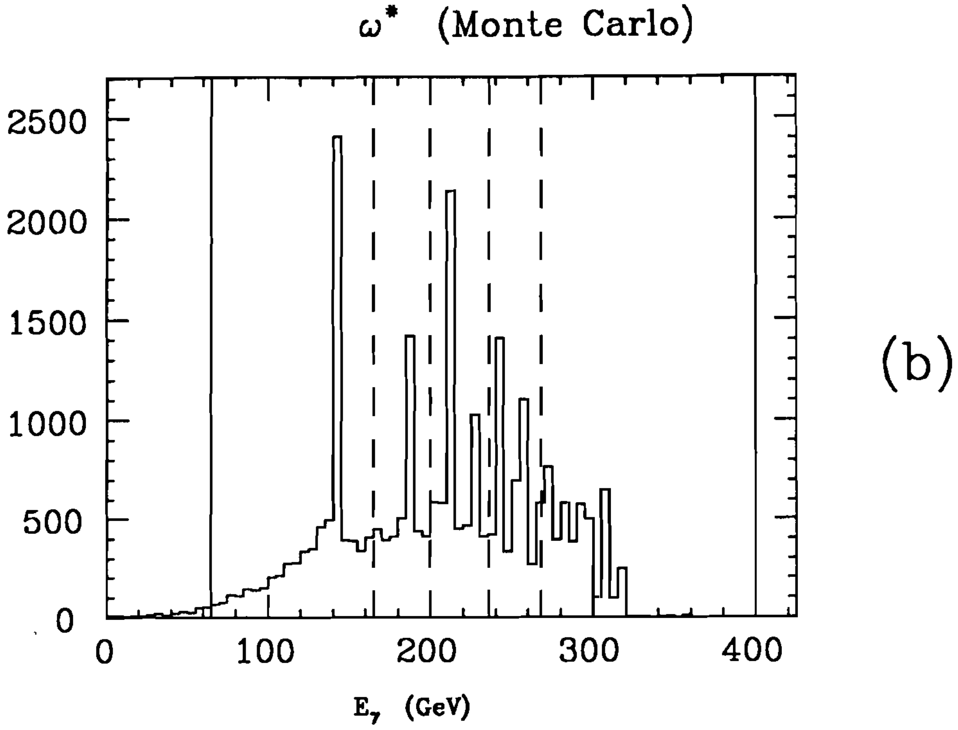

Figure 6-6 : Measured photon energies of D* events in data and Monte Carlo cross section :

$$C_\alpha \equiv \Delta\bar{\sigma}_\alpha = \Delta\omega_\alpha \Delta x_{f\alpha} \, \overline{\frac{d\sigma}{dx_f}}(\omega_\alpha, x_{f\alpha})$$

then these partial cross sections can be summed and the average cross section in a few large bins computed, i.e.

$$\bar{\sigma} = \frac{1}{\Delta\omega \Delta x_f} \sum_\alpha C_\alpha \tag{6.9}$$

The term $\bar{\sigma}$ is the average differential cross section in a large bin of the size $\Delta\omega \cdot \Delta x_f$. In this way bins in the transverse variable (x_f or ω) are concatenated.

In fact binning in α could be extremely fine were it not for limited monte carlo statistics – i.e. there must be at least one entry in each element of the **R** matrix. Another complication is the finite granularity of the RESH counter. Figures 6-6(a) & (b) display the observed energy distribution as computed in Equation 3-6 in both monte carlo and data. Both exhibit pronounced spikes at several energy intervals. These spikes, from the quantized RESH measurement, tend to exacerbate the problem of de-convoluting the energy measurement. Hence it is necessary to carefully place the bins of ω^* so that these spikes are completely contained within a bin. These bin boundaries are shown in the figures as dashed lines. The minimum width of ω^* bins limits the number of i bins, and therefore the number of α bins. Finally, the cross section is not reported in regions where the experiment has little or no acceptance.

In light of these considerations, the choice of binning used to generate ρ matrices is given in Table 6-2. Table 6-2(a) lists the bin boundaries of i bins. These serve as the binning of events measured in data as well. Tables 6-2(b) & (c) are the α bins for two different ρ matrices. The binning in Table 6-2(b) is used to determine cross sections in bins of x_f, and Table 6-2(c) is for bins of ω. In both cases bins of the *transverse* variable are summed over.

Table 6-2(a) : i bins (30 bins)

x_f^*	0.0	0.2	0.3	0.4	0.5	0.7	1.0

ω^*	65	165	200	236	268	400

Table 6-2(b) : α bins (12 bins) – Dependent variable x_f

x_f	0.0	0.25	0.5	0.65	1.0

ω	65	165	236	400

Table 6-2(c) : α bins (18 bins) – Dependent variable ω

ω	65	165	250	400

x_f	0.0	0.2	0.3	0.4	0.5	0.7	1.0

6.3 Data Analysis

The data sample used in the cross section determination is shown in the normalized invariant mass histograms of Figures 6-7(a) & (b). These events represent most of the events reported in these decay channels in section 3.11 . Additional vertex detachment criteria, $\ell/\sigma_\ell > 6$ and $\ell/\sigma_\ell > 12$ for D^* and D° decays respectively, have been imposed to further reduce the background. The energy ω^* of each event was measured according to the description in section 3.7 . Not all events were taken with the RESH requirement in the trigger, and some data lacked BGM information. These are both necessary to properly measure the cross section; the result being a rejection of 20 percent of the events.

6.3.1 Application of the ρ Matrix

Once ω^* of the event is known, x_f^* is calculated using Equation 6.1 and the appropriate bin i is determined from Table 6-2(a). Events not falling in any bin are discarded. The background under the signal introduces a complication which is addressed with a weighting technique. This method involves constructing a weighted histogram of D° or $D^{*\pm} \rightarrow K\pi + K\pi\pi\pi$ normalized mass distributions for each bin of the cross section. The histogram weight is the value of $\rho_{\alpha i}$ for the i bin of the datum and the α bin of interest. A different matrix is used depending on whether the event is Kπ or K$\pi\pi\pi$. If there were no background, the sum of weights would be $\rho_{\alpha i} n_i$. In the weighted histograms the signal will exist in a peak over a smooth background distribution; the area of this peak is the partial cross section C_α. Each histogram could be fit to find C_α, with the error in C_α given by the error in the fit, but α bins are concatenated first. The concatenation, given by Equation 6.9, can be generalized through the use of a summing matrix $S_{\beta\alpha}$ such that

$$\bar{\sigma}_\beta = \frac{1}{\Delta\omega_\beta \Delta x_{f\beta}} S_{\beta\alpha} C_\alpha$$

where $N^{bin}_\alpha > N^{bin}_\beta$ and $S_{\beta\alpha}$ is either 0 or 1. A sum over α is implied in the equation. In this analysis only bins in the transverse variable are summed, so N^{bin}_β is just the number of bins in the dependent variable. Consider, for example, the specific use of the data for determining the cross section in bins of ω, where the binning is given in Tables 6-2(a) & (c). Each event will have 18 independent weights associated with it. These weights are added together in groups of 6 (the number of bins in the transverse variable, x_f), and the results entered into 3 separate histograms. The fit of each histogram yields a partial cross section in an ω bin averaged over x_f.

6.3.2 Results

Fits to the weighted mass histograms are shown in Figures 6-8 through 6-10. The signal contribution was a unit gaussian with an unconstrained mean lying over a polynomial background. Figure 6-8 shows the weighted histograms and the fits for the 3 bins in ω. Each histogram contains contributions from $0 < x_f < 1$. Figure 6-9 is similar, but contributions are restricted to $0.2 < x_f < 1$. These cross sections will be reported in addition to those in Figure 6-8 to avoid the poor acceptance region $0 < x_f < 0.2$, the inclusion of which causes dramatic increases in errors. The restricted range is also less likely to have systematic problems associated with poor acceptance. Figure 6-10 shows histograms and

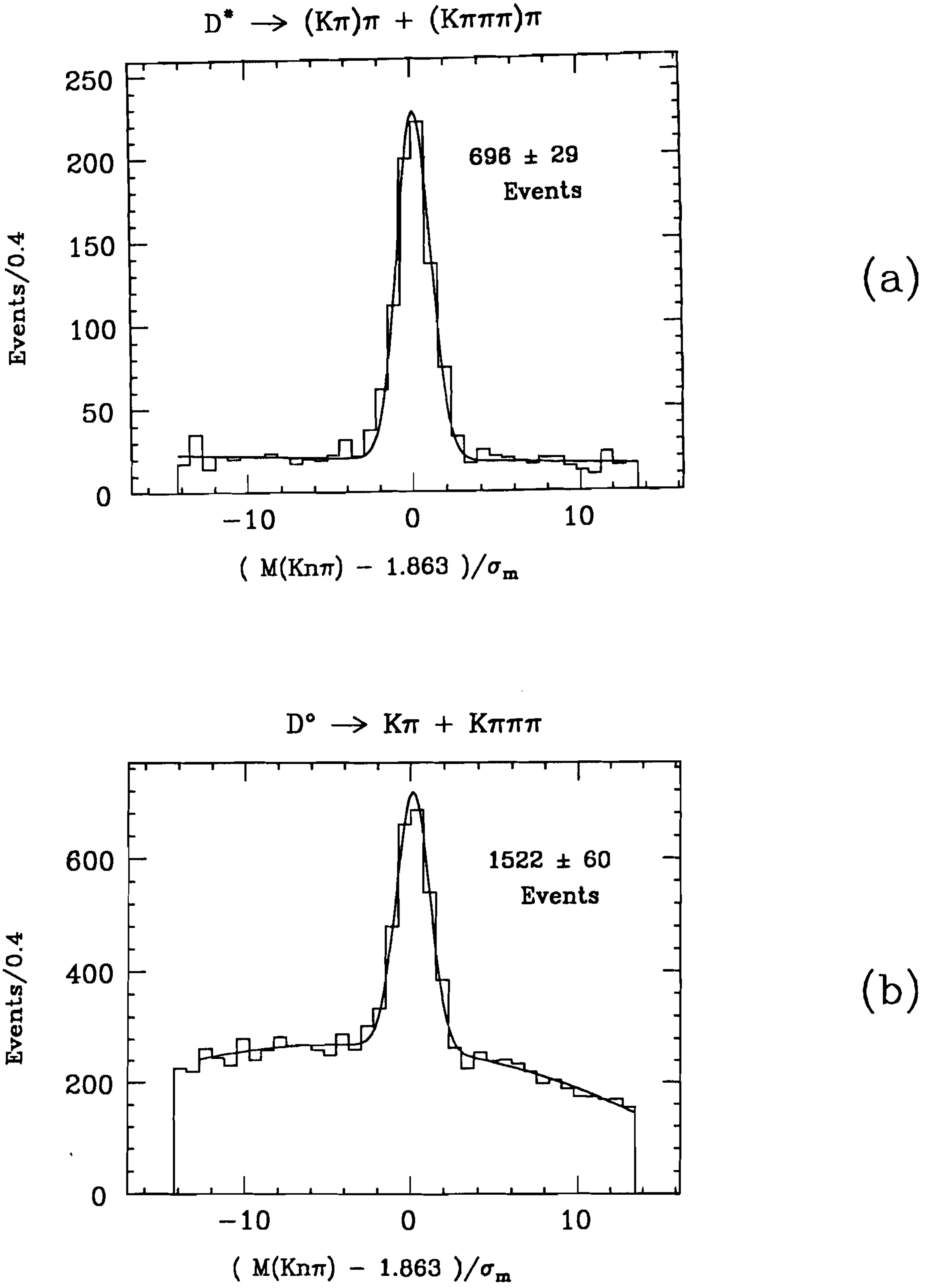

Figure 6-7 : Signals used in the cross section calculation.

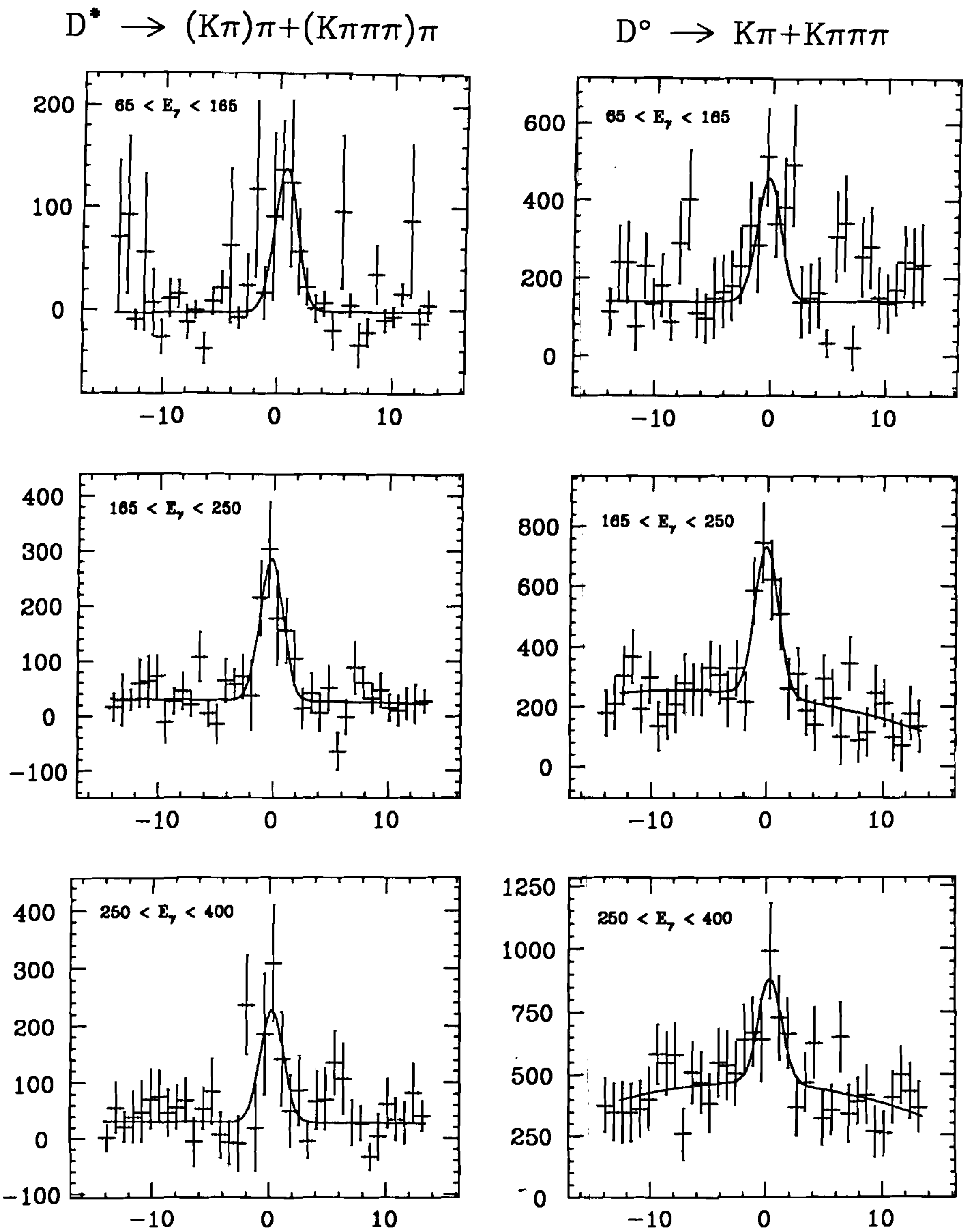

Figure 6-8 : Weighted histograms used to measure cross section versus ω ($0 < x_f < 1$).

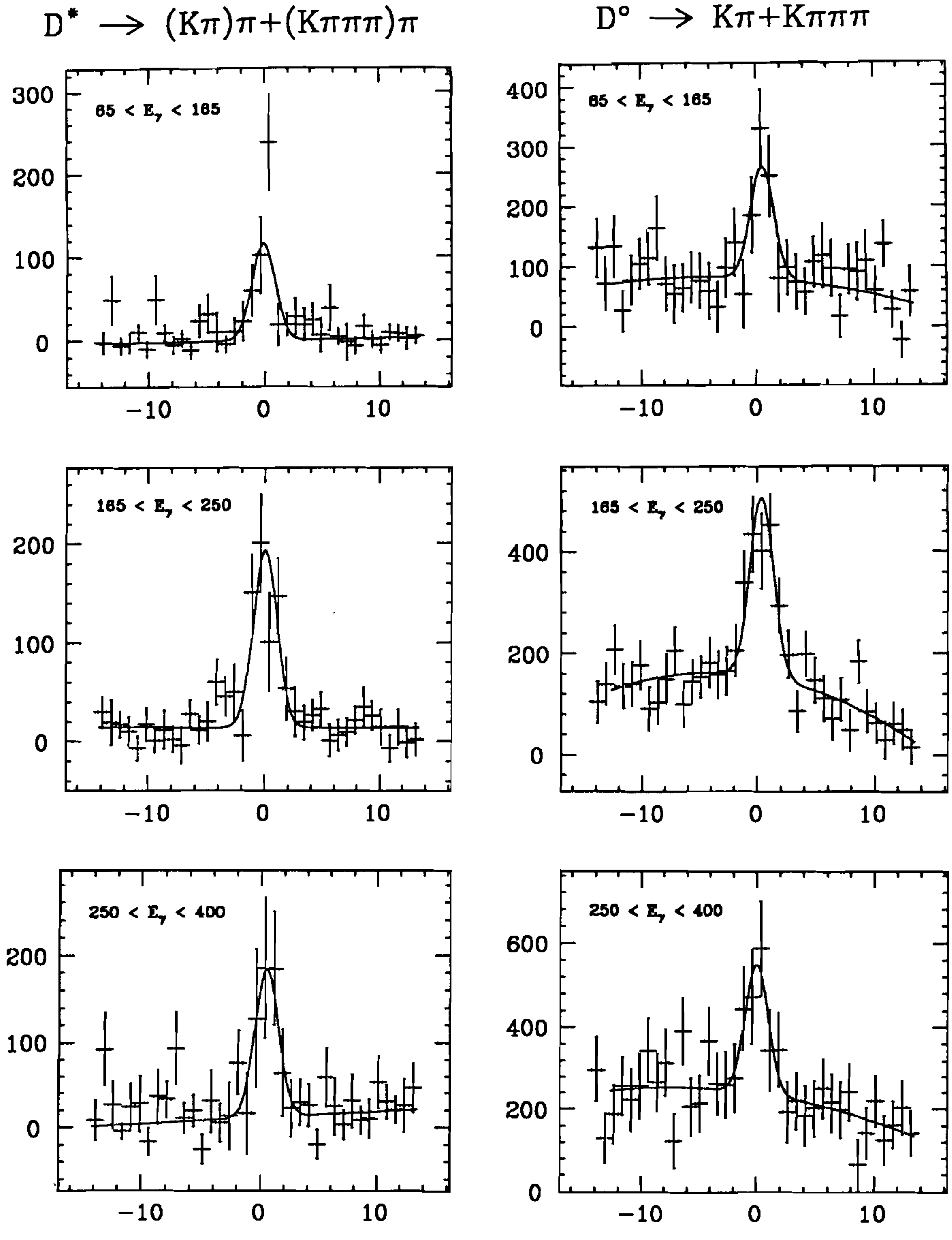

Figure 6-9 : Weighted histograms used to measure cross section versus ω ($0.2 < x_f < 1$).

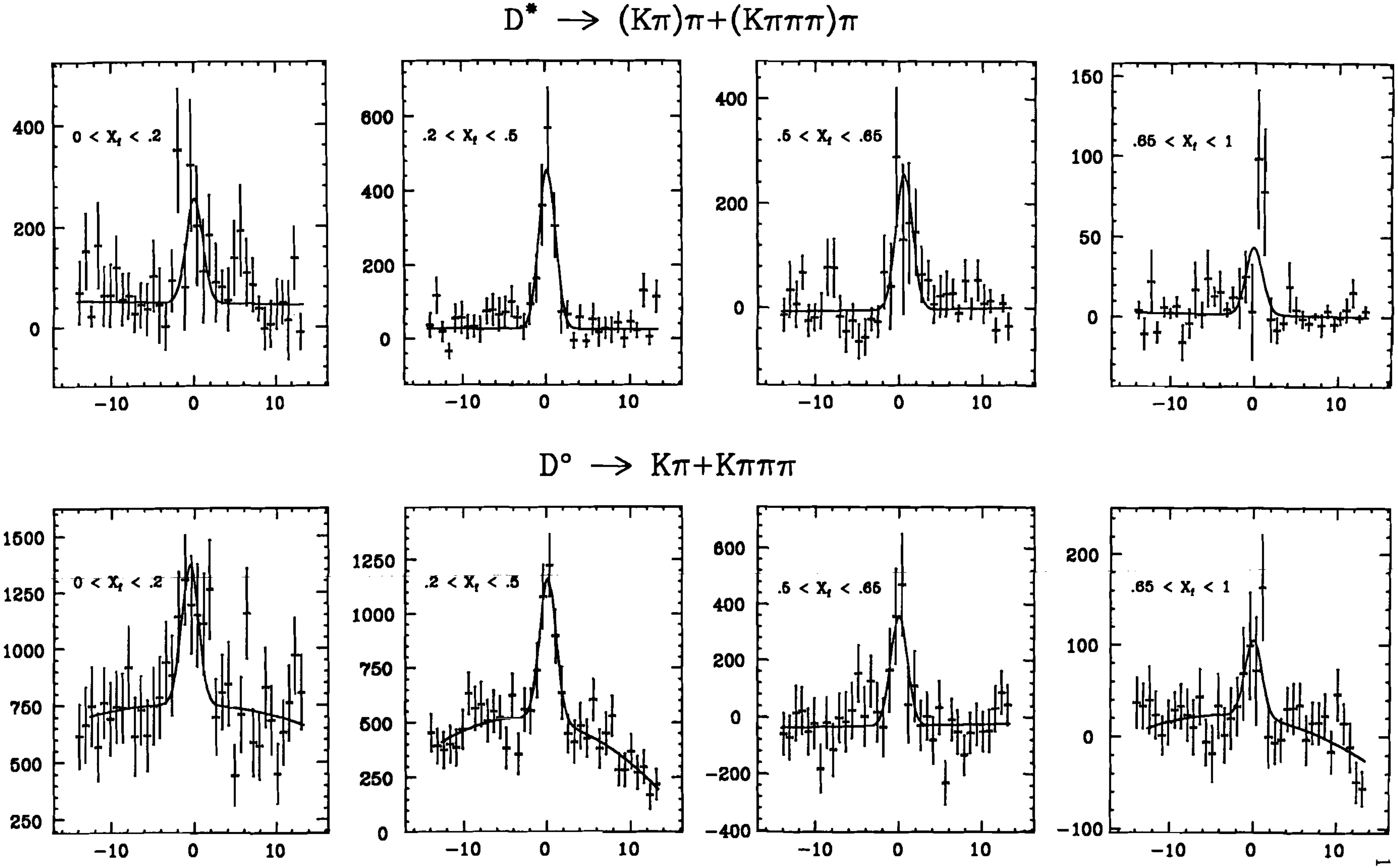

Figure 6-10 : Weighted histograms used to measure cross section versus x_f

fits for the four bins of x_f where all ω are included. The results of all fits are listed in Tables 6-3(a) & (b), where each row refers to a bin in the dependent variable.

The reader should refer to Tables 6-2(b) & (c) for the bin boundaries. The partial cross sections (times branching ratio) listed are for the sum of D and $\bar{D}$ mesons decaying specifically into Kπ and K$\pi\pi\pi$ final states, and are reported in μb per beryllium nucleus. Columns labeled with an asterisk indicate that all ***post hoc*** Monte Carlo corrections have been neglected except absorption. The results for all D* cross sections listed have been reduced by the 5 % over-counting factor discussed in section 3.11.1 .

6.3.3 Statistical Uncertainties

The errors in listed in Tables 6-3(a) & (b) come directly from the fits to the weighted histograms. This follows from the discussion of correlation errors, where an expression was given for the variance of de-convoluted cross sections (Equation 6.6) :

$$\sigma(C_\alpha) = \sqrt{\sum_i n_i \rho_{\alpha i}^2}$$

This states that the variance of a measurement in bin α is the sum in quadrature of all weights contributing to that bin. Indeed this is the standard way of computing the error associated with a sum of weights in a weighted histogram.

$$\sigma\left(\sum W\right) = \sqrt{\sum W^2}$$

An important test that the errors are understood involves an analysis of a comparable number (~1000) of monte carlo events and comparison of the subsequent fit errors to those of the data. Since statistical contributions will be the same, this will test the simulation of resolution effects which give rise to the correlation between points. Figure 6-4(c) illustrates this test in monte carlo for $d\sigma/dx_f$. Table 6-4 compares the fractional fit errors $\sigma(C_\alpha)/C_\alpha$ of Monte Carlo

Table 6-3(a) : Cross section $\sigma(\omega) \cdot \mathrm{Br}^{\dagger}$ vs. ω in μb/nucleus

	D*			D°		
	$x_f > 0$	$x_f > .2$	$x_f > .2$ ‡	$x_f > 0$	$x_f > .2$	$x_f > .2$ ‡
ω_1	.235 ± .059	.195 ± .042	.139 ± .029	1.117± .257	.653 ± .163	.436 ± .104
ω_2	.432 ± .086	.300 ± .049	.210 ± .035	1.736± .319	1.236 ± .173	.877 ± .125
ω_3	.331 ± .104	.288 ± .077	.227 ± .053	1.465± .436	1.092 ± .271	.801 ± .196

Table 6-3(b) : Differential Cross Section

$(d\sigma/dx_f) \cdot \mathrm{Br}^{\dagger}$ vs. x_f in μb/nucleus

	D*	D* ‡	D°	D° ‡
$x_{f,1}$	.345 ± .123	.200 ± .084	2.167 ± .546	1.346 ± .366
$x_{f,2}$	.720 ± .103	.494 ± .071	2.302 ± .351	1.641 ± .264
$x_{f,3}$	.433 ± .131	.359 ± .093	1.365 ± .379	1.017 ± .295
$x_{f,4}$	.071 ± .033	.045 ± .022	0.295 ± .137	0.295 ± .137

† Includes particle and anti-particle contributions

‡ Absorption correction only

events to those of D* events in data. No *post hoc* corrections have been applied to the monte carlo. Agreement is rather good considering the data includes uncertainties due to the background which are absent in the monte carlo.

Table 6-4 : Fractional Fit Errors

ω

	Data	MC
ω_1	.205	.189
ω_2	.173	.208
ω_3	.244	.126

x_f

	Data	MC
$x_{f,1}$	.407	.170
$x_{f,2}$	.143	.111
$x_{f,3}$	.273	.246
$x_{f,4}$	.485	.591

Another source of statistical errors involve Monte Carlo counting statistics. These are discussed in Appendix E. The conclusion is reached that statistical errors obtained from the fit results ($\sigma_o(C_\alpha)$) should be augmented by a factor

$$\sigma(C_\alpha) = \sigma_o(C_\alpha)\sqrt{1+\frac{N_{data}}{N_{mc}}}$$

where N_{data}/N_{mc} is the ratio of the total event samples. This additional uncertainty has not been included in Tables 6-3 or 6-4 but is negligible in the case of D* cross sections and roughly a 7 percent correction to the errors of the D° cross sections.

6.3.4 Systematic Uncertainties

Systematic errors in the cross section measurements are the contributions to uncertainties beyond statistical fluctuations. They will include errors due to the Monte Carlo production model as well as the simulation of the apparatus. Errors from production model dependencies should be rather small because of fine binning and the use of an empirical model. Therefore the lack of a complete Monte Carlo simulation of the experimental conditions is the predominant source of systematic error. Estimation of systematic uncertainties is always difficult, because a quantitative understanding of a systematic problem usually means that it can be accounted for. This is precisely the origin of the ***post hoc*** corrections discussed in section 4.2 .

Studies have been performed to look for systematic problems. The technique used in these studies is to calculate the same quantity with independent data sets. Differences observed in the results are likely to be systematic in origin. One consistency check involves the ratio of $D^\star$ to D° inclusive cross sections. These in principle should agree with the predicted ratio from simple spin counting, the ratio measured in section 5.2, and previous experiments. The values in each ω bin in Table 6-3(a) are in the correct ratio to within statistical uncertainties.

Another study of systematics involves measurement of total D° and $D^\star$ cross sections using the $K\pi$ and $K\pi\pi\pi$ decay modes as independent data sets. In the foregoing analysis their contributions were summed and a cross section reported for the decay into either of the two decay modes. When used separately to compute the total D° and $D^\star$ cross sections, the extent to which the $K\pi$ and $K\pi\pi\pi$ numbers disagree in either case will set a minimum level of systematic uncertainty of the measurements listed in Table 6-3. The cross section for each decay mode was divided by the branching fraction, 3.77 % for $D^\circ \rightarrow K\pi$ and 7.90 % for $D^\circ \rightarrow K\pi\pi\pi$, to obtain the total cross sections shown in Figures 6-11(a)-(d) and listed in Tables 6-5(a) & (b).

$D^\star$ cross sections are obtained by further dividing by the branching fraction for $D^{\star\pm} \rightarrow D^\circ\pi^\pm$ (49 %). Cross sections in bins of ω are for $x_f > 0.2$. Both sets of numbers have relevant branching fraction errors added in quadrature with the original fit errors.

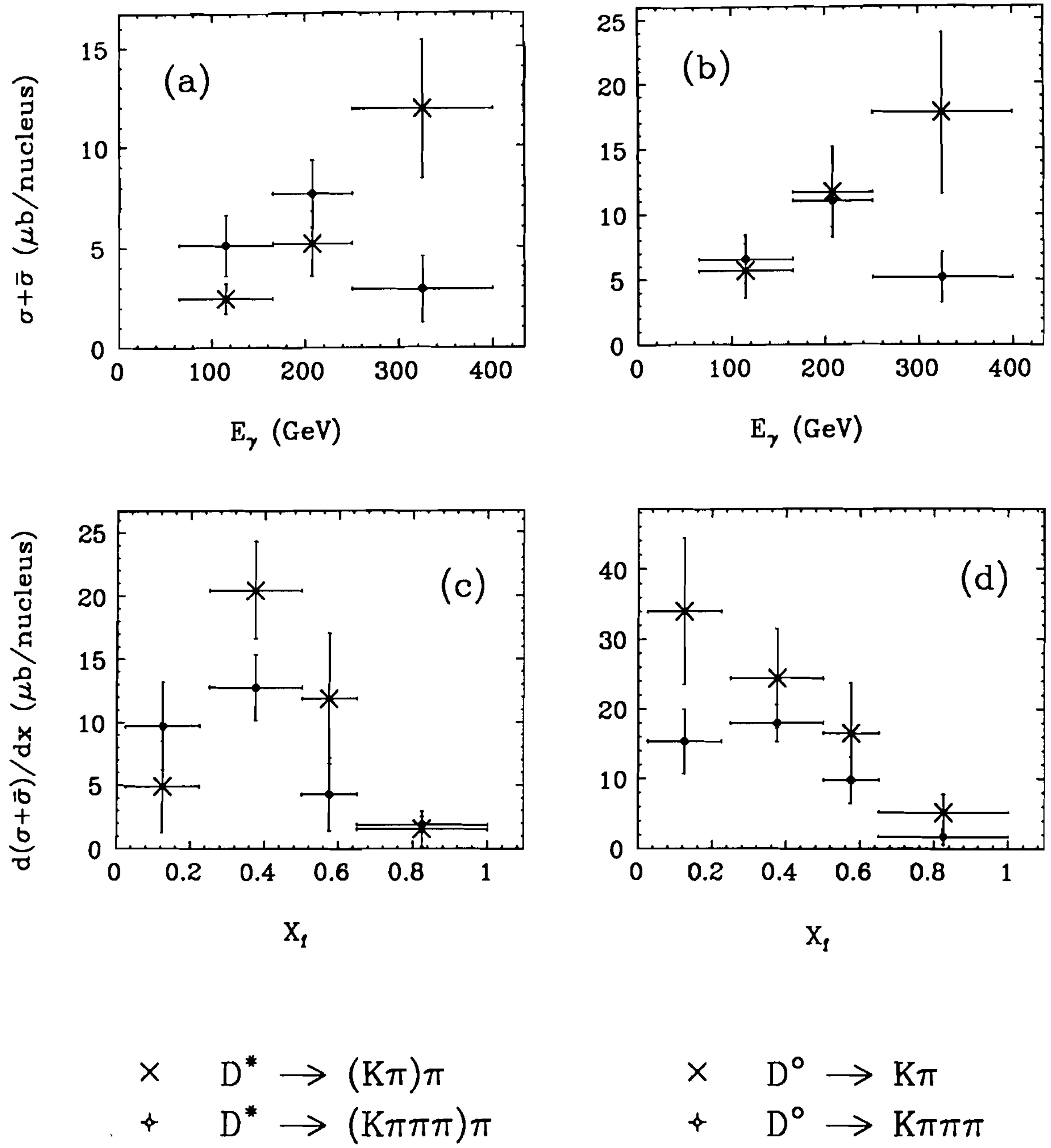

Figure 6-11 : Cross sections measured separately with Kπ and Kπππ signals.

Table 6-5(a) : $\sigma(\omega)$, $x_f > .2$ – Separate Decay Modes

	D*		D°	
	Kπ	Kπππ	Kπ	Kπππ
ω_1	2.45 ± .74	5.11 ± 1.52	5.66 ± 2.10	6.55 ± 1.84
ω_2	5.20 ± 1.62	7.68 ± 1.67	11.68 ± 3.45	11.02 ± 2.00
ω_3	11.88 ± 3.46	2.92 ± 1.65	17.75 ± 6.16	5.16 ± 1.92

Table 6-5(b) : $d\sigma/dx_f$ – Separate Decay Modes

	D*		D°	
	Kπ	Kπππ	Kπ	Kπππ
$x_{f,1}$	4.88 ± 3.61	9.70 ± 3.48	33.93 ± 10.41	15.34 ± 4.67
$x_{f,2}$	20.44 ± 3.83	12.74 ± 2.58	24.35 ± 7.11	17.95 ± 2.66
$x_{f,3}$	11.86 ± 5.18	4.29 ± 2.89	16.48 ± 7.20	9.74 ± 3.29
$x_{f,4}$	1.54 ± 1.39	1.90 ± 0.61	5.16 ± 2.61	1.68 ± 1.12

Upon comparison, cross sections versus ω in the two decay modes do appear strikingly different. In particular the highest energy points in Figures 6-11 (a) & (b) appear to have fluctuated apart. However it is not obvious that these fluctuations are statistically significant. Correlations between cross section bins can create large apparent discrepancies which may not be as large statistically.

A quantitative comparison of the cross sections versus ω is made by computing the χ^2 that the cross sections are the same at each of the 3 points. If $\vec{\alpha}$ and $\vec{\beta}$ represent the independent measurements and $\vec{C}$ represents the hypothetical cross section values, then the quality of agreement with the hypothesis is written as :

$$\chi^2 = (\alpha_i - C_i)\mathbf{A}_{\mathrm{ij}}{}^{-1}(\alpha_j - C_j) + (\beta_i - C_i)\mathbf{B}_{\mathrm{ij}}{}^{-1}(\beta_j - C_j)$$

where summation over repeated indices is implied. **A** and **B** are the cross section correlation matrices, defined in Equation A4.2 . The minimum χ^2 (χ^2_*) can be shown to be :

$$\chi_*^2 = (\alpha_i - \beta_i)(\mathbf{A} + \mathbf{B})_{ij}^{-1}(\alpha_j - \beta_j) \tag{6.10}$$

testing the hypothesis that measurements $\vec{\alpha}$ are the same as $\vec{\beta}$.

Elements of the correlation matrices can be computed in much the same way as the cross section through the use of weighted histograms. Each datum is weighted by $\rho_{im}\rho_{jm}$; the fit yield of the histograms represents the value of $\langle \rho_{im}\rho_{jm}n_m \rangle$ (see Equation 6.6). The relative correlations, defined in Equation 6.7, are tabulated in Table 6-6 in bins of ω only for fits to both monte carlo and data.

Table 6-6 : Relative Correlations ($x_f > .2$)

	D*				D°			
	Kπ		Kπππ		Kπ		Kπππ	
	Data	MC	Data	MC	Data	MC	Data	MC
Corr_{12}	-.66	-.40	-.29	-.25	-.32	-.35	-.17	-.31
Corr_{13}	.35	.14	.09	.09	.17	.12	.05	.03
Corr_{23}	-.57	-.53	-.56	-.57	-.63	-.55	-.52	-.51

The Monte Carlo and data correlations agree quite well in both D* and D° decays. It is important to note the correlation between every second measurement and the anti-correlation between adjacent measurements demonstrated by these numbers. In particular the large anti-correlation between cross sections in the ω_2 and ω_3 bins reinforces the point made earlier regarding the affect of random fluctuations. A fluctuation in one of these two cross section bins will be accompanied by an opposite fluctuation in the other bin. This can dramatically affect the appearance of the cross section, especially with only 3 bins.

To answer the question of the statistical significance of these fluctuations, the χ_*^2 written in Equation 6.10 was calculated for both the D* and D° decays ($\chi_*^2 =$

10.1 and $\chi^2_* = 6.4$ respectively). With 3 degrees of freedom, representing the 3 cross section values, the confidence levels that the measurements are consistent are less than 10 % (about 2 and 9 percent for the D* and D° respectively), suggesting the presence of a systematic problem. Evidence from the $K\pi\pi\pi/K\pi$ branching ratio indeed suggests small systematic differences at high momentum (see Figure 5-7). Such differences would show up mostly in the highest energy bin of the cross section, as observed. Differences in the cross section versus x_f shown in Figures 6-11(c) & (d) do appear less severe.

While studies of the cross section consistency indicate some systematic problem, they quantify only the portion having to do with relative systematic differences. Therefore it is difficult to use cross section consistencies as a measure of overall systematic uncertainty. An estimate of the overall uncertainty is made by identifying aspects of the Monte Carlo simulation which are likely to be inaccurate. Areas where uncertainties are known to exist in the simulation include :

1. The photon beam profile may be incorrectly modeled in the monte carlo. This affects the estimate of the fraction of photons intersecting the target (Appendix D.1), and hence the luminosity η_{mc}. The beam parameterization (see discussion in section 4.1.2) indicates that roughly 25 percent of the photons are missing the large section of the target. If in fact none of the beam was missing, the luminosity could be underestimated by 25 percent. This means that cross sections are actually lower than presently measured. Also, any divergence in the photon beam could lead to photons which arrive outside the active area of the BGM. This would also result in an underestimate of the luminosity.

2. Event *pile up* in the BGM tends to cause an overestimate of *multi-brem* photon energy. If the amount of *pile up* used in the Monte Carlo (25 %) is too low, the energy estimator (section 3.7) would return a systematically low ω^*. This effect would be more prevalent at low ω^* so that a correcting the *pile up* assumption might shift events out of the first bin of ω into higher

bins. Such shifts could affect the shape as well as the overall level of $\sigma(\omega)$.

3. To a surprising extent (see Figure 5-4) the charm state does not self trigger the experiment. Here acceptances as a function of ω depend on the particles accompanying the measured charm particle, creating a significant model dependence to $\sigma(\omega)$.
4. Trigger counters used in the Master Gate may be less efficient than is modeled. Lowering the monte carlo efficiency would then increase the cross section over the value reported here.
5. The *post hoc* Monte Carlo corrections might not be adequate. In particular measured linking efficiencies may not reflect the efficiency in charm events. An increase (or decrease) in the actual efficiency over the measured efficiency would lead to a decrease (or increase) in the measured cross section. The Čerenkov correction factor presently scales the cross section by a factor of 1.2 . The uncertainty of this factor is ±0.1 indicating that cross sections could increase or decrease by as much as 10 percent.
6. Evidence exists for time dependent variations in the amount of charm produced with a given photon luminosity.[19] The exact instability responsible for such variations is not known. A more complete understanding might indicate additional problems with detector efficiencies or luminosity measurements.

Measurement of the time variations in charm production rates can be used to assess systematic uncertainties. Figure 6-12 plots the number of luminosity counts per $D^{\star}$ event in each of 8 run periods.

The figure exhibits two distinct levels suggesting a systematic shift in the measurement of either the luminosity or charm yield. A change in a detector or trigger efficiency could account for a shift in the charm yield, but a shift in the effective luminosity that went undetected is the more likely cause. Whichever is the case, the 24 percent variation from mean shown in the figure relates directly to variations in the cross section. Combining this uncertainty with some

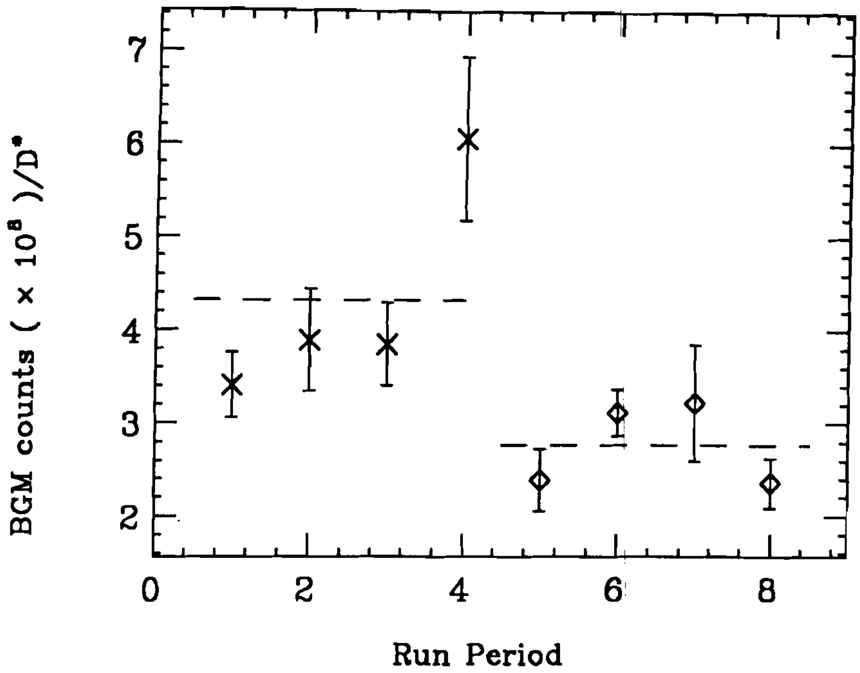

Figure 6-12 : Luminosity monitor fluctuations (BGM counts per reconstructed D*).

of the other uncertainties listed above suggests a value for the total systematic uncertainty of about 30 percent. Comparison with Table 6-4 shows that this uncertainty is comparable or worse than the statistical uncertainties including resolution effects ! The overall uncertainty of each cross section value is found by adding 30 percent of the cross section in quadrature with each of the statistical errors.

6.4 Comparisons and Conclusions

There are several ways to assess the cross sections reported in section 6.3.2 . One of these has already been discussed in the context of studying systematic effects. Another way is to compare these results with similar analyses. The simplest comparisons are made with data taken under the same experimental conditions : beam, target, detector, etc. Somewhat harder are comparisons with experiments which are further afield, while the least meaningful are comparisons made with theoretical predictions. Comparisons will be presented in this order.

6.4.1 Comparisons to Other E687 Data

The naive spin counting argument presented in section 5.2 has proven successful in predicting $D^{\star\pm}$ and D° production ratios. Another result of the argument is a prediction of the production ratio of $D^{\pm}$ and D° mesons. The cross section for the specific decay $D^{\pm} \rightarrow K\pi\pi$ has been measured in E687[4] obtained from the same run period and through the same analysis chain as the D° sample reported here. The cross section analysis was similar as well.

A prediction for the total $D^{\pm}$ cross section is obtained by dividing the cross section, presented in reference [4] in bins of ω, by the relevant branching fraction (7.8 %) into the $K\pi\pi$ decay mode. A hypothesis for the D° cross section is obtained by scaling these numbers by the predicted $D^{\circ}/D^{\pm}$ ratio of 2.16 (from section 5.2). This D° prediction is shown in Figure 6-13 for 3 bins of ω.

An additional 15 percent was added to the $D^{\pm}$ cross section for the *ad hoc* linking correction not included in its calculation.

A prediction of the total D° cross section based on numbers reported in section 6.3.2 are shown in the figure as well. These were obtained by dividing the numbers reported in Table 6-3(a), column 4 by the D° branching fraction (11.7 %) into the $K\pi$ and $K\pi\pi\pi$ decay modes. The agreement between the two predictions is reasonably good. This serves to reinforce the suggestion that the simple spin model is indeed sufficient to describe the relative population of D meson species.

Included as well in Figure 6-13 are the predictions for the D° cross section based on $D^{\star\pm}$ decays. Their agreement with the other two predictions displays the point made in section 6.3.4 that results are in agreement with established $D^{\star}/D^{\circ}$ production ratios.

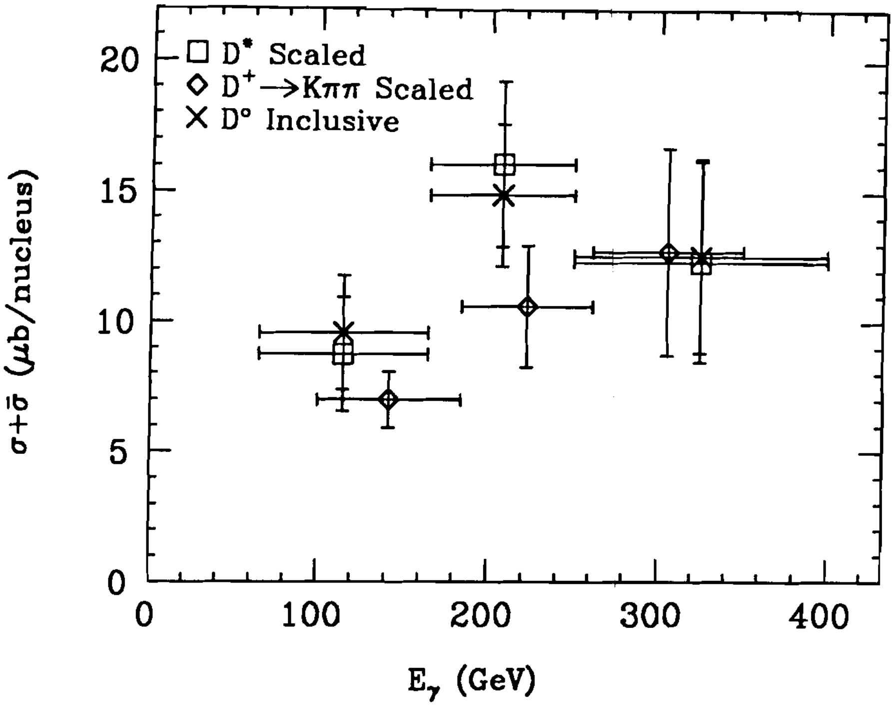

Figure 6-13 : Predicted D° cross sections based on measurements of D° → Kπ+Kπππ inclusive cross section, similar D* cross sections, and the $D^+ \rightarrow K\pi\pi$ cross section.

6.4.2 Comparisons to a Similar Experiment

The D* and D° cross section results can be compared to Experiment 691 at Fermi National Accelerator Laboratory. This experiment, is similar in many respects to E687 and has reported cross sections at a mean photon energy of 145 GeV for decays into specific final states.[2] The energy dependence of the cross section is only reported for combined charm states (D°, $D^{\pm}$, $D_s^{\pm}$, $\Lambda_c^{\pm}$) so it is necessary to scale these down to infer the D* or D° cross section versus ω. Figures 6-14(a) & (b) show plots of the E691 D* and D° cross sections as a function of ω ($x_f > 0.2$) for the decays $D^0 \rightarrow K\pi + K\pi\pi\pi$.

Overplotted in these figures are the cross sections reported in Table 6-3(a). The inner error bars are the statistical errors and the outer bars are the overall

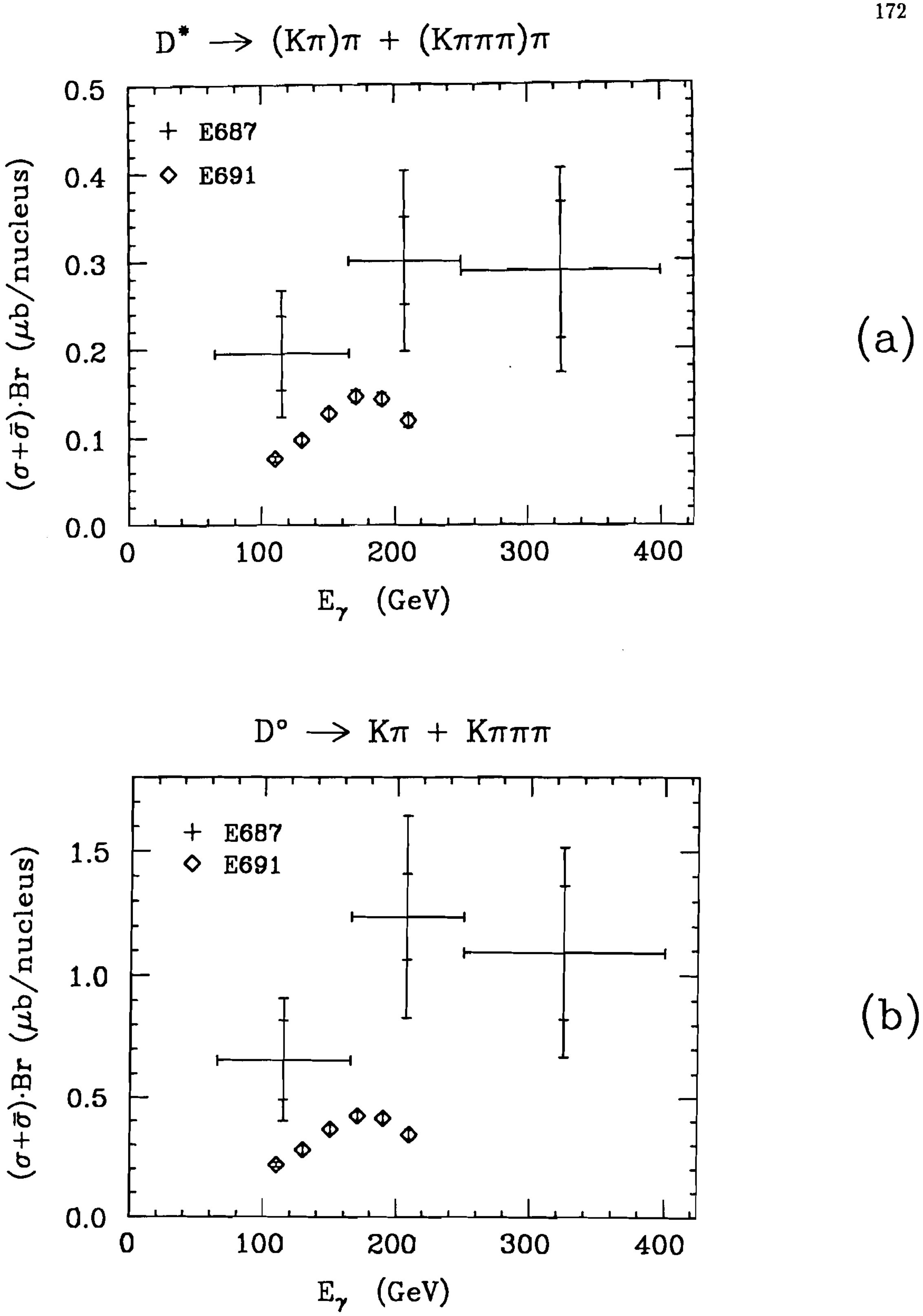

Figure 6-14 : Comparison of cross sections versus ω with E691.

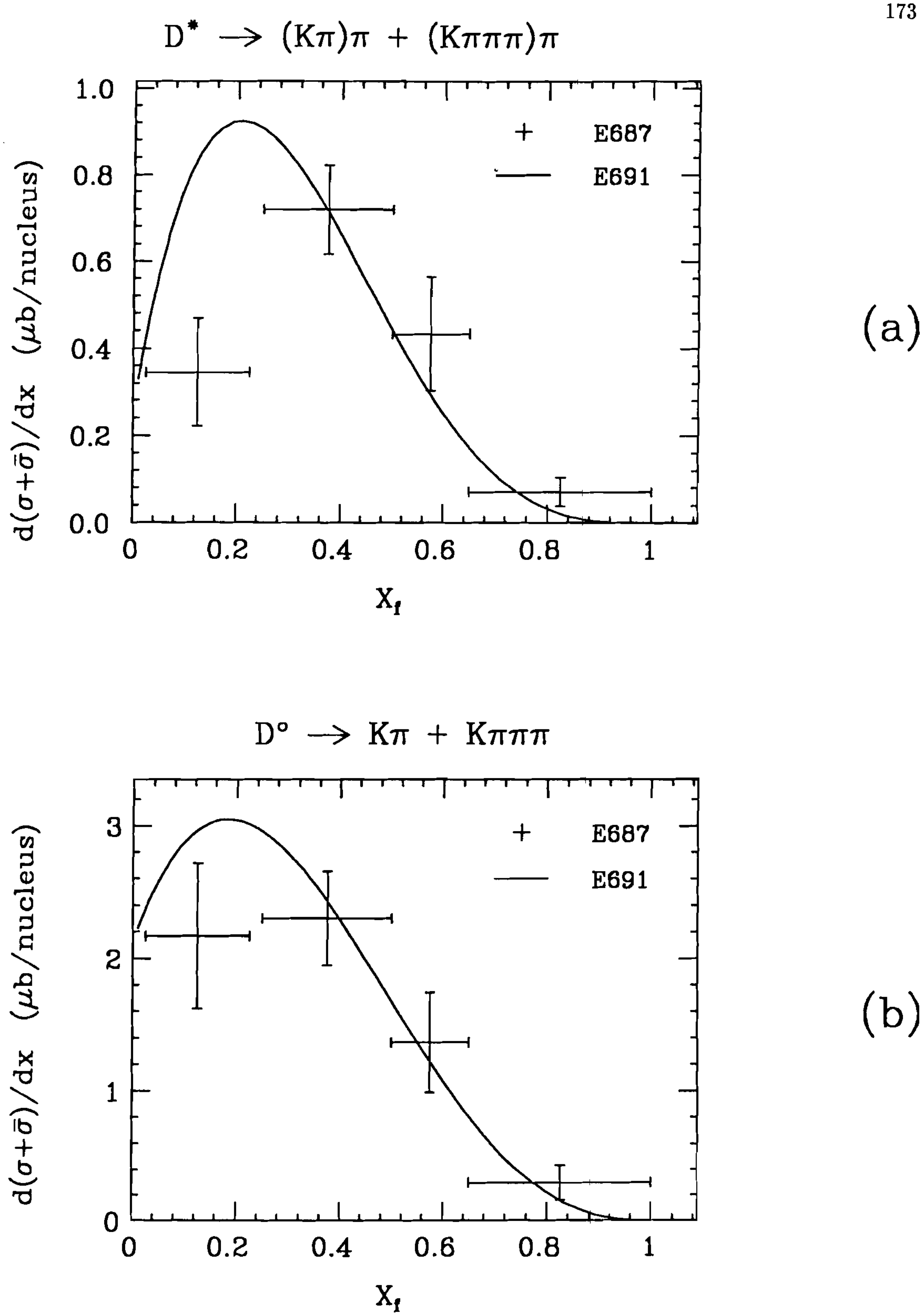

Figure 6-15 : Comparison of cross sections versus x_f with E691.

error described above. The agreement does not appear to be good. However the reader is cautioned on several points :

1. The E691 error bars reflect statistical errors of all charm species combined. These have not been rescaled. In fact their yield of D* and D° mesons alone is only slightly greater than used in the E687 cross section calculations.
2. The problems associated with poor ω resolution probably did not exist in E691. However, little information is available about the procedure used in calculating the E691 cross section. An indication of possible problems is that their cross section appears fall at their highest incident photon energies, a completely unexpected result.
3. The detector efficiencies in most monte carlo simulations have a natural tendency to be higher than the actual efficiencies. Thus as more care is taken in modeling the charm detection efficiency, cross section values will increase. Much of the disagreement would disappear, for example, if the *pot hoc* corrections were neglected.
4. The relative anti-correlation between ω_2 and ω_3 of the E687 data is at least 50 percent (see Table 6-6), meaning that an upward fluctuation of ω_2 will cause ω_3 to shift down. This can have the effect of altering the appearance of the plotted cross section. In fact both E687 and E691 data are very much consistent with a gradually rising cross section.

Figures 6-15(a) & (b) are plots of $d\sigma/dx_f$ as a function of x_f for the D* and D° decays respectively. The values are listed in Table 6-3(b). Only statistical errors are shown since systematic uncertainties contribute solely to the overall scale. Overplotted are the reported fits to the E691 distributions[2] using the parameterization

$$A(1+\alpha x_f)(1-|x_f|)^n$$

The value of A was chosen to scale with the data reported here. The measurements reported in Table 6-3(b) appear to confirm a rather soft x_f distribution of

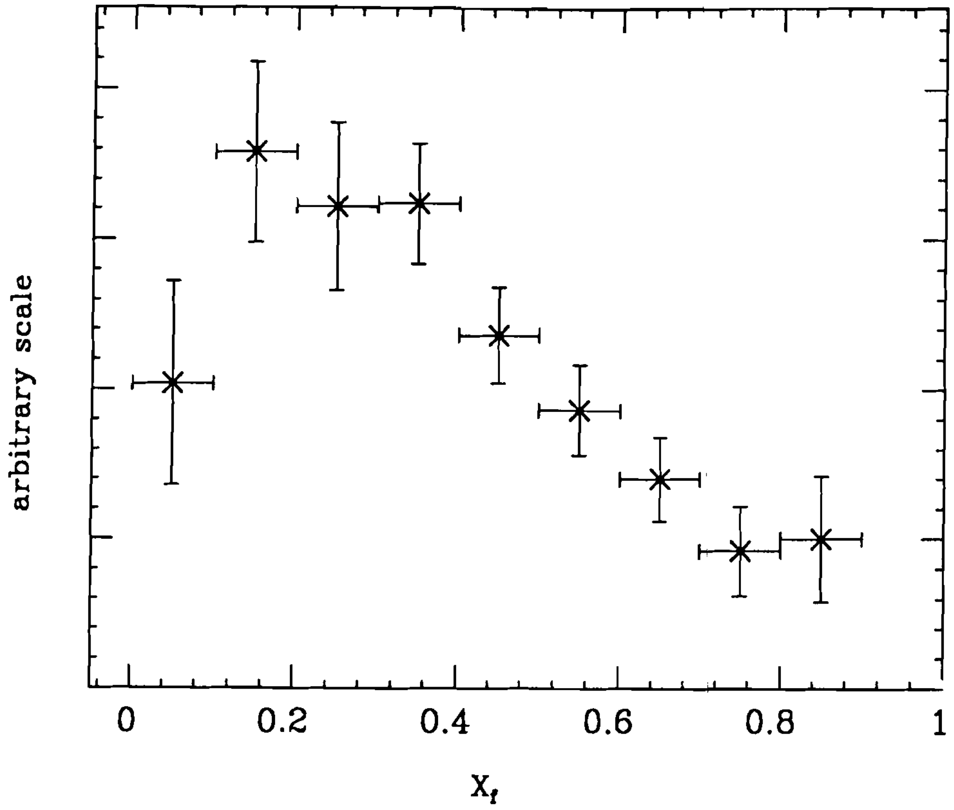

Figure 6-16 : x_f distribution measured by NA14′.

D mesons. This is similar as well to results reported for $D^\pm$ mesons.[4] If it is assumed that the charm quark distribution follows the Photon-Gluon Fusion model prediction, these data imply a significant fraction of the charm quark momentum is lost in the hadronization process (see Figure 1-3). One interesting point to note is that both these and E691 data indicate a more central x_f distribution for the $D^\star$ than for the D° . It is tempting to explain this as a difference in their momentum distributions, since D° mesons are predominantly decays of $D^\star$ mesons, but a kinematic calculation does bear this out. A further comparison of x_f distributions can be made with data reported by NA14′ [20]. These data, shown in Figure 6-16, give the appearance of a slightly harder x_f distribution than E691 data.

While the E687 data are consistent with both, they tend to favor the NA14′ description of the distribution.

6.4.3 Comparisons to Other Experimental Data

It is possible to compare to the measured D° cross section to results of other photoproduction experiments as well. This is not as simple as the comparison with E691, however, as many do not make direct measurements of D meson cross sections. A more universal comparison can be made between total charm cross section predictions. None of the experiments is able to make direct measurements of the total cross section, so each has made assumptions about relative charm meson and baryon production ratios in reporting the total charm cross section. The results are shown in Figure 6-17.

To report on the total charm cross section measured in E687, the values for the total D° cross section are scaled by several factors which follow from a parameterization of the Lund[22] model :

Contributions to cross section from $D^{\pm}$ mesons : × 1.5

Contributions from charm baryons and other mesons : × 1.25

Correct for observation of only 1/2 of the $c\bar{c}$ pair : ÷ 2.0

The total D° cross section in bins of ω is found following the prescription in section 6.4.1 . An A^1 dependence of the nuclear cross section is assumed. In E687 the contribution to the total cross section from x_f below 0 should be negligible, so no factor is included for this.

The E687 total charm prediction based on the D° cross section appears to lie somewhat somewhat higher than other measurements at comparable energies. Large error bars, in fact, cover much of the apparent discrepancy. These reflect the resolution and luminosity uncertainties in E687 data. If the overall scale of E687 cross sections were adjusted downward (by ignoring the *post hoc* corrections, for instance), agreement with the $\sigma_{c\bar{c}}(\omega)$ trend established by the other experiments would be remarkably good.

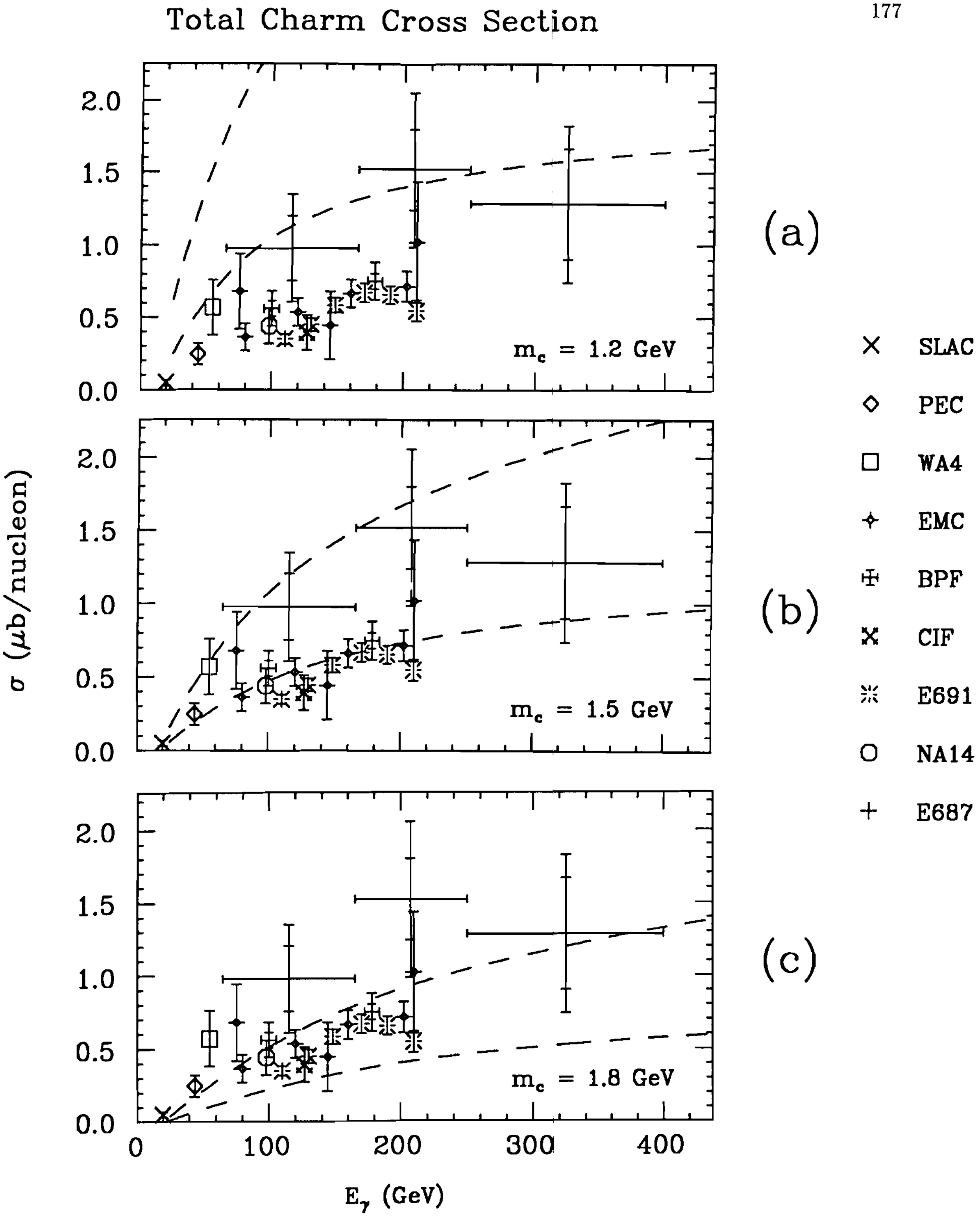

Figure 6-17 : Comparison of total charm cross sections with results reported by various photoproduction experiments[21]. Comparison is also made with a range of Photon-Gluon Fusion model predictions.

6.4.4 Comparisons to Theoretical Predictions

Included in Figure 6-17 are predictions of the total charm cross section calculated from the Photon-Gluon Fusion model by Ellis et al[23] up to $O(\alpha\alpha_s^2)$. The three rows of Figure 6-17 represent m_c = 1.2, 1.5, 1.8 GeV respectively. Each part has two curves representing bounds on the theoretical calculations obtained by "reasonable" variations of the remaining parameters. These variations are in the gluon distribution function $G(x)$ and constituents of α_s, QCD parameters μ and Λ. The cross sections reported in this thesis are inconsistent with only the very highest values of m_c. While the model is most highly dependent on the charm quark mass m_c, the QCD constants are poorly known and their variation significantly affects these second order calculations. It is clear in studying the figure that the ability of data to measure the main Photon-Gluon Fusion model parameters will be limited until these QCD parameters are pinned down.

Chapter 7

The D° Meson Lifetime

The chapter discusses the calculation of the mean lifetime τ_D of the D° meson as observed from the inclusive hadronic decays

$$D^\circ \to K\pi$$

$$D^\circ \to K\pi\pi\pi$$

Measurement of a mean lifetime bears directly on the issue of relative D° /D$^\pm$ decay rates discussed in section 1.2.1 . Also the large sample of D° meson decays should provide a precise measurement capable of corroborating previous results.

The lifetime of the D° events is expected to follow an exponential distribution $P(t) \propto \exp(-t/\tau_D)$ where $P(t)$ is the probability that a particle created at $t = 0$ will have decayed after a time t measured in its rest frame. τ_D is referred to as the mean D° lifetime. The mean distance that a D° meson travels in the laboratory reference frame is given by $d = \gamma\, v\, \tau_D$, where $\gamma v = p_{lab}c/m_D$. In E687 the typical γ of a D meson is about 50 and $\tau_D \simeq 4.3 \times 10^{-13}$s, so the decay distance is on the order of a centimeter. In order to precisely measure the lifetime distribution, the longitudinal vertex resolution must be considerably smaller than this distance scale. Fortunately the high granularity SSD system allows track vertices to be found with a Z resolution in the hundreds of microns.

This analysis uses the candidate driven vertex algorithm, discussed in section 3.9, to find both the production and decay vertex of a candidate D° meson and measure their separation. The distribution of vertex separations, measured in proper time, is then fit to the anticipated distribution in t. The mean lifetime τ_D, which is the only parameter of this fit, is then reported with its anticipated uncertainty. The source of measurement uncertainties is discussed in detail at the end.

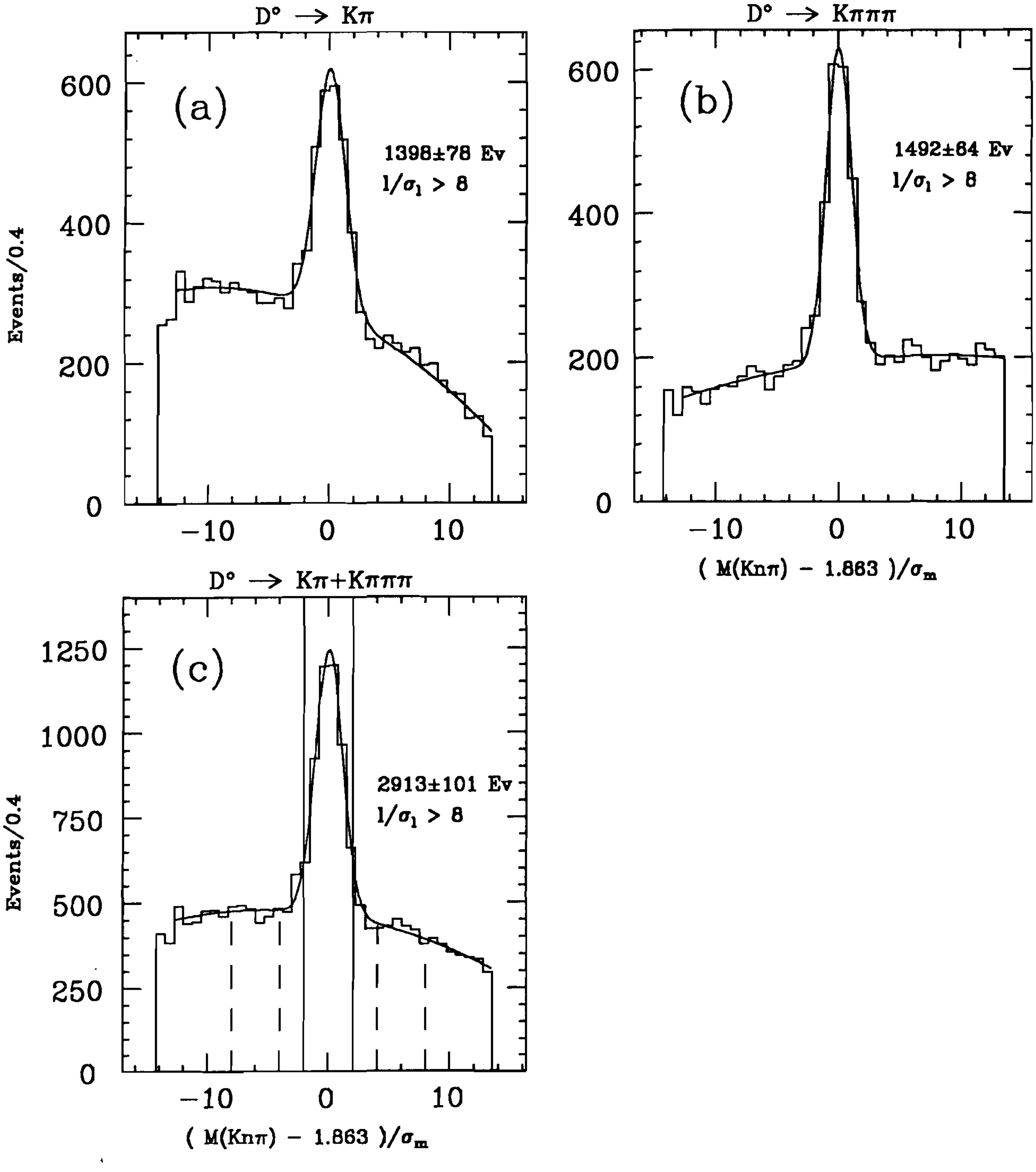

Figure 7-1 : D° signals used in determining the D° mean lifetime. Signal and sideband regions shown for combined decay mode lifetime fit.

7.1 Methodology

Signals of the two decay modes used for this study are shown in Figures 7-1(a) & (b), where the histograms are in normalized invariant mass. Each has minimum vertex detachment criteria imposed to resolve the signal. The combined Kπ and K$\pi\pi\pi$ events, seen in Figure 7-1(c), are used to measure the D° meson mean lifetime. Each event has a lifetime t measured as the time interval, in the rest frame of the meson, between its production and subsequent decay. The lifetime distribution of events is expected to follow a pure exponential, but the presence of systematic distortions means that the measured distribution t is not a pure exponential. These distortions and their corrections are discussed next.

The most prominent of these distortions is a result of the primary editing criteria requiring a minimum detachment of primary and secondary vertices. Vertex separations returned from the candidate driven vertex algorithm were used in the D meson skim (see section 3.10) to reduce non-charm background. Candidate decays of D° → Kπ and D° → K$\pi\pi\pi$ were selected provided they satisfied minimum normalized separations ℓ/σ_ℓ given in Table 3-6. Since $\ell/\sigma_\ell \cong t/\sigma_t$, one would expect that these skim criteria would introduce considerable distortions in the lifetime distribution of the event sample. In fact the potential biases introduced by the D meson skim can be removed by simply recasting the variable describing the time evolution of the events. Since the evolution is expected to be a pure exponential, its measurement can be made anywhere in the lifetime distribution. By measuring lifetimes relative to $t^{\circ} = n_t\sigma_t$, where n_t is the minimum number of standard deviations ℓ/σ_ℓ required in the skim, the skim-induced distortion in the lifetime distribution is removed as will be shown below. par As in the skim, t° will vary between events in a given decay mode because σ_t is determined separately for each event. Consider a variable $\mathcal{S}(\sigma_t)$ describing the distribution of resolutions such that

$$N_D^{tot} = \int \mathcal{S}(\sigma_t)\, d\sigma_t$$

In the absence of instrumental effects and absorption, each class of events in the narrow range σ_t to $\sigma_t + d\sigma_t$ would evolve in time according to $\exp(-(t - t^\circ)/\tau_D)$, where t° is a specific time tuned to the editing cut such that $t^\circ = n_t\sigma_t$. The whole spectrum of events is then expected to evolve according to

$$N_D(t) = \int \mathcal{S}(\sigma_t)\, d\sigma_t\, e^{-(t-n_t\sigma_t)/\tau_D}$$

A substitution

$$t' = t - n_t\sigma_t \tag{7.1}$$

is then made which allows the time evolution to be separated from the event sum

$$N_D(t') = e^{-t'/\tau_D} \int \mathcal{S}(\sigma_t)\, d\sigma_t \tag{7.2}$$

provided $\mathcal{S}(\sigma_t)$ does not depend on t (i.e. σ_t does not depend on t). The lifetime evolution is a pure exponential in t' under this assumption (verified in Monte Carlo).

A recast of the time evolution in the variable t' removes the gross distortions brought about through the editing process. There will, however, be smaller distortions due to measurement effects and absorption which will cause deviations from the anticipated exponential behavior. Such variations from the nominal distribution can be expressed in terms of a modulating function $f(t')$ leading to a revision of Equation 7.2 of the form

$$N_D(t') = N_D^{tot}\, f(t')\, e^{-t'/\tau_D} \tag{7.3}$$

Anticipated contributions to $f(t')$ are as follows[24].

Resolution effects. Since lifetime measurement resolutions are finite ($\bar{\sigma}_t = .043$ picoseconds; see section 3.12), a depletion of events at low lifetimes is expected. The lifetime of each event is measured in a distribution, given by σ_t, about its true lifetime. At large lifetimes the resulting migrations from lower lifetimes and higher lifetimes will tend to leave little distortion in the net measured lifetime evolution. At small lifetimes, however, there are no events with $t < 0$ which can migrate to higher lifetimes to compensate the fluctuation of events out of lifetime bins near $t = 0$. This depletion of events at $t \approx \bar{\sigma}_t$ causes an apparent increase of mean lifetime. This effect is diminished by editing cuts which require $t > 3 \cdot \sigma_t$.

Reconstruction efficiency. Track reconstruction efficiency can depend on the lifetime of the state. Shorter lived mesons tend to decay more upstream in the target and are hence less likely to be accepted. Very long lived mesons may not decay until after entering the silicon microstrip detector (SSD), thus decreasing their reconstruction efficiency.

Hadronic absorption. Absorption in the target will affect the apparent lifetime distribution. The decay particles of shorter lived states will travel a greater distance in the target than those which decay further downstream. Ignoring the absorption of the D meson prior to decay, relatively higher absorption of short lived states will lengthen the apparent mean lifetime.

Vertex *pull*. A small effect of the vertex algorithm is referred to as primary vertex *pull*. Constituents of the recoil charm state are sometimes associated with the primary vertex, thus lessening the apparent separation between the primary and charm secondary vertex. This *pull* will not affect the lifetime distribution unless the amount of *pull* depends on t.

Resolution t dependence. Any dependence of σ_t on t, or a hidden dependence through $\mathcal{S}(\sigma_t)$ in Equation 7.2, will be included in $f(t')$ as well.

Many of these effects, while small, are rather difficult to calculate directly. Therefore it is simpler to use the Monte Carlo to describe $f(t')$. By analyzing the lifetime distribution $N_D(t')$ of Monte Carlo events with known true lifetime τ_p (0.427 picoseconds in this analysis), it is possible to build up the modulation function $f(t')$. Figure 7-2(a) shows the measured distribution $N_D(t')$ in bins of t'. Overplotted is the anticipated distribution in t' if $f(t')$ were 1. This particular example is for the case $n_t = 0$, so the finite resolution effects are quite apparent at low t. The factor $f(t')$ is simply the ratio of the observed Monte Carlo distribution to the anticipated distribution, and is shown in Figure 7-2(b) in bins of t'. If the Monte Carlo correctly models the measurement effects, then the true lifetime distribution in data should be $N_D(t')/f(t')$. Since it is a function of t', the factor depends on the value of n_t chosen for the fit.

7.2 Data Analysis and the Fit

In constructing the lifetime distribution, events are chosen in the signal ($\pm 2\sigma_m$) and sideband regions. The regions are shown in the histogram of D° events in Figure 7-1(c). Since it is impossible to obtain a sample of pure D mesons, events from the sideband regions can be used to estimate the lifetime evolution of background events. Signal and sideband region events are treated exactly the same up to the point of the fit. Both are subject to a set of minimal criteria.

1. The standard kaon identification, described in section 3.11, is required.
2. Ln C.L. ($K\pi$, $K\pi\pi\pi$ vertex) > -5.0
3. The primary vertex must be found within $3\sigma_\ell$ of target region.
4. The secondary vertex must be found at least $3{\cdot}\ell/\sigma_\ell$ downstream of the primary vertex.
5. The primary vertex must contain more than one track (See discussion in section 3.9).
6. The proper time separation of primary and secondary vertex must be less than 6 mean lifetimes. This is done to reduce stray events at large lifetimes.

When the vertex algorithm finds the primary and secondary vertices it performs a fit to find the best value ℓ (with corresponding σ_ℓ) for the vertex separation in the laboratory frame. This value $\ell = c\,\tau_{lab}$ is related to the proper

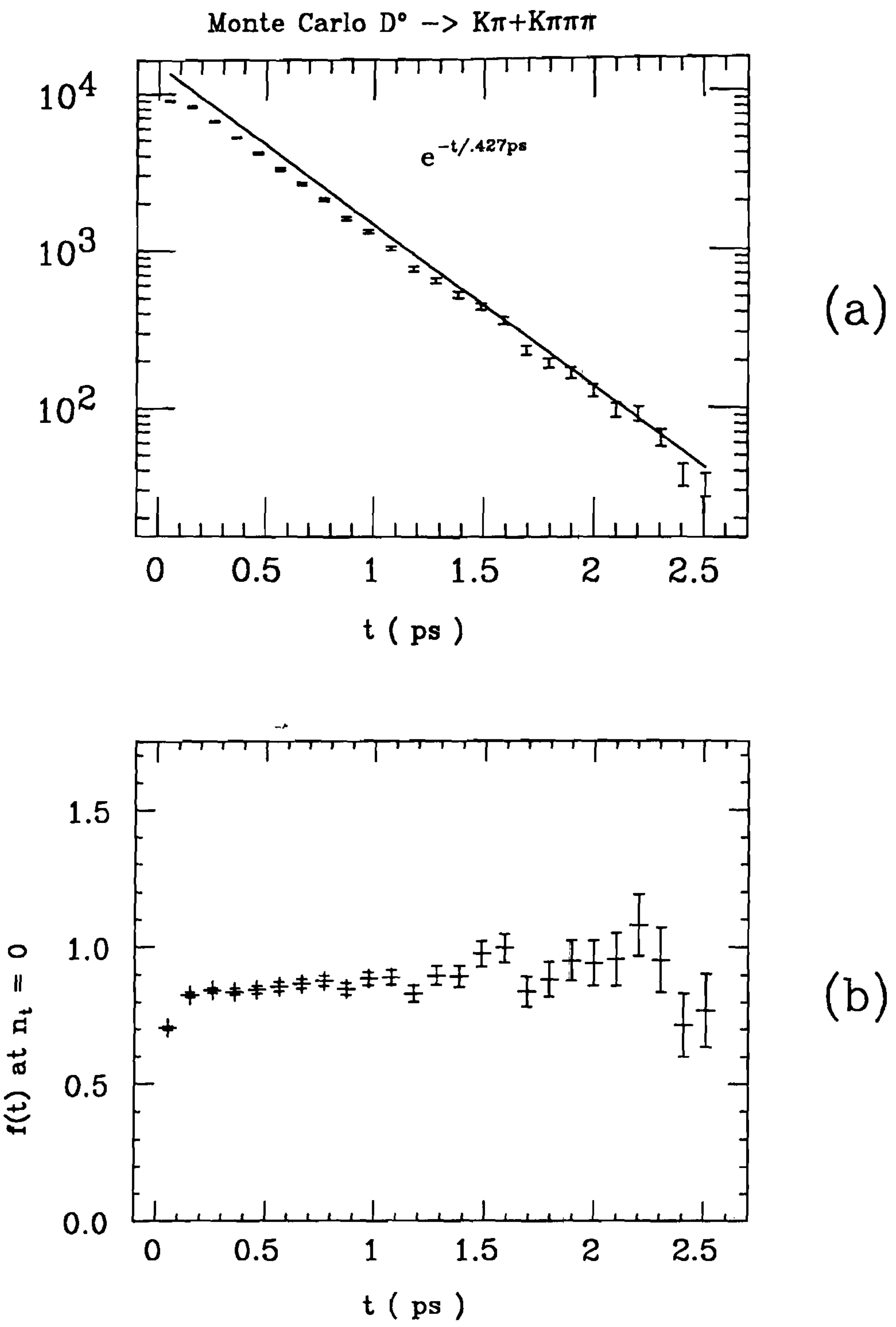

Figure 7-2 : Monte Carlo measured lifetime distribution and a pure exponential representing the "correct" distribution. Their ratio yields the correction factor $f(t)$ (at $n_t = 0$).

time t by the relativistic dilation γ.

$$t = \frac{\ell}{c\gamma} = \frac{m_D}{p_D}\left(\frac{\ell\,(cm)}{.03}\right) \quad \text{picoseconds}$$

A similar relation exists to define σ_t.

Once t and σ_t are known, signal and sideband events are binned separately in t' for a particular value of n_t following Equation 7.1 (Fits will be reported for several values of n_t). The number of bins chosen is 25, spanning the range $0 \leq t' \leq 6\tau_p$. Two distributions, N_i^s and N_i^{sb}, then exist representing the two samples. These yield an estimate of the total number of D mesons, given by :

$$N_D^{tot} = \sum_i N_i^s - R\,N_i^{sb} \tag{7.4}$$

where R, a factor relating the number of events in the sideband regions to the number of background events in the signal region, is $\frac{1}{2}$.

The fitting procedure used is one of binned maximum likelihood, so named because it maximizes the probability that the yield in a particular bin of data fits a given hypothesis. The data is fit by forming the likelihood function

$$\mathcal{L} = \prod_i \frac{\mu_i^{N_i^s}}{N_i^s!}\exp^{-\mu_i} \tag{7.5}$$

and minimizing $\ln \mathcal{L}$ with respect to overall lifetime contained in μ_i. The term μ_i is just the expected number of events from the signal region in a bin i of width Δt;

$$\mu_i = \Delta t\, N_i^s(\tau) \; + R\,N_i^{sb}$$

where τ is the hypothesized lifetime and $N_i^s(\tau)$ represents the predicted signal distribution for that τ . No fit parameter is used to describe the background since it is taken directly from the sidebands. Using the same parameterization as in the Monte Carlo (Equation 7.3), the number of events contained in a bin centered at t'_i should be

$$\mu_i = \left(\frac{N_D^{tot}\Delta t}{\tau}\right) f(t'_i)\exp^{-t'_i/\tau} + R\, N_i^{sb} \tag{7.6}$$

The value of the D° meson mean lifetime, τ_D, is then equal to the value of τ when $|\ln\mathcal{L}|$ is minimized. The normalization condition

$$\sum_i \mu_i(\tau) = \sum_i N_i^s(\tau)$$

is maintained throughout the fitting procedure.

7.3 Discussion of Findings

Before discussing the results in data, it is useful to first apply the technique described above to the Monte Carlo sample. This will serve to demonstrate the effect of distortions on the lifetime fit as well as check the implementation of the technique. Figure 7-3(a) shows the values of τ_D obtained from a series of likelihood fits. Each point represents the results of the fit for a different value of n_t. The dashed line is the seed Monte Carlo lifetime, $\tau_p = 0.427$ picoseconds. Since the modulation factor $f(t')$ is set to 1 in each of these fits, the deviation of the fit result displays the cumulative distortion effects for the particular n_t. Most noticeable is the rise in lifetime at low n_t and the fall at high n_t. Lifetime distributions at lower values of n_t tend to contain more short lived D mesons (σ_t has a fairly narrow distribution), so their depletion due to finite resolution effects yields a longer apparent mean lifetime. The relatively longer lived mesons at very high n_t decay in or near the SSD system, and hence have a lower reconstruction efficiency. This depletion of high lifetime events pulls the mean lifetime lower. The Monte Carlo events can then be refit using the full corrections $f(t')$ for each value of n_t. The results should, and do, match the seed lifetime as seen in Figure 7-3(b). This indicates that even at low values of n_t fit results in data should be

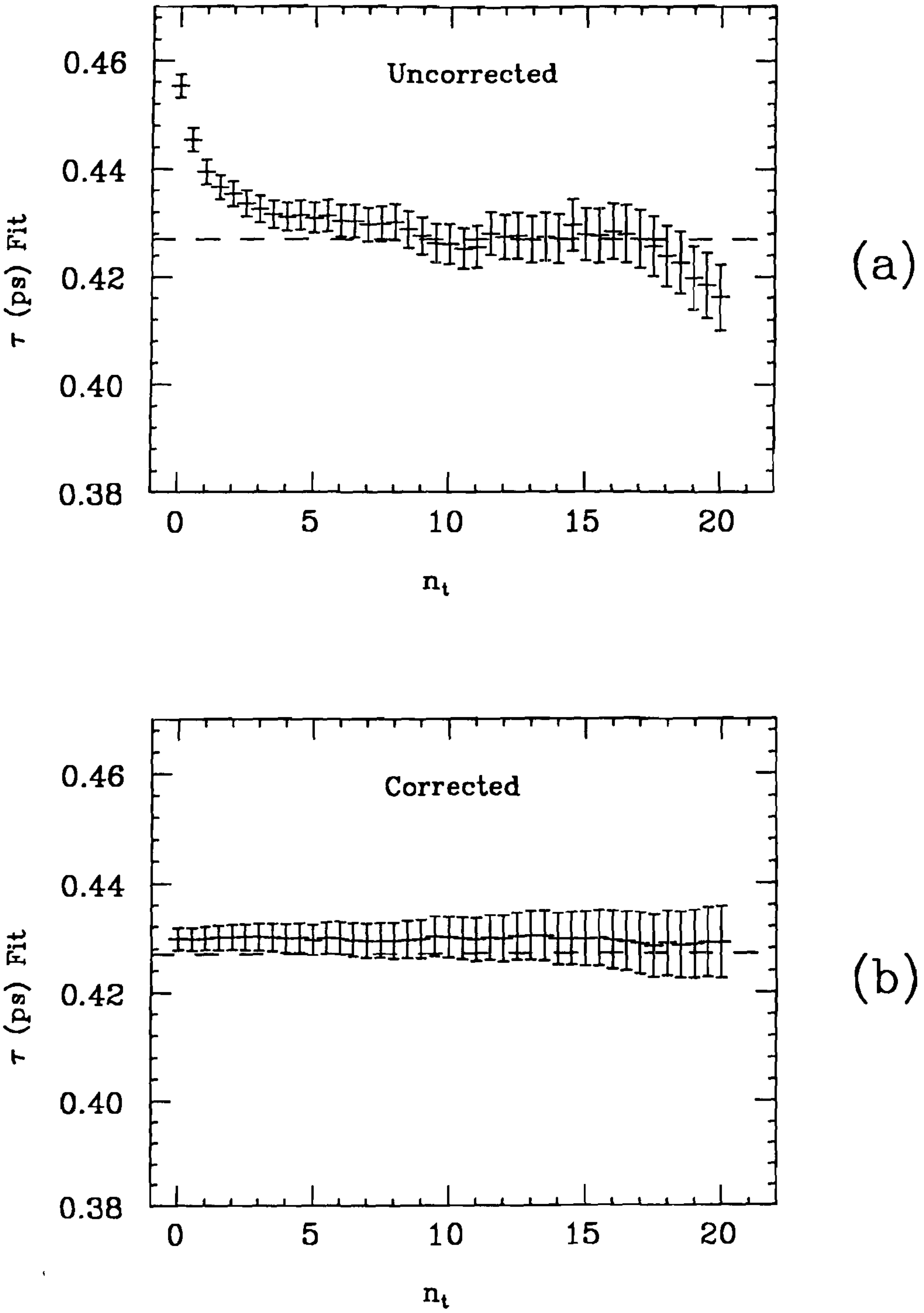

Figure 7-3 : Results of many lifetime fits to Monte Carlo events each with a different value of n_t, a measure of the vertex detachment. Results are shown with and without correction.

good, provided of course that distortions in each data bin are characterized by $f_i(t'_i)$. The extent to which such distortions are not characterized by $f_i(t'_i)$ will degrade the fit and show up as deviations from a flat line in summary plots of the fit results. Thus a display of τ_D as a function of the minimum vertex detachment n_t is a useful monitor of systematic effects and aids in the choice of a single result (one value of n_t) for which to report the mean lifetime.

The same approach to displaying fit results can be used in data. The results of fits to the combined D° inclusive sample are shown in Figure 7-4. An overall minimum vertex detachment is chosen at $n_t = 3$ because background levels overwhelm the signal at smaller separations. Figure 7-4(a) contains the raw fit results and Figure 7-4(b) contains the results where the appropriate $f(t')$ has been applied in each fit. Comparison shows that monte carlo corrections play a negligible role beyond $n_t \simeq 6$. Most of the variation of fit results lies within statistical errors, indicating few systematic problems as a function of t. The mean lifetime appears to measure higher at large values of n_t, but again this is not statistically significant. When viewing the summary plot it must be remembered that these fit results are all correlated; i.e. each distribution at n_t is contained in the distribution at $n_t - 1$.

A solid line has been introduced in Figure 7-4(b) to indicate the present world average value[8] of the D° lifetime; the dashed lines indicate the associated error. The fits reported here are clearly consistent with that value regardless of the minimum vertex detachment (given by n_t). The value of n_t chosen for reporting the fit results is 8. This value was chosen to avoid the bulk of Monte Carlo corrections yet maintain the best possible statistical significance. The data sample corresponding to this minimum vertex detachment is shown in Figure 7-1(c), and contains 2913 ± 101 events above background with a signal/noise ratio of 1.7 . A demonstration of the quality of the fit at $n_t = 8$ is seen in Figure 7-5. Here the measured event distribution has been plotted as a function of t'. Each of the data points has been corrected for distortion effects by plotting $(N_i^s - R\ N_i^{sb})/f_i(t'_i)$, where the number of events is estimated as in Equation

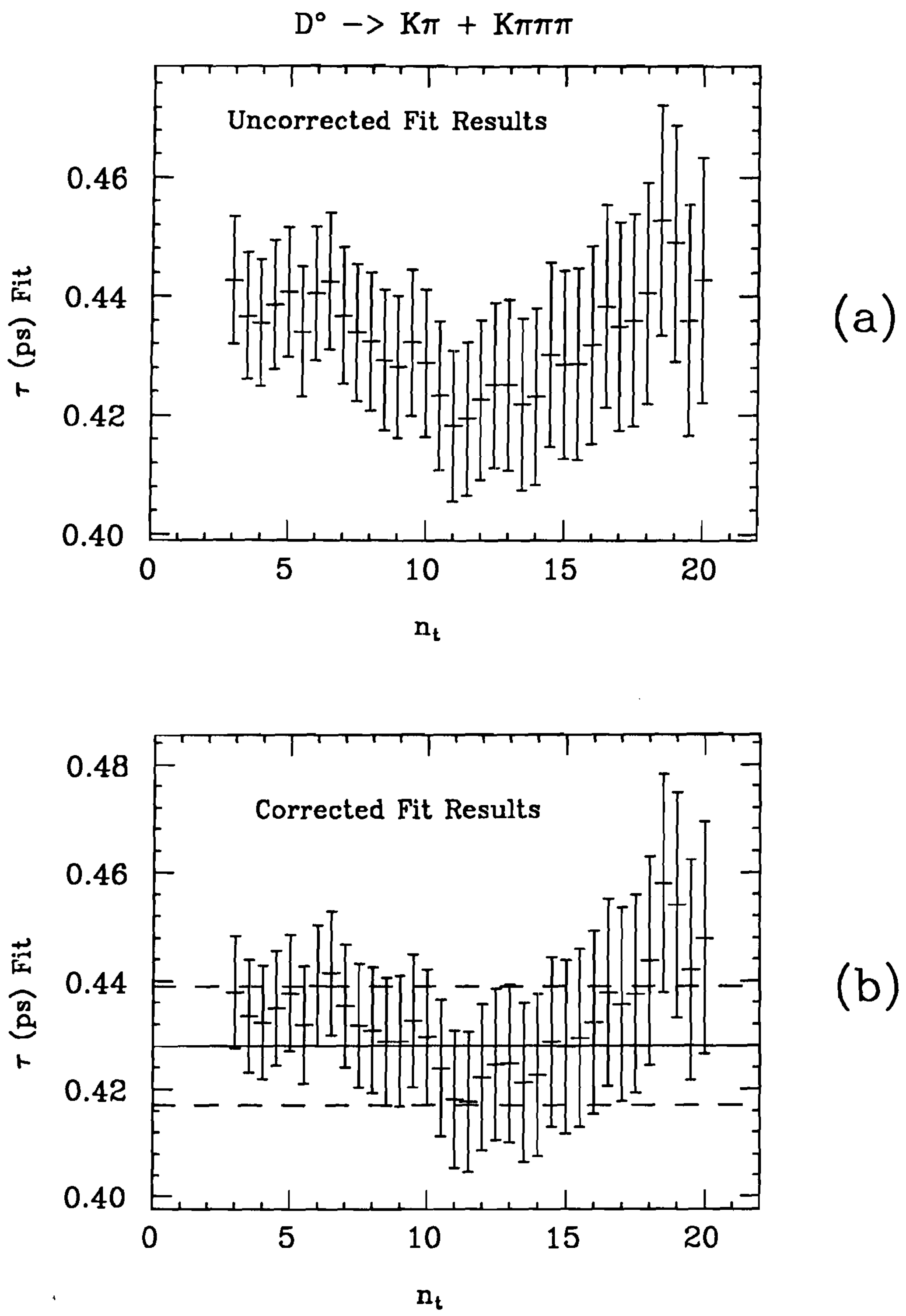

Figure 7-4 : Results of many lifetime fits in data, each with a different value of n_t, a measure of the vertex detachment. Results are shown with and without Monte Carlo correction. The world average is indicated by the line.

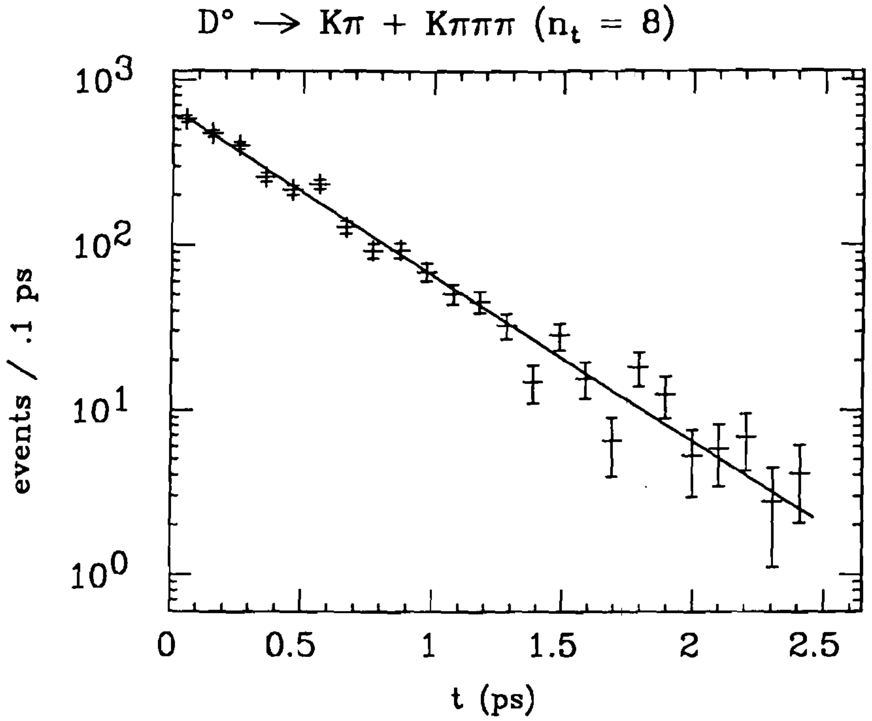

Figure 7-5 : Lifetime distribution in data for events satisfying $\ell/\sigma_\ell > 8$. All points are Monte Carlo corrected. The line represents the result of the fit at $n_t = 8$.

7.4 . The line shown in the figure is a pure exponential distribution with a mean lifetime of the fit value, $\tau_D = 0.431$ picoseconds.

7.4 Statistical Uncertainties

Some care must be taken in reporting the uncertainty in the mean lifetime obtained from the fit. The error bars shown in Figure 7-4(b) represent the statistical uncertainty obtained solely from the fit. In addition, statistical fluctuations occur in distributions not parameterized in the fit. These uncertainties, associated with sideband and monte carlo counting statistics, enter Equation 7.6 through $f(t')$ and N_i^{sb} respectively. These uncertainties, discussed in detail in Appendix F, are treated as separate contributions to the overall statistical uncertainty. As such each additional statistical contribution is represented as a multiplicative factor of the original fit error.

7.4.1 Sideband Statistics

For the case of the sideband statistics, this factor is given by

$$\sigma_{\tau}^{2} = \sigma_{\tau,fit}^{2} \frac{\sum_{i} \frac{(\partial \mu_i / \partial \tau)^2}{N_i}}{\sum_{i} \frac{(\partial \mu_i / \partial \tau)^2}{N_i + R^2 N_i^{sb}}}$$

where N_i is the total number of events in the signal region in the t' interval given by bin i. The scaling of pure fit errors is evident from the fact that contributions of the sidebands are neglected in the numerator and included in the denominator. For the particular fit being reported, $n_t = 8$, the summation over i is performed using the signal and sideband regions shown in Figure 7-1(c). The dependence on time and τ of the signal is known from the fit. The background dependence was assumed to follow an exponential behavior as well, with $\tau_b \approx 0.35$ picoseconds, where this number was gotten from fits to the background distribution. The result is that inclusion of statistical errors from the sideband regions will increase the present statistical uncertainty from the fit by 14 %.

7.4.2 Monte Carlo Statistics

The factor increasing errors due to monte carlo statistics is derived in Appendix F as well :

$$\sigma_{\tau}^{2} = \sigma_{\tau,fit}^{2} \sqrt{1 + \frac{N_{D}^{tot}}{N_{mc}}}$$

A total of 21762 monte carlo events went into the determination of $f(t')$ used in the fit at $n_t = 8$. This implies an increase in statistical errors of 7 %.

7.5 Systematic Uncertainties

There are numerous sources of systematic uncertainty in the measuring the lifetime distribution. An attempt has been made, through the use of the Monte Carlo, to take these into account. It is unlikely, however, that all systematic effects have been removed. One test of the level of systematic problems can be made by separate lifetime fits of the Kπ and K$\pi\pi\pi$ signals. Since these represent independent data sets, any overall difference beyond statistics is attributable to measuring techniques. Some systematic effects will be shared in common between the two decay modes; it will be argued later that these effects are small compared to the relative systematic effects discussed next.

7.5.1 Relative Systematics

An approach to studying systematics involves comparison of the D° lifetime calculated separately from the Kπ and K$\pi\pi\pi$ decay modes. These two signals are shown separately in Figures 7-1(a) & (b) for the case of $t/\sigma_t \geq 8$. Summaries of fit results for a range of n_t are shown in Figures 7-6(a) & (b). Clearly some systematic difference exists between the two beyond the statistical errors. It is possible to estimate the amount of the difference due to systematic effects by considering the shift $\sigma_{\tau,sys}$ necessary for agreement to within one standard deviation. An expression for the relative lifetime difference can be written as :

$$(\tau_{K\pi} - \tau_{K3\pi})^2 = \sigma^2_{st,K\pi} + \sigma^2_{st,K3\pi} + \sigma^2_{sy,K\pi} + \sigma^2_{sy,K3\pi}$$

where σ_{st} are statistical errors, and σ_{sy} refers systematic errors assumed to be the same for the two modes. Using the full statistical errors computed in section 7.4 and this equation, a complete set of uncertainties can be reported for the fit at $n_t = 8$.

$$\tau_D = 0.431 \pm .014 \pm .023 \quad \text{picoseconds}$$

The first uncertainty is a full statistical error and the second is the systematic error obtained through the method just described. Thus the measurement uncertainty is comparable to all previous D° lifetime measurements combined (see

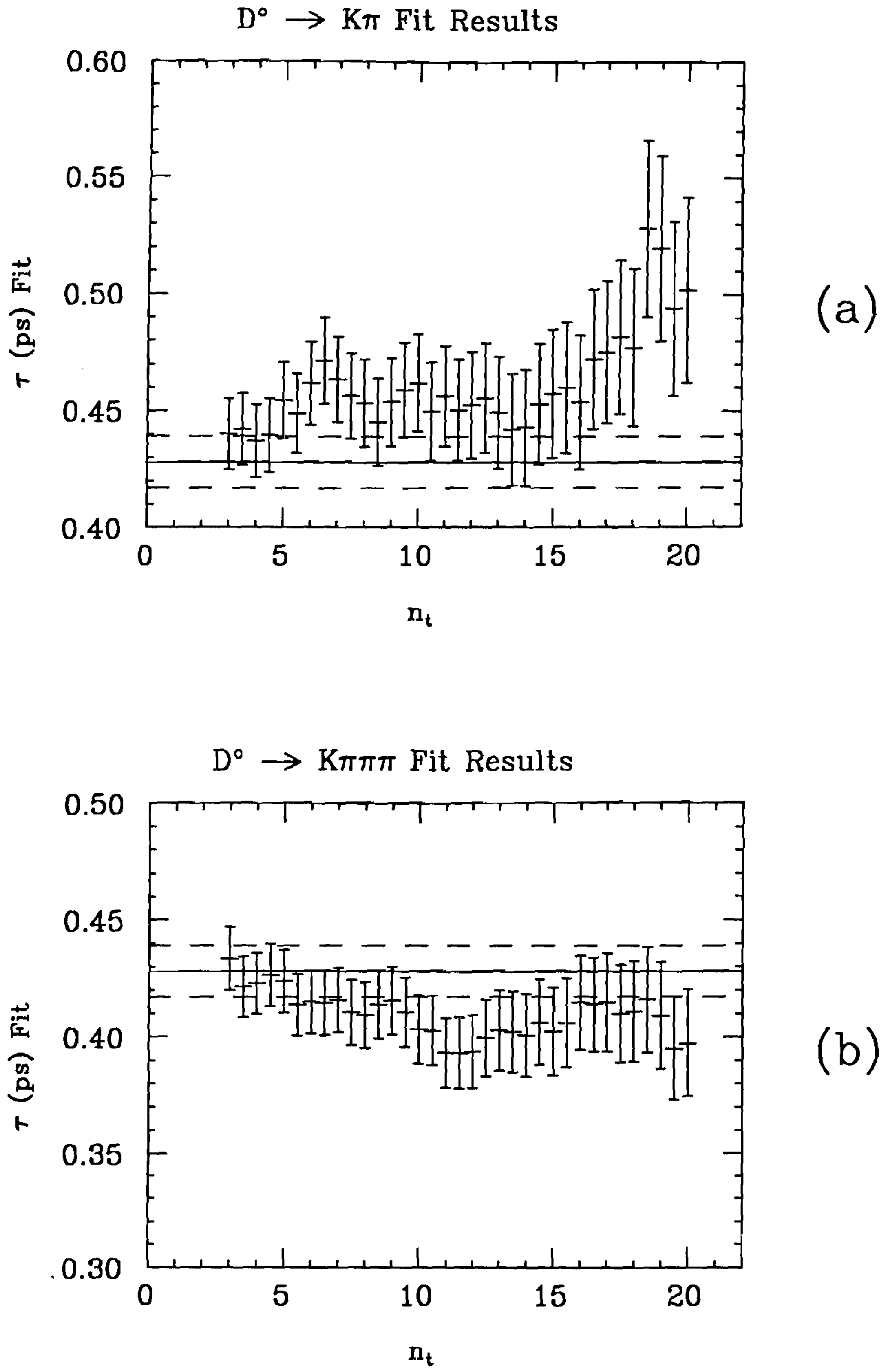

Figure 7-6 : Fit results separated into the Kπ and Kπππ decay modes.

Figure 7-4(b)) ! The systematic uncertainty occurs at about $1\frac{1}{2}$ standard deviations, so a low level systematic problem may exist. One possible source is now discussed.

7.5.2 Source of Systematic Problems

The estimate of the systematic uncertainty has been based entirely on relative differences, ignoring shared effects of the two decay modes. The reasoning behind this is that the dominant source of systematic uncertainty is probably related to the lifetime distribution of the background. Background events are the one aspect of the lifetime fit which is not simulated by the Monte Carlo. The sideband method of describing the background works well only when the lifetime distribution of events in the sidebands is the same on average as the distribution of background events in the signal region. Any variation in the mean lifetime of the background across the invariant mass spectrum would be rather suggestive of a systematic problem.

In view of the statement, the lifetime distributions of sideband regions at $t/\sigma_t \geq 8$ were fit using the maximum likelihood method described above, ignoring the N_i^{sb} contributions. Since background events are not expected to exhibit pure exponential behavior, the fit was approximated by two pure exponentials in separate lifetime regions. The distributions and fits are shown in Figure 7-7. Figures 7-7(a) & (b) are the lifetime distributions of low ($-12 < \Delta m/\sigma_m < -8$) and high ($8 < \Delta m/\sigma_m < 12$) sidebands respectively for the Kπ decay mode. Figures 7-7(c) & (d) are the same for the K$\pi\pi\pi$ decay mode. There does not appear to be any gross differences between the low and high sideband distributions in either decay mode. This tends to rule out any obvious problems with the sideband method of fitting. However several interesting points are apparent in these figures.

First of all double exponential fits appear very good at describing the background distribution, especially in the K$\pi\pi\pi$ decays. This suggests there may be two basic sources of background. The short lived background is consistent with

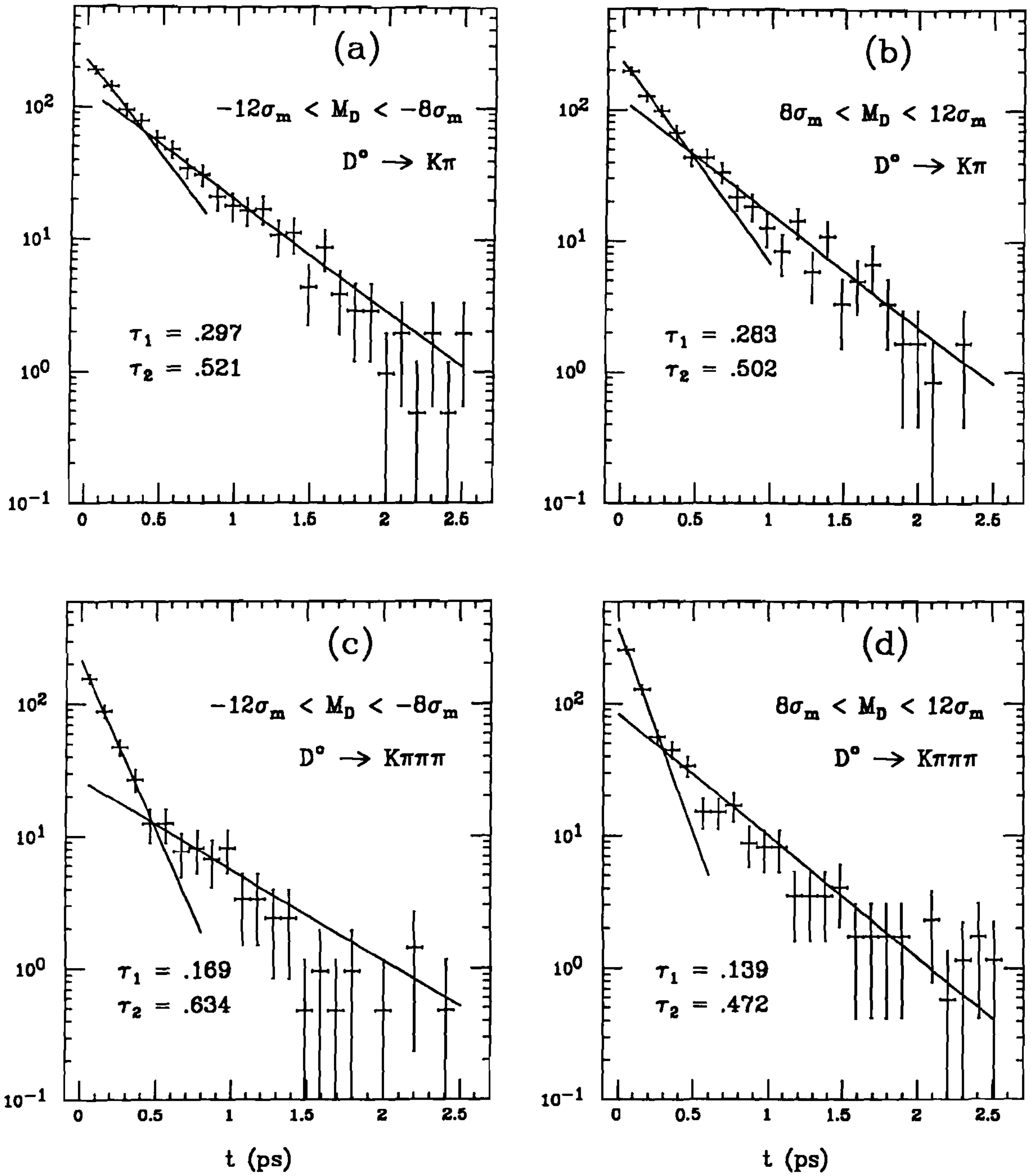

Figure 7-7 : Lifetime distribution of background events from sideband regions.

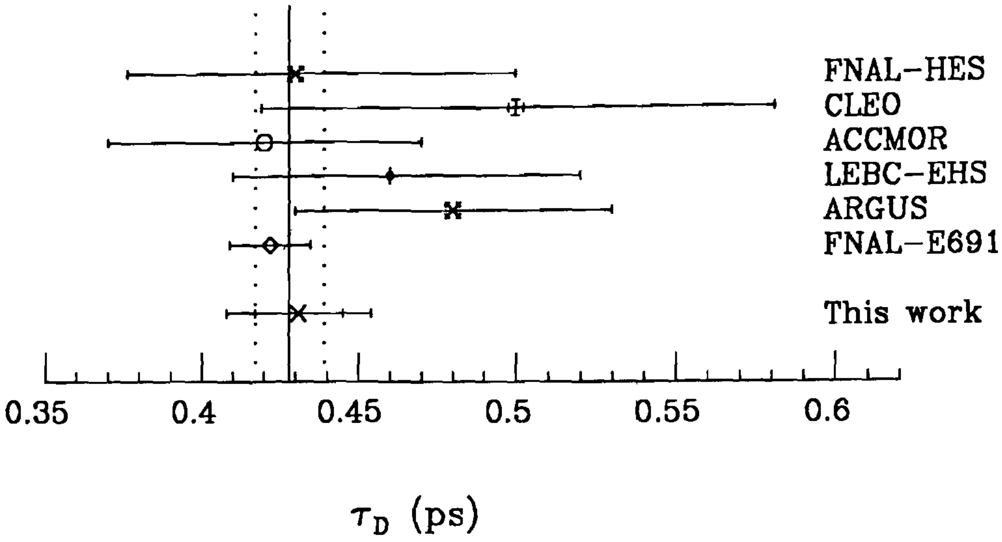

Figure 7-8 : Comparison of D° mean lifetime results with those of recent experiments [8,25,26,27,28,29,30]. The world average is indicated by the line.

being purely combinatoric. The mean lifetime of the long lived component, given by τ_2 in the figures, is curiously near that of the D° meson. This is exactly the conclusion reached in the signal/background study reported in section 3.13 for the case of $D^0 \rightarrow K\pi$. The explanation posed in section 3.13 for this apparent difference is that the probability of forming a good 2-track vertex from a random set of tracks is much higher than a 4-track vertex. In fact the distributions in Figures 7-7(c) & (d) show that long lived background does exist at a low level in the $K\pi\pi\pi$ decay mode. It is quite likely, then, that "false charm vertex" background in D° meson events is the source of low level systematic differences observed in the two decay modes. An appropriate change in the analysis technique to reduce this background should therefore reduce systematic uncertainties in measuring the mean lifetime.

7.6 Conclusions

The mean D° lifetime has been found to be

$$\tau_D = 0.431 \pm .014 \pm .023 \quad \text{picoseconds}$$

A statistical uncertainty of 0.014 picoseconds is obtained from the lifetime fit and the statistical contributions of sideband and Monte Carlo events. The 0.023 picosecond systematic uncertainty is estimated from independent lifetime measurements of the $D^\circ \rightarrow K\pi$ and $D^\circ \rightarrow K\pi\pi\pi$ decay modes.

A comparison has been made with recent experimental measurements of the mean D° lifetime, and is shown in Figure 7-8. The figure exhibits good agreement with other experiments, as well as the excellent precision of the E687 measurements made possible by the SSD system. The measurement presented here also agrees well with the D° lifetime found using the *free form* vertex algorithm[11] (see section 3.2). The capability of precise lifetime measurements brought about by the fine lifetime resolution has been applied to $D^\pm$, $D_s^\pm$ and $\Lambda_c^\pm$ lifetimes as well.[4,31] All are in excellent agreement with recent measurements.

Chapter 8

Conclusions

In conclusion, evidence has been presented for about 10,000 reconstructed D mesons in E687, of which 9700 are in the decay modes $D^\circ \rightarrow K\pi$, $D^+ \rightarrow K\pi\pi$, and $D^\circ \rightarrow K\pi\pi\pi$. Several Cabbibo suppressed decay modes of the D° were observed as well.

Approximately equal numbers $D^{\star+}$ and $D^{\star-}$ mesons were observed in the E687 data sample. The ratio $N(D^{\star-})/N(D^{\star+})$ was found to be $0.93 \pm .08$ which suggests a low level ($< 10\%$) of associated production.

A measurement was also made of the fraction of inclusive D° mesons resulting from $D^{\star\pm}$ decays. This fraction was found to be $.237 \pm .013$ which agrees with the simple spin counting prediction of $.27 \pm .03$.

The branching ratio $\Gamma(D^\circ \rightarrow K\pi\pi\pi)/\Gamma(D^\circ \rightarrow K\pi)$ has been measured over a range of $D^\star$ and D° momenta and has been shown to be in good agreement with the world average ratio of $2.10 \pm .20$.

The branching ratio $\Gamma(D^\star \rightarrow (KK)\pi)/\Gamma(D^\star \rightarrow (K\pi)\pi)$ has been measured to be $0.118 \pm .032$ which confirms earlier results of a surprisingly high ratio. The branching ratio $\Gamma(D^\circ \rightarrow \pi\pi\pi\pi)/\Gamma(D^\circ \rightarrow K\pi\pi\pi)$ has also been measured. The value $0.114 \pm .026$ is somewhat more accurate than has previously been reported. Both of these branching ratios indicate decay processes are occurring which are somewhat more complicated than suggested by the lowest order spectator diagram.

Approximately 50 out of 7700 $D^\circ \rightarrow K\pi$, $D^+ \rightarrow K\pi\pi$, and $D^\circ \rightarrow K\pi\pi\pi$ events were observed with two recconstructed D mesons. This is in good agreement with the anticipated number based on the Monte Carlo.

The cross section for D° inclusive and $D^\star$ production in the combined $K\pi$ and $K\pi\pi\pi$ decay modes was measured as a function of photon energy and Feynman x. Cross sections were reported at photon energies higher than any previous measurements and appear to be consistent with predictions of the Photon-Gluon Fusion model. The poor resolution in the measurement of the photon energy dominates statistical errors. Systematic errors were also sizeable, due in large part to uncertainties in the incident photon luminosity. Despite the poor resolution it was possible to confirm a somewhat surprising result of earlier experiments that the distribution of D mesons peaks in the region between $x_f = 0.2$ and $x_f = 0.3$. Assuming diffractive production of charm, this implies a large fraction of charm quark momentum is lost in the hadronization process.

Finally, measurements of the mean D° lifetime were presented based on a binned maximum likelihood fit of 2913 events. The result of $\tau_D = 0.431 \pm .010 \pm .023$ picoseconds is consistent with the present world average. The statistical uncertainty of 1.0×10^{-14}s is comparable to the combined uncertainty of previous measurements. The systematic uncertainty was determined by comparing lifetime measurements from two independent D° decay samples.

Appendix A

Čerenkov Algorithm

The heart of the Čerenkov algorithm, as discussed in section 3.6, is the procedure for deciding the *on/off/confused* status of individual tracks passing through the Čerenkov system. This decision is based on matching Čerenkov cells with individual tracks and checking the on/off status of individual PMT's. A Čerenkov cone associated with a track may overlap several cells at once. If the track were well isolated in a perfect set of detectors the cells might be expected to all have the same response, on or off. In the real situation the cells will not all agree because of confusion of light from multiple tracks, detector noise and detector inefficiency. In order to properly weight the importance of each cell's response it is first necessary to know how much light was anticipated in each.

A.1 Calculation of Anticipated Light Yield

The point at which a track intersects the cell plane of a Čerenkov detector is defined as the center of its Čerenkov cone in the absence of magnetic fields, and can be found by extrapolation of the track. The angle of incidence at the cell plane is rather small, so it is possible to assume that the cone is a perfect circle centered at the origin of a coordinate system. Each cell which could possibly overlap the cone is considered one at a time. Were the cone completely contained in that cell the amount of anticipated light, measured in photoelectrons, would be completely determined by the particle hypothesis, the momentum of the particle, and the calibrated maximum yield of the cell. The problem of determining the amount of light in a cell consequently involves computing the fraction of total light which falls into a rectangular cell (an approximation) extending from X_1 to X_2 and Y_1 to Y_2. The discussion of this computation is broken into four parts :

1. It will be shown how the light fraction within an arbitrary rectangle can be computed from the sum of "corner" functions at each of the rectangle corners.

2. These corner function will be derived.
3. A method for storing the corner function in a table and performing a two dimensional linear interpolation to rapidly compute light fractions is described.
4. Modifications of these techniques are discussed, which cover rectangular holes in mirrors and the effects of plane mirrors inclined at 45 degees.

1. Corner Functions

Denote the normalized light density as $\rho(x, y)$. Because the center of the light cone is located at the origin , the density has the symmetry: $\rho(\pm x, \pm y) = \rho(x, y)$ Assume that the coordinates are ordered such that: $X_2 \geq X_1$, $Y_2 \geq Y_1$. The fraction of light within a rectangle is then:

$$F = \int_{X_1}^{X_2} dx \int_{Y_1}^{Y_2} dy \ \rho(x, y)$$

These integrals can be referenced to the origin via:

$$f = \left(\int_0^{X_2} dx - \int_0^{X_1} dx \right) \left(\int_0^{Y_2} dy - \int_0^{Y_1} dy \right) \ \rho(x, y)$$

Defining the corner function $I(X, Y)$ as follows:

$$I(X, Y) \equiv \int_0^{X} dx \int_0^{Y} dy \ \rho(x, y)$$

the fraction can be written as:

$$F = I(X_2, Y_2) + I(X_1, Y_1) - I(X_1, Y_2) - I(X_2, Y_1)$$

Because of the reflection symmetries of the light density, the corner function for any quadrant can be obtained from the positive X and Y quadrant. As an example consider I (X , Y) with $X < 0$:

$$I(X,Y) = \int_{0}^{-|X|} dx \int_{0}^{Y} dy \; \rho(x,y)$$

one can change variable ($x \to -x$) to obtain:

$$I(X,Y) = -\int_{0}^{|X|} dx \int_{0}^{Y} dy \; \rho(-x,y) = -I(|X|,Y)$$

In general then:

$$I(X,Y) = S_X \; S_Y \; I(|X|,|Y|)$$

where S_X and S_Y are the sign of X and Y (That is $S_X, S_Y = \pm 1$ depending on the sign of X and Y). Using these formulae one can compute the light yield for an arbitrary rectangle as a sum over corner functions:

$$F = \sum_{m=1}^{2} \sum_{n=1}^{2} (-1)^{m+n} \; S_{X_m} S_{Y_n} \; I(|X_m|,|Y_n|)$$

2. Derivation of the Corner Function

In calculating the light sharing function I($|X|$,$|Y|$), a light cone of unit radius is used where x=$\frac{|X|}{R}$ and y=$\frac{|Y|}{R}$. I(x,y) is defined to be the amount of light left of and below the corner located at (x,y) as seen in Figure A-1. It is calculated by integrating the normalized light density

$$dI = \frac{d\phi dr}{2\pi}$$

over that area and has a maximum value of $\frac{1}{4}$.

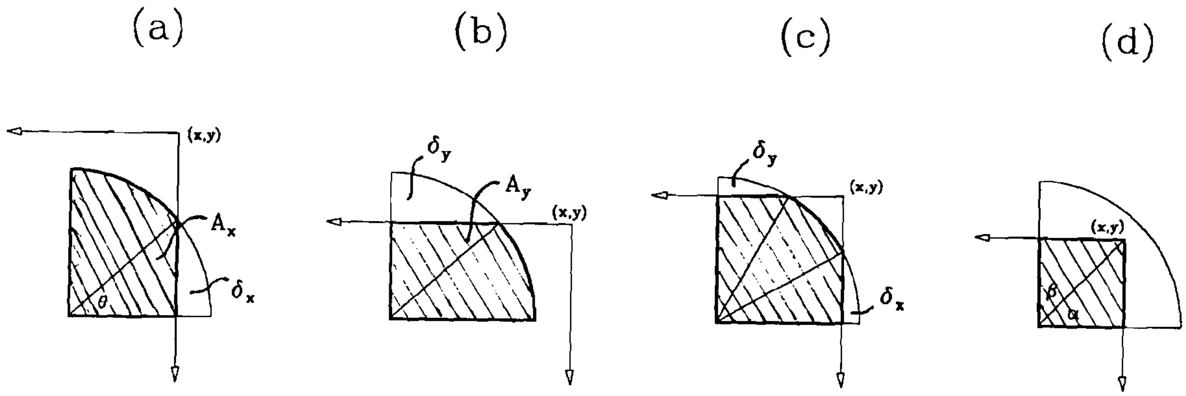

Figure A-1 : Four basic corner functions.

There are four distinct cases to be considered when finding I(x,y) based on the location of the corner with respect to the cone. These are illustrated in Figures A-1(a) through A-1(d).

The value of I(x,y) in all the cases are found by integrating over two basic shapes. The first of these is marked A_x in Figure A-1(a) and is found to be

$$\begin{aligned} A_x &= \frac{1}{2\pi}\int_0^\theta d\phi \int_0^{\frac{x}{\cos\phi}} dr = \frac{x}{2\pi}\int_0^\theta \frac{d\phi}{\cos\phi} \\ &= \frac{x}{2\pi}\ln(\sec\theta + \sqrt{\sec^2\theta - 1}) \end{aligned}$$

The second is the arc equal to the sum of A_x and δ_x. Its light fraction is then

$$A_x + \delta_x = \frac{1}{2\pi}\int_0^{\arccos x} d\phi \int_0^1 dr$$

so that

$$\delta_x = \frac{1}{2\pi}\arccos x - A_x$$

For the case where y>1 and x<1, shown in Figure A-1(a), the light sharing fraction is $F_a = \frac{1}{4} - \delta_x$ and $\sec\theta = \frac{1}{x}$. Solving for δ_x and substituting:

$$F_a = \frac{1}{4} - \frac{1}{2\pi}[\arccos x - x\ln(\sec\theta + \sqrt{\sec^2\theta - 1})]$$

$$= \frac{1}{2\pi}\left[\arcsin x + x\ln\left(\frac{1}{x} + \sqrt{\frac{1}{x^2} - 1}\right)\right] \tag{A.1}$$

The case where x>1 and y<1, shown in Figure A-1(b), is found, by symmetry, to be

$$\begin{aligned} F_b &= \frac{1}{4} - \delta_y \\ &= \frac{1}{2\pi}\left[\arcsin y + y\ln\left(\frac{1}{y} + \sqrt{\frac{1}{y^2} - 1}\right)\right] \end{aligned} \tag{A.2}$$

When x,y<1 and $x^2 + y^2 > 1$, the situation shown in Figure A-1(c) exists such that $F_c = \frac{1}{4} - \delta_x - \delta_y$. This gives

$$\begin{aligned} F_c = \frac{1}{4} + \frac{1}{2\pi}\Big[& x\ln\left(\frac{1}{x} + \sqrt{\frac{1}{x^2} - 1}\right) \\ & + y\ln\left(\frac{1}{y} + \sqrt{\frac{1}{y^2} - 1}\right) - \arccos x - \arccos y\Big] \end{aligned} \tag{A.3}$$

The final case, shown in Figure A-1(d), exists when $x^2 + y^2 < 1$. The overall fraction is just the sum of the two sections so that

$$F_d = \frac{1}{2\pi}\left[x\ln(\sec\alpha + \sqrt{\sec^2\alpha - 1}) + y\ln(\sec\beta + \sqrt{\sec^2\beta - 1})\right.$$

Substituting $\tan\alpha = \frac{y}{x}$ and $\tan\beta = \frac{x}{y}$

$$F_d = \frac{1}{2\pi}\left[x\ln\left(\sqrt{1 + \frac{y^2}{x^2}} + \frac{y}{x}\right) + y\ln\left(\sqrt{1 + \frac{x^2}{y^2}} + \frac{x}{y}\right)\right] \tag{A.4}$$

3. Two Dimension Linear Interpolation of the Corner Function

In order to save time in evaluation of the corner functions a two dimension linear interpolator routine was written which used values of the corner function evaluated on a two dimensional lattice. The coordinates of the corner function were normalized to the Cerenkov radius as described above so that I (X,Y) was stored in 0.1 steps with $0 \leq X \leq 1$ and $0 \leq Y \leq 1$.

The interpolation was performed by finding the lattice cell appropriate to a given (X,Y) argument. The form of the interpolation was assumed to be linear in x and y which are coordinates relative to the lattice cell center :

$$I(X,Y) = \alpha + \beta x + \gamma y$$

where α , β , γ are essentially fits to the function evaluated at four corners of the lattice cell defined in the figure.

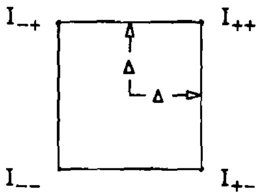

The fit is to the form:

$$I\pm\pm \; = \; \alpha \pm \beta \, \Delta \pm \gamma \, \Delta$$

where the lattice spacing is 2Δ by 2Δ. This fit has one degree of freedom since their are four function evaluations and three linear parameters. The fit parameters are obtained by minimizing the χ^2 given by:

$$\chi^2 = (\alpha - \beta\Delta - \gamma\Delta - I_{--})^2 + (\alpha + \beta\Delta - \gamma\Delta - I_{+-})^2 + \cdots$$

The results of this fit are:

$$\alpha = \frac{I_{++} + I_{+-} + I_{-+} + I_{--}}{4} \quad \beta = \frac{I_{++} + I_{+-} - I_{-+} - I_{--}}{4\Delta}$$

$$\gamma = \frac{I_{++} + I_{-+} - I_{+-} - I_{--}}{4\Delta}$$

The values of α , β , γ were stored for each lattice cell in order to further accelerate the interpolation procedure.

In addition to the two dimensional interpolation procedure , one dimensional interpolation data was stored for cases where $|X| > 1$ or $|Y| > 1$ and thus $I(X,Y)$ became a function of X or Y only.

4. Modifications to Light Fractions

The light sharing algorithm was used with several simple modifications to cover the cases of rectangular holes in the light collection cells (to allow uninteracted beam to pass through) and for the case of light collection via thin mirrors inclined at 45 degrees with respect to the beam axis. In both cases one computes the collected light fraction by subtracting an appropriate uncollected fraction of light from that fraction collected in the absence of such effects. The case of the rectangular hole is obvious while the case of the 45 degree mirrors is less so.

The use of 45 degree mirrors creates two effects. The first effect is that active radiator length and photoelectron yield depends on the the location (typically $|X|$) of the track intersection with the mirror. The second effect is that the projected light pattern at the light collection image plane is a donut rather than a space filling disk. The outer radius of the donut is proportional to the total optical path from the the upsteam window to the location of the light collection cells. The inner radius is proportional to the fraction of this path which does not form active radiator – that is the optical path the light takes after the track strikes the mirror until it strikes the collection plane. This effect can be handled by computing the light yield assuming an effective radiator equal to the total optical path and then subtracting out the light from the inactive optical path. In other words, compute the light from the complete donut and subtract out the light in the donut hole. In most designs the total light in the donut will be independent of the track-mirror intersection; while the light in the donut hole will maximize towards the median plane of the counter.

A.2 Čerenkov Track Status

This section discusses the specific approach used in determining the *on/off/ confused* status of a track in a given detector. A diagram of the portion of the

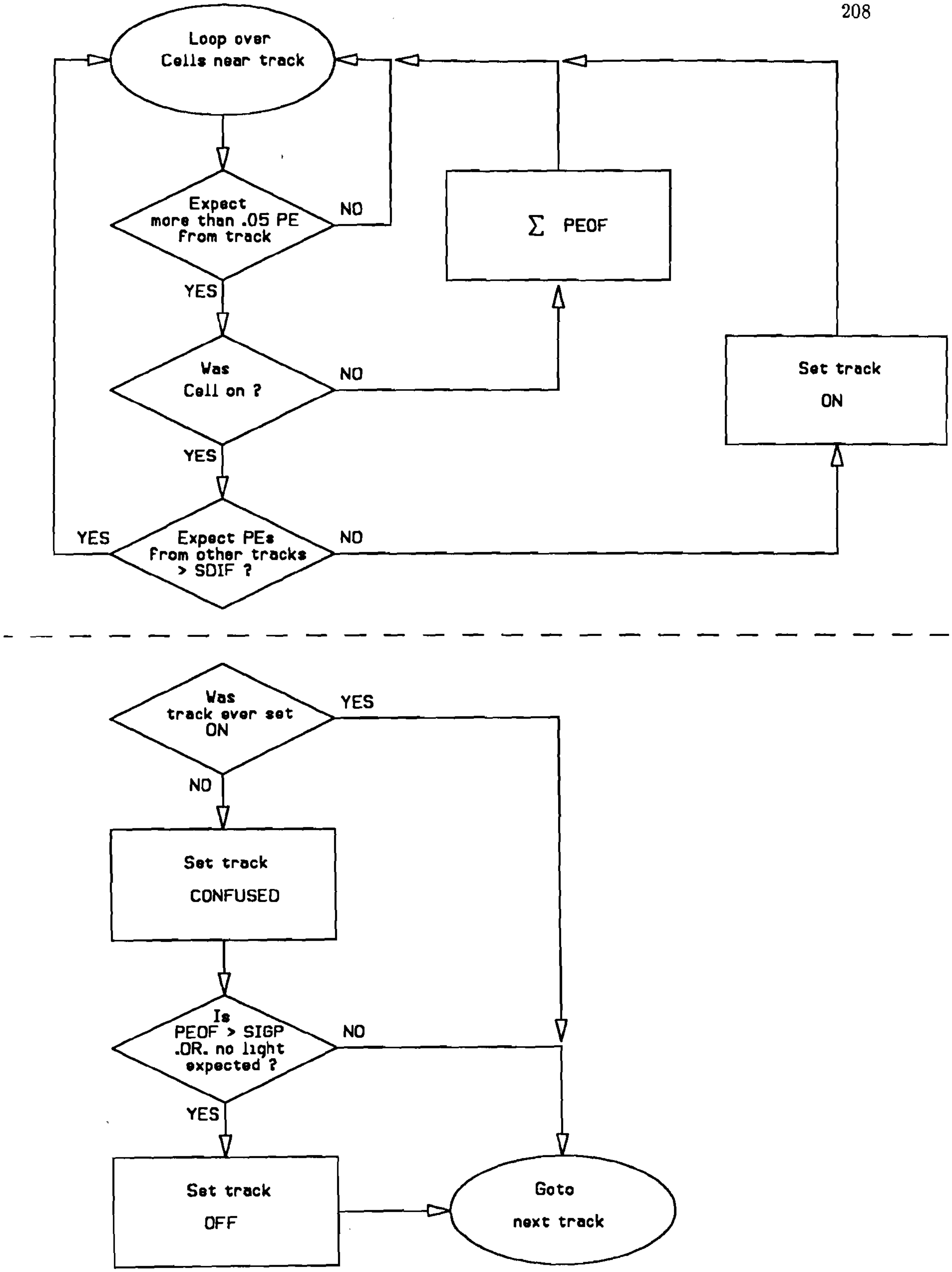

Figure A-2 : Schematic of *track status* portion of Čerenkov algorithm.

algorithm dealing with this issue is shown in Figure A-2. The status of a track is found by first calculating the amount of light expected in each cell under the electron or pion hypothesis. This calculation was discussed in Appendix A.1 . Each cell is considered in turn and is checked as to whether or not a phototube pulse was detected. For isolated tracks the procedure is simple. The track status follows from the cell status. Only one cell need be on for the track to be *on*. All cells overlapping the Čerenkov cone must be off for the track to be called *off*. But tracks are often not well isolated. With a typical charged track multiplicity in a charm event of almost 10, Čerenkov light cones from more than one track often illuminate a single cell. It then becomes difficult to attribute the detected light to one track or the other. Light from a single track generally falls into more than one cell, so often at least one unconfused cell exists to make the decision. Frequently all cells are confused though. The solution used in these cases is to allow low levels of confusion, and make the on/off decision for the track assuming no confusion had occurred. As this level (determined by the SDIF cut) increases, more tracks will be called *on* which might otherwise be left as confused. The affect of a mistake due to a non-zero SDIF is to identify a track as *on* which was really *off*, but never visa versa. This approach then reduces the likelihood of incorrectly identifying a light particle, such as a pion, as a heavier particle, such as a kaon. This is a desirable feature, but is done at the cost of efficiency for identifying heavy particles. The value of SDIF used in these analyses is 0.2 photoelectrons.

Another variable which significantly affects overall particle identification is the minimum light expected (SIGP) in an off cell for the track to be called *off*. A cell which detects no light but which should have seen light is allowed to call the track *off*. While light missing in one cell can never negate another on cell, it can be used to call the track *off* if all other cells were either off or confused. This again is a bias towards calling tracks *on*, as was discussed above. For each track a sum (called PEOF) is kept of the total number of photoelectrons which were expected in cells which were off. Only if this sum exceeds SIGP can the track be called *off*.

A.3 Tuning the Čerenkov Algorithm

Most aspects of Čerenkov identification are fixed by the capabilities and specifications of each Čerenkov detector. However decisions related to the track status are made in the Čerenkov algorithm via the variables SDIF and SIGP. Both variables were tuned using pions and protons from neutral vee decays, specifically the ones shown in Figure 3-1. By using both these particles it was possible to study the trade-off between light particle identification and heavy particle identification which these variables control. The identity and momentum of the particle in question tells if a particular detector should return an *on* status or an *off* status. Comparing this with the actual detector response as a function of the SDIF or SIGP value facilitates the choice of an optimal value. For example the choice of SIGP is made on the basis of the histograms in Figure A-3. Figure A-3(a) shows the PEOF distribution for pions with momenta above the pion threshold of each of the three detectors. These entries should all be below the SIGP cut value. Figure A-3(b) shows the PEOF distribution of protons with momenta below the proton threshold of each of the three detectors. These entries should all be above the SIGP cut value. Clearly there is no single value for any one of the detectors which satisfies both these requirements. The value of SIGP was chosen as 2.0 photoelectrons in all three detectors in an attempt to minimize incorrect identification. The value of SIGP is shown in each of the histograms.

These variables were also studied in the context of the entire Čerenkov system response. Studies of the identification code ISTAT were made while varying SIGP and SDIF, again in an effort to maximize the positive identification of pions and protons. The overall ability of the Čerenkov system to identify particles is discussed in section 3.14 .

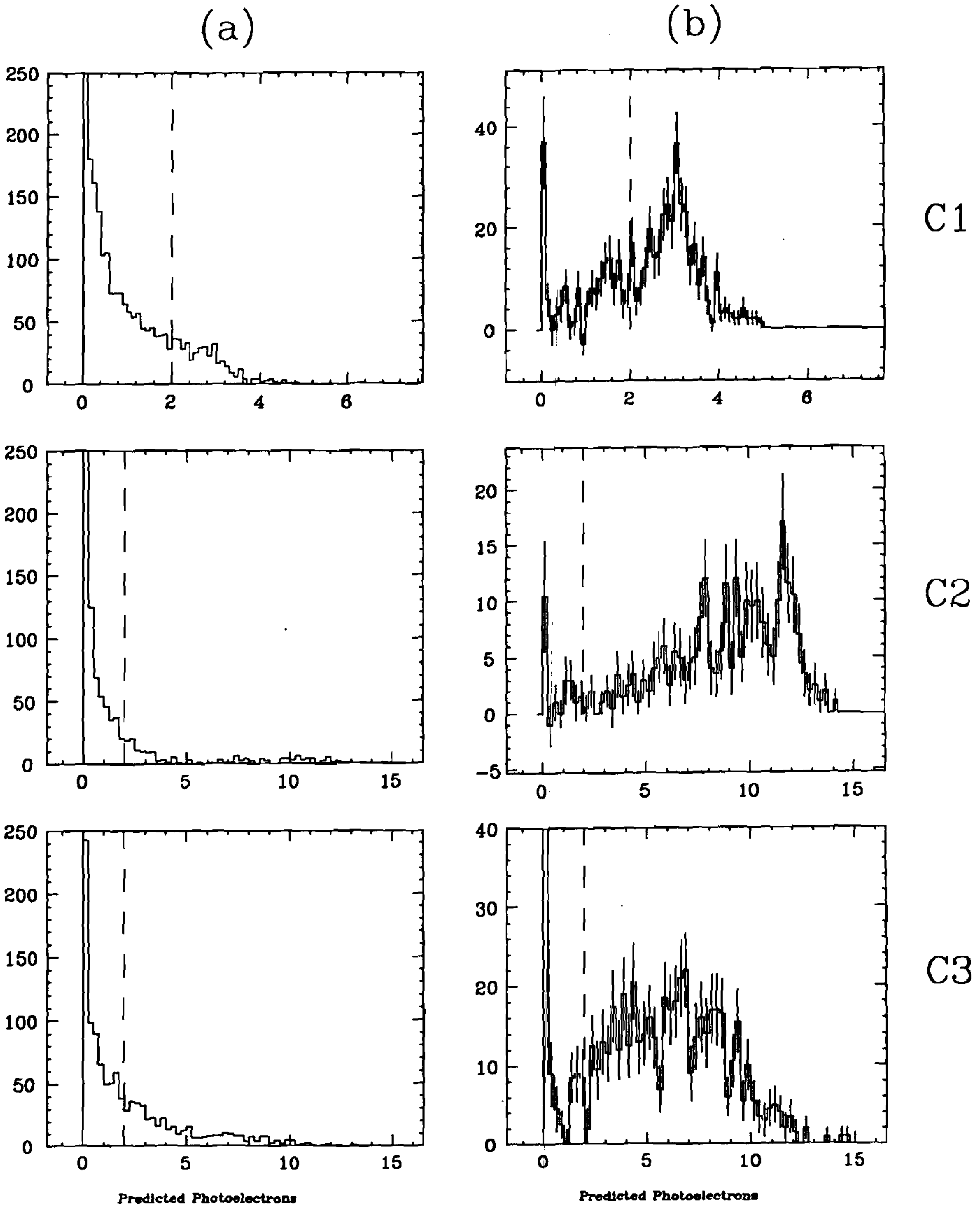

Figure A-3 : PEOF distribution for pions below threshold and protons above threshold in each of the three Čerenkov detectors.

Appendix B

K$\pi\pi\pi$ Production Dynamics

The Monte Carlo model of decay dynamics used in these analyses for all decay modes is one of isotropic decay in momentum phase space. Many of the D meson decay modes are known to have resonant substructure, so an isotropic decay model may be too naive. Such a simplification may be acceptable, though, if the anisotropies do not significantly affect the overall acceptance. This appendix explores whether or not such a simplification is acceptable in the decay mode D° → K$\pi\pi\pi$.

Recent results[32] have indicated that the decay dynamics of D° → K$\pi\pi\pi$ involve somewhat complex resonant structure. The various K$\pi\pi\pi$ decay modes with their various branching fractions are listed in Table B-1.

Table B-1 : Resonant Substructure of D° → K$\pi\pi\pi$.

Channel	Branching Fraction
4-body non-resonant	.233 ± .025 ± .10
$\bar{K}^{*0}\rho^0$ Longitudinal	.014 ± .009 ± .01
$\bar{K}^{*0}\rho^0$ Transverse	.152 ± .021 ± .05
$K^-a_1^+$	.442 ± .021 ± .10
$K_1^-(1270)\pi^+$	.113 ± .028 ± .04
$K_1^-(1400)\pi^+$	.011 ± .009 ± .03
$\bar{K}^{*0}\pi^+\pi^-$	.091 ± .018 ± .04
$K^-\rho^0\pi^+$ Transverse	.088 ± .023 ± .04

Since the decay into $K^-a_1^+$ dominates and is the most structured, it can be used as a test case to judge the extent to which the geometrical acceptance differs from the non-resonant decay. If this decay exhibits strong angular dependencies

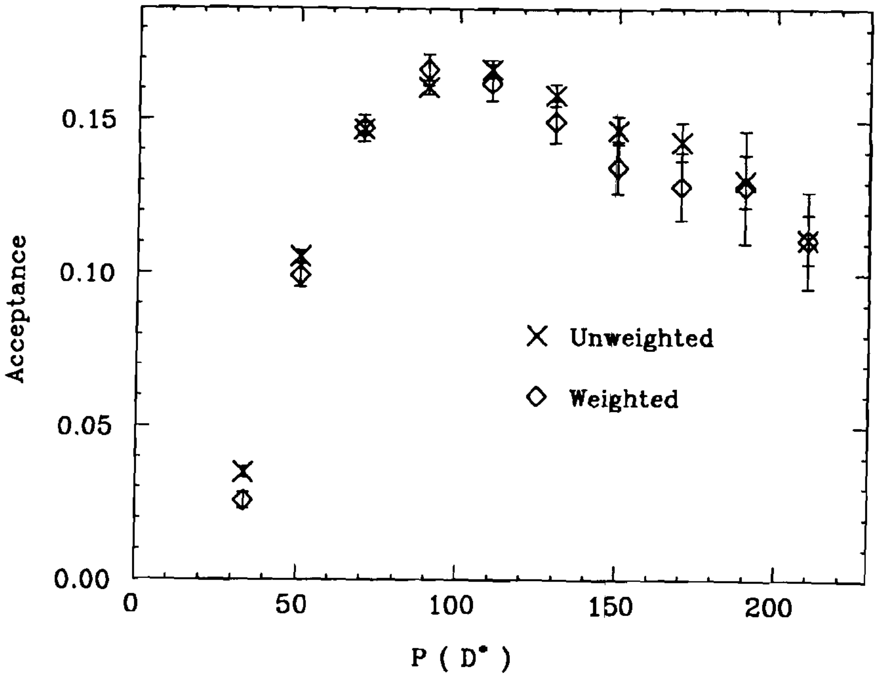

Figure B-1 : Comparison of weighted and unweighted D* → (Kπππ)π acceptances.

which are not modeled correctly in the Monte Carlo, then estimates of the Kπππ acceptance may be inaccurate.

The $a_1^{\pm}$ is a broad resonance which decays into $\rho\pi^{\pm}$. The amplitude for the entire process is therefore a product of two Breit-Wigners and angular factors. The expression for the decay amplitude involves two identical pions, and can therefore be symmetrized through their exchange. If indices 1 and 2 refer to the identical pions and index 3 to the opposite signed pion, the expression for the decay amplitude becomes

$$F \propto \frac{1}{s_{123} - (m_{a_1} - \frac{i\Gamma_{a1}}{2})^2} \left[\frac{\vec{P}_k \cdot (\vec{P}_{\pi_3} - \vec{P}_{\pi_2})}{s_{23} - (m_\rho - \frac{i\Gamma_\rho}{2})^2} + \frac{\vec{P}_k \cdot (\vec{P}_{\pi_3} - \vec{P}_{\pi_1})}{s_{13} - (m_\rho - \frac{i\Gamma_\rho}{2})^2} \right]$$

In calculating this amplitude, all 3-vector products are taken in the rest frame of the $a_1^{\pm}$.

To test the acceptance hypothesis the decay amplitude of $D^\circ \rightarrow Ka_1$ was used to alter the Monte Carlo distributions of the 3 pions relative to the kaon. Differences in the number of reconstructed events would then indicate that previous estimates of the $K\pi\pi\pi$ acceptance were misconceived. Instead of modifying the decay routine in the Monte Carlo, the D mesons were allowed to decay isotropically and were then weighted according to modulus of a properly normalized Ka_1 decay amplitude. An efficiency curve is obtained with the new decay amplitude which is directly comparable to the distribution, derived for an isotropic decay, presented in section 5.3 . Both these distributions, which reflect the complete analysis efficiencies for $D^\star$ mesons at $\ell/\sigma_\ell > 2$, are shown in Figure B-1 as a function of momentum. Very little difference is evident, and since these curves represent uncut efficiencies, differences will be even smaller once analysis cuts are employed. Systematic effects related to the simulation of D meson decays have therefore been neglected in all Monte Carlo simulations.

Appendix C

The ρ Matrix Fit

If two linear arrays n_i and C_α are related by a matrix $R_{i\alpha}$ through the equation

$$n_i = \sum_\alpha R_{i\alpha} C_\alpha$$

then the solution in terms of C_α, if $i = \alpha$, is just

$$C_\alpha = \sum_i R^{-1}_{\alpha i}\, n_i$$

In the more general case when $i \neq \alpha$, the solution for C_α will involve a fit. The condition must necessarily exist that $i \geq \alpha$ lest C_α be over-constrained. The fit is a minimization of the χ^2 (assuming Poisson errors on n_i)

$$\chi^2 = \sum_i \frac{(n_i - \sum_\alpha R_{i\alpha} C_\alpha)^2}{n_i}$$

whose solution can be written as

$$C_\alpha = \sum_i \rho_{\alpha i}\, n_i$$

where

$$\rho_{\alpha i} = \sum_i \sum_\beta \frac{H^{-1}_{\alpha\beta} R_{i\beta}}{n_i}$$

$$H_{\alpha\beta} = \sum_i \frac{R_{i\alpha} R_{i\beta}}{n_i}$$

Appendix D

Charm Cross Sections in the Monte Carlo

This discussion of how cross sections are dealt with in the Monte Carlo is broken into 3 sections. The first section describes the procedure for choosing a photon for charm production. A formula is obtained which relates Monte Carlo luminosity and charm yield to that of data. This relationship is used in the second section to introduce a scale factor used in the matrix de-convolution method. Section 3 discusses the cross section binning procedure used for the Monte Carlo cross section.

D.1 Photon Interactions

In simulating the photoproduction of a charmed particle, the Monte Carlo includes a simulation of the bremsstrahlung process producing photons. The bremsstrahlung of a 350 GeV electron (constituting a single event) in a 27 % radiator typically produces 2 - 3 photons with energy greater than 10 MeV. Each of these photons can potentially interact in the target to produce a charmed interaction. The Monte Carlo allows at most one photon-charm interaction per event, choosing the photon proportional to the assumed charm cross section. Additional charm interactions in the same event are disregarded, which without a correction would lead to an under-counting of the charm yield.

By artificially lowering the probability that photons interact to form charm particles, the level of additional interactions is reduced to a negligible level. A trial vertex is drawn uniformly in Z between the upstream end of the target and a distance

$$\Lambda = \Lambda_o \sigma_o / \sigma(\omega) \qquad (D.1)$$

downstream, where Λ_o is the physical length of the target, $\sigma(\omega)$ is the energy dependent cross section from the photon-gluon fusion model, and σ_o is a constant scale factor called the reference cross section. Vertices not falling in the physical target are rejected. If the value of σ_o (typically 1000 nb) is maintained at a level higher than the highest value of $\sigma(\omega)$ (typically 300 nb), the probability will always be less than 1 that a single charm interaction takes place. Since the photon-gluon fusion model for charm cross section rises with ω, this technique has the added advantage that the interaction probability is lowest at small ω, where multiple bremsstrahlung photons are most likely. As σ_o is raised, the number of incident photons necessary to produce a charm pair also increases. So as a practical matter, the size of σ_o beyond a certain point is driven by the available computing time.

The technique of drawing a trial vertex also allows for varying target topologies and beam profiles. Information on the various targets used in this run of the experiment are given in Table D-1.

Table D-1 : Target Information

target	ρ_i	Λ_o	# triggers
Be-5	1.848	4.06 cm	33.01×10^6
Be-4	1.848	3.25 cm	12.01×10^6
Si-Be	2.33/1.848	2.43 cm	9.44×10^6

In addition, the centering of the beam on the target is known to have varied throughout the run. These changes have been characterized by discrete run periods i where the target parameters are roughly constant. A population function describing the probability for finding a photon anywhere in a homogeneous target of length L is written in terms of the photon flux $\Phi(x, y)$ as

$$\mathcal{P}(x, y, z) = \frac{1}{L\, n_\gamma} \frac{\Phi(x, y)\rho(x, y, z)}{\bar{\rho}}$$

$$n_\gamma = \int d^2x\; \Phi(x, y)$$

where $\rho(x, y, z)/\bar{\rho}$ is 0 or 1 if $\vec{x}$ is inside or outside the physical target. The photon flux $\Phi(x,y)$ follows the parameterization of the photon beam discussed in section 4.1.2 . The population function can be generalized to one describing the probability that a photon is near an interaction center (i.e. a nucleus) at $\vec{x}$ in the highest density material, the Si-Be target, during run period i.

$$\mathcal{P}_i(x,y,z) = \frac{1}{\Lambda_o\, n_{\gamma,i}} \frac{\Phi_i(x,y)\rho_i(x,y,z)}{\rho_{Si}}$$

where Λ_o is the length of the Be-5 target (the longest target), and

$$\rho_i(\vec{x}) = \begin{cases} 0 & \text{if outside target} \\ \rho_{Si} & \text{if inside Si section} \\ \rho_{Be} & \text{if inside Be section} \end{cases}$$

The ratio $\rho_i(\vec{x})/\rho_{Si}$ gives the probability that an interaction will take place in a given material, and $\int d^3x\mathcal{P}_i(x,y,z)$ is the probability (with a maximum value of 79 %, corresponding to the Be-5 target) of an interaction occurring in the target used in run period i. But instead of normalizing $\mathcal{P}$ to the full physical length Λ_o, it is normalized to the arbitrary length Λ given in Equation D.1 such that

$$\mathcal{P}_i(x,y,z) = \frac{1}{n_{\gamma,i}} \left(\frac{\sigma(\omega)}{\Lambda_o\sigma_o}\right) \frac{\Phi_i(x,y)\rho_i(\vec{x})}{\rho_{Si}} \qquad (D.2)$$

Since $n_{\gamma,i}\,\mathcal{P}_i(x,y,z)$ is the probability that $n_{\gamma,i}$ photons at $\vec{x}$ will each interact to produce charm, Equation D.2 can be rearranged to yield the Monte Carlo prediction of the total number of charm pairs produced during the run.

$$N_c^{mc} = \left(\frac{\sigma(\omega)}{\Lambda_o\sigma_o}\right) \frac{1}{\rho_{Si}} \sum_i \int d^3x\; \Phi_i(x,y)\rho_i(\vec{x}) \qquad (D.3)$$

In data, the probability that an incident photon interacts in a distance dz to form charm is

$$d\mathcal{P}_{c,i}(\vec{x}) = \left(\frac{\mathcal{N}_a}{A_i}\right) \sigma_{c,i}\, \rho_i(\vec{x}) dz$$

where $\sigma_{c,i}$ is the true charm cross section per nucleus in the target material used in period i. Convoluting this with the photon flux;

$$dn_{c,i} = \Phi_i(\vec{x})\, d\mathcal{P}_{c,i}(\vec{x})$$

and summing over run periods;

$$N_c^{dat} = \sum_i \left(\frac{\mathcal{N}_a}{A_i}\right) \sigma_{c,i} \int d^3x\ \Phi_i(\vec{x})\rho_i(\vec{x}) \qquad (D.4)$$

If the assumption is made that

$$\sigma_c^{Be} \simeq \frac{A_{Be}}{A_{Si}}\, \sigma_c^{Si}$$

then Equation D.4 becomes

$$N_c^{dat} = \left(\frac{\mathcal{N}_a}{A_{Si}}\right) \sigma_c^{Si} \sum_i \int d^3x\ \Phi_i(x,y)\rho_i(\vec{x}) \qquad (D.5)$$

If the photon flux and target configuration in each run period is simulated in Monte Carlo to match that of data, then

$$\frac{\int d^3x\ \Phi_i(x,y)_{dat}\ \rho_i(\vec{x})_{dat}}{\int d^3x\ \Phi_i(x,y)_{mc}\ \rho_i(\vec{x})_{mc}} = \frac{N_\gamma^{dat}}{N_\gamma^{mc}}$$

N_γ^{dat} and N_γ^{mc} can refer to any luminosity scale, such as from the BGM scaler, provided the luminosity monitor is adequately simulated in data. Dividing Equation D.3 and Equation D.5 yields a relation between N_c^{dat} and N_c^{mc}.

$$N_c^{dat} = \left(\frac{\mathcal{N}_a}{A_{Si}}\right) \sigma_c^{Si}\ \frac{\Lambda_o \sigma_o \rho_{Si}}{\sigma_{mc}(\omega)} \left(\frac{N_\gamma^{dat}}{N_\gamma^{mc}}\right) N_c^{mc} \qquad (D.6)$$

Then if the relation

$$\sigma_{mc} \models \frac{\sigma_c}{A}$$

were true, Equation D.6 would define a scale factor relating the number of charm events expected in data given the luminosity and event yield in the Monte Carlo.

$$N_c^{dat} = \left\{ \mathcal{N}_a \sigma_o \Lambda_o \rho_{Si} \left(\frac{N_\gamma^{dat}}{N_\gamma^{mc}} \right) \right\} N_c^{mc} \tag{D.7}$$

D.2 ρ Matrix Scaling

The relation involving the ρ matrix and C_α in Equation 6.5 is strictly true only when applied to Monte Carlo events. This is because the amount of Monte Carlo charm produced per η_{mc} is far greater than the actual charm produced per η_{data}. So if Equation 6.5 is to be used with data to obtain an actual cross section, each $\rho_{\alpha i}$ must be scaled appropriately. The relationship between charm yields in Monte Carlo and data is given by Equation D.7 :

$$\begin{aligned} n_i^{dat} &= \mathcal{N}_a \, \varrho_o \, L \, \sigma_o \left(\frac{\eta_{data}}{\eta_{mc}} \right) n_i^{mc} \\ &= g \, n_i^{mc} \end{aligned}$$

which gives the predicted yield in data for a given yield of Monte Carlo events in terms of the Monte Carlo luminosity η_{mc} and the actual photon luminosity η_{data}. In these cross section calculations, the luminosity is measured by the BGM scaler. The ρ matrix is such that it will return the Monte Carlo cross section when applied to generated events :

$$C_\alpha = \sum_i \rho_{\alpha i} \, n_i^{mc} \tag{D.8}$$

If the data were to yield the same cross section in a bin α as the Monte Carlo, the relation would be

$$C_\alpha = \frac{1}{g} \sum_i \rho_{\alpha i} \, n_i^{dat} \tag{D.9}$$

The cross section will be reported per beryllium nucleus not per nucleon as is done in the Monte Carlo, so an additional factor A_{Be} must be included. This means that the Monte Carlo generated ρ matrix will undergo the scaling

$$\rho_{\alpha i} \longrightarrow \left\{ \left(\frac{A_{Be}}{\mathcal{N}_a} \right) \frac{1}{\varrho_o \, L \, \sigma_o} \left(\frac{\eta_{mc}}{\eta_{data}} \right) \right\} \rho_{\alpha i}$$

before being applied to data.

$$\begin{aligned} \sigma_o &= 1000 \text{ nb/nucleon} \\ L &= 4.06 \text{ cm} \\ \rho_o &= 1.848 \text{ g/cm}^2 \\ A_{Be} &= 9 \text{ nucleons/nucleus} \\ \mathcal{N}_a &= 6.023 \times 10^{23} \text{ nucleons/g} \\ \eta_{mc} &= 3,350,686 \quad \text{BGM counts} \\ \eta_{data} &= 2.07 \times 10^{11} \quad \text{BGM counts} \end{aligned}$$

The value entered for η_{data} includes a correction for the live time of the master gate. The scaling factor is evaluated as

$$\frac{1}{g} = 32.2$$

This is the factor used when reporting the sum of particle and anti-particle cross sections for producing D mesons which subsequently decay into specific final states. A prediction of the total D* or D$^\circ$ cross sections must include the overall branching fraction into the measured decay modes in the denominator.

D.3 Binning the Monte Carlo Cross Section

This appendix discusses the construction of partial cross sections C_α (section 6.2.1) from the cross section information provided with each Monte Carlo event.

The **R** matrix, defined in Equation 6.4, is formed by binning Monte Carlo events in both i (x_f^*,ω^*) and α (x_f,ω) bins. Each element $R_{i\alpha}$ is then a count of the number of events in a bin α which are measured in a bin i, normalized by

C_α. The value C_α is related to the average of Monte Carlo cross sections in a particular bin α. In general the average value of the cross section over a specific interval in ω is given by

$$\bar{\sigma}(\omega) = \frac{\int_{\omega_1}^{\omega_2} \mathcal{P}(\omega)\sigma(\omega)d\omega}{\int_{\omega_1}^{\omega_2} \mathcal{P}(\omega)d\omega} \qquad (D.10)$$

where $\mathcal{P}(\omega)$ is a function describing the population of photons as a function of energy. If the energy interval defined in Equation D.10 is to form part of the limits of a bin α then ω_1^α and ω_2^α must be well separated to reduce correlations. But large α bins will introduce production model dependencies through the ρ matrix because $\sigma(\omega)$ will vary considerably in the interval $\omega_2^\alpha - \omega_1^\alpha$. Since each energy interval $\omega_2 - \omega_1$ must necessarily be large in order to reduce correlations, $\sigma(\omega)$ introduces model dependencies in the α interval $\omega_2^\alpha - \omega_1^\alpha$. If the interval is divided into many small bins such that $\mathcal{P}(\omega)\sigma(\omega)$ does not vary significantly over a range ϵ, then the average cross section in each small bin is

$$\bar{\sigma}_\epsilon(\omega) = \frac{1}{2\epsilon}\int_{\bar{\omega}-\epsilon}^{\bar{\omega}+\epsilon} \sigma(\omega)d\omega \qquad (D.11)$$

which, when represented as a summation, is just a numerical average.

Equation 6.8 defines the average partial cross section in a bin α

$$\overline{\frac{d\sigma}{dx_f}}(\omega_\alpha, x_{f\alpha}) = \frac{1}{\Delta\omega_\alpha}\int_{\omega_1^\alpha}^{\omega_2^\alpha} \sigma(\omega)d\omega \quad \frac{1}{\Delta x_{f\alpha}}\int_{x_1^\alpha}^{x_2^\alpha} f_x(x_f)dx_f \qquad (D.12)$$

Equation D.11 can be used to yield a relation for the energy dependence in Equation D.12

$$\int_{\omega_1^\alpha}^{\omega_2^\alpha} \sigma(\omega)d\omega = \sum_{\epsilon\in\alpha} \bar{\sigma}_\epsilon(\omega)\Delta\omega_\epsilon$$

The x_f dependence is just the fraction of the events in an ω bin which are in a particular x_f interval, so that

$$\int_{x_1^\alpha}^{x_2^\alpha} f_x(x_f)dx_f = \frac{N(\Delta x_{f\alpha}, \Delta\omega_\alpha)}{N(\Delta\omega_\alpha)}$$

From the definition of C_α

$$C_\alpha = \Delta\omega_\alpha \Delta x_f \, \overline{\frac{d\sigma}{dx_f}}(\omega_\alpha, x_{f\alpha})$$

an expression is obtained by substitution of the preceding formulae

$$C_\alpha = \frac{N(\Delta x_{f\alpha}, \Delta\omega_\alpha)}{N(\Delta\omega_\alpha)} \sum_{\epsilon\in\alpha} \bar{\sigma}_\epsilon(\omega)\Delta\omega_\epsilon \qquad (D.13)$$

Thus the value of C_α can be found by summing over narrow ϵ entries, each of which is the numerical average of the cross section in a histogram bin (like the standard PLOT function used in this analysis), weighted by their bin widths. The factor dealing with the fraction of the x_f distribution can be found either by a histogram method or direct integration of the generated distribution.

Appendix E

Statistical Uncertainties in the Cross Section

The cross section in a particular bin α is given by Equation 6.5 by

$$C_\alpha = \rho_{\alpha i}\, n_i$$

where a sum over the repeated index i is implied. Elements of the cross section covariance matrix are $\langle \delta C_\alpha \delta C_\beta \rangle$ where

$$\delta C_\alpha = \rho_{\alpha i}\, \delta n_i + (\delta \rho_{\alpha j}) n_j$$

Under the assumption that n_i are Poisson distributed and their errors uncorrelated,

$$\langle \delta n_i \delta n_j \rangle = n_i \delta_{ij}$$

so that

$$\langle \delta C_\alpha \delta C_\beta \rangle = \rho_{\alpha i}\, \rho_{\beta i}\, n_i + \langle \delta \rho_{\alpha j} \rho_{\beta l} \rangle\, n_j\, n_l \qquad (E.1)$$

The first term in this expression represents correlations due to variations in the data. Since the matrix ρ is a construct of the Monte Carlo, the second term reflects the effects of Monte Carlo statistics and will vanish in the limit of large statistics.

$$\langle \delta C_\alpha \delta C_\beta \rangle = \rho_{\alpha i}\, \rho_{\beta i}\, n_i \qquad (E.2)$$

The statistical variance of cross section measurements are then

$$\sigma(C_\alpha) = \langle \delta C_\alpha \delta C_\alpha \rangle = \rho_{\alpha i}\, \rho_{\alpha i}\, n_i \qquad (E.3)$$

The second term in Equation E.1 describes uncertainties in the cross section due to fluctuations in the Monte Carlo. This term can be re-written in the case of correctly determined cross sections

$$n_i = R_{i\beta}C_\beta \quad , \quad n_j = R_{j\gamma}C_\gamma$$

$$\sigma^2_{mc} = \langle R_{i\beta}\delta\rho_{\alpha i}\, R_{j\gamma}\delta\rho_{\alpha j}\rangle C_\beta C_\gamma \tag{E.4}$$

In the case when the ρ matrix fit is just constrained, $\rho = R^{-1}$. The resultant errors should not differ significantly from the over constrained case so that fluctuations in ρ and R are correlated

$$\begin{aligned}(\rho_{\alpha i} + \delta\rho_{\alpha i})(R_{i\beta} + \delta R_{i\beta}) &= 1\\ \text{or} \quad \delta\rho_{\alpha i}\, R_{i\beta} &= -\rho_{\alpha i}\, \delta R_{i\beta}\end{aligned} \tag{E.5}$$

Using Equation E.5 to manipulate Equation E.4 yields

$$\sigma^2_{mc} = \rho_{\alpha i}\langle \delta R_{i\beta}\delta R_{j\gamma}\rangle \rho_{\alpha j} C_\beta C_\gamma \tag{E.6}$$

Together Equations E.8 and E.9 describe the relation between the R matrix in data and Monte Carlo

$$R^{data}_{i\alpha} = g\, R^{mc}_{i\alpha}$$

so that the bracketed term in Equation E.6 can be written as

$$\begin{aligned}\langle \delta R_{i\beta}\delta R_{j\gamma}\rangle &= \frac{g^2}{C^{mc}_\beta C^{mc}_\gamma}\langle \delta m_{i\beta}\, \delta m_{j\gamma}\rangle\\ &= \frac{g^2}{C^{mc}_\beta C^{mc}_\gamma} m_{i\beta}\delta_{ij}\delta_{\beta\gamma}\end{aligned}$$

where $m_{i\beta}$ represents Monte Carlo events. This may be substituted into Equation E.6 . If $C^{mc} = C^{data}$ it then becomes

$$\sigma^2_{mc} = g^2\, \rho^2_{\alpha i}\, m_i$$

where a sum over beta is implied. This is close in appearance to the first term in Equation E.1 . Under the assumption that the data and Monte Carlo cross sections are close,

$$n_i = g\, m_i \tag{E.7}$$

which follows from Equations E.8 and E.9 . Equation E.1 becomes

$$\langle \delta C_\alpha \delta C_\alpha \rangle = (1 + g)\, \rho_{\alpha i}^2 n_i$$

Summing Equation E.7 over i gives $g = N_{data}/N_{mc}$ so that taking into account Monte Carlo statistics amounts to rescaling the statistical errors from data by

$$\sigma(C_\alpha) = \sigma_o(C_\alpha) \sqrt{1 + \frac{N_{data}}{N_{mc}}} \tag{E.8}$$

Appendix F

Statistical Analysis of the Lifetime Fit

The maximum likelihood fit of lifetime distributions will return an error related to statistical fluctuations in the signal region of the fit. Contributions to distribution function (Equation 7.6) from the Monte Carlo and sideband events are not parameters of the fit. Therefore statistical fluctuations in these quantities must be considered as well in reporting an overall statistical uncertainty.

In general an element in the the fit parameter covariance matrix of a likelihood fit is

$$\langle \delta\alpha_i \delta\alpha_j \rangle = \left[\int d\vec{x} \frac{1}{\mathcal{L}(\vec{x})} \frac{\partial \mathcal{L}(\vec{x})}{\partial \alpha_i} \frac{\partial \mathcal{L}(\vec{x})}{\partial \alpha_j} \right]^{-1}$$

where $\mathcal{L}(\vec{x})$ represents the probability distribution of the data in the variables $\vec{x}$ with associated parameters $\vec{\alpha}$. For the specific case of this lifetime fit where τ is the only parameter, the variance about $\mathcal{L}(t;\tau)$ is

$$\frac{1}{\sigma_\tau^2} = \int dt \frac{1}{\mathcal{L}(t;\tau)} \left(\frac{\partial \mathcal{L}(t;\tau)}{\partial \tau} \right)^2 \qquad (F.1)$$

When N_D is a binned variable with infinitesimally small bins, and the predicted values μ_i are near the observed values N_i, the factors in the sum can be interpreted as

$$\Delta t \frac{\partial \mu_i}{\partial \tau} \qquad \text{changes in the fit } \chi^2$$

$$\frac{1}{\mu_i \Delta t} = \frac{1}{\sigma^2} \qquad \text{Poisson variance (reciprocal) of } \mu \text{ in a bin } i$$

This variance can be written as $\sigma^2(N_i - \mu_i)$. Equation F.1 is then

$$\frac{1}{\sigma_\tau^2} = \Delta t \sum_i \frac{1}{\sigma^2(N_i - \mu_i)} \left(\frac{\partial \mu_i}{\partial \tau} \right)^2 \qquad (F.2)$$

As discussed in section 7.2 the predicted distribution is $\mu_i = N_i^{s,p} + R\ N_i^{sb}$, where $N_i^{s,p} = N_D^{tot} f_i(t_i) \exp^{-t_i/\tau}/\tau$ and N_i^{sb} are the actual events from the sidebands.

Each element contributes separately to the variance

$$\begin{aligned}\sigma^2(N_i-\mu_i) &= \sigma^2(N_i)+\sigma^2(\mu_i)\\ &= \sigma^2(N_i)+\sigma^2(N_i^{s,p})+R^2\sigma^2(N_i^{sb})\end{aligned} \tag{F.3}$$

To some degree, then, their overall contributions to σ_τ^2 may be treated separately as well.

Uncertainty from sideband

When considering only the contribution to the uncertainty from the background prediction, Equation F.3 becomes

$$\sigma^2(N_i-\mu_i)=N_i+R^2\ N_i^{sb}$$

assuming $\sigma^2(N_i^{s,p})=0$ and normal statistical fluctuations of N_i and N_i^{sb}. Returning to Equation F.2, an expression can be written for the statistical contribution of the sideband regions to the anticipated uncertainty σ_T. A ratio of this number to one with no sideband uncertainty yields an estimate for the increase in statistical errors.

$$\sigma_\tau^2=\sigma_{\tau,fit}^2\ \frac{\displaystyle\sum_i\frac{(\partial\mu_i/\partial\tau)^2}{N_i}}{\displaystyle\sum_i\frac{(\partial\mu_i/\partial\tau)^2}{N_i+R^2N_i^{sb}}}$$

Uncertainty from Monte Carlo

Statistical uncertainties from the Monte Carlo enter the predicted lifetime distribution $\mu(t;\tau)$ through $f(t)$. In analogy with the sideband discussion, the effect of finite Monte Carlo statistics on σ_τ is calculated independently. Thus neglecting background contributions, Equation F.3 becomes

$$\begin{aligned}\sigma^2(N_i-\mu_i) &= \sigma^2(N_i^s+N_i^{s,p})\\ &= \sigma^2(N_i^s)+\sigma^2(N_i^{s,p})\\ &= N_i^s+\frac{(N_i^{s,p})^2}{N_i^{mc}}\end{aligned} \tag{F.4}$$

In the last step the relationship between the variance of the Monte Carlo sample and that of the predicted signal distribution is used

$$\frac{\sigma^2(N_i^{s,p})}{(N_i^{s,p})^2} = \frac{\sigma^2(N_i^{mc})}{(N_i^{mc})^2} = \frac{1}{N_i^{mc}}$$

At the minimization point of the fit, $N_i^s \simeq N_i^{s,p}$. The Monte Carlo distribution should also be the same as the data, $N_i^s \propto N_i^{mc}$ provided the generated lifetime was close to the fit value, $\tau_D \approx \tau_p$. Thus

$$\frac{N_i^s}{N_i^{mc}} = \frac{N_D^{tot}}{N_{mc}}$$

and

$$\sigma^2(N_i - \mu_i) = N_i^s \left(1 + \frac{N_D^{tot}}{N_{mc}}\right)$$

The enclosed term can then be removed from the integral in Equation F.1 and a ratio of statistical uncertainties written

$$\sigma_\tau^2 = \sigma_{\tau,fit}^2 \sqrt{1 + \frac{N_D^{tot}}{N_{mc}}}$$

where the value of $\sigma_{\tau,fit}^2$ assumes errors appropriate to $N_{mc} = \infty$.

References

1. L.M. Jones and H.W. Wyld, Phys. Rev. **D17**:759 (1978)
2. J.C. Anjos et al. (E691), Phys. Rev. Lett. **62**:513 (1989)
3. J.J. Aubert et al., Nucl. Phys. **B213**,31 (1983)
4. K. Lingel, Ph.D. Thesis, University of Illinois, (1990) unpublished.
5. R.J. Morrison and M.S. Witherall, Ann. Rev. Nucl. and Part. Sci., **39**:183 (1989)
6. Abrams et al. (Mark II), Phys. Rev. Lett. **43**:481
7. R.M. Baltrusaitus et al. (Mark III),Phys. Rev. Lett. **55**:150 (1985)
8. Particle Data Group, Phys. Lett. **B204** (1988)
9. K. Lingel, "Photon Energy Measurement", E687 Internal Memo (1989)
10. K. Lingel, "Luminosity and Trigger Studies", E687 Internal Memo (1990)
11. P. Frabetti et al.,"D^+, D° Signals and Lifetimes in E687", Proceedings of the 25th International Conference on High Energy Physics, Singapore, August 1990.
12. J. Wiss and R. Culbertson, "DVERT", E687 Internal Memo (1989)
13. P. Sheldon, personal communication
14. K. Lingel, "ROGUE Improvements", E687 Internal Memo (1989)
15. S. Park, Ph.D. Thesis, Northwestern University, (1990) unpublished.
16. J. Wiss and K. Lingel, "Finding Cross Sections", E687 Internal Memo (1989)
17. S. Barlag et al. (ACCMOR), Phys. Lett. **B232**:561
18. S. Holmes et al., Ann. Rev. Nucl. Part. Sci. **35**:397-454 (1985)
19. K. Lingel, "Targeting Studies", E687 Internal Memo (1990)

20. R. Forty, Proceedings of the XXIV Conference on High Energy Physics, Munich, Springer-Verlag (Berlin 1989) p.668

21. M. Purohit, "Heavy Quark Production and QCD", FNAL pub. FERMILAB-Conf-88/191 (1988)

22. H. Bengtsson and T. Sjöstrand, "The Lund Monte Carlo for Hadronic Processes–PYTHIA version 4.8 ", Comput. Phys. Commun. **46**:43 (1987)

23. R. Ellis and P. Nason, Nucl. Phys. **B312**:551 (1989)

24. R. Culbertson and J. Wiss, "D° Lifetime Study", E687 Internal Memo (1990)

25. J. Anjos et al. (E691), Phys. Rev. Lett., **58**:311 (1987)

26. H. Albrecht et al. (ARGUS), Phys. Lett., **B210**:267 (1988)

27. M. Aguilar-Benitez et al. (LEBC-EHS), Phys. Lett., **B193**:1401 (1988)

28. S. Csorna et al. (CLEO), Phys. Lett., **B191**:318 (1987)

29. S. Barlag et al. (ACCMOR), Zeit. Phys., **C37**:17 (1987)

30. N. Ushida et al. (HES), Phys. Rev. Lett., **56**:1771 (1986)

31. P. Frabetti et al., "Measurement of the Λ_c^+ and D_s^+ Lifetimes", submitted to Phys. Lett. B (September 1990)

32. F. DeJongh, Symposium on Heavy Quark Physics, Cornell (June 1989) p.197

Vita

Glen Jaross was born in Idaho Falls, Idaho on October 26, 1960 and moved to Illinois at an early age. He attended Sandwich Community High School from 1974 to 1977, spending his senoir year as an exchange student in Iceland. In spite of receiving his first formal physics training in Icelandic (or possibly because of it) he chose the physics curriculum at the University of Illinois as his undergraduate major. He graduated with a B.S. degree in Engineering Physics in May of 1982. His senior project involved the study of differential rotation in neutron stars. Two of his summers as an undergraduate, plus one after graduating, were spent working on nuclear reactor safety at Argonne National Laboratory.

During the first two years in graduate school Glen was a lab instructor and grader for an undergraduate optics course, and studied high energy phenomenology briefly before joining the E687 group in 1984. He was married in 1988 and his first gray hairs were noticed just several months prior to completing this thesis.